Dipartimento Interateneo di Fisica "M. Merlin"

DOTTORATO DI RICERCA IN FISICA
Ciclo XXXI
Settore scientifico disciplinare Fis/01

Search for resonances decaying into muon pairs with the CMS experiment at LHC

Dottorando:
Filippo Errico

Supervisore:
Dott.ssa Anna Colaleo

Coordinatore:
Ch.mo Prof. Giuseppe Iaselli

ESAME FINALE 2019

Contents

Introduction

The current understanding of particle physics is well described by the so-called Standard Model (SM). Developed during the '60s, it has predicted a wide variety of physics phenomena, confirmed experimentally, crowned by the discovery of the Higgs boson in 2012.
The discovery of the Higgs boson at the Large Hadron Collider (LHC) has opened a completely new path of investigation. Increased understanding of the properties of this new, very special particle remains a key focus of analysis at the LHC. as well as the searches for new physics phenomena. In fact, despite the Higgs boson observation, the SM is not complete and there are physics aspects it is not able to take into account. In order to solve these issues, many models have been developed beyond the Standard Model (BSM) and within these, new bosons are introduced.
This Ph.D. thesis deals with the search for resonances decaying into muon[1] pairs with the CMS experiment at LHC. Two different dimuon mass spectra have been investigated: low mass, for the Standard Model Higgs and high mass, for new narrow resonances (with a mass of the order of TeV) predicted in several models BSM, decaying into muons.
Muons play a central role in the CMS experiment being the most natural and powerful tool to detect interesting events over the background. They are less affected than electrons by radiative losses in the tracker material, stand out after the high magnetic field and stand out from the large hadronic background typical of hadron colliders. CMS has a dedicated system to detect muons (the so called muon system) composed of different detectors which allows to measure muon momentum with good precision till the order of TeV. Very accurate and efficient algorithms have been developed to reconstruct and identify muon over a large momentum spectrum. In particular for high-energetic muon, CMS has also developed specialised algorithms for reconstruction and momentum assignment which take into account multiple scattering and radiative processes. I have deeply studied the performance of these new algorithms with the aim to evaluate their impact on the search for the Higgs boson and physics BSM with muons in the final state.
The Higgs boson observation in 2012 has been driven by $H \to ZZ^*$ and $H \to \gamma\gamma$ decay modes, thanks to their very high sensitivity. In the last years, the observation has been done also in $b\bar{b}$, $\tau^+\tau^-$ and WW^* decay channels. Despite the $H \to \mu\mu$ observation still misses, this decay mode plays a fundamental role to study the properties of the second generation leptons. This decay channel is the only way to directly measure the

[1] In this thesis the term muons describes both muons and anti-muons, unless stated otherwise.

Higgs-muon Yukawa coupling strength. Latest CMS published results, using 2016 data, for the SM Higgs boson decaying into muon pairs are 2.45 on the expected cross section ratio (σ/σ_{SM}) at the 95% C.L. upper limit and an expected significance of 0.9 standard deviations [1]. For ATLAS collaboration instead, the expected upper limit on the σ/σ_{SM} is 3.1 at the 95% C.L. for a Higgs boson mass of 125 GeV [2]. In order to improve the cross section ratio and the significance, I have conducted a feasibility study on the use of the multivariate analysis (MVA) to distinguish signal events from the backgrounds in dimuon decay from the Vector Boson Fusion (VBF) production of the SM Higgs boson. About high mass region, new physics could manifest itself in a change of the dilepton invariant mass spectrum. The production cross section of the new massive particles is very small compared to the one from the Z boson, but already a few reconstructed events at very high mass, on top of the small non-resonant background contribution from SM processes, can lead to a discovery. High accuracy in muon reconstruction and a well known background, make the dimuon final state a golden channel for new physics searches. CMS collaboration has previously reported searches for new massive resonances decaying into muon pairs [3] combining 20 fb^{-1} from Run I at 8 TeV with 3 fb^{-1} from 2015 Run II data at 13 TeV. The results have been found consistent with Standard Model predictions and exclude at 95% C.L. a Z'_{SSM} from the Sequential Standard Model with SM-like couplings, with a mass less than 3.22 TeV and a Z'_{ψ} from Grand Unified Theories with the E_6 gauge group, with a mass less than 2.77 TeV. The corresponding limits for Kaluza-Klein gravitons arising in the Randall-Sundrum model of Extra Dimensions with coupling parameters 0.01 and 0.10 are 1.26 and 3.03 TeV, respectively. Same models have been tested also by the ATLAS Collaboration: 2.83 TeV lower limit for the mass of Z'_{SSM} and 2.29 for Z'_{ψ} [4]. In this thesis, I have tested different models BSM using 2016 and 2017 data.

The thesis is structured in 5 chapters.
Chapter 1 describes the theoretical framework of the Standard Model with the basilar concepts of different models Beyond the Standard Model (BSM).
Chapter 2 presents the experimental framework: the Large Hadron Collider and the main components of the CMS apparatus are described.
Chapter 3 explains the algorithms used in CMS for the reconstruction and identification of the main physics objects. Muon reconstruction and identification performance are treated in more details.
Chapter 4 presents the new approach of using multivariate analysis on the search for the SM Higgs boson produced via VBF and decaying into two muons. The objects selection, the MVA methods optimisation and validation and the statistical interpretation of the results are described.
Chapter 5 reports the search for new resonances decaying into two muons describing muon reconstruction and selection, muon momentum scale and dimuon mass resolution measurement, background estimation, invariant mass spectrum and statistical interpretation of the results in different theoretical models.

VBF Higgs boson production decaying into muon pairs search has been presented during the CMS Collaboration Meeting in Budapest on the 4th of October 2018. Due to the very promising results, the VBF channel treated with the MVA method will be used in combination with the other production modes to extract final results on the search for the Higgs boson, in view of the 2019 Winter conferences.
The search for new resonances, with 2016 and 2017 data, has been approved on the 9th of January 2019 by the CMS Collaboration. I have presented results using 2016 data [5] at La Thuile conference, during the *Les Rencontres de Physique de la Vallèe d'Aoste* at the end of February 2018.

Chapter 1

The Standard Model and beyond

Particle Physics studies the building blocks of the matter, the so called fundamental particles, and how their interactions are governed by the four fundamental forces[1].
The best theory, explaining our understanding of these particles and forces, is the Standard Model (SM). Developed during the '60s, it has successfully explained almost all experimental results and precisely predicted a wide variety of physics phenomena. Nevertheless, there are fundamental physics observations in nature that the SM is not equipped to address, thus leading to the formulation of theories aiming to extend it.
In this chapter, the theoretical framework of the Standard Model is given with the basilar concepts of different models Beyond the Standard Model (BSM), used to interpret the experimental results of the research.

1.1 The Standard Model

1.1.1 Fundamental Particles

The SM describes the Universe in terms of fermions (spin s = 1/2), representing the fundamental blocks of observable matter, and bosons (integer spin), representing the force carriers.
All matter around us is made of elementary particles with no substructure, all having half-integer spin. These particles are divided into two groups: *leptons*, with an entire value of electric charge, and *quarks*, with a fractional charge. Each group consists of six particles, which are related in pairs or generations. The six quarks are paired in three generations: the up and the down quark form the first generation (u, d), followed by the charm and strange (c, s), then the top and bottom (or beauty) quark (t, b). The six leptons are also similarly arranged in three generations: the electron (e) and the electron neutrino (ν_e), the muon (μ) with the muon neutrino (ν_μ), and the tau (τ) with the tau

[1] In the thesis, Natural Units will be used: $c = \hbar = 1$, where $\hbar = h/2\pi = 6.58211889(26) \cdot 10^{-23} MeVs$ and $c = 299792458\ ms^{-1}$.

neutrino (ν_τ). While electron, muon and tau are charged particles, the neutrinos are electrically neutral. Table 1.1 and 1.2 summarise the properties of leptons and quarks.

Lepton				
Flavor	Charge	Mass [MeV]	Spin	Lepton number
electron neutrino (ν_e)	0	< 0.002	1/2	1
electron (e)	-1	0.511	1/2	1
muon neutrino (ν_μ)	0	< 0.19	1/2	1
muon (μ)	-1	105.66	1/2	1
tau neutrino (ν_τ)	0	< 18.2	1/2	1
tau (τ)	-1	1776.86±0.12	1/2	1

Table 1.1: Standard Model lepton properties [6].

Quark				
Flavor	Charge	Mass [GeV]	Spin	Baryon number
up (u)	+2/3	$0.0022^{+0.0006}_{-0.0004}$	1/2	1/3
down (d)	-1/3	$0.0047^{+0.0005}_{-0.0004}$	1/2	1/3
charm (c)	+2/3	1.28 ± 3	1/2	1/3
strange (s)	-1/3	0.096 ± 0.084	1/2	1/3
top (t)	+2/3	173.1 ± 0.6	1/2	1/3
bottom (b)	-1/3	$4.18^{+0.04}_{-0.03}$	1/2	1/3

Table 1.2: Standard Model quark properties [6].

Beside leptons and quarks, there are other particles, called *bosons*, responsible of carrying (or mediating) the fundamental forces and all having integer spin. Electromagnetic Force, responsible of all electrical and magnetic phenomena, is mediated by the photons γ; the Weak Force, which acts on particles with weak charge and is responsible of processes like beta-decay, is mediated by $W^\pm$ and Z bosons; the Strong Force, which acts on particles with color charge and is responsible for the attracting force between quarks, is mediated by the gluons (g). Last fundamental force, but not yet included in the SM due to its low strength compared to the others (it is the weakest), is the Gravity. Table 1.3 summarises the properties of the bosons.
A fundamental component of the Standard Model is the Higgs boson (H), a scalar particle ($spin = 0$) responsible for particle's mass generation through a spontaneous symmetry breaking mechanism that is commonly known as *the Higgs mechanism*. The Higgs particle couples to any other particle which has mass, including itself.
Figure 1.1 shows the elementary particles described above.

Bosons	Interaction	Charge	Mass [GeV]	Spin
photon (γ)	Electromagnetic	0	0	1
$W^{\pm}$	Weak	± 1	80.385$\pm$0.015	1
Z^0	Weak	0	91.1876$\pm$0.0021	1
gluons	Strong	0	0	1

Table 1.3: Standard Model bosons features [6].

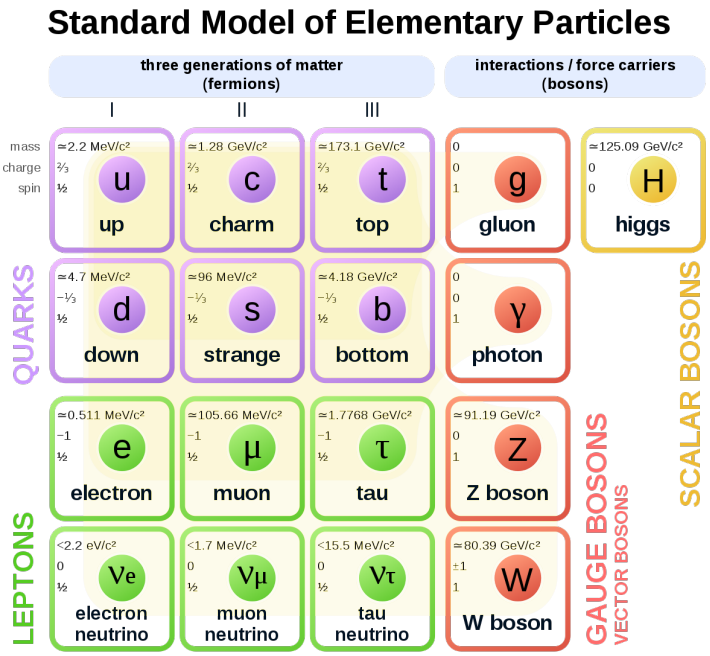

Figure 1.1: Elementary particles.

1.1.2 Gauge Symmetries

From the theoretical point of view, the SM is based on the idea that all interactions in nature are manifestation of symmetry properties and that they are in terms of irreducible representations of symmetry groups. For the SM, the associated symmetry group can be written as:

$$SU(3)_C \otimes SU(2)_L \otimes U(1)_Y$$

where $SU(3)_C$ is the non-abelian group of strong interaction (QCD) and $SU(2)_L \otimes U(1)_Y$ is the group of the electroweak sector (EWK) in which the Electromagnetic and the Weak forces are described by one unified theory.

In Quantum Field Theory (QFT) the gauge invariance is the key for the description of all the interactions in nature. The innovative idea is the requirement of an invariance under local symmetry transformations of the gauge groups. The conservation laws and the description of the interactions depend on the symmetry properties of the Lagrangian. What is relevant is the study of the Lagrangian transformation properties under the so called "internal symmetries". These particular transformations do not involve the space - time coordinate x_μ, from which the fields depend, and reduce essentially to a phase transformation.

Quantum Electrodynamics (QED)

Quantum Electrodynamics (QED) is the relativistic quantum field theory of electrodynamics. QED mathematically describes all phenomena involving electrically charged particles interacting by means of exchange of photons.
A free electron with mass m is described by a doublet of complex fields ψ with the Lagrangian

$$\mathcal{L} = \bar{\psi}(i \not{\partial} - m)\psi \tag{1.1}$$

Its equation of motion can be deduced by the Dirac Equation

$$(i \not{\partial} - m)\psi = 0 \tag{1.2}$$

The electromagnetic field is described by the four-vector gauge potential A_μ. The field strength tensor is defined as:

$$F_{\mu\nu} = \partial_\mu A_\nu - \partial_\nu A_\mu \tag{1.3}$$

and the equation of motion, in presence of an external current J^μ is:

$$\partial_\mu F^{\mu\nu} = QeJ^\nu \tag{1.4}$$

In case now the electron interacts with the electromagnetic field, the new Lagrangian is:

$$\mathcal{L}_{EM} = \bar{\psi}(i\gamma^\mu D_\mu - m)\psi - \frac{1}{4}F_{\mu\nu}F^{\mu\nu} \tag{1.5}$$

where D_μ, known as covariant derivative, is defined as

$$D_\mu = \partial_\mu + ieQA_\mu \tag{1.6}$$

and the last term in 1.5 stands for Maxwell's equation.
It can be demonstrated that 1.5 is invariant under the phase transformation:

$$\psi(x) \to e^{-iQ\theta}\psi(x) \tag{1.7}$$

with $\theta \in \Re$. This transformation belongs to the group $U(1)_{em}$ and according to Noether's theorem[2], it implies the existence of a conserved quantity: in this case, the electric charge. Since once the value of θ is fixed, the invariance is specified for all space and time, it is known as *global gauge invariance*.
More interesting is the case in which the parameter θ depends on space and time in a completely arbitrary way:

$$\psi(x) \to e^{-iQ\theta(x)}\psi(x) \tag{1.8}$$

and the Lagrangian 1.5 is not invariant. It can be demonstrated that, in oder to restore the Lagrangian invariance, the potential A_μ must satisfy following condition:

$$A_\mu \to A_\mu + \frac{1}{e}\partial_\mu\theta \tag{1.9}$$

Under 1.8 and 1.9 the Lagrangian 1.5 is invariant. Since θ depends on x_μ, this invariance is known as *local gauge invariance*.
It can be observed the absence of mass term in the Lagrangian: this means that the boson associated to the potential A_μ, the photon, must be massless. The presence of a mass term would make the Lagrangian not invariant under gauge transformation.

Quantum Chromodynamics (QCD)

The interaction between quarks and gluons is described by the Quantum Chromodynamics.
A new quantum number is introduced in the theory, the colour, such that each species of quark may have three different colours: $q_{j,\ j=1,2,3}$ (red, green, blue). In order to avoid the existence of non-observed extra states with non-zero colour, one needs to further postulate that all asymptotic states are colourless, i.e. singlets under rotations in colour space. This assumption is known as the confinement hypothesis, because it implies the non-observability of free quarks: since quarks carry colour they are confined within colour-singlet bound states.
For free quark described by the field q_j, the Lagrangian is:

$$\mathcal{L} = \bar{q_j}(i\ \not{\partial} - m)q_j \tag{1.10}$$

[2]A Lagrangian invariant under a continuous group of transformations corresponds to a conservation law.

In order to describe the interaction between quarks and gluons, it is needed to change the quark derivative by covariant objects. Since there are now eight independent gauge parameters, eight different gauge bosons $G_a^\mu(x)$, the so-called gluons, are needed:

$$D_{q_j}^\mu = \partial^\mu - ig_s \frac{\lambda^a}{2} G_a^\mu(x) \tag{1.11}$$

where g_s is the coupling constant and λ^a are the 8 3×3 Gell-Mann matrices. The corresponding field strengths are also introduced:

$$G_a^{\mu\nu} = \partial^\mu G_a^\nu - \partial^\nu G_a^\mu + g_s f^{abc} G_b^\mu G_c^\nu \tag{1.12}$$

Hence, in case of interaction, the new Lagrangian is:

$$\mathcal{L}_{QCD} = \bar{q_j}(i\gamma^\mu D_\mu - m)q_j - \frac{1}{4} G_a^{\mu\nu} G_{\mu\nu}^a \tag{1.13}$$

It can be shown 1.13 is invariant under arbitrary global $SU(3)_C$ transformations in colour space 1.14:

$$q(x) \to q'(x) = Uq(x) \equiv e^{i\theta_a T^a} q(x), \quad a = 1, 2, ..., 8 \tag{1.14}$$

where T_a are the generators of the SU(3) (a $= N^2 - 1 = 3^2 - 1 = 8$) group linked with the λ_a matrices.
More interesting is the case in which θ depends on local coordinates, $\theta_a = \theta_a$(x):

$$q(x) \to q'(x) = Uq(x) \equiv e^{i\theta_a(x)\frac{\lambda^a}{2}} q(x), \quad a = 1, 2, ..., 8 \tag{1.15}$$

The group is non-Abelian since not all the generators λ_a commute with each other.
To ensure the invariance of the Lagrangian 1.13, the gauge fields must transform as follow:

$$G_{\mu a} \to G_{\mu a} - \frac{1}{g_s} \partial_\mu \theta_a - f_{abc} \theta^b G_\mu^c \tag{1.16}$$

The field tensor $G_a^{\mu\nu}$ has a remarkable new property: imposing gauge symmetry (1.15 and 1.16), it has required kinematic energy term in 1.13 that is not purely kinetic but includes an induced self-interaction between the gauge bosons. Decomposing the Lagrangian into its different pieces, there are three terms analogues to QED describing the free propagation of quarks and gluons and the quark-gluon interaction and two terms showing the presence of three and four gluon self-coupling in QCD reflecting the fact that gluons themselves carry color charge. They have no analogue in QED and arise on account of the non-Abelian character of the gauge group. As in QED, the absence of a mass term implies gluons must be massless.

The electroweak theory

Developed in 1961 by Glashow, the Electroweak theory is the unified theory of the Weak and Electromagnetic force.
Low-energy experiments have provided a large amount of information about the dynamics underlying flavour-changing processes. The detailed analysis of the energy and angular distributions in β decays, such as $\mu^- \to e^- \bar{\nu}_e \nu_\mu$, made clear that only the left-handed (right-handed) fermion (antifermion) chiralities participate in those weak transitions. Moreover, the strength of the interaction appears to be universal.
Using gauge invariance, it is possible to determine the QED (1.5) and QCD (1.13) Lagrangians. To describe weak interactions, a more elaborated structure is needed, with several fermionic flavours and different properties for left- and right-handed fields. Moreover, the left-handed fermions should appear in doublets, and would like to have gauge bosons in addition to the photon. The simplest group with doublet representations is SU(2) while to include also the electromagnetic interactions an additional U(1) group is needed. The obvious symmetry group to consider is then:

$$G \equiv SU(2)_L \otimes U(1)_Y \tag{1.17}$$

where L and Y are the left-handed weak isospin and the hypercharge, related to the electromagnetic charge through the equation Q = Y/2 + T_3. The $U(1)_Y$ gauge group should not be mistaken for the $U(1)_{em}$ one: the generator of $U(1)_{em}$ is the electromagnetic charge Q, while Y is the generator of $U(1)_Y$, and T_3 is one of the $SU(2)_L$ generators (a component of weak isospin).
A single family of lepton can be described as

$$\chi_L = \begin{pmatrix} \nu_l \\ l^- \end{pmatrix}_L, \quad \psi_R = l_R^- \tag{1.18}$$

or for quarks

$$\chi_L = \begin{pmatrix} u \\ d \end{pmatrix}_L, \quad \psi_R = u_R, \ or \ d_R \tag{1.19}$$

As in QED and QCD case, start with free Lagrangian:

$$\mathcal{L} = i\bar{\chi}_L \gamma^\mu \partial_\mu \chi_L + i\bar{\psi}_R \gamma^\mu \partial_\mu \psi_R \tag{1.20}$$

The interaction is again introduced changing the derivative with the covariant:

$$D_\mu = \partial_\mu + igW_\mu^a T_a + ig' B_\mu Y \tag{1.21}$$

where W_μ^a a = 1, 2, 3 are the three gauge bosons associated with the group $SU(2)_L$, T^a its generators and g the coupling constants; B_μ, Y and g' are instead respectively the gauge boson, the generator and the coupling constant for the group $U(1)_Y$. With W_μ^a and B_μ can be introduced also the tensor strength fields:

$$\begin{aligned} W_a^{\mu\nu} &= \partial^\mu W_a^\nu - \partial^\nu W_a^\mu + g\epsilon^{abc} W_b^\mu W_c^\nu \\ B^{\mu\nu} &= \partial^\mu B^\nu - \partial^\nu B^\mu \end{aligned} \tag{1.22}$$

Therefore, the proper Lagrangian is given by:

$$\mathcal{L} = i\bar{\chi}_L \gamma^\mu D_\mu \chi_L + i\bar{\psi}_R \gamma^\mu D_\mu \psi_R - \frac{1}{4} B_{\mu\nu} B^{\mu\nu} - \frac{1}{4} W_{\mu\nu} W^{\mu\nu} \tag{1.23}$$

In 1.23 $W_{\mu\nu} = W^a_{\mu\nu}\sigma^a/2$ with σ^a 2×2 Pauli's matrices.
As in QED and QCD case, also electroweak interaction is invariant under global transformation:

$$\begin{aligned} \chi_L &\to \chi'_L = e^{i\alpha_a T^a + i\beta Y} \chi_L \\ \psi_R &\to \psi'_R = e^{i\beta Y} \psi_R \end{aligned} \tag{1.24}$$

Moving to local transformation, in order to guarantee Lagrangian 1.23 to be invariant, the gauge bosons must follow transformation rules:

$$\begin{aligned} &W^a_\mu \to U_L(x) W^a_\mu U_L(x)^\dagger - \frac{i}{g} \partial_\mu U_L(x) U_L(x)^\dagger, \\ &B_\mu \to B_\mu + \frac{1}{g'} \partial_\mu \beta \end{aligned} \tag{1.25}$$

where $U(x)_L = e^{i\sigma_a/2\ \alpha(x)^a}$. The transformation of B_μ is identical to the one obtained in QED for the photon, while the $SU(2)_L$ W^a_μ fields transform in analogous way to the gluon fields of QCD.
The gauge symmetry forbids to write a mass term for the gauge bosons in 1.23. Fermionic masses are also not possible, because they would break gauge symmetry since the left- and right-handed fields have different transformation properties. Thus, the $SU(2)_L \otimes U(1)_Y$ Lagrangian in 1.23 only contains massless fields.
The term containing the $SU(2)_L$ matrix:

$$\frac{\sigma_a}{2} W^a_\mu = \frac{1}{\sqrt{2}} \begin{pmatrix} \sqrt{2} W^3_\mu & W^+_\mu \\ W^-_\mu & -\sqrt{2} W^3_\mu \end{pmatrix} \tag{1.26}$$

gives rise to charged-current interactions with the bosons field $W^\pm_\mu \equiv (W^1_\mu \mp i W^2_\mu)/\sqrt{2}$. The Lagrangian 1.23 contains also interactions with the neutral gauge field W^3_μ and B_μ; one can define

$$Z_\mu = \frac{g W^3_\mu - g' B_\mu}{\sqrt{g^2 + g'^2}}, \quad A_\mu = \frac{g W^3_\mu + g' B_\mu}{\sqrt{g^2 + g'^2}} \tag{1.27}$$

and thinking them as a rotation, introducing the Weinberg angle θ_W, so that $\cos\theta_W = g/\sqrt{g^2 + g'^2}$ and $\sin\theta_W = g'/\sqrt{g^2 + g'^2}$:

$$Z_\mu = \cos\theta_W W^3_\mu - \sin\theta_W B_\mu, \quad A_\mu = \sin\theta_W W^3_\mu + \cos\theta_W B_\mu \tag{1.28}$$

or reversing:

$$\begin{pmatrix} W_\mu^3 \\ B_\mu \end{pmatrix} \equiv \begin{pmatrix} \cos\theta_W & \sin\theta_W \\ -\sin\theta_W & \cos\theta_W \end{pmatrix} \begin{pmatrix} Z_\mu \\ A_\mu \end{pmatrix} \tag{1.29}$$

With these definitions, it can be observed the A_μ in 1.23 couples in the same way with l_L and l_R as the photon; to get QED from these one needs to impose

$$g \sin\theta_W = g' \cos\theta_W = e \tag{1.30}$$

At the same time, Z_μ can be identified with the Z boson, mediator of the Weak Interaction.
Once again, no mass term is present in 1.23 and this means that $W^\pm$ and Z must be massless: this is in contrast with experimental evidence [7, 8].
The way to generate the mass of the particle is through the so called *Spontaneous Symmetry Breaking* mechanism (SSB): this mechanism appear in those cases where one has a symmetric Lagrangian, but a non-symmetric vacuum state.

1.1.3 Spontaneous Symmetry Breaking: SSB

Consider a complex scalar field $\phi(x) = (\phi_1 + \phi_2)/\sqrt{2}$, with Lagrangian:

$$\mathcal{L} \equiv T - V = (\partial_\mu \phi)^* (\partial^\mu \phi) - \mu^2 (\phi^* \phi) - \lambda (\phi^* \phi)^2 \tag{1.31}$$

1.31 is invariant under global phase transformation of the scalar field (it possesses a U(1) global gauge symmetry).
Considering the case when $\lambda > 0$, for the quadratic piece there are two possibilities:

- $\mu^2 > 0$: the potential has only the trivial minimum $\phi = 0$
- $\mu^2 < 0$: the minimum is every point belonging to the circle (in the ϕ_1, ϕ_2) of radius ν such that:

  $$(\phi_1)^2 + (\phi_2)^2 = \nu^2 \quad with\ \nu^2 = -\frac{\mu^2}{\lambda} \tag{1.32}$$

  as shown in Figure 1.2

Owing to the U(1) phase-invariance of the Lagrangian 1.31, there is an infinite number of degenerate states of minimum energy. By choosing a particular solution, $\phi_1 = \nu$ and $\phi_2 = 0$, as the ground state, the symmetry gets spontaneously broken. Parametrising the excitations over the ground state as:

$$\phi(x) \equiv \frac{1}{\sqrt{2}} [\nu + \eta(x) + i\xi(x)] \tag{1.33}$$

and substituting into 1.31, one obtains:

$$\mathcal{L}' = \frac{1}{2}(\partial_\mu \xi)^2 + \frac{1}{2}(\partial_\mu \eta)^2 + \mu^2 \eta^2 + const. + O(\eta^3) + O(\xi^3) \tag{1.34}$$

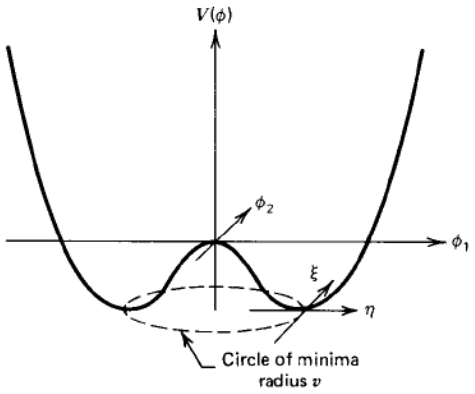

Figure 1.2: The potential $V(\phi)$ for a complex scalar field with $\lambda > 0$ and $\mu^2 < 0$.

The third term has the form of a mass term for η-field: the η-mass is $m_\eta = \sqrt{-2\mu^2}$. The first term in 1.34 represents the kinetic energy of the ξ-field but there is no corresponding mass term for the ξ. The fact there are massless excitations associated with the SSB mechanism is completely general result, known as the *Goldstone theorem*: if a Lagrangian is invariant under a continuous symmetry group G, but the vacuum is only invariant under a subgroup $H \subset G$, then there must exist as many massless spin-0 particles (Goldstone bosons) as broken generators (i.e., generators of G which do not belong to H).

Brout-Englert-Higgs mechanism

The SSB mechanism can be now studied for the U(1) local gauge symmetry.
Taking into account the covariant derivative 1.6, in which the gauge field transforms as in 1.9, the new Lagrangian can be written as

$$\mathcal{L} = D^\mu \phi^* D_\mu \phi - \mu^2 \phi^* \phi - \lambda(\phi^* \phi)^2 - \frac{1}{4} F_{\mu\nu} F^{\mu\nu} \tag{1.35}$$

If $\mu^2 > 0$, 1.35 is just the QED Lagrangian for a charged scalar particle of mass μ. For the case $\mu^2 < 0$, it is interesting to note that to lowest order in ξ, 1.33 can be expressed as

$$\phi(x) \equiv \frac{1}{\sqrt{2}}[\nu + \eta(x)] e^{i\xi(x)/\nu} \tag{1.36}$$

and this suggests to use different set of real field: h, θ, A_μ where now

$$\begin{aligned} \phi(x) &\to \frac{1}{\sqrt{2}}[\nu + h(x)] e^{i\theta(x)/\nu}, \\ A_\mu &\to A_\mu + \frac{1}{e\nu} \partial_\mu \theta \end{aligned} \tag{1.37}$$

This is a particular choice of gauge, with $\theta(x)$ chosen so that h is real. Substituting 1.37 in 1.35, one obtains:

$$\begin{aligned}\mathcal{L}' =& \frac{1}{2}(\partial_\mu h)^2 - \lambda\nu^2 h^2 + \frac{1}{2}e^2\nu^2 A_\mu^2 - \lambda\nu h^3 - \frac{1}{4}\lambda h^4 \\ &+ \frac{1}{2}e^2 A_\mu^2 h^2 + \nu e^2 A_\mu^2 h - \frac{1}{4}F_{\mu\nu}F^{\mu\nu}\end{aligned} \tag{1.38}$$

The Goldstone boson does not appear in the theory: this is because it corresponds only to the degree of freedom to make a gauge transformation. The Lagrangian 1.38 describes just two interacting massive particles, a vector gauge boson A_μ and a massive scalar h, which is called *Higgs particle*.
Consider now the case of $SU(2)_L \otimes U(1)_Y$ symmetry [9], with the Lagrangian

$$\mathcal{L} = (D_\mu\phi)^\dagger(D^\mu\phi) - \mu^2\phi^\dagger\phi - \lambda(\phi^\dagger\phi)^2 \tag{1.39}$$

D_μ is the covariant derivative 1.21 and ϕ is an SU(2) doublet of complex scalar fields:

$$\phi(x) \equiv \begin{pmatrix}\phi^+(x) \\ \phi^0(x)\end{pmatrix} \tag{1.40}$$

1.39 is invariant under local $SU(2)_L \otimes U(1)_Y$ transformations.
In $\mu^2 < 0$ and $\lambda^2 > 0$ conditions, to generate gauge boson masses, a vacuum expectation value of $\phi(x)$ must be chosen:

$$\phi_0 \equiv \frac{1}{\sqrt{2}}\begin{pmatrix}0 \\ \nu\end{pmatrix} \tag{1.41}$$

In this way, the symmetry is broken and this generates a mass for the corresponding gauge boson. This particular choice of ϕ_0 breaks both $SU(2)$ and $U(1)_Y$ gauge symmetries but since it is neutral, the $U(1)_{em}$ remains unbroken and this means the photon remains massless.
Now, substituting the vacuum expectation value ϕ_0 for $\phi(x)$ in the Lagrangian 1.39, the expression for W and Z bosons mass are:

$$M_W^2 = \frac{\nu^2 g^2}{4}, \quad M_Z^2 = \frac{\nu^2 g^2}{4\cos^2\theta_W} = \frac{M_W^2}{\cos^2\theta_W} \tag{1.42}$$

From experimental observation [6]:

$$M_Z = 91.1876 \pm 0.0021\ GeV, \quad M_W = 80.385 \pm 0.015\ GeV \tag{1.43}$$

From these experimental numbers, one obtains the electroweak mixing angle:

$$\sin^2\theta_W = 1 - \frac{M_W^2}{M_Z^2} = 0.22336 \pm 0.00010 \tag{1.44}$$

The scalar vacuum expectation value is:

$$\nu = (\sqrt{2}G_F)^{-1/2} = 246\ GeV \tag{1.45}$$

where $G_F = 1.1663787 \times 10^{-5} GeV^{-1}$ is the Fermi coupling whose value can be measured from muon lifetime [10].
From 1.39, the potential $V(\phi)$ can be seen as:

$$V(\phi) = -\frac{1}{4}\lambda\nu^2 + V_H + V_{HG^2} \tag{1.46}$$

The first term stands for mass of the new Higgs boson: $m_H = \sqrt{2\lambda\nu^2}$; the second represents Higgs boson self-interaction and the last the coupling with the weak bosons (W and Z).
It is interesting to note the same Higgs doublet which generates weak bosons masses can give masses also to leptons and quarks.
For the fermions, the following Lagrangian can be considered:

$$\mathcal{L} = -G_e[(\bar{\nu}_e,\ \bar{e})_L \begin{pmatrix} \phi^+ \\ \phi^0 \end{pmatrix} e_R + \bar{e}_R(\phi^-,\ \bar{\phi^0}) \begin{pmatrix} \nu_e \\ e \end{pmatrix}_L] \tag{1.47}$$

Substituting the expression of ϕ:

$$\phi = \frac{1}{\sqrt{2}} \begin{pmatrix} 0 \\ \nu + h(x) \end{pmatrix} \tag{1.48}$$

into 1.47, the Lagrangian becomes:

$$\mathcal{L} = -\frac{G_e}{\sqrt{2}}\nu(\bar{e}_L e_R + \bar{e}_R e_L) - \frac{G_e}{\sqrt{2}} h(\bar{e}_L e_R + \bar{e}_R e_L) \tag{1.49}$$

Choosing G_e so that $m_e = G_e\nu/\sqrt{2}$, since the G_e is arbitrary, the actual mass of the electron is not predicted.
The quark masses are generated in the same way with the difference that to generate a mass for the upper member of a quark doublet, a new Higgs doublet from ϕ must be used:

$$\phi_c = i\tau\phi^* = \begin{pmatrix} -\bar{\phi^0} \\ \phi^- \end{pmatrix} \xrightarrow[breaking]{} \frac{1}{\sqrt{2}} \begin{pmatrix} \nu + h(x) \\ 0 \end{pmatrix} \tag{1.50}$$

The new Lagrangian can be written as:

$$\mathcal{L} = -G_d(\bar{u},\ \bar{d})_L \begin{pmatrix} \phi^+ \\ \phi^0 \end{pmatrix} d_R - G_u(\bar{u},\ \bar{d})_L \begin{pmatrix} -\bar{\phi^0} \\ \phi^- \end{pmatrix} u_R \ +\ \textit{hermitian coniugate} \tag{1.51}$$

In 1.51, the (u, d) quark doublet are considered even if the weak interactions operate on $(u,\ d')_L$ where the primed states are linear combinations of the flavour eigenstates[3]. Using these new doublets, 1.51 is therefore of the form:

$$\mathcal{L} = -G_d^{ij}(\bar{u},\ \bar{d'})_L \begin{pmatrix} \phi^+ \\ \phi^0 \end{pmatrix} d_{jR} - G_u^{ij}(\bar{u},\ \bar{d'})_L \begin{pmatrix} -\bar{\phi^0} \\ \phi^- \end{pmatrix} u_{jR} \ +\ \textit{hermitian coniugate} \tag{1.52}$$

[3]Linear combination of the flavour eigenstates considering Cabibbo-Kobayashi-Maskawa (CKM) matrix: $d_i' = \sum_{n=1}^{N} V_{in} d_n$ where N = 3 is the number of quarks, V_{in} is CKM matrix and d_n are the d type quarks d, s, b.

with i, j = 1, ..., N, where N is the number of quark doublet. Substituting ϕ_c expression, the masses depend on the arbitrary couplings $G_{u,d}$ but, as for electron, it cannot be predicted.
The choice of a particular single Higgs doublet is sufficient on one hand to generate the masses of both the gauge bosons and the fermions but on the other hand, the masses of the fermions are just parameters of the theory and are not predicted.
To summarise, the complete Lagrangian of the SM is:

$$\begin{aligned}\mathcal{L}_{SM} = &\frac{1}{4}W_{\mu\nu}\cdot W^{\mu\nu} + \frac{1}{4}B_{\mu\nu}B^{\mu\nu} + \bar{L}\gamma^{\mu}(i\partial_{\mu} - g\frac{1}{2}\tau\cdot W_{\mu} - g'\frac{Y}{2}B_{\mu})L \\ &+ \bar{R}\gamma^{\mu}(i\partial_{\mu} - g'\frac{Y}{2}B_{\mu})R + |i\partial_{\mu} - g\frac{1}{2}\tau\cdot W_{\mu} - g'\frac{Y}{2}B_{\mu}|^2 - V\phi \\ &- (G_1\bar{L}\phi R + G_2\bar{L}\phi_c R) + \ hermitian\ conjugate\end{aligned} \tag{1.53}$$

The first two terms represent the $W^{\pm}$, Z, γ kinetic energies and the self-interactions; the third and the fourth term the lepton and quark kinetic energies and their interaction with the W, Z and γ; the last terms stand for masses and coupling of the Higgs, bosons, leptons and quark.

1.2 The Higgs boson

On the 4th of July 2012, the ATLAS and CMS experiments at the Large Hadron Collider (LHC) announced they had observed a new particle in the mass region around 125 GeV [11, 12]. This particle was consistent with the Higgs boson predicted by the SM. Since that day, Higgs boson properties have been studied.
The SM Higgs boson is a CP-even scalar of spin 0 [6]. Its mass is given by $m_h = \sqrt{2\lambda\nu^2}$, where λ is the Higgs self-coupling parameter in the potential $V(\phi)$.
The experimental Higgs boson mass is [6]:

$$m_H = 125.09 \pm 0.21(stat.) \pm 0.11(syst.)\ GeV$$

The Higgs boson couplings to the fundamental particles are set by their masses: very weak for light particles, such as up and down quarks, and electrons, but strong for heavy particles such as the W and Z bosons and the top quark. In particular, the SM Higgs boson couplings to fundamental fermions are linearly proportional to the fermion masses m_f ($y_f = m_f/\nu$ where y_f is the Yukawa coupling) whereas the couplings to bosons are proportional to the squares of the boson masses. As consequence, the dominant mechanism for Higgs boson production and decay involve the coupling of H to W, Z and/or the third generation quarks and leptons. The Higgs boson coupling to gluons is induced at leading order by a one-loop process in which H couples to a virtual $t\bar{t}$ pair. Likewise, the Higgs boson couplings to photon is also generated via loops, although in this case the one-loop graph with a virtual W^+W^- pair provides the dominant contribution and the one involving a virtual $t\bar{t}$ pair is subdominant.

1.2.1 Production mechanisms

The main production mechanisms at the LHC are gluon fusion, weak-boson fusion, associated production with gauge boson and associated production with a pair of top/antitop quarks. The corresponding Feynman diagrams are reported in Figure 1.3. Figure 1.4 summarises the cross section as a function of Higgs mass for these dominant Higgs production processes for a centre-of-mass energy of 13 TeV [13].

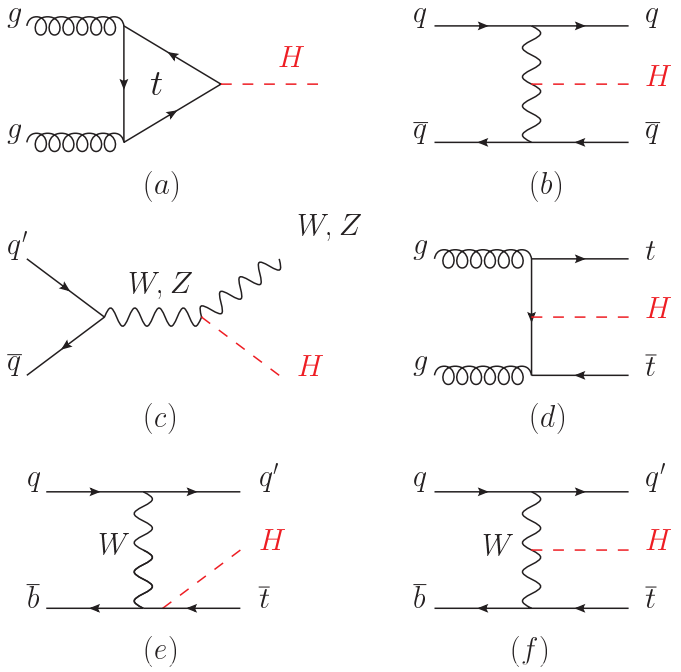

Figure 1.3: Main Leading Order Feynman diagrams contributing to the Higgs production: (a) gluon fusion, (b) Vector-boson fusion, (c) Higgs-strahlung (or associated production with a gauge boson), (d) associated production with a pair of top (or bottom quarks), (e-f) production in association with a single top quark.

Production mechanism: gluon fusion

The Higgs boson production mechanism with the largest cross section is the gluon-fusion process (ggF) $gg \to H + X$, mediated by the exchange of a virtual, heavy top quark (Figure 1.3a). Contributions from lighter quarks q, propagating in the loop, are suppressed proportional to their mass m_q^2. QCD radiative corrections to this process are also very important. At the LHC, with a $\sqrt{s} = 13\ TeV$, the value for the production cross section at the next-to next- to next to leading order is [14]:

$$\sigma_{ggF}^{N3LO} = 48.6pb^{+2.2pb(+4.6\%)}_{-3.3pb(+6.7\%)}(theory) \pm 1.6(3.2\%)(PDF + \alpha_s) \tag{1.54}$$

where α_s is the QCD running coupling.

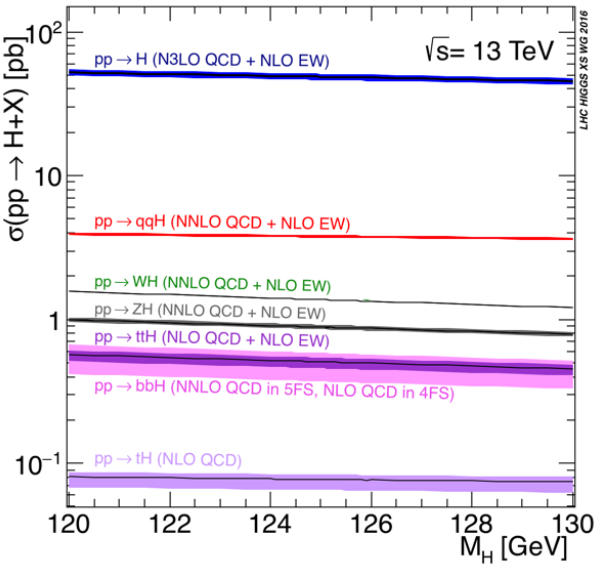

Figure 1.4: Cross section at $\sqrt{s} = 13\ TeV$ as a function of Higgs boson mass [13].

Production mechanism: Weak-boson fusion

The SM Higgs production mode with the second-largest cross section is Vector Boson Fusion (VBF): $qq \rightarrow qqH$ (Figure 1.3b). This mechanism proceeds by the scattering of two (anti-)quarks, mediated by exchange of a W or Z boson, with the Higgs boson radiated off the weak-boson propagator. The scattered quarks give rise to two hard jets in the forward and backward regions of the detector. Gluon radiation in the central-rapidity is suppressed thanks to the color-singlet nature of the weak-gauge boson exchanged: this feature let to distinguish VBF from overwhelming QCD backgrounds including gluon-fusion induced Higgs plus two jets production and production of H in association with a W or Z boson hadronically decaying. This process receives contributions at NLO from EW and QCD that also contributes at NNLO.

Production mechanism: Higgs-strahlung

The next most relevant Higgs boson production mechanism is the Higgs-strahlung, the production of the Higgs boson with W or Z gauge bosons: $pp \rightarrow VH+X$ with $V = W^{\pm}, Z$ (Figure 1.3c). As in VBF, at NLO EW and QCD (due to corrections to the Drell-Yan cross section) give their contributions to this cross section. In addition, Higgs-strahlung receives non Drell-Yan-like corrections in the $q\bar{q}$ channel where the Higgs is radiated off top-quarks loops.

Production mechanism: $t\bar{t}H$

Higgs radiation off top quarks (Figure 1.3d), $pp \to t\bar{t}H$, provides a direct probe of the top-Higgs Yukawa coupling. On the 10th April 2018, CMS announced the observation of the production of the Higgs boson together with a top-quark pair [15, 16]. Figure 1.5 shows a possible $t\bar{t}$H event.

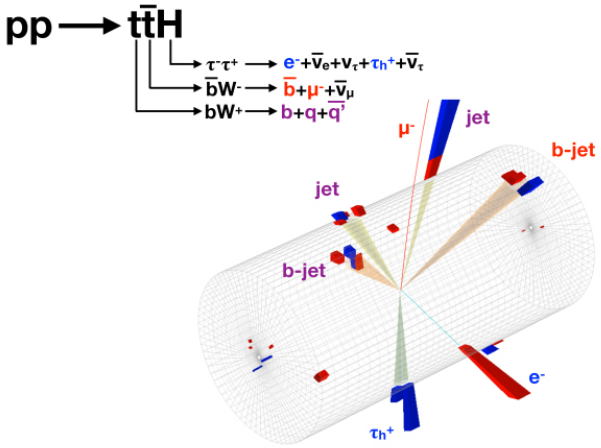

Figure 1.5: An event candidate for the production of a top quark and top anti-quark pair in conjunction with a Higgs boson in the CMS detector. The Higgs decays into a τ^+ lepton and a τ^- lepton; the τ^+ in turn decays into hadrons and the τ^- decays into an electron. The decay product symbols are in blue. The top quark decays into three jets (sprays of lighter particles) whose names are given in purple. One of these is initiated by a b-quark. The top anti-quark decays into a muon and b-jet, whose names appear in red [16].

1.2.2 Decay channels

As reported in Figure 1.6, the dominant decay modes for the Higgs boson are $H \to b\bar{b}$, $H \to WW^*$ followed by $H \to \gamma\gamma$, $H \to \tau^+\tau^-$ and $H \to ZZ^*$; Table 1.4 summarises the branching ratios and the relative uncertainty for these decay channels. All these channels have been used to observe the Higgs boson, analysing data collected since 2012 (at 7, 8 and 13 TeV). As example, in Figure 1.7 is reported the four-leptons invariant mass distribution comparing simulation and data collected by both CMS [17] and ATLAS detectors [18] during 2016 and 2017. Data reproduce simulation, well describing also the peak around 125 GeV compatible with the Higgs boson.
Due to its small branching ratio (2.18×10^{-4}), the observation of the Higgs boson in the dimuon channel still misses, but it plays a fundamental role to study properties of the leptons belonging to the second generation. This decay channel is the only way to directly measure the Higgs-muon Yukawa coupling strength.

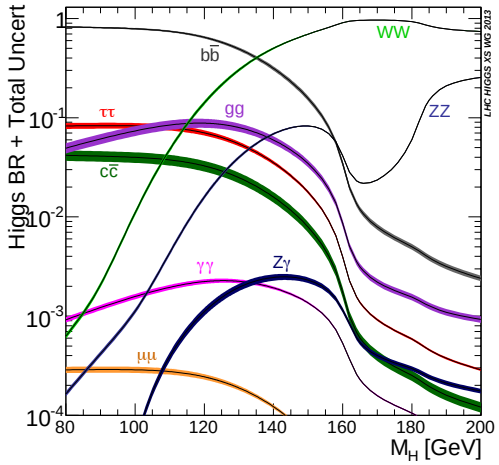

Figure 1.6: Standard Model Higgs boson production cross section at $\sqrt{s} = 13\ TeV$ as a function of Higgs boson mass [13].

Decay channel	Branching ratio	Rel. uncertainty
$H \to b\bar{b}$	5.84×10^{-1}	+3.2% -3.3%
$H \to WW^*$	2.14×10^{-1}	+4.3% -4.2%
$H \to \tau^+\tau^-$	6.27×10^{-2}	+5.7% -5.7%
$H \to ZZ^*$	2.62×10^{-2}	+4.3% -4.1%
$H \to \gamma\gamma$	2.27×10^{-3}	+5.0% -4.9%
$H \to \mu\mu$	2.18×10^{-4}	+6.0% -5.9%

Table 1.4: Branching ratio for a Higgs boson with $m_H = 125$ GeV [14, 19].

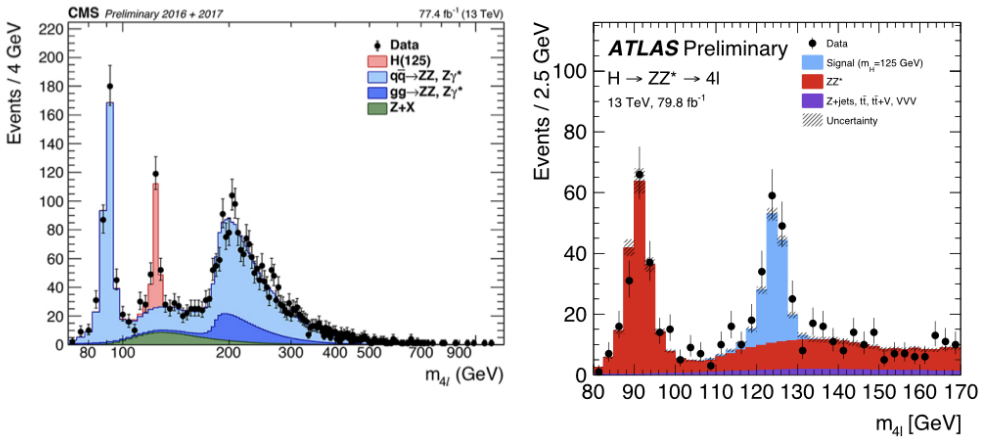

Figure 1.7: Distribution of the four-lepton reconstructed invariant mass m_{4l} in the full mass range combining 2016 and 2017 data collected at 13 TeV by CMS (on the left) and by ATLAS (on the right). Points with error bars represent the data and stacked histograms represent expected distributions of the signal and background processes [17, 18].

1.2.3 Signal Strength modifiers

In Figure 1.8 and 1.9 [20, 21] are reported the fit to the signal strength modifiers μ_i obtained analysing data collected during Run II at 13 TeV: μ_i is defined as the ratio between the measured Higgs boson yield and its SM expectation. No deviation from SM predictions can be observed.
For a specific production and decay channel $i \to H \to f$, the signal strengths for the production, μ_i, and for the decay, μ_f , are defined as,

$$\mu_i = \frac{\sigma_i}{(\sigma_i)_{SM}}, \quad \mu^f = \frac{BR^f}{BR^f_{SM}}$$

where σ_i is the production cross section for $i \to H$ and μ^f is the branching ratio for $H \to f$; the "SM" refers to their respective SM predictions, so by definition, the SM corresponds to $\mu_i = \mu^f = 1$. Since σ_i and BR^f cannot be separately measured without additional assumptions, only the product of μ_i and μ^f can be extracted experimentally, leading to a signal strength μ_i^f for the combined production and decay:

$$\mu_i^f = \frac{\sigma_i \cdot BR^f}{(\sigma_i)_{SM} \cdot BR^f_{SM}} = \mu_i \times \mu^f$$

The combined measurement of the common signal strength modifier is [20]

$$\mu = 1.17^{+0.06}_{-0.06}(stat.)^{+0.06}_{-0.05}(sig.th.)^{+0.06}_{-0.06}(other\ syst.)$$

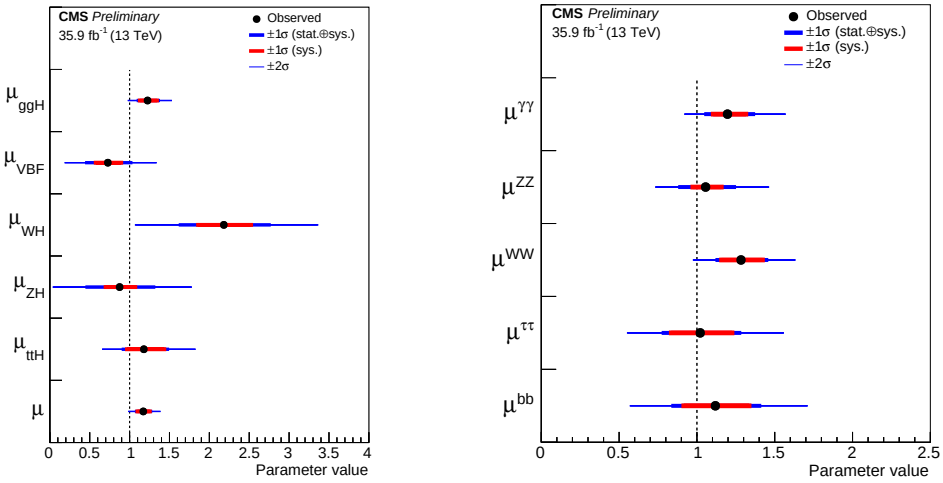

Figure 1.8: Summary plot of the fit to the per-production mode (on the left) and per-decay mode (on the right) signal strength modifiers μ_i. The thick and thin horizontal bars indicate the $\pm 1\sigma$ and $\pm 2\sigma$ uncertainties, respectively. Also shown are the $\pm 1\sigma$ systematic components of the uncertainties. The last point in the per-production mode summary plot is taken from a separate fit and indicates the result of the combined overall signal strength μ.

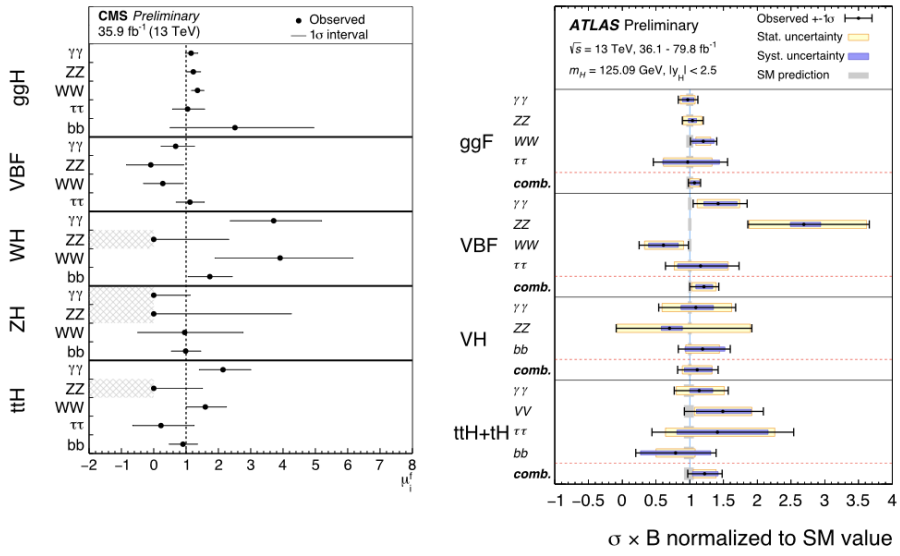

Figure 1.9: Summary plot of the fit to the production-decay signal strength products $\mu_i^f = \mu_i \times \mu^f$ for CMS (on the left) and ATLAS (on the right). The points indicate the best-fit values while the horizontal bars indicate the 1σ C.L. intervals. On the left, the hatched areas indicate signal strengths which are restricted to positive values due to low background contamination; on the right, combined result for each production mode is also shown.

1.2.4 Coupling constant

In order to test and parametrise for deviations in the couplings of the Higgs boson to other particles, a set of coupling modifiers, $\vec{\kappa}$, is introduced. For a given production process or decay mode j, a coupling modifier κ_j is introduced:

$$\kappa_j^2 = \sigma_j/\sigma_j^{SM}, \ or \ \kappa_j^2 = \Gamma^j/\Gamma_{SM}^j$$

Under the assumption that there are no new particles contributing to the ggF production or $H \to \gamma\gamma$ decay loops, these processes can be expressed in terms of the coupling modifiers to the others SM particles. In this model six free coupling parameters are introduced: κ_Z, κ_W, κ_t, κ_b, κ_τ, κ_μ and it is assumed that there is no Beyond SM (BSM) contribution to the total Higgs boson width. In the SM, all κ_j^2 values are positive and equal to unity: the results of the fits with this parametrisation are given in Figure 1.10. An other way to fit the possible deviation to the SM in the Higgs coupling

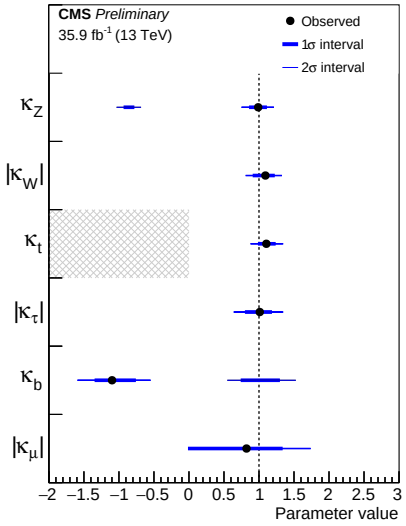

Figure 1.10: Summary of the κ-framework model with BR_{BSM}= 0. The points indicate the best-fit values while the thick and thin horizontal bars show the 1σ and 2σ C.L. intervals, respectively. In this model, the ggF and H$\to \gamma\gamma$ loops are resolved in terms of the remaining coupling modifiers. For this model, both positive and negative values of κ_Z and κ_b are considered while κ_W is assumed to be positive [20].

is to parametrise κ in term of other two parameters, M and ϵ [22,23]. In this model one can relate the coupling modifiers to M and ϵ as $\kappa_F = \nu\ m_f^\epsilon/M^{1+\epsilon}$ for fermion of mass m_f and $\kappa_V = \nu\ m_V^{2\epsilon}/M^{1+2\epsilon}$ for vector boson of mass m_V. In absence of BSM contribution, in the SM, $\kappa_i = 1$ and considering $\nu = 246.22$ GeV, (M, ϵ) = (ν, 0). Figure 1.11 shows the 1σ and 2σ C.L. regions in the (M, ϵ) fit; in Figure 1.12 are reported the reduced coupling strength modifiers, for CMS [20] and ATLAS [21], $\kappa_F \cdot\ m_F/\nu$ for fermions (F = t, b, τ, μ) and $\sqrt{\kappa_V} \cdot m_V/\nu$ for weak gauge bosons (V = W, Z) as a function of their

masses m_F and m_V. All the particles shown have their coupling to SM Higgs boson compatible with SM prediction within the 2σ band. For the muon, there is still margin to improve the results reducing the uncertainties, that is driven by the statistical one, and the search at low mass, within my thesis, deals with this measurement.

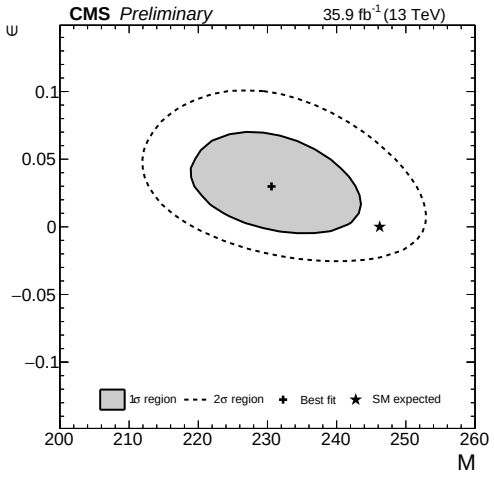

Figure 1.11: Likelihood scan in the M-ϵ plane. The best-fit point and 1σ, 2σ C.L. regions are shown, along with the SM prediction.

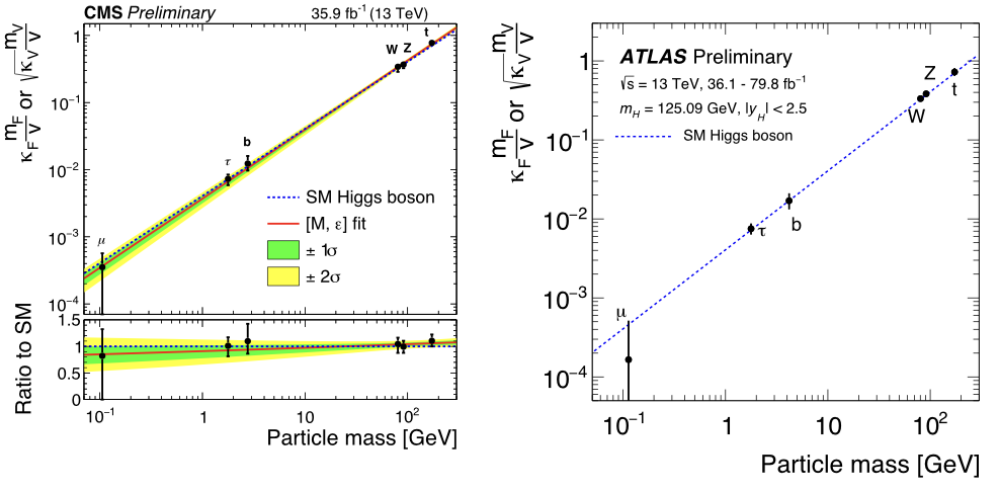

Figure 1.12: Reduced coupling strength modifiers, for CMS (on the left) [20] and ATLAS (on the right) [21], $\kappa_F \cdot m_F/\nu$ for fermions (F = t, b, τ, μ) and $\sqrt{\kappa_V} \cdot m_V/\nu$ for weak gauge bosons (V = W, Z) as a function of their masses m_F and m_V, respectively. The SM prediction for both cases is also shown (dotted line).

1.3 Beyond Standard Model (BSM)

The SM aims to describe all fundamental interaction in a common way but at the same time, considering the gauge group symmetry (see sec. 1.1.2), it introduces three different running constant couplings, whose value depends on the energy: in this view, it is expected to reach an energy value at which these three coupling constants converge. Within the SM, this convergence is not verified: Figure 1.13 shows couplings behaviour as a function of energy.

The SM has different open questions it is not equipped to address: e.g. it does not have

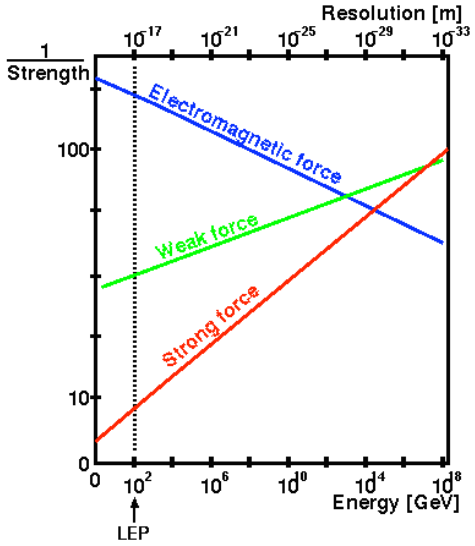

Figure 1.13: Evolution of the inverse of the three running coupling constants of the SM.

a quantum description of the Gravity, treated currently only classically; it has no candidate for Dark Matter and no explanation for Dark Energy. An other problem, linked with the Higgs boson mass within the SM, is the so called "hierarchy problem": in the theory, the Higgs boson receives quantum corrections from heavy particles. While the Higgs boson has a mass $m_H \approx$125 GeV, the corrections are of the order of the Planck mass, $M_P = \sqrt{\hbar c/G} \approx 10^{19}$GeV, and not, as one might expect, of the same order of m_H.

With the aim to try to solve these issues, many models beyond SM have been developed, introducing new particles/interactions and more symmetries. The easiest way to do this, is to consider a larger unification groups.

1.3.1 Sequential Standard Model

The Sequential Standard Model (SSM) [24] predicts, by introducing a new U(1) group, the existence of a new boson, Z'_{SSM}, with the same features of the SM Z boson. In this

model, the decay width of the boson into a pair of fermions is given by:

$$\Gamma(Z'_{SSM} \to f\bar{f}) = \frac{\alpha}{48} N_C \frac{M_{Z'_{SSM}}}{\sin^2\theta_W \ \cos^2\theta_W}[1 + (1 - 4|Q_f|cos^2\theta_W)^2]$$

where, α is the fine-structure constant, N_C is the number of colours, θ_W is the Weinberg angle and Q_f is the electric charge of the fermion. This is often used as a benchmark model for experimental Z$'$ searches.

1.3.2 Grand Unified Theories

Grand Unified Theories, GUT's [25], try to describe all fundamental interaction by one simple gauge group G at very high energies $E > E_{GUT}$. For energy $E \ll E_{GUT}$ the gauge group must be broken and obtain the SM gauge symmetry group, similar to the breaking of the $SU(2)_L \times U(1)_Y$ symmetry to $U(1)_{em}$ in the SM which occurs at E_{weak}= O(100GeV). The smallest simple gauge group G which can contain the SM is G = SU(5) with 4 neutral gauge bosons.
GUT can be tested measuring proton decay: to be consistent with present experiments on proton decay, E_{GUT} must be greater than 10^{15} GeV, much larger than E_{weak} and smaller than the Planck mass. At energies above the Planck mass, Gravity is expected to become as strong as the other interactions. At energies well below M_P, as it happens in GUT, the effects of Gravity can be neglected. E_{GUT} is also predicted as the energy where the three running gauge couplings of the SM gauge group become equal. All GUT's with gauge groups larger than SU(5) predict at least one extra neutral gauge boson (Z$'$).
The next interesting gauge group larger than SU(5) is SO(10). The SO(10) theory predicts one extra neutral gauge boson because rank[SO(10)] = 5.
More interesting is the case of E_6: when it is broken, to the effective strong-electroweak group at low energy, different models are possible. The gauge group E_6 is broken at the GUT scale to SO(10) and a $U(1)_\psi$ gauge group

$$E_6 \to SO(10) \times U(1)_\psi$$

The SO(10) is further broken to SU(5) and a $U(1)_\chi$ gauge group,

$$SO(10) \to SU(5) \times U(1)_\chi$$

Finally the SU(5) is broken to the Standard Model (SM) gauge group.
From the linear combination

$$U(1)' = U(1)_\chi \cos\theta + U(1)_\psi \sin\theta$$

is possible for the two generators, T_ψ and T_χ to survive down to the TeV scale.
At different value of the mixing angle θ, free parameter of the theory, corresponds different Z$'$ phenomenology. The most widely used models, with their corresponding mixing angle, are: Z'_ψ (θ=0), Z'_χ (-π/2), Z'_η (arccos(5/8)) and Z'_I (arccos(5/8) $- \pi/2$).
These theories unify the three gauge interactions of the Standard Model and reduce the number of independent parameters.

1.3.3 Extra dimensions model

While electroweak interactions have been probed at distances $\sim m_{EW}^{-1}$, gravitational forces have not remotely been probed at distances $\sim m_{Pl}^{-1}$ and Gravity has only been accurately measured in the $\sim$1 cm range. The interpretation of M_P as a fundamental energy scale (where gravitational interactions become strong) is then based on the assumption that Gravity is unmodified over the 33 orders of magnitude between where it is measured at $\sim$1 cm down to the Planck length $\sim 10^{-33}$ cm. This reason leads to the idea of abandoning the interpretation of M_P as a fundamental energy scale, and leaving only m_{EW} as fundamental scale.
To account for the observed weakness of Gravity compared to electroweak interactions, new n extra compact spatial dimensions of radius $\sim$R are introduced, with Gravity being the only fundamental interaction that sees them [26].
Two test masses of mass m_1, m_2 placed within a distance r$\ll$ R will feel a gravitational potential dictated by Gauss's law in (4 + n) dimensions:

$$V(r) \sim \frac{m_1 m_2}{M_{P(n+4)}^{n+2}} \frac{1}{r^{n+1}}$$

If now, the masses are placed at distances r $\gg$ R, their gravitational flux lines can not continue to penetrate in the extra dimensions, and the usual 1/r potential is obtained:

$$V(r) \sim \frac{m_1 m_2}{M_{P(n+4)}^{n+2} R^n} \frac{1}{r}$$

so the effective 4 dimensional M_P is

$$M_P^2 \sim M_{P(n+4)}^{n+2} R^n$$

The fundamental Planck mass can, thus, be in the TeV range, which would solve the hierarchy problem. The observed strength of Gravity can be reproduced with a suitable choice of R and n. If one assumes the mass scale at 1 TeV, a condition for the size of the extra dimension arises

$$R \sim 10^{\frac{30}{n}-17}\ cm \times \frac{1\ TeV}{m_{EW}}^{1+\frac{n}{2}}$$

Randall-Sundrum model and Kaluza-Klein tower

Consider, in the case n = 1, a massless (4+1)D scalar field ϕ^M with M= 0,1, ..., 4, with action

$$S_{5D} = \int d^5x\ \partial^M \phi \partial_M \phi \tag{1.55}$$

Set the extra dimension x^4 = y defining a circle of radius r with y $\equiv$ y + 2πr. The periodicity in y direction implies discrete Fourier expansion

$$\phi(x^\mu, y) = \sum_{n=-\infty}^{\infty} \phi_n(x^\mu)\ e^{iny/r} \tag{1.56}$$

Notice that the Fourier coefficients are functions of the standard 4D coordinates and therefore are (an infinite number of) 4D scalar fields. The equations of motion for the Fourier modes are (in general massive) wave equations

$$\partial^\mu \partial_\mu \phi_n(x^\mu) - \frac{n^2}{r^2}\phi_n(x^\mu) = 0$$

These are then an infinite number of Klein Gordon equations for massive 4D fields. This means that each Fourier mode ϕ_n is a 4D particle with mass $m_n^2 = \frac{n^2}{r^2}$. Only the zero mode (n = 0) is massless. One can visualise the states as an infinite tower of massive states (with increasing mass proportional to n). This is called Kaluza Klein (KK) tower and the massive states (n $\neq$ 0) are called Kaluza Klein or momentum states, since they come from the momentum in the extra dimension. Substituting 1.56 in 1.55, it can be demonstrated that the 5D action reduces to one 4D action for a massless scalar field plus an infinite sum of massive scalar actions in 4D.
In the Randall-Sundrum model [27], the fifth dimension y is confined in $0 < y < 2\pi$ with the additional condition (x^μ, y) $\equiv$ (x^μ, -y). The solution to Einstein's equations in such 5-dimensional space is an anti-de Sitter (AdS5) space with non-factorizable geometry, given by the metric

$$ds^2 = e^{-2kr_c|y|}\eta_{\mu\nu}dx^\mu dx^\nu + r_c^2 dy^2$$

where k $\sim M_P$ is the AdS5 curvature parameter, r_c is the compactification radius and $\eta_{\mu\nu}$ is the 4-dimensional metric tensor. Assuming that the SM fields are confined to the brane located at y = π, any fundamental 5-dimensional mass parameter m_0, has an effective 4-dimensional value of

$$m = e^{-kr_c\pi}m_0$$

This gives rise to massive leptonically decaying KK gravitons in the 4- dimensional world, with masses at the TeV scale, easily generated from parameters of order of the Planck scale. The compactification scale $1/r_c$ is of the order of M_P, so no additional hierarchy is introduced and the masses of KK excitations modes are

$$m_n = kx_n e^{-kr_c\pi}$$

where x_n is the n-th root of the J_1 Bessel function.
The Randall-Sundrum model phenomenology is governed by two free parameters, with the mass of the first graviton excitation m_1 (G_{KK} in the future) and the coupling parameter of the graviton to the SM, c = k/$\bar{M}_P$[4], as being the usual choice.

1.3.4 Dark Matter Model

Many models have been developed to describe how Dark Matter (DM) can be produced: these models involve TeV-scale mediating particles that couple to quarks and a Dirac fermion DM candidate.

[4] $\bar{M}_P$ is the reduce Planck mass defined as $M_P/\sqrt{8\pi}$

DM does not interact with ordinary matter and this means that it does not leave any tracks in the detector: it looks like a neutrino. This leads to search for a large missing transverse energy as possible signal signature. An other possibility to detect DM is to look at the decay product of the mediator particle DM-SM. The simplified models contain a Dirac DM particle, and a mediator which can be a (pseudo-)scalar, vector, or axial-vector particle, which is produced in the s-channel [28]. The Lagrangian for these models, here for the case of a vector mediator, is of the form

$$\mathcal{L}_{\text{vector}} = -g_\chi Z'_\mu \overline{\chi}\gamma^\mu \chi - g_q \sum_q Z'_\mu \overline{q}\gamma^\mu q - g_\ell \sum_\ell Z'_\mu \overline{\ell}\gamma^\mu \ell,$$

where Z' denotes the mediator. The Lagrangian for the axial-vector case is identical except for an additional γ_5 matrix. (Pseudo-)Scalar mediator are not relevant in the leptonic final state as the branching fraction into leptons would be very small because of their small Yukawa couplings. The free parameters of the models are the masses of the DM particle and the mediator, m_{DM} and m_{med}, and the couplings of the mediator to quarks and the DM particle, g_q and g_{DM}. For the new models relevant to this thesis, a non-zero couplings to lepton g_ℓ has been added. The two relevant models are

- V2: Vector model with small couplings to leptons: $g_{\text{DM}} = 1.0$, $g_q = 0.1$, $g_\ell = 0.01$.
- A2: Axial-vector model with equal couplings to leptons and quarks: $g_{\text{DM}} = 1.0$, $q_q = g_\ell = 0.01$.

1.3.5 BSM search in dilepton decay channel

As described in sec. 1.3, new bosons are introduced within BSM, either Spin-1 like Z'_{SSM} in the Sequential Standard Model and Z'_ψ in the framework of Grand Unification or Spin-2 like the Kaluza-Klein Graviton, G_{KK}, predicted in the extra dimension model.
A promising search for new physics is the dilepton decay channel, in which the resonance decays emitting two opposite-sign leptons. New physics would manifest itself in a change of the dilepton invariant mass spectrum.
The low background, in the case of heavy resonances, and the resonance peak as a signal, in combination with the high accuracy of the muon reconstruction, make the dimuon final state an experimentally well motivated channel. As the SM Z boson, these new bosons are expected to be a very short-lived particle. They can only be observed through their decay products or through indirect interference effects. They can be detected either in very high energy processes or in high precision experiments at lower energies. In the first kind of processes, the energy of the colliding particles must be large enough to produce a Z'. The decay products of the Z' must be then detected above the SM background. Such a background is always present because the SM Z boson or the photon are produced by the same processes, which create a Z'.

Chapter 2

The CMS detector at LHC

2.1 The Large Hadron Collider

Approved in the early '90s and started up in the 2008, the *Large Hadron Collider* (LHC) is currently the world's largest and most powerful particle accelerator. Its main purpose is to help in testing the predictions of different theories of particle physics.
LHC [29], situated at the CERN laboratories of Geneva, is a proton-proton (pp) and heavy ions ($PbPb$) collider built to work at the design centre-of-mass energy of $\sqrt{s} =$ 14 TeV, with a bunch crossing every 25 ns and a design luminosity of 10^{34} cm^{-2}s^{-1}. It is installed in the same circular underground tunnel occupied until the year 2000 by the Large Electron Positron collider (LEP). The pp collision are used to reduce the synchrotron radiation, in order to accelerate the particles up to a very large energy. It was preferred to a $p\bar{p}$ collider because it allows to reach higher rate of events. The low anti-proton production efficiency (10^5 protons are needed to create an anti-proton) and larger time needed to accumulate them, would make almost impossible to reach the high design luminosity of the LHC. The luminosity L is the parameter to quantify the performance of a collider, because the event rate R_i of a given process i, defined as the number of events occurring per unit of time, can be written as:

$$R_i = \frac{dN_i}{dt} = L \cdot \sigma_i \tag{2.1}$$

where σ_i is the cross section of the process i. The luminosity depends only on the machine parameters. Assuming a small crossing angle between the beams and Gaussian-shaped beam bunches, the luminosity L can be written as:

$$L = \frac{f n_b N^2}{4\pi\sigma^2} \tag{2.2}$$

where f is the revolution frequency of particle bunches, n_b is the number of bunches rotating in the accelerator, N is the number of protons in the two colliding bunches and σ is the RMS of beam profile distributions in the plane orthogonal to the beam direction.

In Figure 2.1 is shown the complete scheme of the accelerator chain of the LHC: the proton beam is created by using an electric field to pull the electrons from hydrogen atoms and start the acceleration. Protons are injected into the PS Booster (PSB) at an energy of 50 MeV from Linac2 (Linear Accelerator 2). The booster comprises four superposed rings: this is because at low energy intensity, the quality of the beams suffers from the repulsive forces between particles. By splitting up the injected beam this effect gets reduced. Once the beam reaches the energy of 1.4 GeV it is extracted and injected into Proton Synchrotron (PS). With a circumference of 628 m, the PS accelerates the beams up to 26 GeV when they are extracted and sent to the Super Proton Synchrotron (SPS). Built in the '70, the SPS has a length of 7 km. The beam is injected at 26 GeV, ramped up to 450 GeV and extracted to the LHC. Once the energy-working point is reached, the beams are made to collide at four locations around the LHC, corresponding to the position of four particles detectors: ALICE (*A Large Ion Collider Experiment*), ATLAS (*A Toroidal LHC ApparatuS*), CMS (*Compact Muon Solenoid*) and LHCb (*Large Hadron Collider beauty*). In addition to these, there are other three experiment installed at the LHC: TOTEM (*TOTal Elastic and diffractive cross section Measurement*) installed close to CMS, MoEDAL (*Monopole and Exotics Detector at the LHC*) close to LHCb and LHCf (*Large Hadron Collider forward*) near ATLAS.

The beams at LHC have a bunch structure as a direct consequence of the radio frequency

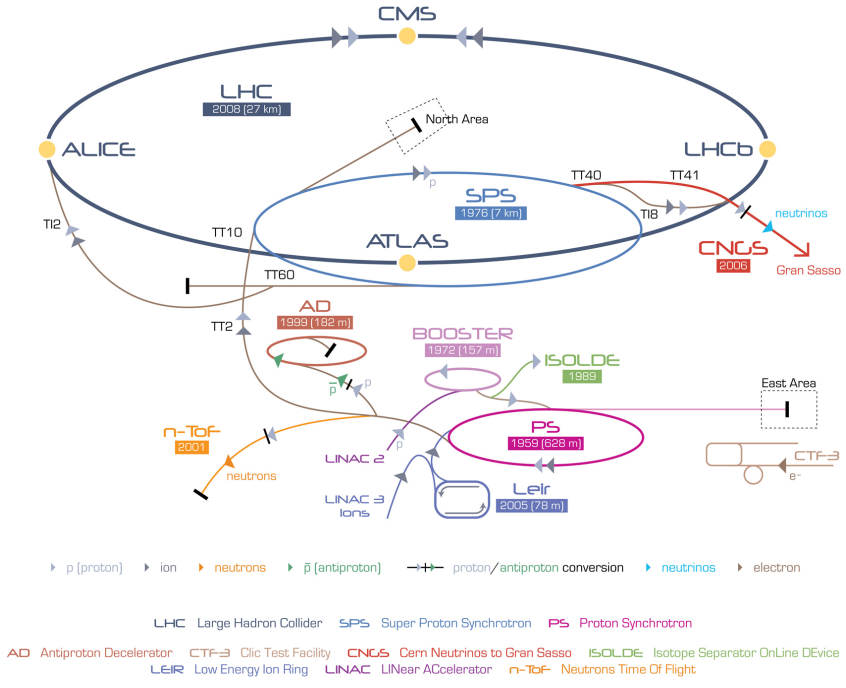

Figure 2.1: Accelerator scheme at CERN.

(RF) acceleration scheme. Protons can only be accelerated when the RF field has the

correct orientation when particles pass through an accelerating cavity. Under nominal operating conditions, each proton beam has 2808 bunches, with each bunch containing about 10^{11} protons. The bunch size is not constant around the ring getting squeezed as much as possibile around the interaction points in order to increase the probability of collision. They measure a few centimetres long and a millimetre wide when they are far from a collision point; as the bunches approach the collision points, they are squeezed to about 20 μm. LHC uses a bunch spacing of 25 ns (or 7.5 m) corresponding to a frequency of 40 MHz.
In Table 2.1 are reported the designed LHC parameters and the ones reached at the end of Run II in 2018.

		Design	2018
Centre of mass energy	E	14 TeV	13 TeV
Luminosity	L	10^{34} cm^{-2}s^{-1}	$2.2 \cdot 10^{34}$ cm^{-2}s^{-1}
Time spacing		25 ns	25 ns
Num. of bunches	k_B	2808	2556
Num. protons per bunch	N_p	1.15×10^{11}	1.15×10^{11}

Table 2.1: LHC parameters

Figure 2.2 shows the cumulative luminosity versus day delivered by LHC and recorded by the CMS experiment during stable beams for pp collisions since 2010 and in particular for 2016 and 2017 data taking at 13 TeV [30].

2.1.1 Proton - proton physics

The total inelastic proton-proton cross-section, for the process $pp \to X$, is $\sim 80\ mb$ at 13 TeV; Figure 2.3 shows various hard-scattering processes at hadron colliders, as a function of the machine centre-of-mass energy [31].
Therefore, the event rate R, defined as the number of events produced per second by the pp interactions, is expected to be

$$R = \sigma \times \mathcal{L} \simeq 10^9/s$$

running at 25 ns per bunch crossing.
These events belong to two classes:

- **Soft interaction**: due to large-distance collisions between the two incoming protons. In this case the momentum transfer of the interaction is small ("soft collisions") and therefore particle scattering at large angle is suppressed. The particles produced in the final state of such interactions have large longitudinal momentum, but small transverse momentum so most of them escape down the beam pipe. The final states arising from these soft interactions are called "minimum bias" events.

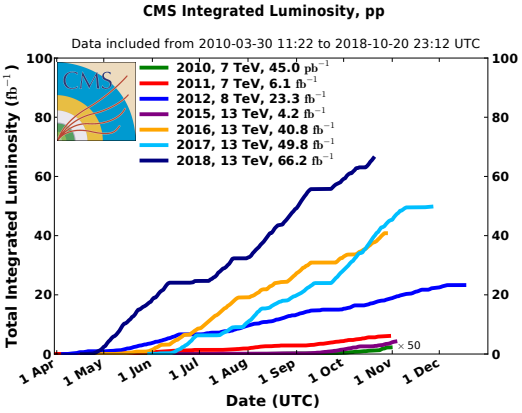

(a) Delivered luminosity for 2010 - 2018 period (pp data only)

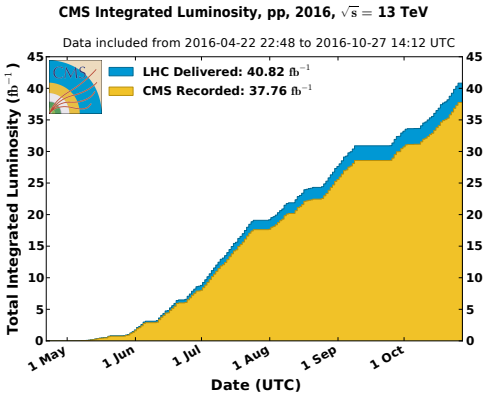

(b) Cumulative day-by-day integrated luminosity, 2016

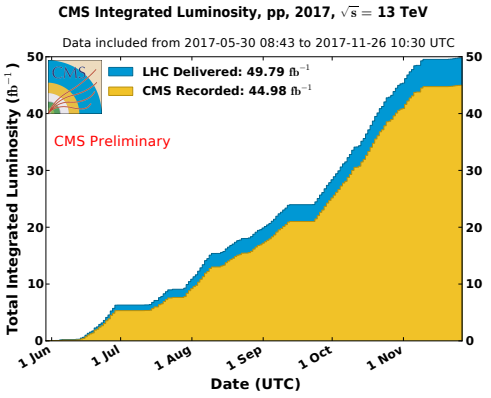

(c) Cumulative day-by-day integrated luminosity, 2017

Figure 2.2: On the top: cumulative luminosity versus day delivered to CMS during stable beams for pp collisions at nominal centre-of-mass energy. This is shown for data-taking in 2010 (green), 2011 (red), 2012 (blue), 2015 (purple), 2016 (orange), 2017 (light blue), and 2018 (navy blue). On the bottom left: cumulative day-by-day integrated luminosity in 2016; on the bottom right: cumulative day-by-day integrated luminosity in 2017.

- **Hard interaction**: due to partons (quarks or gluon) collision with high transverse momentum transferred. The effective centre-of-mass energy of the hard scattering, $\sqrt{\hat{s}}$, is proportional to the fractional energies x_a and x_b carried by the two interacting partons: $\sqrt{\hat{s}} = \sqrt{x_a x_b s}$ where $\sqrt{s}$ is the centre-of-mass energy of the proton beams. The probability density $f_p(x_p, Q)$ to find a parton p, with the fraction x of the longitudinal proton momentum in the proton-proton centre-of-mass frame, depends on the squared four-momentum transfer Q between the partons of the collision, and is described by the Parton Distribution Function (PDF). PDFs are different for gluons, u and d valence quarks and low-momentum sea quark-

antiquark pairs of all flavours and depend on the energy scale at which the interaction between the partons takes place. Figure 2.4 shows an example for parton distribution functions for two different values of Q [32].

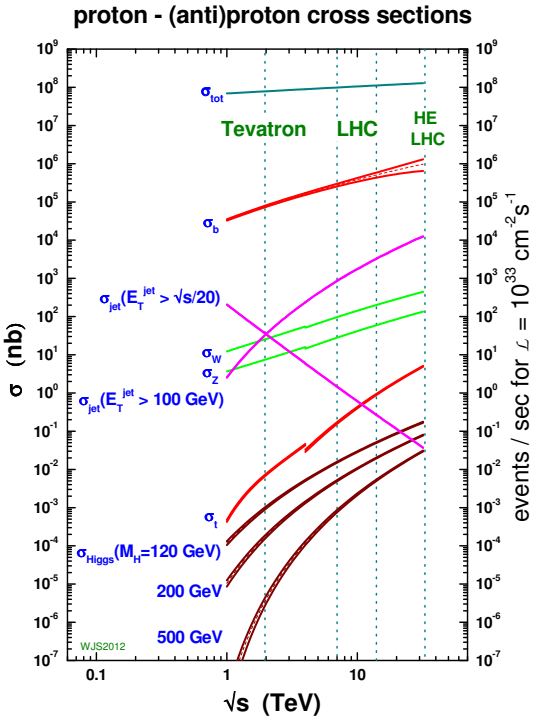

Figure 2.3: Production cross-sections for various hard-scattering processes at hadron colliders, as a function of the machine centre-of-mass energy.

During LHC operation, along with the luminosity, the mean number of proton-proton collision per bunch crossing, $< \mu >$, increased from ∼10 in 2011 up to ∼38 in 2018, with an overall mean of ∼34. Figure 2.5 reports interactions per crossing (pileup) for different data taking periods [30].

2.2 The Compact Muon Solenoid

The Compact Muon Solenoid (CMS) is one of the general purpose experiments which takes data at the LHC. Its physics goals range from the search for the Higgs boson to the searches for physics beyond the Standard Model, to the precision measurements of already known particles and phenomena [33].
The overall layout of CMS is shown in Figure 2.6. The central feature is a superconducting solenoid of 6 m internal diameter, providing a magnetic field of 3.8 T. Within the

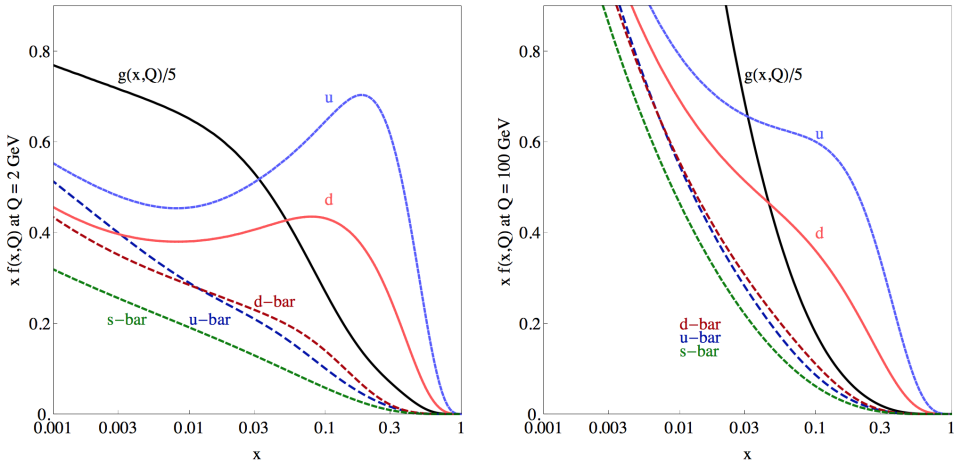

Figure 2.4: Parton distribution functions at Q = 2 GeV (left) and Q = 100 (right) GeV for u, $\bar{u}$, d, $\bar{d}$, s = $\bar{s}$, and g.

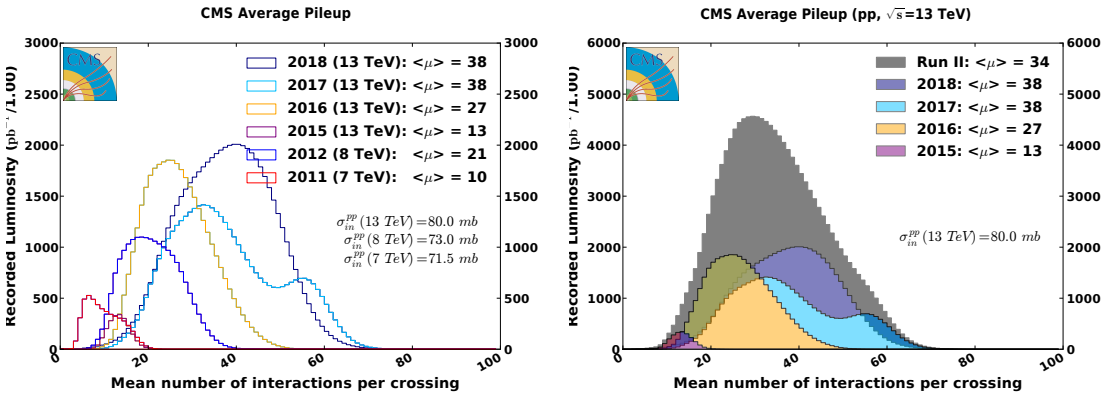

(a) Interactions per crossing (pileup) for 2011-2012 and 2015-2018

(b) Interactions per crossing (pileup) for 2015-2018

Figure 2.5: On the left: distribution of the average number of interactions per crossing (pileup) for pp collisions in 2011 (red), 2012 (blue), 2015 (purple), 2016 (orange), 2017 (light blue), and 2018 (navy blue). On the right: solid histograms of the distribution of the average number of interactions per crossing (pileup) for pp collisions only in Run II and for the overall mean values (grey).

solenoid volume are a silicon pixel and strip tracker, a lead tungstate crystal electromagnetic calorimeter (ECAL), and a brass and scintillator hadron calorimeter (HCAL), each composed of a barrel and two endcap sections. Forward calorimeters extend the pseudorapidity coverage provided by the barrel and endcap detectors. Muons are detected in gas-ionisation chambers embedded in the steel flux-return yoke outside the solenoid.

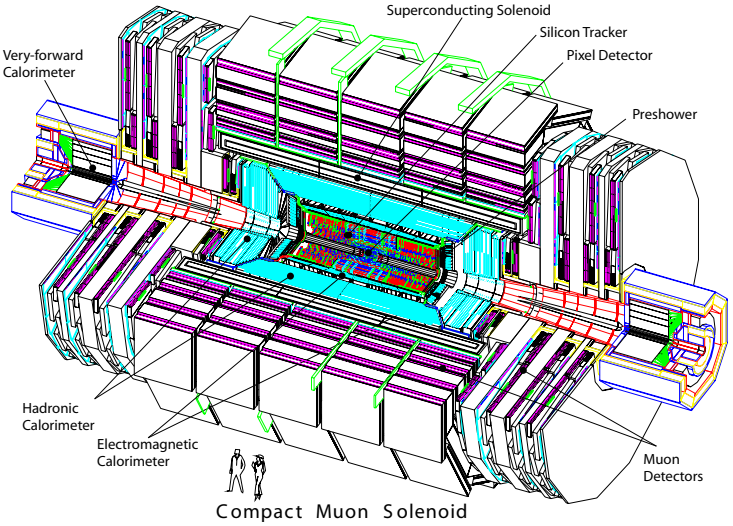

Figure 2.6: CMS detector overview.

Coordinate Conventions

The coordinate system adopted by CMS has the origin centred at the nominal collision point inside the experiment, the y-axis pointing vertically upward, and the x-axis pointing radially inward toward the centre of the LHC. Thus, the z-axis points along the beam direction toward the Jura mountains from LHC Point 5 (where CMS is located). The azimuthal angle ϕ is measured from the x-axis in the x-y plane. The polar angle θ is measured from the z-axis. Pseudorapidity is defined as

$$\eta = -\ln\tan(\theta/2) \tag{2.3}$$

The value $\eta = 0$ corresponds to a direction perpendicular to the beamline, while the limit $\eta = \infty$ gives a direction parallel to the beamline. In Figure 2.7 is shown a longitudinal view of the detector, with different η values highlighted.

The momentum and energy measured transverse to the beam direction, denoted by p_T and E_T, respectively, are computed as follow:

$$p_T = psin\theta \tag{2.4}$$

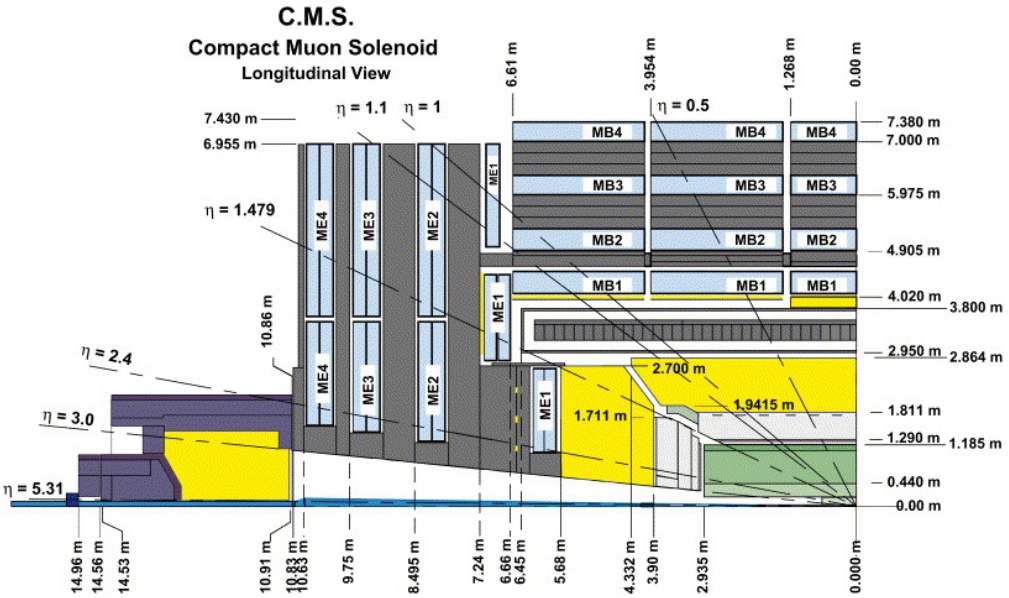

Figure 2.7: CMS longitudinal view.

$$E_T = Esin\theta \tag{2.5}$$

Finally, particles which escape the detection leave an imbalance in the transverse plane which is quantified as missing transverse energy in the following way:

$$E_T^{miss} = -\sum_i p_T^i \tag{2.6}$$

as the negative vectorial sum of the transverse momentum of all the visible particles in the event.
In the following, different CMS subdetectors have been described, starting from the tracker, that is the closest to the interaction point, moving outwards.

2.2.1 The tracking system

The tracker [34, 35], placed within the magnetic field, is the subdetector which is closer to the interaction point. It is dedicated to track and vertex finding. The silicon (Si) technology has been chosen for the whole tracker in order to provide good radiation hardness, high granularity and large hit redundancy to perform a good pattern recognition. The layout of the CMS tracker is shown in Figure 2.8. Close to the interaction vertex there are respectively 3 and 2 layers of hybrid pixel detectors in the barrel and in the endcap region that have been upgraded during winter 2016/2017 in the end-of-year shutdown, building an additional barrel layer and a disk. The external part of the tracker is composed of microstrip detectors: Tracker Inner Barrel and Disks (TIB/TID), Tracker

Outer Barrel (TOB) and Tracker EndCaps (TEC). The total area of the Si detectors is around 200 m^2, providing a coverage up to $\eta = 2.5$. The material budget inside the active volume of the tracker increases from 0.4 radiation length (X_0) at $\eta = 0$ to around 1 X_0 at $|\eta| = 1.6$, before decreasing to 0.6 X_0 at $|\eta| = 2.5$.

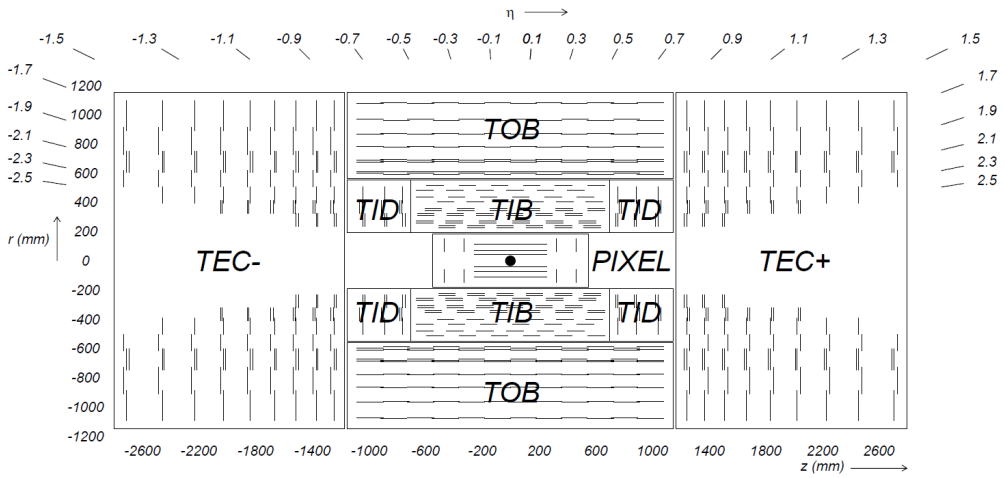

Figure 2.8: Schematic cross section through the CMS tracker in the $r - z$ plane: each line represents a detector module. Double lines indicate back-to-back modules which deliver stereo hits.

The pixel detector

The pixel detector is the part of the tracking system that is closest to the interaction region and covers a pseudorapidity range $-2.5 < \eta < 2.5$, matching the acceptance of the central tracker. Figure 2.9 shows the geometric pixel structure. It contributes precise tracking points in $r - \phi$ and z and therefore is responsible for a small impact parameter resolution that is important for good secondary vertex reconstruction. With a pixel cell size of 100×150 μm^2 emphasis has been put on achieving similar track resolution in both $r - \phi$ and z directions: 10 μm in $r - \phi$ direction and 20 μm along z. The pixel detector is essential for the reconstruction of secondary vertices from b quark and tau decays, and forming seed tracks for the outer track reconstruction and high level triggering. It consists of three barrel layers (BPix) with two endcap disks (FPix). The 53-cm-long BPix layers are located at mean radii of 4.4, 7.3 and 10.2 cm. The FPix disks, extending from $\approx$ 6 to 15 cm in radius, are placed on each side at z=$\pm$34.5 and z=$\pm$46.5 cm. BPix (FPix) contain 48 million (18 million) pixels covering a total area of 0.78 (0.28) m^2. The arrangement of the 3 barrel layers and the forward pixel disks on each side gives 3 tracking points over almost the full η range. In the high η region the 2 disk points are combined with the lowest possible radius point from the 4.4 cm barrel layer.

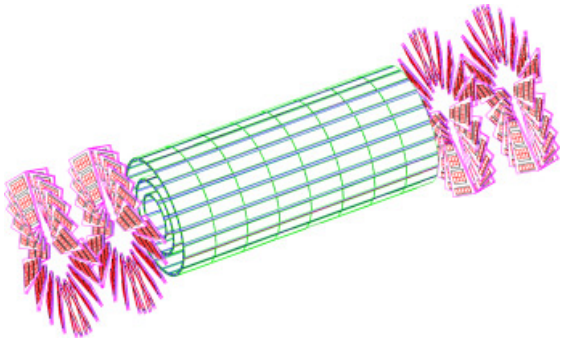

Figure 2.9: Geometrical layout of the pixel detector.

Pixel Upgrade

Due to the radiation damage and significant data losses due to high occupancy in the readout chip of the pixel detector, the pixel system has been replaced by a new one in the end-of-year shutdown during winter 2016/2017 in order to maintain the excellent tracking and other physics performance [36]. The main new features of the upgraded pixel detector are a ultra-light mechanical design with four barrel layers and three end-cap disks, digital readout chip with higher rate capability and a new cooling system. The geometrical layout of the upgrade system, shown in Figure 2.10, consists of four

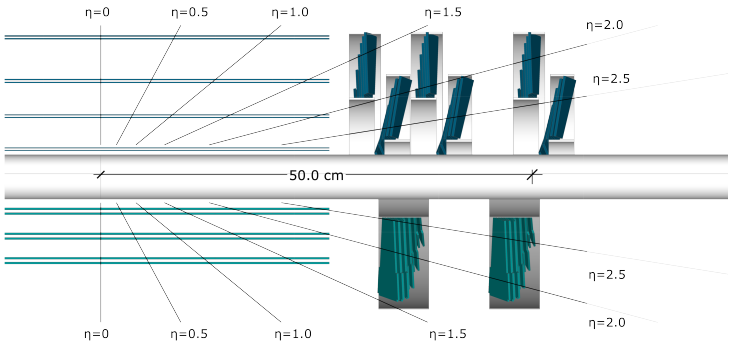

Figure 2.10: Comparison of the geometrical layouts of the old (bottom) and upgraded (top) CMS pixel detectors.

cylindrical barrel layers placed at radii of 29, 68, 109, 160 mm and three disks in each of the forward regions placed at a distance from the nominal interaction point of 291, 396 and 516 mm. This layout is optimised in order to offer full 4-hit tracking coverage up to pseudorapidity of 2.5, with an increased redundancy compared to the present system.

The silicon strip detector

The silicon strip detector is composed of three different subsystem. The TIB/TID (see Figure 2.8) are composed of 4 barrel layers, supplemented by 3 disks at each end. TIB/TID delivers up to 4 $r-\phi$ measurements on a trajectory using 320 μm thick silicon microstrip sensors with their strips parallel to the beam axis in the barrel and radial on the disks. The strip pitch is 80μm on layers 1 and 2 and 120 μm on layers 3 and 4 in the TIB, leading to a single point resolution of 23 μm and 35 μm, respectively. In the TID the mean pitch varies between 100μm and 141μm. The TIB/TID is surrounded by the TOB. It has an outer radius of 116 cm and consists of 6 barrel layers of 500μm thick microstrip sensors with strip pitches of 183μm on the first 4 layers and 122μm on layers 5 and 6. It provides another 6 $r-\phi$ measurements with single point resolution of 53μm and 35μm, respectively. The TOB extends in z between ±118cm. Beyond this z range, the TECs (±TEC, where the sign indicates the location along the z axis) cover the region 124 cm $< |z| <$ 282 cm and 22.5 cm $< |r| <$113.5 cm. Each TEC is composed of 9 disks, carrying up to 7 rings of silicon microstrip detectors (320μm thick on the inner 4 rings, 500μm thick on rings 5-7) with radial strips of 97μm to 184μm average pitch. Thus, they provide up to 9 ϕ measurements per trajectory. In addition, the modules in the first two layers and rings, respectively, of TIB, TID, and TOB as well as rings 1, 2, and 5 of the TECs carry a second microstrip detector module which is mounted back-to-back with a stereo angle of 100 mrad in order to provide a measurement of the second coordinate (z in the barrel and r on the disks). The achieved single point resolution of this measurement is 230μm and 530μm in TIB and TOB, respectively, and varies with pitch in TID and TEC.
The sensor elements in the strip tracker are single sided p-on-n type silicon micro-strip sensors shown in Figure 2.11: in TIB/TID and on the inner 4 rings of the TECs, thin sensors of (320 ± 20) μm wafer thickness are used, with substrate resistivity of ρ = 1.55 - 3.25 kΩcm; TOB and the outer 3 rings of the TECs are equipped with thicker sensors of (500 ± 20) μm thickness, with substrate resistivity of ρ = 4 - 8 kΩcm.

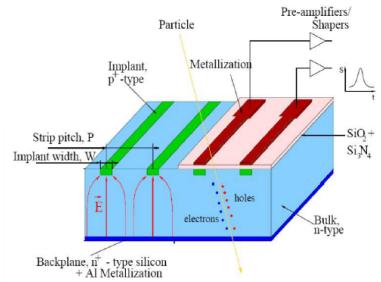

Figure 2.11: Single sided p-on-n type silicon micro-strip sensor.

2.2.2 Electromagnetic calorimeter

The electromagnetic calorimeter (ECAL) is a homogeneous calorimeter of almost 76000 Lead Tungstate ($PbWO_4$) [6] scintillating crystals divided into a barrel and two endcaps. A 3D view of the barrel and endcap electromagnetic calorimeter is shown in Figure 2.12.

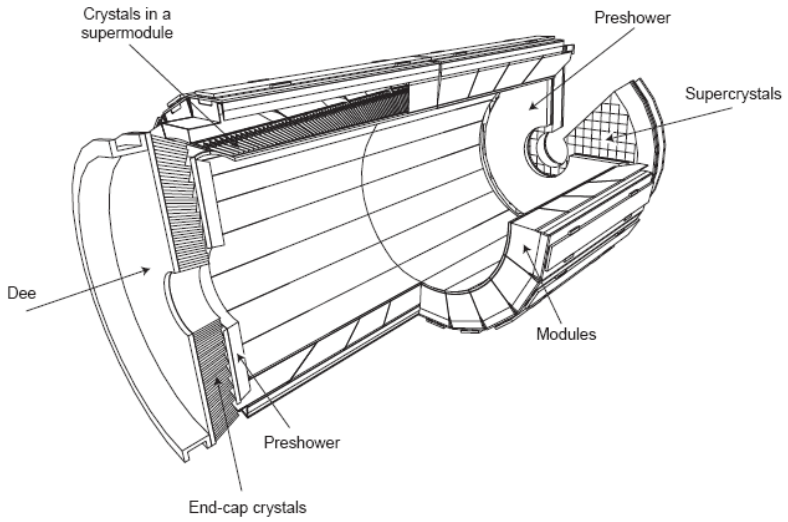

Figure 2.12: A 3D view of the electromagnetic calorimeter.

The Barrel Calorimeter

The barrel part of the ECAL covers the pseudorapidity range $|\eta| < 1.479$. The front face of the crystals is at a radius of 1.29 m and each crystal has a square cross-section of $22 \times 22\,\mathrm{mm}^2$ and a length of 230 mm corresponding to $25.8\,\mathrm{X}_0$. The truncated pyramid-shaped crystals are mounted in a geometry which is off-pointing with respect to the mean position of the primary interaction vertex, with a 3° tilt in both ϕ and in η. The crystal cross-section corresponds to $\Delta\eta \times \Delta\phi = 0.0175 \times 0.0175$. The barrel granularity is 360-fold in ϕ and (2×85)-fold in η, resulting in a total number of 61 200 crystals. The crystal volume in the barrel amounts to $8.14\,\mathrm{m}^3$ (67.4 t). Crystals for each half-barrel are grouped in 18 supermodules each subtending 20° in ϕ. Each supermodule comprises four modules with 500 crystals in the first module and 400 crystals in each of the remaining three modules. For simplicity of construction and assembly, crystals have been grouped in arrays of 2×5 crystals which are contained in a very thin wall ($200\,\mu$m) alveolar structure and form a submodule.

The Endcap Calorimeter

The endcap part of the crystal calorimeter covers a pseudorapidity range from 1.48 to 3.0. The design of the endcaps provides precision energy measurement up to $|\eta| = 2.5$. Crystals are however installed up to $|\eta| = 3$ in order to augment the energy-flow measurement in the forward direction. The mechanical design of the endcap calorimeter is based on an offpointing pseudo-projective geometry using tapered crystals of the same shape and dimensions ($24.7 \times 24.7 \times 220\,\mathrm{mm}^3$) grouped together into units of 36, referred to as supercrystals. A total of 268 identical supercrystals is used to cover each endcap with a further 64 sectioned supercrystals used to complete the inner and outer perimeter. Each endcap contains 7324 crystals, corresponding to a volume of $1.52\,\mathrm{m}^3$ (12.6 t). Both endcaps are identical. Each endcap detector is constructed using Dee-shaped sections. Because of the high radiation levels in the endcaps all materials used in this region must tolerate very large doses and neutron fluence.
Within the endcap part, it is also installed the preshower detector.

The Preshower Detector

The endcap preshower covers a pseudorapidity range from $|\eta| = 1.65$ to 2.61. Its main function is to provide π^0-γ separation. The preshower detector, placed in front of the crystals, contains two lead converters of a total thickness of $2\,\mathrm{X}_0$ and $1\,\mathrm{X}_0$ respectively, followed by detector planes of silicon strips with a pitch less then 2 mm. The impact position of the electromagnetic shower is determined by the centre-of-gravity of the deposited energy. The accuracy is typically $300\,\mu$m at 50 GeV. In order to correct for the energy deposited in the lead converter, the energy measured in the silicon is used to apply corrections to the energy measurement in the crystal. The fraction of energy deposited in the preshower (typically 5% at 20 GeV) decreases with increasing incident energy.

2.2.3 Hadronic Calorimeter

Figure 2.13 shows the longitudinal view of the CMS detector with the locations of the hadron calorimeters [37]. The dashed lines are at fixed η values. The hadron calorimeter barrel and endcaps sit behind the tracker and the electromagnetic calorimeter as seen from the interaction point. The hadron calorimeter barrel is radially restricted between the outer extent of the electromagnetic calorimeter (R = 1.77 m) and the inner extent of the magnet coil (R = 2.95 m). This constrains the total amount of material which can be put in to absorb the hadronic shower. Therefore, an outer hadron calorimeter or tail catcher is placed outside the solenoid complementing the barrel calorimeter. Beyond $|\eta| = 3$, the forward hadron calorimeters placed at 11.2 m from the interaction point extend the pseudorapidity coverage down to $|\eta| = 5.2$ using a Cherenkov-based, radiation-hard technology.

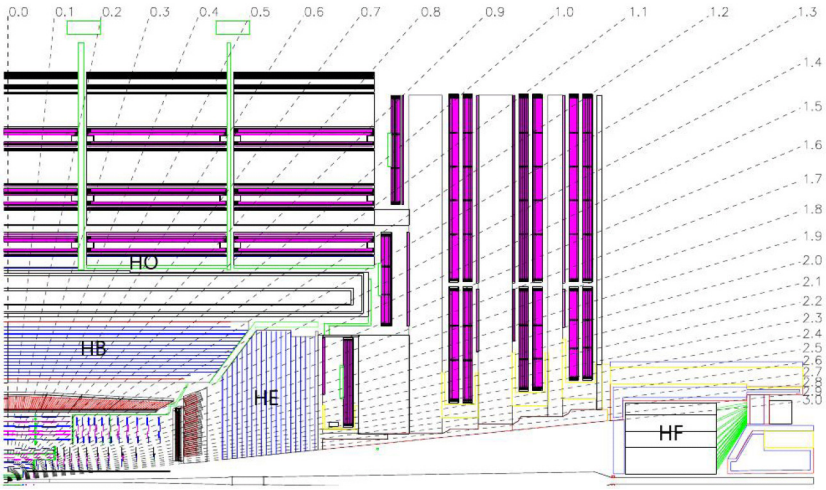

Figure 2.13: Longitudinal view of the CMS detector showing the locations of the hadron barrel (HB), endcap (HE), outer (HO) and forward (HF) calorimeters.

Hadron barrel (HB)

The HB is a sampling calorimeter covering the pseudorapidity range $|\eta| < 1.3$. It is divided into two half-barrel sections, each half-section being inserted from either end of the barrel cryostat of the superconducting solenoid and subsequently hung from rails in the median plane. The HB consists of 36 identical azimuthal wedges which form the two half-barrels (HB+ and HB-). The wedges are constructed out of flat brass absorber plates aligned parallel to the beam axis. Each wedge is segmented into four azimuthal angle (ϕ) sectors. The plates are bolted together in a staggered geometry resulting in a configuration that contains no projective dead material for the full radial extent of a wedge. The innermost and outermost plates are made of stainless steel for structural strength. The active medium is a plastic scintillator and it is divided into 16-η sectors, resulting in a segmentation $(\Delta\eta \times \Delta\phi) = (0.087 \times 0.087)$. The wedges are themselves bolted together, in such a fashion as to minimise the crack between the wedges to less than 2 mm. The absorber consists of a 40 mm-thick front steel plate, followed by eight 50.5 mm-thick brass plates, six 56.5 mm-thick brass plates, and a 75 mm-thick steel back plate. The total absorber thickness at 90° is 5.82 interaction lengths (λ_I). The HB effective thickness increases with polar angle (θ) as $1/\sin\theta$, resulting in 10.6 λ_I at $|\eta| = 1.3$. The electromagnetic crystal calorimeter in front of HB adds about 1.1 λ_I of material.

Hadron endcap (HE)

The hadron calorimeter endcaps (HE) cover a substantial portion of the rapidity range, $1.3 < |\eta| < 3$. Since the calorimeter is inserted into the ends of a 4-T solenoidal magnet, the absorber must be made from a non-magnetic material in order not to distort it. It

must also have a maximum number of interaction lengths to contain hadronic showers, good mechanical properties and reasonable cost, leading to the choice of cartridge brass. The endcaps are attached to the muon endcap yoke. Only a small part of the calorimeter structure can be used for the fixation to the magnet iron, because the majority of the space between HE and muon absorber is occupied with muon cathode strip chambers. The 10-t electromagnetic calorimeter with the 2-t preshower detector is attached at the front face of HE. The design of the absorber is driven by the need to minimise the cracks between HB and HE, rather than single-particle energy resolution, since the resolution of jets in HE will be limited by pileup, magnetic field effects, and parton fragmentation. The plates are bolted together in a staggered geometry resulting in a configuration that contains no projective dead material. The design provides a self-supporting hermetic construction. The brass plates are 79-mm-thick with 9-mm gaps to accommodate the scintillators. The total length of the calorimeter, including electromagnetic crystals, is about 10 λ_I. The granularity of the calorimeters is $\Delta\eta \times \Delta\phi = 0.087 \times 0.087$ for $|\eta|$ <1.6 and $\Delta\eta \times \Delta\phi \approx 0.17 \times 0.17$ for $|\eta| \geq 1.6$.

Hadron outer (HO)

In the central pseudorapidity region, the combined stopping power of EB plus HB does not provide sufficient containment for hadron showers. To ensure adequate sampling depth for $|\eta| < 1.3$, the hadron calorimeter is extended outside the solenoid with a tail catcher called the HO or outer calorimeter. The HO utilises the solenoid coil as an additional absorber equal to $1.4/\sin\theta$ interaction lengths and is used to identify late starting showers and to measure the shower energy deposited after HB. Outside the vacuum tank of the solenoid, the magnetic field is returned through an iron yoke designed in the form of five 2.536 m wide (along z-axis) rings. The HO is placed as the first sensitive layer in each of these five rings; the nominal central z positions of the five rings are respectively -5.342 m, -2.686 m, 0, +2.686 m and +5.342 m. At $\eta = 0$, HB has the minimal absorber depth. Therefore, the central ring (ring 0) has two layers of HO scintillators on either side of a 19.5 cm thick piece of iron (the tail catcher iron) at radial distances of 3.82 m and 4.07 m, respectively. All other rings have a single HO layer at a radial distance of 4.07 m. The total depth of the calorimeter system is thus extended to a minimum of 11.8 λ_I except at the barrel-endcap boundary region. The HO is constrained by the geometry of the muon system. The segmentation of these detectors closely follows that of the barrel muon system. Each ring has 12 identical ϕ-sectors. The 12 sectors are separated by 75 mm-thick stainless steel beams which hold successive layers of iron of the return yoke as well as the muon system.

Hadron forward (HF)

The forward calorimeter is a cylindrical steel structure with an outer radius of 130.0 cm. The front face of the calorimeter is located at 11.2 m from the interaction point. The hole for the beam pipe is cylindrical, with radius 12.5 cm from the centre of the beam line. This structure is azimuthally subdivided into 20° modular wedges. Thirty-six such

wedges (18 on either side of the interaction point) make up the HF calorimeters. The fibres run parallel to the beam line, and are bundled to form 0.175 × 0.175 ($\Delta\eta \times \Delta\phi$) towers. The detector is housed in a hermetic radiation shielding which consists of layers of 40 cm thick steel, 40 cm of concrete, and 5 cm of polyethylene. A large plug structure in the back of the detector provides additional shielding. It consists of a steel absorber structure that is composed of 5 mm thick grooved plates. Fibres are inserted in these grooves. The detector is functionally subdivided into two longitudinal segments. Half of the fibres run over the full depth of the absorber (165 cm $\approx$ 10 λ_I) while the other half starts at a depth of 22 cm from the front of the detector. These two sets of fibres are read out separately. This arrangement makes it possible to distinguish showers generated by electrons and photons, which deposit a large fraction of their energy in the first 22 cm, from those generated by hadrons, which produce nearly equal signals in both calorimeter segments on average. The long fibre section is referred as L (measuring the total signal), and the short fibre section as S (measuring the energy deposition after 22 cm of steel). The absorber has grooves which make a square grid separated by 5.0 ± 0.1 mm centre-to-centre. Long and short fibres alternate in these grooves.

2.2.4 Magnet

The required performance of the muon system, and hence the bending power, is defined by the narrow states decaying into muons and by the unambiguous determination of the sign for muons with a momentum of the order of TeV. The momentum analysis of charged particles is performed by measurement of particles trajectories inside the solenoid and the momentum resolution is given by:

$$\frac{\Delta p_T}{p_T} = \Delta s \frac{8 p_T}{0.3 B R^2}$$

where p = γmv is the particle momentum, B is the magnetic induction, s is the sagitta and R is the solenoid radius. Therefore strong field and large radius are an efficient approach to reach optimal momentum resolution: CMS preferred a high field within a compact space.
A long superconducting solenoid (L = 12.5 m) has been chosen with a free inner diameter of 5.9 m and a uniform magnetic field of 3.8 T[1]. The superconducting is cooled down to 4.45 K by circulating liquid helium.
Figure 2.14 shows a representation of the CMS magnet field [38]; Table 2.2 summarises the parameters of the solenoid.

2.2.5 Muon System

The muon system is the outermost of the CMS subdetectors. Its main goals are the identification of muons, thanks to their high penetrating power, and a precise measurement of their momentum, with the help of the information coming from the tracker.

[1]It was designed to produce a magnetic field of up to 4 T in the inner region. In order to maximise its lifetime, the magnet is operated at 3.8 T

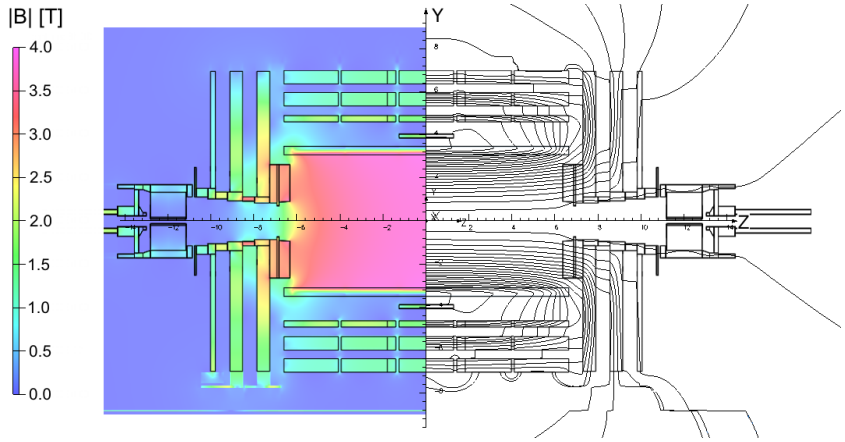

Figure 2.14: Value of |B| (left) and field lines (right) predicted on a longitudinal section of the CMS detector, for the underground model at a central magnetic flux density of 3.8 T.

Parameter	Value
Field	3.8 T
Inner bore	5.9 m
Length	12.5 m
Number of turns	2168
Current	19.5 kA
Stored energy	2.7 GJ

Table 2.2: Parameters of the CMS superconducting solenoid.

The muon system also works as trigger for events which involve muons and it provides a precise time measurement of the bunch crossing. The CMS muon system [39] relies on three kinds of gaseous detectors: drift tubes (DT), cathode strip chambers (CSC) and resistive plate chambers (RPC). The DT and the CSC provide an excellent spatial resolution for the measurement of charged particle momentum; the RPC are used for trigger issues because of the very good timing. The active parts of the muon system are hosted into stations which are interleaved by the iron layers of the return yoke of the magnet. The longitudinal view of a quarter of the muon system is given in Figure 2.15 [40]. The barrel extends up to $|\eta| < 1.2$, the endcaps up to $|\eta| < 2.4$.

DT

The CMS barrel muon detector consists of 4 stations forming concentric cylinders around the beam line: the 3 inner cylinders have 60 drift chambers each and the outer cylinder has 70. It is possible to use drift chambers as the tracking detectors for the barrel muon system because of the low expected rate and the relatively low strength of the local

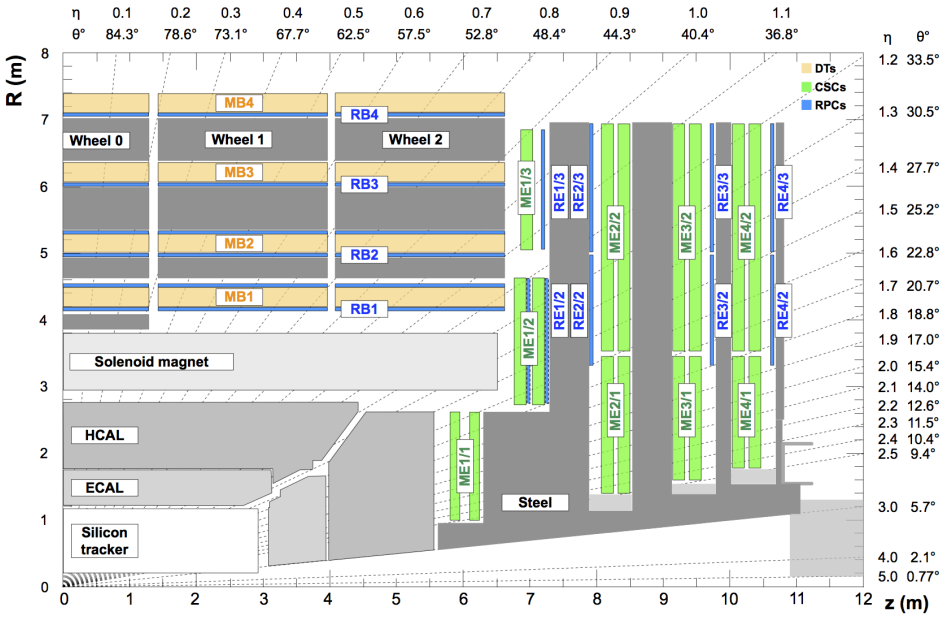

Figure 2.15: An R-z cross section of a quadrant of the CMS detector with the axis parallel to the beam (z) running horizontally and the radius (R) increasing upward. The interaction point is at the lower left corner. The locations of the various muon stations and the steel flux-return disks (dark areas) are shown. The drift tube stations (DTs) are labeled MB ("Muon Barrel") and the cathode strip chambers (CSCs) are labeled ME ("Muon Endcap"). Resistive plate chambers (RPCs) are mounted in both the barrel and endcaps of CMS, where they are labeled RB and RE, respectively.

magnetic field. In each of the 12 sectors of the yoke there are 4 muon chambers per wheel, labeled MB1, MB2, MB3, and MB4 (Figure 2.16). The yoke-iron supports that are between the chambers of a station generate 12 unavoidable dead zones in the ϕ coverage, although the supports are placed so as not to overlap in ϕ. A DT chamber is made of 3 (or 2) superlayers (SL, see Figure 2.17), each made of 4 layers of rectangular drift cells staggered by half a cell. The SL is the smallest independent unit of the design. The wires in the 2 outer SLs are parallel to the beam line and provide a track measurement in the magnetic bending plane (r-ϕ). In the inner SL, the wires are orthogonal to the beam line and measure the z position along the beam. This third, z-measuring, SL is not present in the fourth station, which therefore measures only the ϕ coordinate. The main element in the DT is the drift cell, shown in Figure 2.18. The maximum drift time is almost 400 ns. The maximum drift length is 2.0 cm and the single point resolution is 200 μm (see Figure 2.19 [41]). The z coordinate is measured with a resolution of 150 μm. The gas used is $\mathrm{Ar} - \mathrm{CO}_2$ mixture (85% - 15%).

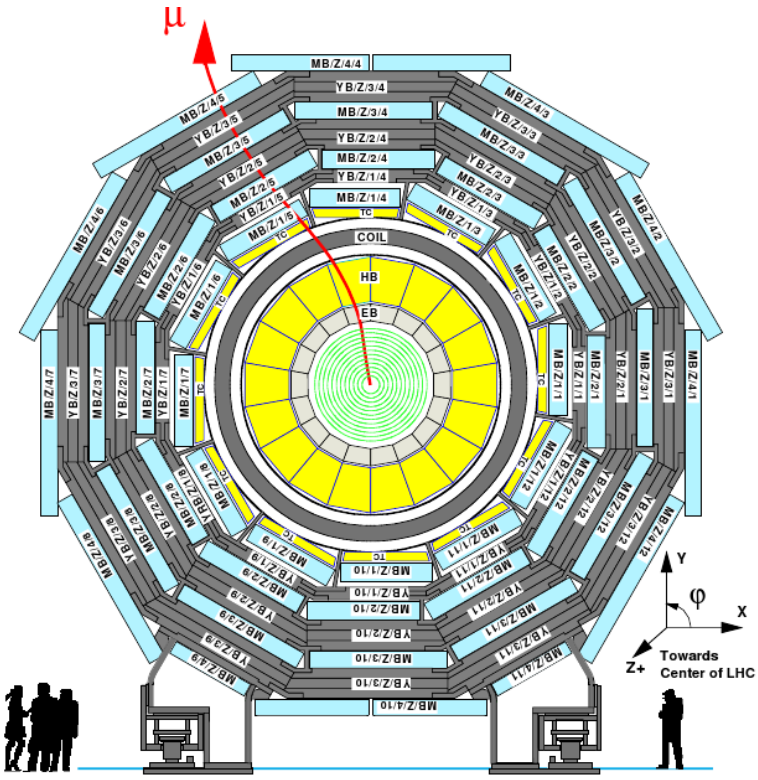

Figure 2.16: Layout of the CMS barrel muon DT chambers in one of the 5 wheels. The chambers in each wheel are identical with the exception of wheels -1 and +1 where the presence of cryogenic chimneys for the magnet shortens the chambers in 2 sectors. Note that in sectors 4 (top) and 10 (bottom) the MB4 chambers are cut in half to simplify the mechanical assembly and the global chamber layout.

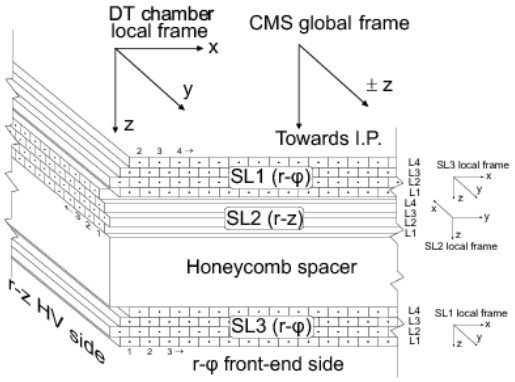

Figure 2.17: Layout of the DT chamber: each chamber is made of 3 Superlayers of Drift Tube and each SL is made of 4 layers of Drift Tube.

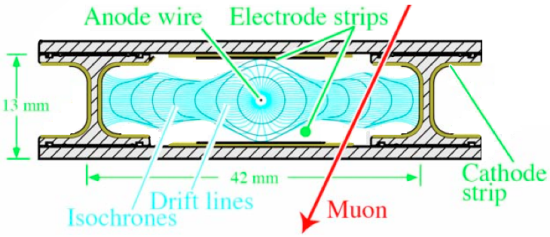

Figure 2.18: Sketch of a cell showing drift lines and isochrones. The plates at the top and bottom of the cell are at ground potential. The voltages applied to the electrodes are +3600V for wires, +1800V for strips, and -1200V for cathodes.

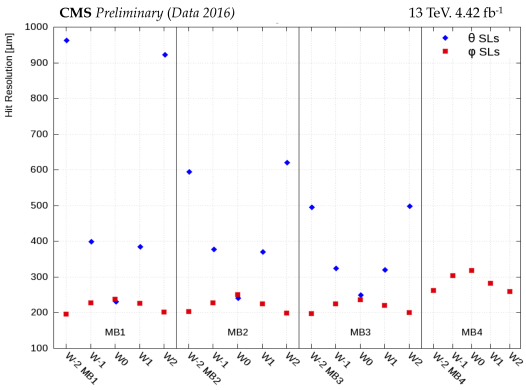

Figure 2.19: Reconstructed hit resolution for DT ϕ superlayers (squares) and DT θ superlayers (diamonds) measured with the 2016 data, plotted as a function of station and wheel. The uncertainties in these values are smaller than the marker size in the figure.

CSC

The Cathode Strip Chambers (CSC) are arranged in 4 stations (ME1, ME2, ME3, ME4). The chambers are grouped into rings, with the first station (ME1) consisting of three rings, and the remaining three (ME2-ME4) having two rings of chambers (see Figure 2.15).
The chambers are trapezoidal and cover either 10° or 20° in ϕ; all chambers, except for the ME1/3 ring, overlap and provide contiguous ϕ -coverage. A muon in the pseudo-rapidity range $1.2< |\eta| <2.4$ crosses 3 or 4 CSCs. In the endcap-barrel overlap range, $0.9< |\eta| <1.2$, muons are detected by both the barrel drift tubes and endcap CSCs.
The CSCs are multiwire proportional chambers comprised of 6 anode wire planes interleaved among 7 cathode panels (Figure 2.20). Wires run azimuthally and define a track's radial coordinate. Strips are milled on cathode panels and run lengthwise at constant $\Delta\phi$ width. Spatial resolutions is reported in Figure 2.21 comparing 2012, 2015 and 2016

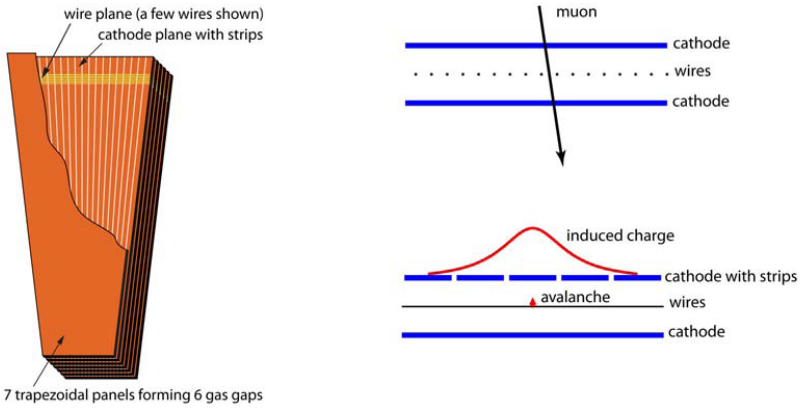

(a) (b)

Figure 2.20: (a) Layout of a CSC made of 7 trapezoidal panels. The panels form 6 gas gaps with planes of sensitive anode wires. (b) A schematic view of a single gap illustrating the principle of CSC operation. By interpolating charges induced on cathode strips by avalanche positive ions near a wire, one can obtain a precise localisation of an avalanche along the wire direction.

data taking [41]. The nominal gas mixture used is $40\%\mathrm{Ar} + 50\%\mathrm{CO}_2 + 10\%\mathrm{CF}_4$.

Station	Spatial resolution (μm)		
	Run 1	Run 2	
	2012	2015	2016
ME1/1a	66	50	45
ME1/1b	57	55	52
ME1/2	93	95	90
ME1/3	108	112	105
ME2/1	132	133	125
ME2/2	140	145	134
ME3/1	125	128	120
ME3/2	142	147	135
ME4/1	127	130	123
ME4/2	147	146	139

Figure 2.21: The table summarises the resolutions per station measured for all chamber types in the CSC system in 2016 data, and values measured in 2015 and 2012 for comparison. Statistical uncertainties from the fits are negligible, and systematic uncertainties dominate.

RPC

Resistive Plate Chambers (RPC) are gaseous parallel-plate detectors that combine adequate spatial resolution with a time resolution comparable to that of scintillators. An RPC is capable of tagging the time of an ionising event in a much shorter time than the 25 ns between 2 consecutive LHC bunch crossings (BX) (see Figure 2.23 [41]). The CMS RPC basic double-gap module consists of 2 gaps, hereafter referred as up and down gaps, operated in avalanche mode with common pick-up read-out strips in between. The total induced signal is the sum of the 2 single-gap signals. Six layers of RPC chambers are embedded in the barrel iron yoke, 2 located in each of the first and second muon stations and 1 in each of the 2 last stations. The redundancy in the first 2 stations allows the trigger algorithm to perform the reconstruction always on the basis of 4 layers, even for low p_T particles, which may stop inside the iron yoke. In the endcap region, 4 layers up to $\eta = 1.9$ are built. In the barrel iron yoke, the RPC chambers form 6 coaxial sensitive cylinders (all around the beam axis) that are approximated with concentric dodecagon arrays arranged into 4 stations (Figure 2.22). In the first and second muon stations there are 2 arrays of RPC chambers located internally and externally with respect to the Drift Tube chambers: RB1in and RB2in at smaller radius and RB1out and RB2out at larger radius. In the third and fourth stations there are again 2 RPC chambers, both located on the inner side of the DT layer (named RB3+ and RB3-, RB4+ and RB4-). A special case is RB4 in sector 4, which consists of 4 chambers, RB4±±, RB4±. Finally, in sectors 9 and 11 there is only 1 RB4 chamber. In the forward and backward regions of the CMS detector, 4 iron disks constitute the RPC endcap system, each divided into two rings. In station 1, the RPC rings are mounted adjacent to the corresponding CSC rings. In the other stations, RPC ring 2 plus ring 3 cover the same area as CSC ring 2.

2.3 Trigger and Data Acquisition

The trigger system in CMS is the start of the physics event selection process. A decision to retain an event for further consideration has to be made every 25 ns. This decision is based on the event's suitability for inclusion in one of the various datasets to be used for analysis. The datasets to be taken are determined by CMS physics priorities as a whole. These datasets include dilepton and multilepton datasets, diphoton datasets, lepton plus jet datasets for top, Higgs and BSM physics, and inclusive electron datasets for calorimeter calibrations. In addition, other samples are necessary for measuring efficiencies in event selection and studying backgrounds. The trigger has to select these samples in real time along with the main data samples. The input rate of 10^9 interactions every second must be reduced by a factor of at least 10^7 reaching 100 Hz, the maximum rate that can be archived by the on-line computer farm. CMS has chosen to reduce this rate in two steps. At the first level (L1 [42]) all data is stored for 3.2 μs, after which no more than 100 kHz of the stored events are forwarded to the High Level Triggers (HLT). The L1 system uses only coarsely segmented data from calorimeter and muon detectors, while holding all the high-resolution data in pipeline memories in the front-end

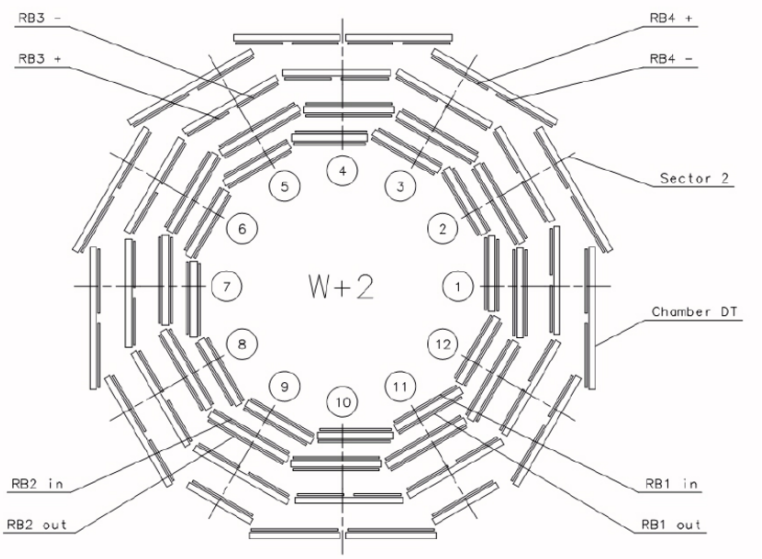

Figure 2.22: Schematic layout of one of the 5 barrel wheels, which are labeled -2, -1, 0, +1, and +2, respectively. Each wheel is divided into 12 sectors that are numbered as shown.

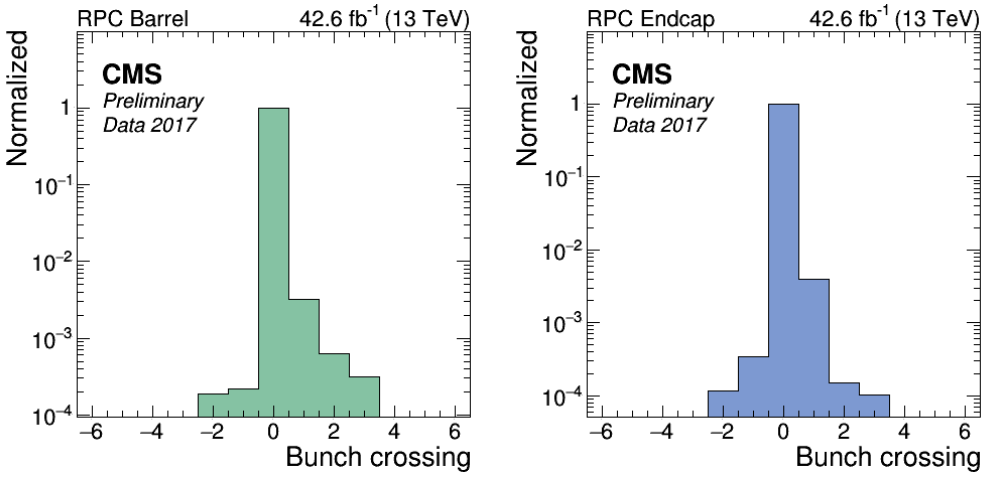

Figure 2.23: The bunch crossing distribution of RPC hits in the Barrel (left) and the Endcap (right) from muons, using full 2017 dataset at 13 TeV.

electronics. The HLT [43] is provided by a subset of the on-line processor farm which, in turn, passes a fraction of these events to the remainder of the on-line farm for more complete processing.

2.3.1 Level 1 Trigger

The design of the CMS L1 Trigger system is illustrated in Figure 2.24. At the first

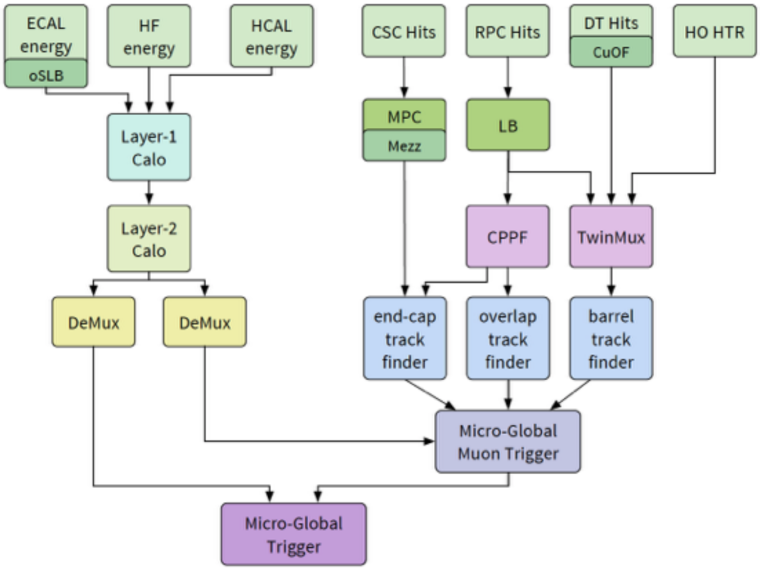

Figure 2.24: CMS L1 Trigger system.

level all information about the event is preserved. The first level decision is made, with negligible dead-time, on a subset of the total information available for the events. Since signal propagation delays are included in this pipeline time, the L1 trigger calculations must be done in many cases in less than 1 μs. If the first level trigger generates an accept, the event data are moved or assigned to a buffer for readout and processing by the High Level Triggers. The L1 trigger involves the calorimetry and muon systems as well as some correlation of information from these systems. The L1 decision is based on the presence of local objects such as photons, electrons, muons, and jets, using information from calorimeters, and muon systems in a given element of η-ϕ space. It also employs global sums of E_T and E_T^{miss}. Each of these items is tested against several p_T or E_T thresholds.

L1 muon trigger

L1 muon trigger elaborates information coming from the three muon detectors, in the form of segment for DT and CSC and single hits for RPC. Before to be injected in the track finder (TF), DT and RPC barrel information are combined by the concentrator

card, the TwinMux, in order to improve BX assignment to the segment exploiting RPC better time resolution and DT better spatial resolution. According to the pseudorapidity, there are three different TFs:

- *Barrel Muon Track Finder* (BMTF) for muon in the barrel region, $|\eta|$ <0.9
- *Overlap Muon track Finder* (OMTF) for overlap region between barrel and endcap, 0.9< $|\eta|$ <1.2
- *Endcap Muon Track Finder* (EMTF) for muon in the endcap region, $|\eta|$ >1.2

Each TF reconstructs different muons that are sent to the micro-Global Muon trigger (μGMT). The μGMT combines and ranks muon candidates from the 3 systems by p_T and quality, removes, if necessary, duplicated muons and evaluates the isolation (see 3.6.4) around the L1 muon candidate.
Finally, muons from μGMT are combined with the information elaborated by the calorimeters to obtain final micro-Global trigger (μGT).

2.3.2 High Level Trigger

The CMS Level-1 Trigger System is required to reduce the input interaction rate of 1 GHz to a filtered event rate of 75 kHz. To match the capabilities of the mass storage and offline computing systems, the final output of the experiment should not exceed 100 events per second. The High Level Triggers have access to all the information used in L1 since this is stored locally in the L1 trigger crates. Consequently, High Level Triggers can make further combinations and other topological calculations on the digital list of objects transmitted from L1. Eventually, the High Level Triggers use the full event data for the decision to keep an event.
There are about 400 different HLT trigger paths, looking for different objects and signatures in an event. After some parts of the data are reconstructed, a filter module decides if the reconstructed objects pass the thresholds and the next step in reconstruction is started, or if the event is not accepted by the path. In the later case, the execution of the path is stopped and the following reconstruction steps and filter steps are not performed to save computation time. If an event is not accepted by a path, it can still be accepted by a different path.
If, for some paths with low thresholds, the acceptance rate is too high, they can be prescaled to lower the rate. The prescale value for one trigger path has several predefined levels, depending on the instantaneous luminosity of the LHC machine. During an LHC fill, the instantaneous luminosity decreases, and the prescale values can be changed during a CMS run to keep the global trigger rate at an optimal level.

HLT for muon

Muon reconstruction at HLT starts with track fitting in the outer muon spectrometer, which builds the so called level-2 (L2) muons. The level-3 (L3) muon reconstruction is the muon HLT step that builds full muon tracks (including tracker information) starting

from those L2 muons. A sequence of three algorithms is tried in cascade from the fastest to the slowest and the cascade is interrupted when a L3 candidate is reconstructed. For the first two algorithms the seeds to reconstruct the tracker tracks are built on the basis of L2 muons propagated to tracker layers with the addition of information from one tracker hit for the second algorithm. For the last algorithm, starting from inside and going outward, the L2 muons are used to build regions where to look for hits but the seeds to reconstruct tracker tracks are built using pixel/tracker hit information.

2.4 CMS computing system

Events that have fired HLT must be stored and reprocessed in order to be analysed. The real and simulated data are stored in an infrastructure called *World LHC Computing Grid* whose task is also to transfer and process them: this computing system is made up of more than 170 computer centres distributed in 34 countries and connected via high-speed networks, sketched in Figure 2.25 [44].

Data from the HLT and the online CMS acquisition (RAW data) are stored in the

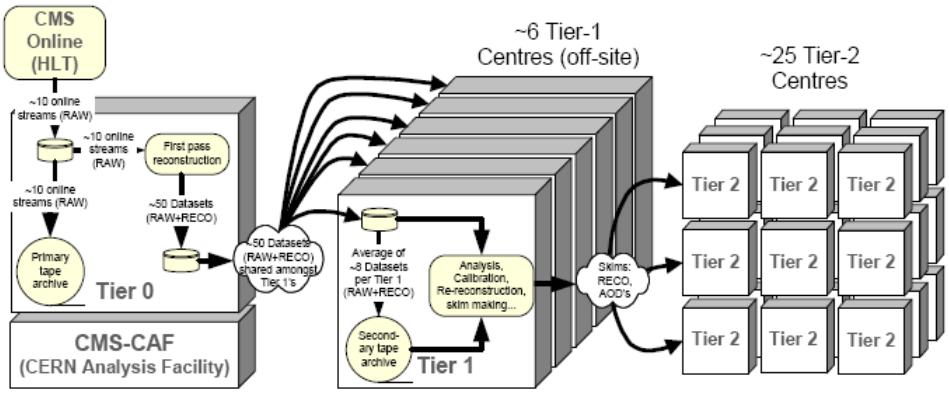

Figure 2.25: Scheme of data produced in CMS and transfer to the various Tiers

Tier-0 (T0), present at CERN, which does not provide useful material for the analysis, but organises the material collected in different groups, called Primary Datasets, according to the trigger path with which they were acquired. In addition, T0 takes care of transforming RAW into a data format useful for analysis, RECO and AOD (Analysis Object Data), which are transferred to the seven computing centres Tier-1 (T1), spread around the world.

In addition to storing the data sent by the T0, the T1 have the task of reconstructing, calibrating and screening the RAW DATA; they retain the various MCs produced in Tier-2 (T2) and redistribute them to the various nodes. Finally, T2 are the calculation centres to which all users can access to make their analysis. Users can then process the

data (real and simulated, that is derived from collisions and revealed or simulated with appropriate Monte Carlo techniques), submitting their analyses to the Grid, which in turn distributes to run them on various calculation centres.
For data, CMS has established three types of formats for different levels of detail and precision: RAW, RECO and AOD.
The RAW format refers to the data that contain the information collected by the detector and which have exceeded the trigger requests. The RECO format refers to the reconstructed data to which reconstruction, identification and correction algorithms have been applied, in such a way as to promote them to physical objects at a higher level. Algorithms include subdetector filters, particle identification, reconstruction of primary and secondary vertices. The AOD format is obtained from RECOs using filtering processes, so as to obtain compact and easily accessible objects. It is in this format that data reaches Tier-2s outside CERN. CMS provides another data format, called PAT (Physics Analysis Toolkit), in which the user has the possibility to decide what to store the AOD or RECO, further reducing the weight of the events.
Beside PAT, CMS has developed new data formats, miniAOD and nanoAOD in order to reduce space for data storage. Both formats are produced from AOD applying very loose cut on the object reconstructed (e.g. number of leptons, number of jets, p_T of the leptons).
For MC simulations instead of RAW, the generated events are used. MC generation involves different steps, called GEN, SIM and DIGI. GEN stands for Generation, i.e. for the generation of physics events, using complex simulation algorithms, such as PYTHIA [45], POWHEG [46–51] and MADGRAPH [52]. SIM stands for Simulation, i.e. the physics processes that occur when particles pass through the CMS detectors and their responses are simulated. The software is based on GEANT [53]. DIGI stands for Digitisation, which is the simulation of the electronics response.
Events, both real data and MC simulations, are stored in root files, a format readable by the data analysis framework called ROOT [54]. The environment in which the data is analysed is CMSSW, a set of software running on Scientific Linux. The software structure reflects the modular one of the events; there is a single executable that reads the configuration files and loads the modules requested by the user in a given analysis. There are three modules specified for a particular operation: EDProducer that creates new collections of objects and inserts them into the Event Data Model, EDAnalyser that allows to analyse, without manipulating, the data creating histograms, and EDFilter that allows to set conditions (of filters) on objects. The module is written in C++ and is managed by external files written in python, called configuration files, in which are defined the data to be analysed, the sequence of the modules to be used and the parameters they need and the format of the output.

Chapter 3

Object reconstruction in CMS

Event reconstruction in CMS is based on an optimised combination of all sub-detectors information. In this process, the identification of the particle type (photon, electron, muon, charged hadron, neutral hadron) plays an important role in the determination of the particle direction and energy. Photons (e.g. coming from π^0 decays or from electron bremsstrahlung) are identified as ECAL energy clusters not linked to the extrapolation of any charged particle trajectory to the calorimeter. Electrons are identified as a primary charged particle track and potentially many ECAL energy clusters corresponding to this track extrapolated to the calorimeter and to possible bremsstrahlung photons emitted along the way through the tracker material. Muons are identified as a track in the central tracker consistent with either a track or several hits in the muon system. Charged hadrons are identified as charged particle tracks neither identified as electrons, nor as muons. Finally, neutral hadrons are identified as HCAL energy clusters not linked to any charged hadron trajectory, or as ECAL and HCAL energy excesses with respect to the expected charged hadron energy deposit (see Figure 3.1).

In this chapter I describe how different particles are reconstructed in CMS, according to their different interaction with the sub-detectors. In particular, muons play a central role in this thesis so their reconstruction and identification have been treated in more details. Description of new specialised algorithms, developed by CMS for muons with p_T of the order of TeV, to take into account multiple scattering and radiative processes, is also provided.

3.1 Particle Flow algorithm

Particle Flow (PF) algorithm [55] is based on combining the information coming from all the sub-detectors, known as PF elements, for the reconstruction and identification of all the stable particles such as muons, photons and charged hadrons; from this information it is possible to determine the missing transverse energy (MET), and to reconstruct the jets. MET gives indications on energy and direction of invisible particles such as neutrinos and neutral hadrons while from the jets it is possible to identity τ leptons and

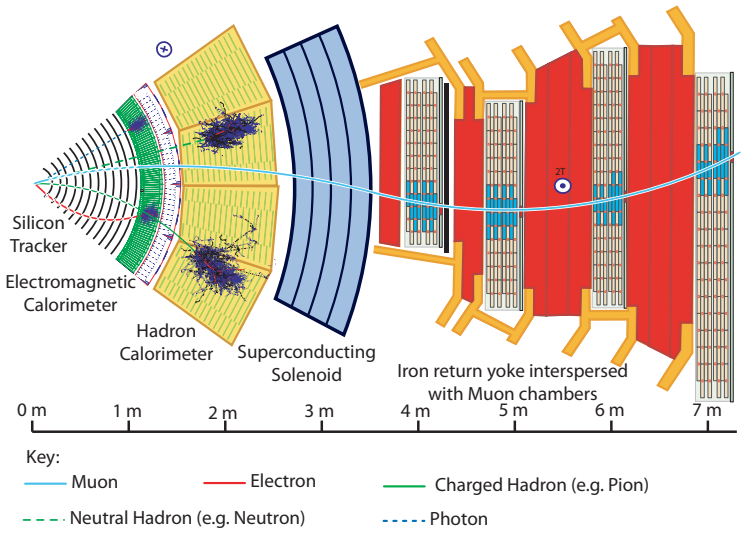

Figure 3.1: Particle interaction and reconstruction in a transverse slice of the CMS detector, from the beam pipe to the muon detector.

jets produced by the fragmentation of a quark.
The reconstruction of a particle first proceeds with a link algorithm that connects the PF elements from different sub-detectors. The link algorithm can try to combine any pair of elements in the event. In order to prevent the computing time of the link algorithm from growing quadratically with the number of particles, the pairs of elements considered by the link procedure are restricted to the nearest neighbours in the (η, ϕ) plane. The link algorithm then produces PF blocks of elements associated either by a direct link or by an indirect link through common elements. In each PF block, the identification and reconstruction sequence proceeds in the following order. First, muon candidates are identified and reconstructed and the corresponding PF elements (tracks and clusters) are removed from the PF block. The electron identification and reconstruction follows, with the aim of collecting the energy of all bremsstrahlung photons. Energetic and isolated photons, converted or unconverted, are identified in the same step. The corresponding tracks and ECAL or preshower clusters are excluded from further consideration. At this level, tracks with a p_T uncertainty in excess of the calorimetric energy resolution expected for charged hadrons are masked, which allows the rate of misreconstructed tracks at large p_T to be adequately reduced. The remaining elements in the block are then subject to a cross-identification of charged hadrons, neutral hadrons, and photons, arising from parton fragmentation, hadronization, and decays in jets. Hadrons experiencing a nuclear interaction in the tracker material create secondary particles. When an incoming track is identified, it is used to refine the reconstruction outcome, but is otherwise ignored in the track-cluster link algorithm as well as in the particle reconstruction algorithms. Finally, when the global event description becomes available, i.e. when all blocks have

been processed and all particles have been identified, the reconstructed event is revisited by a post-processing step.

3.2 Tracker reconstruction

Track reconstruction aims to obtain estimates for the momentum and position parameters of the charged particles from the hits collected by the tracker detector [56]. The tracking software at CMS is commonly referred to as the Combinatorial Track Finder (CTF), which is an adaptation of the combinatorial Kalman filter (KF [57, 58]), which in turn is an extension of the Kalman filter [57]. The collection of reconstructed tracks is produced by multiple passes (iterations) of the CTF track reconstruction sequence, in a process called iterative tracking. The basic idea of iterative tracking is that the initial iterations search for tracks that are easiest to find (e.g., of relatively large p_T and produced near the interaction region). After each iteration, hits associated with tracks are removed, thereby reducing the combinatorial complexity, and simplifying subsequent iterations in a search for more difficult classes of tracks (e.g., low p_T or greatly displaced tracks). Each iteration proceeds in four steps: seed generation, track finding, track fitting and track selection.

3.2.1 Seed generation

The seeds define the starting trajectory parameters and associated uncertainties of potential tracks. In the quasi-uniform magnetic field of the tracker, charged particles follow helical paths and therefore five parameters are needed to define a trajectory. Extraction of these five parameters requires either three 3-D hits, or two 3-D hits and a constraint on the origin of the trajectory based on the assumption that the particle originated near the beam spot (BS)[1].
The seed generation algorithm is controlled by two main sets of parameters: seeding layers and tracking regions. The seeding layers are pairs or triplets of detector layers in which hits are searched for. The tracking regions specify the limits on the acceptable track parameters, including the minimum p_T and the maximum transverse and longitudinal distances of closest approach to the assumed production point of the particle, taken to be located either at the centre of the reconstructed beam spot or at a pixel vertex. If the seeding layers correspond to pairs of detector layers, then seeds are constructed using one hit in each layer. A hit pair is accepted as a seed if the corresponding track parameters are consistent with the requirements of the tracking region. If the seeding layers correspond to triplets of detector layers, then, after pairs of hits are found in the two inner layers of each triplet, a search is performed in the outer detector layer for another hit. If the track parameters, derived from the three hits, are compatible with the tracking region requirements, the seed is accepted.

[1]The beam spot represents a 3-D profile of the luminous region, where the LHC beams collide in the CMS detector

3.2.2 Track finding

The track-finding module of the CTF algorithm is based on the Kalman filter method. The filter begins with a coarse estimate of the track parameters provided by the trajectory seed, and then builds track candidates by adding hits from successive detector layers, updating the parameters at each layer. The information needed at each layer includes the location and uncertainty of the detected hits, as well as the amount of material crossed, which is used to estimate the effects of multiple Coulomb scattering and energy loss. The track finding is implemented in four different steps. All resulting track candidates found at each layer are then propagated to the next compatible layers, and the procedure is repeated until a termination condition is satisfied. However, to avoid a rapid increase in the number of candidates, only a limited number (default is 5) of the candidates are retained at each step, with the best candidates chosen based on the normalised χ^2. Once the search for hits in the outward direction reveals a minimum number of valid hits, an inwards search is initiated for additional hits.

3.2.3 Track fitting

For each trajectory, the track-finding stage yields a collection of hits and an estimate of the track parameters. However the full information about the trajectory is only available when all hits are known. Furthermore, the estimate can be biased by constraints, such as a beam spot constraint applied to the trajectory during the seeding stage. The trajectory is therefore refitted using a Kalman filter and smoother. The Kalman filter is initialised at the location of the innermost hit, with the trajectory estimate obtained by performing a Kalman filter fit to the innermost hits (typically four) on the track. The fit then proceeds in an iterative way through the full list of hits, from the inside outwards, updating the track trajectory estimate sequentially with each hit. For each valid hit, the estimated hit position uncertainty is re-evaluated using the current values of the track parameters.

3.2.4 Track selection

The track-finding procedure described above yields a significant fraction of fake tracks. Reconstructed tracks that are not associated with a simulated particle are referred to as fake tracks. A reconstructed particle is associated with a simulated track if at least 75% of the hits assigned to the reconstructed track originate from the simulated particle.
In order to reduce fake rate, defined as fraction of reconstructed tracks that are fake, tracks are selected on the basis of the number of layers that have hits, whether their fit yielded a good χ^2/ndf, and how compatible they are with originating from a primary interaction vertex. To optimise track selection, several requirements are imposed as a function of the track η and p_T, and on the number of layers with an assigned hit (where a layer with both r-ϕ and stereo strip modules is counted as a single layer).
The loose criteria denote the minimum requirements for a track to be kept in the general track collection. The tight and high-purity criteria provide progressively more stringent

requirements, which reduce the efficiency and fake rate. In general, high-purity tracks are used for scientific analysis, although in cases where efficiency is essential and purity is not a major concern, the loose tracks can be used. The criteria for the initial tracking iterations emphasise compatibility with originating from a primary vertex as a means of assuring quality, while the criteria used for the later iterations rely on other measures of track quality such as fit χ^2 and the number of hits, ensuring thereby that they are still useful for selecting displaced tracks.
The fraction of fake tracks decreases roughly exponentially as a function of the number of layers in which the track has associated hit. As a consequence, weaker selection criteria can be applied for tracks having many hit layers. For tracks with hits in at least 10 layers, the selection requirements on χ^2 and impact parameters are found to reject no tracks. However, the criteria become far more stringent for tracks with relatively few hit layers.
After the track selection is complete, the tracks found are merged into a single collection.

3.2.5 Tracking reconstruction performance

Defined the tracking efficiency as the number of matched reconstructed tracks divided by number of simulated tracks, Figure 3.2 shows tracking efficiency as a function of $|\eta|$ and the number of primary vertices, using 2016 data collected at 13 TeV and $t\bar{t}$ simulated events. Tracking efficiency is around 99% up to $|\eta| < 2.4$ but it shows some discrepancies at high pileup values due to pixel dynamic inefficiency. The effect of the pileup is reported in Figure 3.3 that shows tracking efficiency in simulation, in different pileup scenarios as a function of η and p_T [59]. Figure 3.4 compares 2016 and 2017 tracking efficiencies, showing the improvement of the new tracker detector (see sec. 2.2.1).

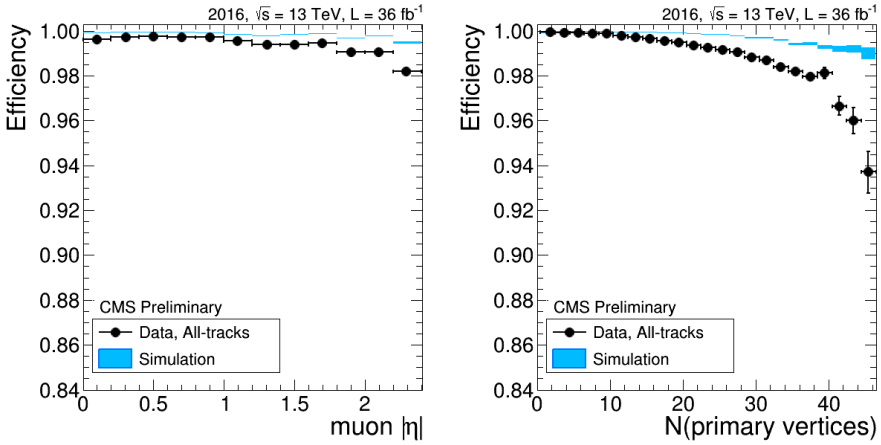

Figure 3.2: Data (black dots) and simulation (light blue rectangles) tracking efficiency for muons coming from the Z decay as a function of $|\eta|$ (left) and the number of primary vertices (right) of the probe (for the Tag and Probe method, see sec. 5.3.1) muon using 2016 data collected at 13 TeV.

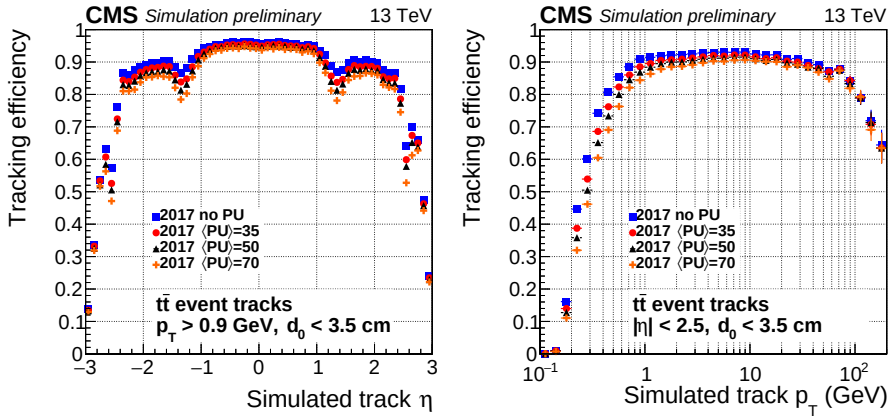

Figure 3.3: Track reconstruction efficiency as a function of simulated track η (on the left) and p_T (on the right) for the Phase I tracker (2017) at different pileup conditions.

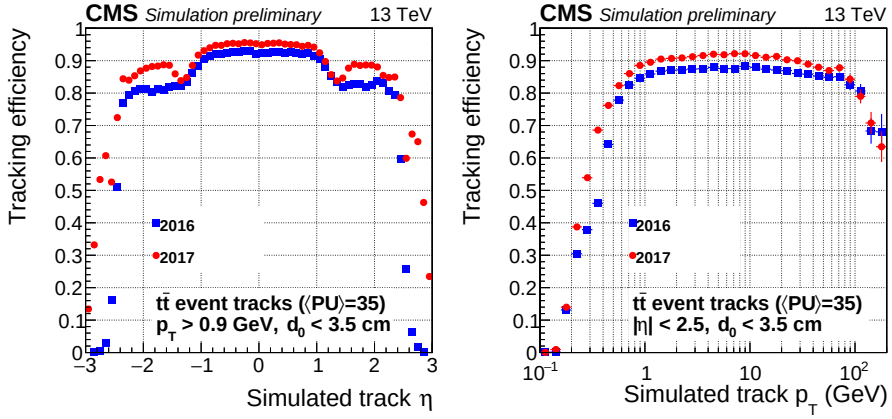

Figure 3.4: Track reconstruction efficiency as a function of simulated track η (on the left) and p_T (on the right) for 2016 and 2017 detectors. The 2017 detector shows better performance than 2016 over all spectra.

3.3 Vertices

The goal of primary-vertex (PV) reconstruction is to measure the location, and the associated uncertainty, of all proton-proton interaction vertices in each event, including the signal vertex and any vertices from pileup collisions, using the available reconstructed tracks. It consists of three steps:

- selection: imposing several requirements, tracks consistent with being produced promptly in the primary interaction region are selected;

- clustering: the selected tracks are clustered on the basis of their z-coordinates at their point of closest approach to the centre of the beam spot. In this step, all proton-proton interactions in the same LHC bunch crossing are reconstructed. The clustering is performed using a deterministic annealing (DA) algorithm [60];
- fitting: all the vertices containing at least two tracks are then fitted using an adaptive vertex fitter [61] to compute the best estimate of vertex parameters, including 3-D position and coordinate covariance matrix, as well as the indicators for the success of the fit, such as the number of degrees of freedom for the vertex, and weights of the tracks used in the vertex.

3.4 Photons

Photons [62], for use as signals or signatures in measurements and searches, rather than for use in the construction of jets or missing transverse energy, are reconstructed from energy deposits in the ECAL using algorithms that constrain the clusters to the size and shape expected for electrons and photons with $p_T \geq 15$ GeV. The reconstructed ECAL showers are generally limited to a fiducial region excluding the last two crystals at each end of the barrel ($|\eta| < 1.4442$). The outer circumferences of the endcaps are obscured by services passing between the barrel and the endcaps, and this area is removed from the fiducial region by excluding the first ring of trigger towers of the endcaps ($|\eta| > 1.566$). The fiducial region terminates at $|\eta| = 2.5$ where the tracker coverage ends. The photon reconstruction proceeds through several steps:

- calibration: the calorimeter signals in data must be calibrated and corrected for several detector effects;
- clusterisation: clustering algorithms collect the energy from radiating electrons and converted photons that gets spread in the ϕ direction by the magnetic field; these algorithms are evolved from fixed matrices of 5 x 5 crystals, which provide the best reconstruction of unconverted photons, by allowing extension of the energy collection in the ϕ direction, to form "superclusters";
- correction of cluster energy: main effects (e.g. variation of longitudinal containment, variation of lateral containment or variation in the amount of energy absorbed before reaching the ECAL for showers starting before the ECAL) force to correct the initial sum of energy deposits.

Figure 3.5 shows a good agreement in photon transverse energy distribution, split in barrel and endcaps, comparing 2016 data collected at 13 TeV with simulation.

3.5 Electrons

Electron reconstruction and selection is of great importance in many analyses performed using data from the CMS detector, such as standard model precision measurements,

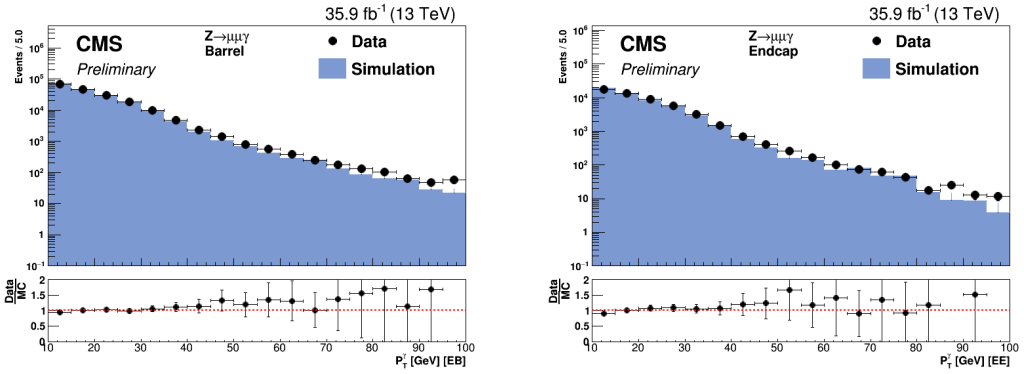

Figure 3.5: Photon transverse energy of selected photons in the barrel (left) and in the endcaps (right) comparing 2016 data collected at 13 TeV with simulations.

searches and measurements in the Higgs sector, and searches for processes beyond the standard model.

Electrons are reconstructed by associating a track reconstructed in the silicon detector with a cluster of energy in the ECAL. A mixture of a standalone approach and the complementary PF is used to maximise the performance. The electron energy usually spreads out over several crystals of the ECAL. This spread can be quite small when electrons lose little energy via bremsstrahlung before reaching ECAL. To measure the initial energy of the electron accurately, it is essential to collect the energy of the radiated photons that mainly spreads along the ϕ direction because of the bending of the electron trajectory in the magnetic field. The spread in the η direction is usually negligible, except for very low p_T (p_T<5 GeV). Two clustering algorithms, the hybrid algorithm in the barrel, and the "multi-5x5" in the endcaps, are used for this purpose.

The starting point of the hybrid algorithm is a seed crystal, defined as the one containing most of the energy deposited in any considered region: arrays of 5 x 1 crystals in η x ϕ are added around the seed crystal, in a range of N_{steps} crystals in both directions of ϕ if their energies exceed a minimum threshold. The contiguous arrays are grouped into clusters, with each distinct cluster required to have a seed array with energy greater than a threshold in order to be collected in the final global cluster, called the supercluster seed-array (SC).

The multi-5x5 algorithm is used in the ECAL endcaps (EE), where crystals are not arranged in an $\eta \times \phi$ geometry. It starts with the seed crystals, the ones with local maximal energy relative to their four direct neighbours. Around these seeds and beginning with the largest E_T, the energy is collected in clusters of 5x5 crystals, that can partly overlap. These clusters are then grouped into an SC if their total E_T is greater than a minimum, within a range in η of $\pm\eta_{range}$, and a ϕ of $\pm\phi_{range}$ around each seed crystal. The SC energy corresponds to the sum of the energies of all its clusters. The SC position is calculated as the energy-weighted mean of the cluster positions.

In addition, as part of the PF-reconstruction algorithm, another clustering algorithm is

introduced that aims at reconstructing the particle showers individually. The PF clusters are reconstructed by aggregating around a seed all contiguous crystals with energies of two standard deviations above the electronic noise observed at the beginning of the data-taking run.
Electron tracks can be reconstructed in the full tracker using the standard KF track reconstruction procedure used for all charged particles. However, the large radiative losses for electrons in the tracker material compromise this procedure and lead in general to a reduced hit-collection efficiency (hits are lost when the change in curvature is large because of bremsstrahlung), as well as to a poor estimation of track parameters. For these reasons, a dedicated tracking procedure is used for electrons.

3.5.1 Seeding

The seeding consists of finding and selecting the two or three first hits in the tracker from which the track can be initiated. The seeding is of primary importance since its performance greatly affects the reconstruction efficiency. Two complementary algorithms are used and their results combined. The ECAL-based seeding starts from the SC energy and position, used to estimate the electron trajectory in the first layers of the tracker, and selects electron seeds from all the reconstructed seeds. The tracker-based seeding relies instead on tracks that are reconstructed using the general algorithm for charged particles, extrapolated towards the ECAL and matched to a SC.

3.5.2 Tracking

The selected electron seeds are used to initiate electron-track building, which is followed by track fitting. The track building is based on the combinatorial KF method, which for each electron seed proceeds iteratively from the track parameters provided in each layer, including one-by-one the information from each successive layer. The electron energy loss is modelled through a Bethe-Heitler function. To follow the electron trajectory in case of bremsstrahlung and to maintain good efficiency, the compatibility between the predicted and the found hits in each layer is chosen not to be too restrictive. When several hits are found compatible with those predicted in a layer, then several trajectory candidates are created and developed, with a limit of five candidate trajectories for each layer of the tracker. At most, one missing hit is allowed for an accepted trajectory candidate and, to avoid including hits from converted bremsstrahlung photons in the reconstruction of primary electron tracks, an increased χ^2 penalty is applied to trajectory candidates with one missing hit. Once the hits are collected, a Gaussian sum filter (GSF [63]) fit is performed to estimate the track parameters. The energy loss in each layer is approximated by a mixture of Gaussian distributions. A weight is attributed to each Gaussian distribution that describes the associated probability.

3.5.3 Electron particle-flow clustering

The PF clustering of electrons is driven by GSF tracks, and is independent of the way they are seeded. For each GSF track, several PF clusters, corresponding to the electron at the ECAL surface and the bremsstrahlung photons emitted along its trajectory, are grouped together. The PF cluster corresponding to the electron at the ECAL surface is the one matched to the track at the exit of the tracker. Since most of the material is concentrated in the layers of the tracker, for each layer a straight line is extrapolated to the ECAL, tangent to the electron track, and each matching PF cluster is added to the electron PF cluster. Most of the bremsstrahlung photons are recovered in this way, but some converted photons can be missed. For these photons, a specific procedure selects displaced KF tracks through a dedicated MVA algorithm, and kinematically associates them with the PF clusters. In addition, for ECAL-seeded isolated electrons, any PF clusters matched geometrically with the hybrid or multi-5x5 SC are also added to the PF electron cluster.

3.5.4 Association between track and cluster

The electron candidates are constructed from the association of a GSF track and a cluster in the ECAL. For ECAL-seeded electrons, the ECAL cluster associated with the track is simply the one reconstructed through the hybrid or the multi-5x5 algorithm that led to the seed. For electrons seeded only through the tracker-based approach, the association is made with the electron PF cluster.
Figure 3.6 [64] shows electron reconstruction efficiency using data collected at 13 TeV during 2017. The efficiency is evaluated with the Tag and Probe method and it is defined as the number of probe electrons obtained from a fit to the $Z \to ee$ invariant mass. $Z \to ee$ mass is shown in Figure 3.7 [62], comparing data collected at 13 TeV during 2016, 2017 and 2018.

3.6 Muons

3.6.1 Muon reconstruction

Muons are first reconstructed independently in the inner tracker (tracker track) and in the muon system (standalone-muon track) [65, 66]. Tracker tracks are built using an iterative approach, running a sequence of tracking algorithms each with slightly different logic. After each iteration step, hits that have been associated with reconstructed tracks are removed from the set of input hits to be used in the following step. Standalone-muon tracks are built instead by exploiting information from muon sub-detectors to gather all CSC, DT, and RPC information along a muon trajectory using a Kalman-filter technique [67]. Reconstruction starts from seeds made up of groups of DT or CSC segments.
Based on tracker track and Standalone-muon, two reconstruction approaches are used:

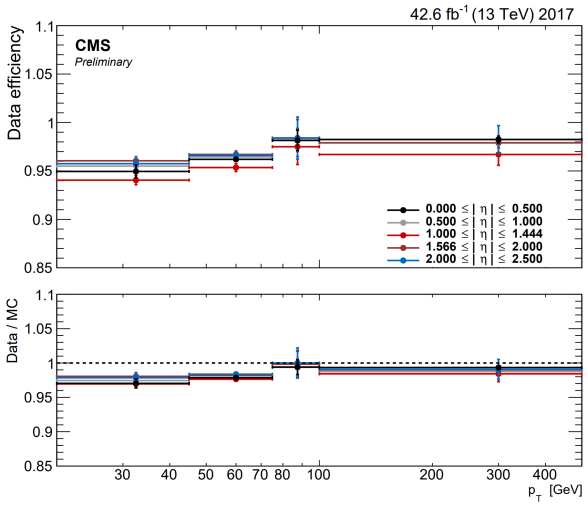

Figure 3.6: Electron reconstruction efficiency in 2017 data (top) and data to simulated efficiency ratios (bottom). The efficiency is measured with the tag and probe method and shown as a function of p_T for different SC $|\eta|$. The error bars on the data/MC ratio represent the combined statistical and systematic errors.

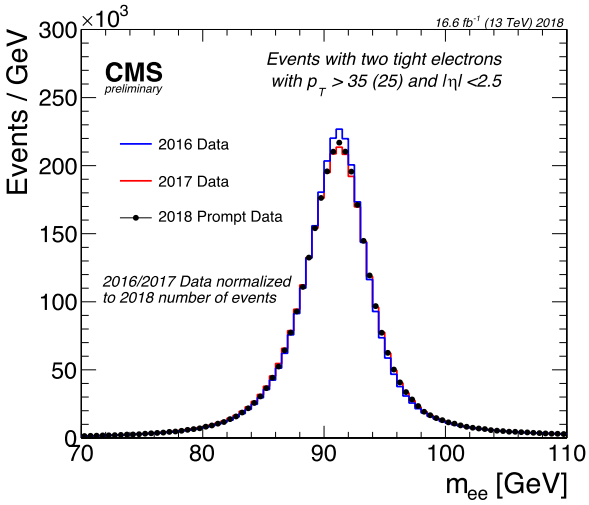

Figure 3.7: Reconstructed dielectron invariant mass using data collected during 2016 (blue), 2017 (red) and 2018 (black; only $16.6 fb^{-1}$) at 13 TeV.

- Global Muon reconstruction (outside-in): for each standalone-muon track, a matching tracker track is found by comparing parameters of the two tracks propagated onto a common surface. A global-muon track is fitted combining hits from the tracker track and standalone-muon track, using the KF technique. At large transverse momentum, $p_T \geq 200$ GeV, the global-muon fit can improve the momentum

resolution compared to the tracker-only fit.

- Tracker Muon reconstruction (inside-out): in this approach, all tracker tracks with $p_T > 0.5$ GeV and total momentum p > 2.5 GeV are considered as possible muon candidates and are extrapolated to the muon system taking into account the magnetic field, the average expected energy losses, and multiple Coulomb scattering in the detector material. If at least one muon segment (i.e., a short track stub made of DT or CSC hits) matches the extrapolated track, the corresponding tracker track qualifies as a Tracker Muon. Track-to-segment matching is performed in a local (chamber) coordinate system, where local x is the best-measured coordinate (in the r-ϕ plane) and local y is the coordinate orthogonal to it. The extrapolated track and the segment are considered to be matched if the distance between them in local x is less than 3 cm or if the value of the pull for local x is less than 4, where the pull is defined as the difference between the position of the matched segment and the position of the extrapolated track, divided by their combined uncertainties.

Tracker Muon reconstruction is more efficient than the global muon reconstruction at low momentum, p $\geq$ 5 GeV, because it requires only a single muon segment in the muon system, whereas Global Muon reconstruction is designed to have high efficiency for muons penetrating through more than one muon station and typically requires segments in at least two muon stations. Reconstructed muons are fed into the CMS PF algorithm that applies a set of selection criteria to candidates reconstructed with the standalone, global, or tracker muon algorithms. The requirements are based on various quality parameters from the muon reconstruction as well as make use of information from other CMS sub-detectors.

3.6.2 High-p_T muon

Beside the algorithms described above, for analyses involving high-p_T muons (the so called TeV-muon), CMS has also developed specialised algorithms for reconstruction and momentum assignment.
Since in the search for resonances in the high mass range, new bosons are predicted with mass of the order of TeV, muon reconstruction and selection was optimised for high efficiency at high energies. Muon reconstruction plays a crucial role since the muon performance at high momentum is strongly affected by radiative processes and by the muon detector alignment. As the muon passes through the steel of the magnet return yoke, multiple scattering and radiative processes can alter the muon trajectory. In particular, these radiative processes can result in large energy losses and can produce electromagnetic showers, whose probability increases with p_T, giving rise to additional hits in the muon chambers.
Therefore, a set of dedicated TeV-muon track refit algorithms has been developed:

- Tracker plus first muon station (TPFMS): this algorithm refits the global-muon track using hits from the tracker and the innermost muon station to reduce the

sensitivity to possible showering deeper in the muon system, due to the larger amount of iron traversed by the muon.

- Picky: this algorithm again starts with the hit list of the global-muon track, but, in chambers appearing to have hits from showers (determined by the hit occupancy of the chamber), retains only the hits that, based on a χ^2 comparison, are compatible with the extrapolated trajectory.

- Dynamic truncation (DYT): this fit takes into account possible energy losses from radiative processes and tries to avoid hits produced after a large energy loss in the muon system. For every silicon tracker track identified as belonging to a muon by the global fit, the result of the tracker-only fit is propagated out to the muon stations and attempts are made to add compatible muon hits to the fit. For each hit the compatibility between the extrapolated tracker track and the reconstructed segment in the muon chambers is calculated, using an estimator that in absence of correlation reduces to a χ^2.

Each muon in the event is reconstructed using all of them (including also global and tracker reconstructions). To further improve the resolution at high p_T, mainly by reducing the tails of the momentum resolution distribution, combinations of the above algorithms is used. Momentum assignment is so performed by the *TuneP* algorithm, which chooses the best muon reconstruction between global-track, tracker-track, TPFMS, Picky, and DYT. The selection is made on a track-by-track basis, using the track fit χ^2/ndf probability and the relative p_T error, σ_{p_T}/p_T.

TuneP performance

TuneP algorithm has been developed after Run I for a better assignment of p_T for muon with $p_T > 200$ GeV. I have, for the first time in CMS, studied TuneP assignment using data, collected during Run II at 13 TeV (Table 5.1) corresponding to an integrated luminosity of 36.3 fb^{-1} for 2016 and 42.4 fb^{-1} for 2017, and 2016 simulation (Table 5.2). Muons for these studies are selected applying high-p_T muon selection, defined in sec. 5.4, with the extra condition of $p_T > 200$ GeV in order to focus only on muons whose p_T has been assigned by the TuneP.
I have focused only on Picky and DYT reconstructions (see sec. 3.6.2) because they are chosen in around 95% of the cases by TuneP: the rest 5% is split among TPFMS (∼3-4%), Global (∼1-2%) and Tracker track reconstruction (<1%).
In Figure 3.8 is reported the p_T distribution for TuneP, Picky and DYT comparing 2016 data and simulation. For $p_T < 400$ GeV, data and simulation are in agreement in all p_T assignment; above this threshold and in particular for $p_T > 600$ GeV, a deficit of data with respect to MC prediction is observable in TuneP assignment. No experimental sources for the deficit were identified, and it is therefore considered compatible with a statistical fluctuation in data. In Figure 3.9, 3.10 and 3.11, η distribution for TuneP, Picky and DYT are reported comparing 2016 data and simulation in three different p_T

ranges: $200 < p_T < 400$ GeV, $400 < p_T < 600$ GeV and $p_T > 600$ GeV.

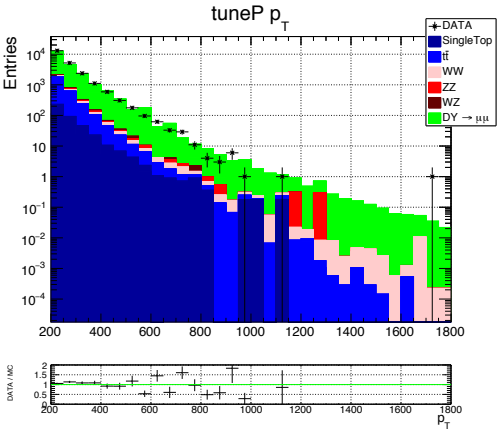

(a) TuneP assignment

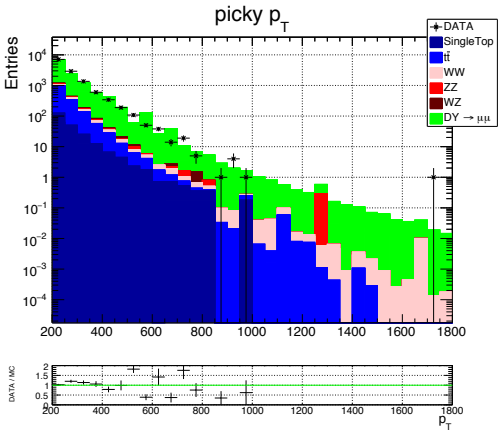

(b) Picky reconstruction

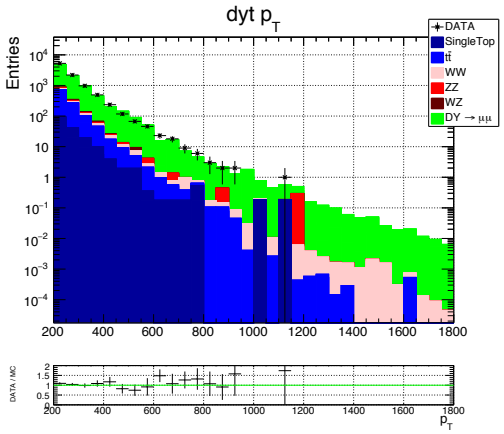

(c) DYT reconstruction

Figure 3.8: p_T distribution for TuneP, Picky and DYT. Stack plot is the simulation; 2016 data are the black dots. On the bottom panel, data/MC ratio is reported.

Below 400 GeV, there is a good agreement data/MC also in η; for $p_T > 600$ GeV the deficit in TuneP is observable (Figure 3.11). For $400 < p_T < 600$ GeV, there is a slight deficit in data for $|\eta|$ <0.9 in Picky reconstruction (Figure 3.10(b)): to better investigate it, I have decided to perform the studies in two mass regions: around (for masses between 60 and 120 GeV) and above (for masses greater than 120 GeV) Z peak. For the region above Z peak, η distribution is observable in Figure 3.12. Applying mass cut the deficit in Picky disappear and this means that the deficit observed affects only mass range around Z peak. This mass range, at the same time, is well known and it is

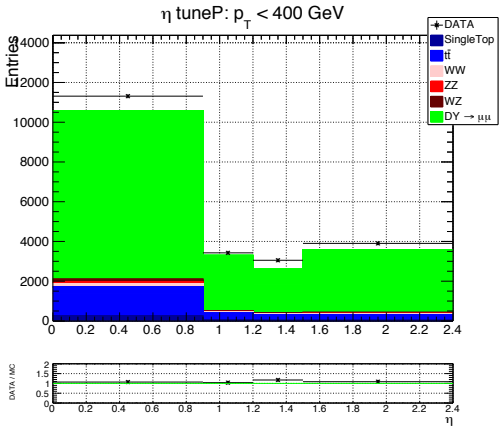

(a) TuneP assignment

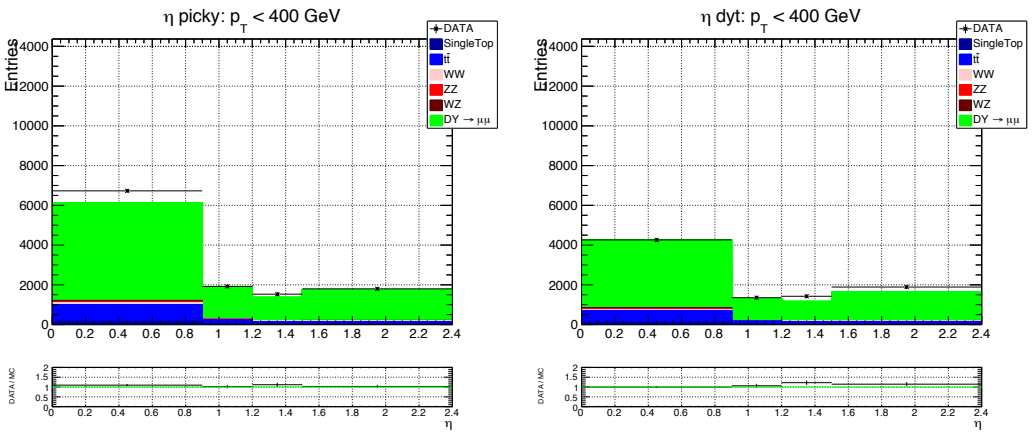

(b) Picky reconstruction

(c) DYT reconstruction

Figure 3.9: η distribution for TuneP, Picky and DYT for $200 < p_T < 400$ GeV. Stack plot is the simulation; 2016 data are the black dots. On the bottom panel, data/MC ratio is reported.

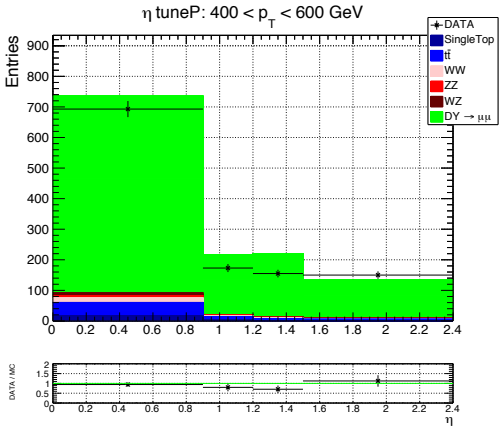

(a) TuneP assignment

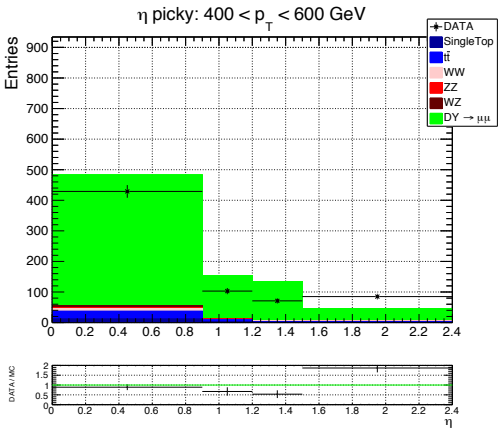

(b) Picky reconstruction

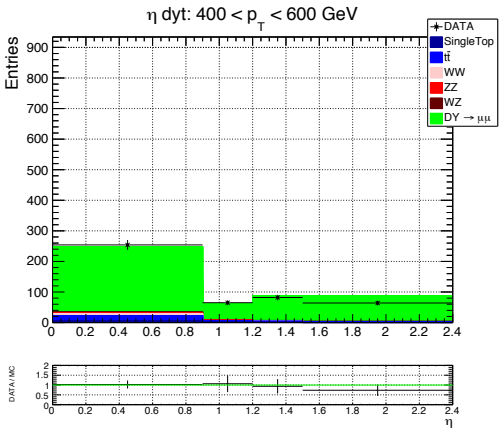

(c) DYT reconstruction

Figure 3.10: η distribution for TuneP, Picky and DYT for $400 < p_T < 600$ GeV. Stack plot is the simulation; 2016 data are the black dots. On the bottom panel, data/MC ratio is reported.

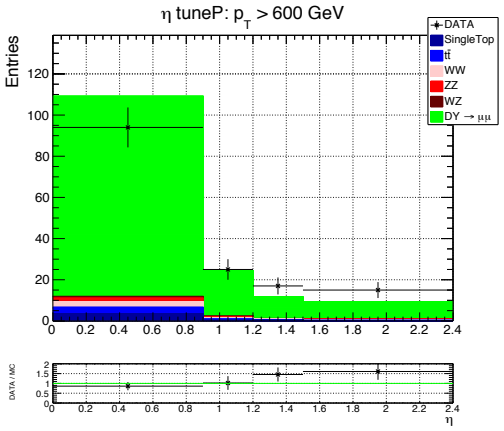

(a) TuneP assignment

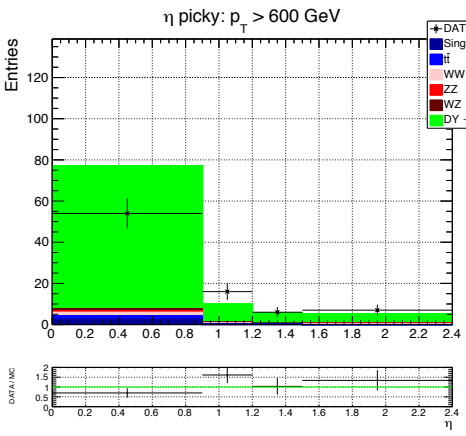

(b) Picky reconstruction

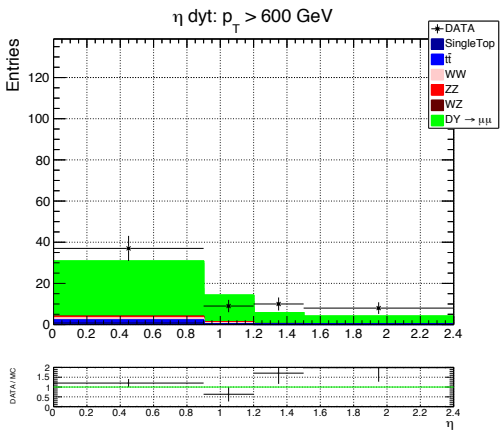

(c) DYT reconstruction

Figure 3.11: η distribution for TuneP, Picky and DYT for $p_T > 600$ GeV. Stack plot is the simulation; 2016 data are the black dots. On the bottom panel, data/MC ratio is reported.

used as control region for my studies. Therefore I have investigated two possible causes for the deficit: a problem at generator level (POWHEG, in this case) or a statistical fluctuation.

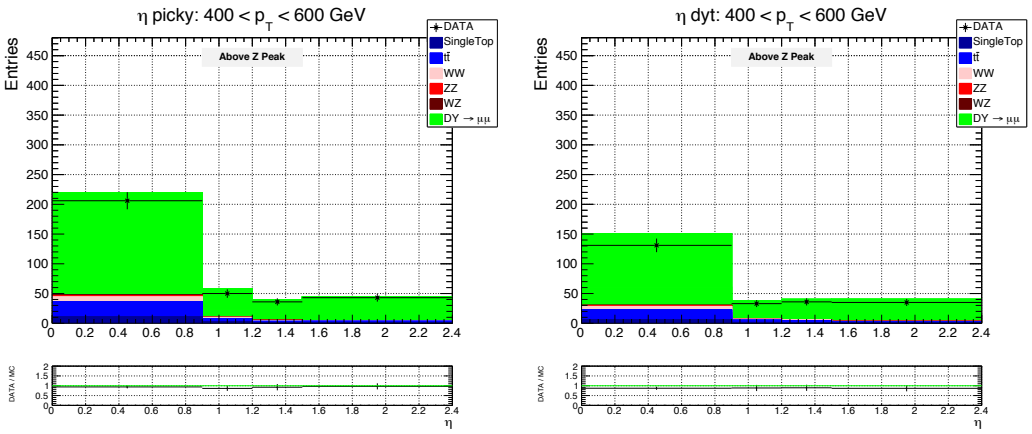

(a) Picky reconstruction

(b) DYT reconstruction

Figure 3.12: η distribution for Picky and DYT for $400 < p_T < 600$ GeV after applying mass cut (greater than 120 GeV). Stack plot is the simulation; 2016 data are the black dots. On the bottom panel, data/MC ratio is reported.

POWHEG vs aMC@NLO

In order to exclude a problem at generator level and to increase the statistics for $p_T >$ 400 GeV, I have compared results shown above with the one produced using aMC@NLO (based on MADGRAPH5 generator). While POWHEG simulates Drell-Yan process with virtual mass up to 6 TeV, MADGRAPH5 simulates that process only around Z peak but binned in Z boson p_T (from few GeV up to TeV scale).
Comparison between the generators is reported in Figure 3.13, for dimuon mass, p_T and η distributions.

As can be observed, there is a good agreement in all distributions: both generators behave in the same way; aMC@NLO, as expected, has also more statistics above 400 GeV.
Therefore, in the analysis presented in this thesis, for studies around Z peak, I have used these samples, exploiting the higher statistics for high p_T.

TuneP performance for $400 < p_T < 600$ GeV around Z peak

In Figure 3.14, η distribution for TuneP, Picky and DYT comparing 2016 simulation with data around Z peak and for $400 < p_T < 600$ GeV. Good agreement between data

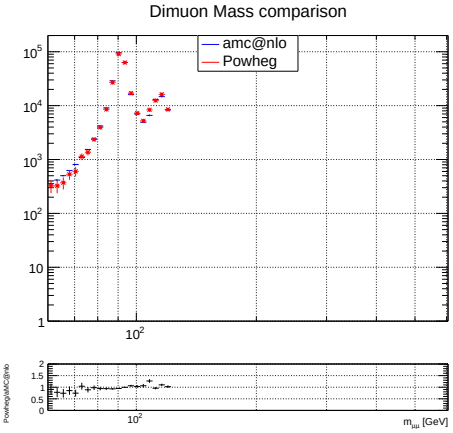

(a) Dimuon mass distribution

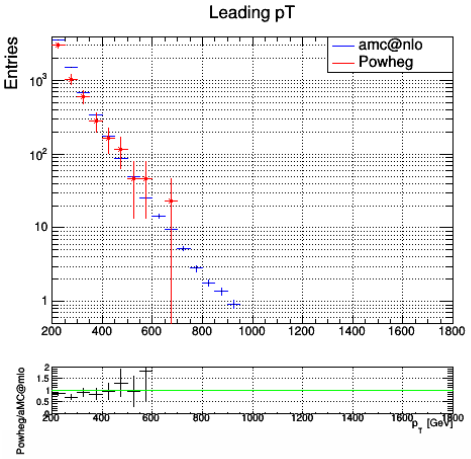

(b) Leading p_T distribution

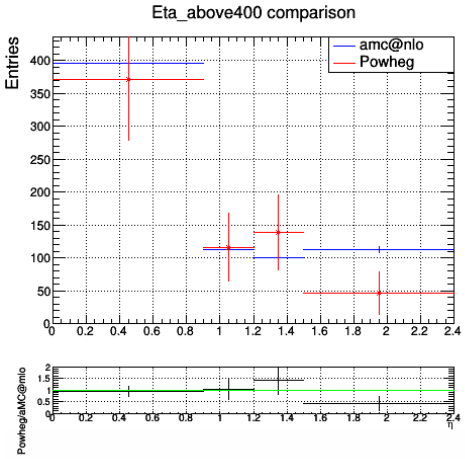

(c) η distribution

Figure 3.13: Dimuon mass, leading p_T and η distribution using POWHEG (in red) and aMC@NLO (in blue). On the bottom panel, POWHEG/aMC@NLO ratio is reported.

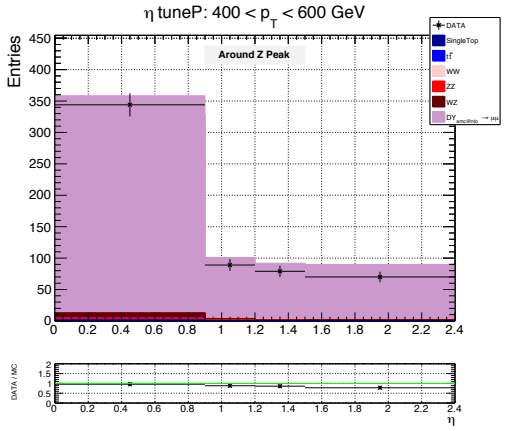

(a) TuneP assignment

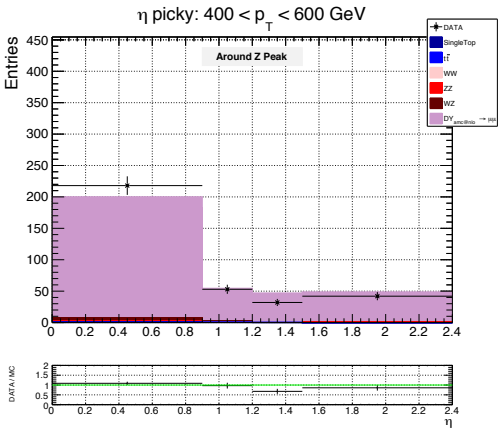

(b) Picky reconstruction

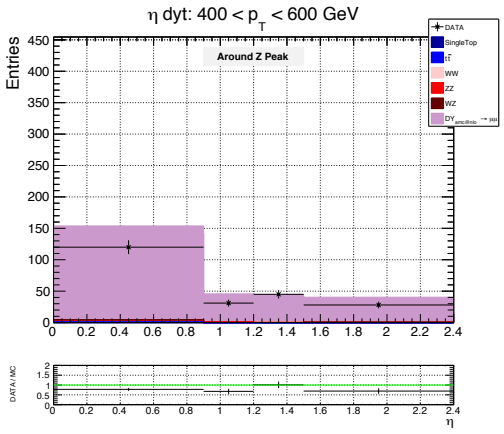

(c) DYT reconstruction

Figure 3.14: η distribution for TuneP, Picky and DYT for $400 < p_T < 600$ GeV around Z peak. Stack plot is the simulation; 2016 data are the black dots. On the bottom panel, data/MC ratio is reported.

and simulation is observable in TuneP distribution. The deficit observed in Picky (Figure 3.10) is not present neither in this mass region thanks to the improved statistics: I can conclude that it was due to a statistical problem. Results combining 2016 and 2017 dataset are shown in Figure 3.15 compared with 2016 simulation. Still, TuneP shows a

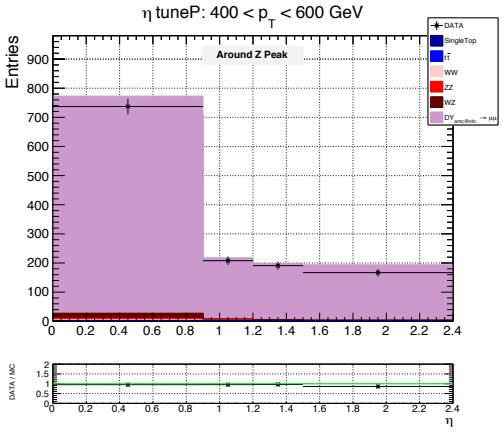

(a) TuneP assignment

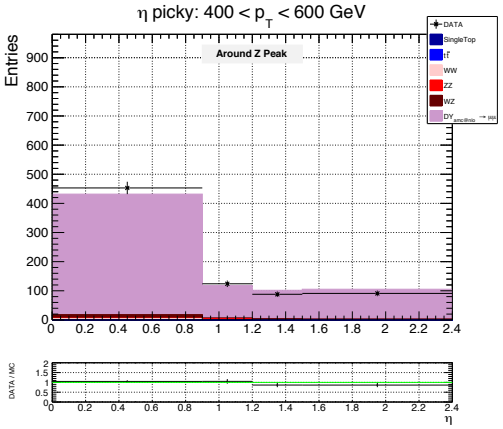

(b) Picky reconstruction

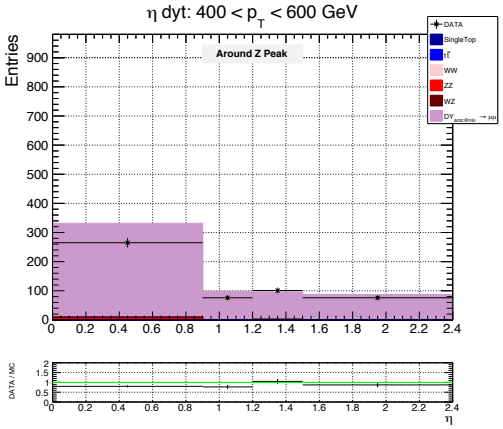

(c) DYT reconstruction

Figure 3.15: η distribution for TuneP, Picky and DYT for $400 < p_T < 600$ GeV around Z peak. Stack plot is the simulation; data (2016 plus 2017) are the black dots. On the bottom panel, data/MC ratio is reported.

very good agreement between data and simulation.

TuneP performance for $p_T > 600$ GeV

Consider now the p_T region above 600 GeV, the one affected by data deficit.
η distributions around Z peak for $p_T > 600$ GeV comparing simulation to 2016 only and to combination 2016 plus 2017 data are shown in Figure 3.16 and 3.17.

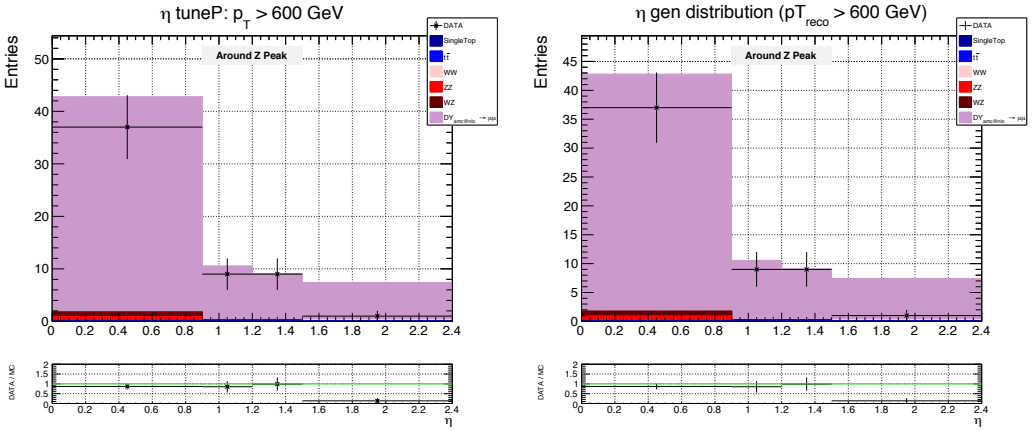

(a) TuneP assignment

(b) Generated distribution

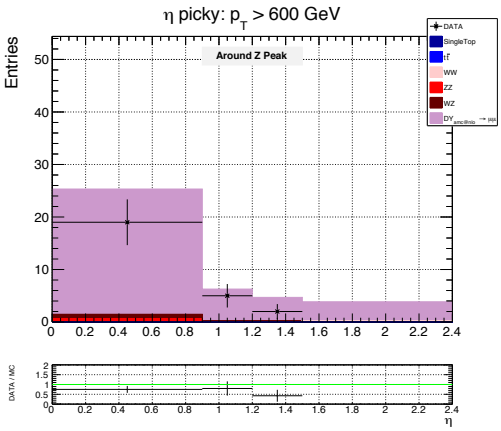

(c) Picky reconstruction

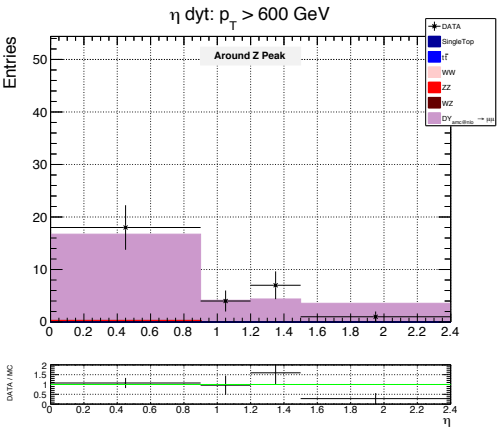

(d) DYT reconstruction

Figure 3.16: η distribution for TuneP, generated value, Picky and DYT for $p_T > 600$ GeV around Z peak. Stack plot is the simulation; 2016 data are the black dots. On the bottom panel, data/MC ratio is reported.

In both cases, a deficit in the endcap region ($|\eta| > 1.4$) is observed: in 2016 plus 2017 I expect 15 events but only 5 are observed. I could have an issue in data (like different alignment between simulation and data) that could affect the p_T assignment

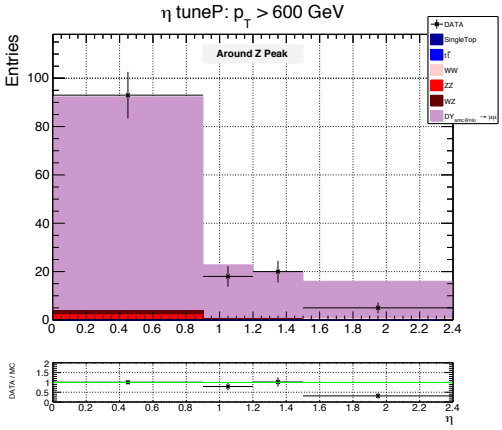

(a) TuneP assignment

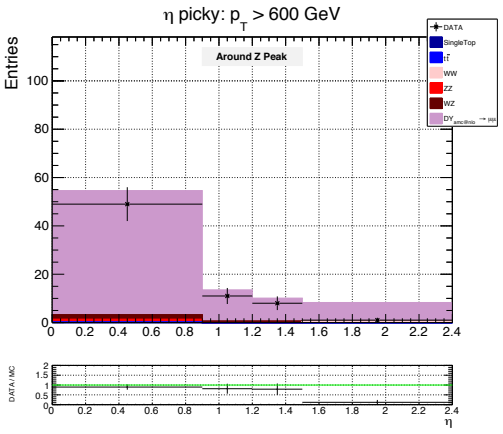

(b) Picky reconstruction

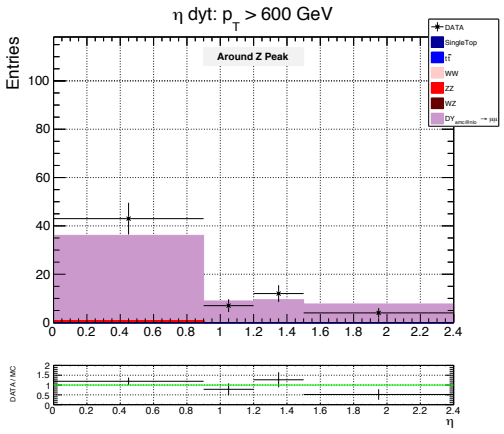

(c) DYT reconstruction

Figure 3.17: η distribution for TuneP, Picky and DYT for $p_T > 600$ GeV around Z peak. Stack plot is the simulation; data (2016 plus 2017) are the black dots. On the bottom panel, data/MC ratio is reported.

for $p_T > 600$ GeV in this η region: if it was the case, then I should see it for all muons with $p_T > 600$ GeV in this η region but it is not the case. Looking at Figure 3.18 (same p_T range but for m>120 GeV), there is no discrepancy in the forward η range. At the same time, as can be seen in Figure 3.16(b) the expectation is greater than data also in generated distribution: I can exclude any reconstruction or p_T shift between generated and reconstructed value in simulation. It seems that simulation over-predicts the number of boosted Z events falling in the endcap region (they are not well handled in simulation).

The region above Z peak and for $p_T > 600$ GeV is affected by the deficit that is ∼40% considering only 2016 data but it is mitigated considering 2016 plus 2017 data: Figure 3.18 shows η distribution for TuneP, Picky and DYT in this region. The agreement is good for $|\eta|$ >1.4 but the agreement is around 25% in the barrel region.

After these studies I can fully trust on TuneP assignment since no differences have been observed in treating data and MC.

3.6.3 Muon Identification

According to the required identification efficiency and purity, different selection based on a set of variables can be applied. Some variables are based on muon reconstruction, such as track fit χ^2, the number of hits per track (either in the inner tracker or in the muon system, or both), or the degree of matching between tracker tracks and standalone-muon tracks (for global muons). Other variables exploit inputs from outside the reconstructed muon track, such as compatibility with the primary vertex (the reconstructed vertex with the largest value of summed physics-object p_T^2). Using these variables, the main identification types of muons used in CMS physics analyses include:

- Loose muon Identification (Loose ID): aims to identify prompt muons originating at the primary vertex, and muons from light and heavy flavour decays, as well as maintain a low rate of the misidentification of charged hadrons as muons. A loose muon is a muon selected by the PF algorithm that is also either a tracker or a global muon. Figure 3.19 shows Loose ID efficiency as a function of p_T and η for 2017 data (collected at 13 TeV) and simulation. The efficiency is evaluated using the Tag and Probe method [68].

- Medium muon ID: optimised for prompt muons and for muons from heavy flavour decay. A medium muon is a loose muon with a tracker track that uses hits from more than 80% of the inner tracker layers it traverses. According if the muon is only reconstructed as a tracker muon or as both a tracker muon and a global muon, the muon segment compatibility need to be greater than a fixed threshold. The constraints on the segment compatibility were tuned after application of the other constraints to target an overall efficiency of 99.5% for muons from simulated W and Z events.

- Tight muon ID: aims to suppress muons from decay in flight and from hadronic

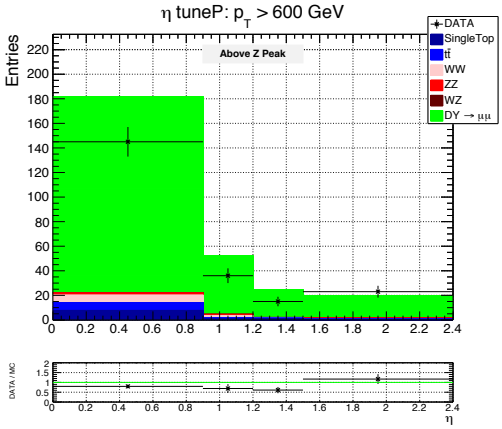

(a) TuneP assignment

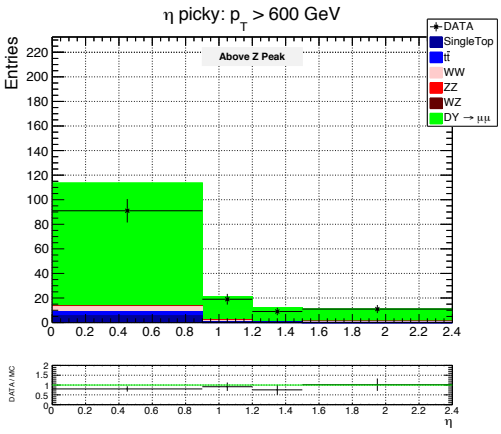

(b) Picky reconstruction

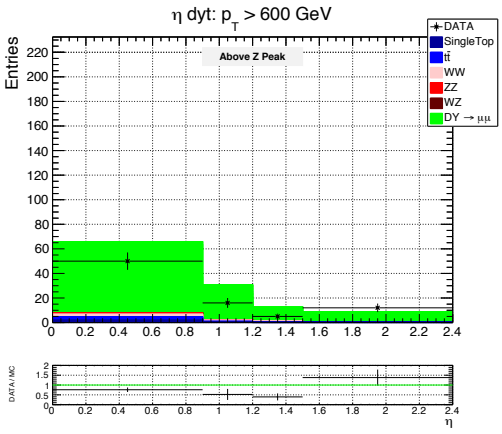

(c) DYT reconstruction

Figure 3.18: η distribution for TuneP, Picky and DYT for $p_T > 600$ GeV above Z peak. Stack plot is the simulation; data (2016 plus 2017) are the black dots. On the bottom panel, data/MC ratio is reported.

punch-through. A tight muon is a loose muon with a tracker track that uses hits from at least six layers of the inner tracker including at least one pixel hit. The muon must be reconstructed as both a tracker muon and a global muon. The tracker muon must have segment matching in at least two of the muon stations. The global muon fit must have χ^2/ndf <10 and include at least one hit from the muon system. A tight muon must be compatible with the primary vertex, having a transverse impact parameter $|dxy| < 0.2$ cm and a longitudinal impact parameter $|dz| < 0.5$ cm. This selection is used in many physics analyses in CMS, in particular in the measurements of inclusive W and Z cross sections. Figure 3.20 shows Tight ID efficiency as a function of p_T and η for 2017 data (collected at 13 TeV) and simulation. The efficiency is evaluated using the Tag and Probe method [68].

- Soft muon ID: optimized for low-p_T muons for B-physics and quarkonia analyses. A soft muon is a tracker muon with a tracker track that satisfies a high purity flag and uses hits from at least six layers of the inner tracker including at least one pixel hit. The tracker muon reconstruction must have tight segment matching, having pulls less than 3 both in local x and in local y. A soft muon is loosely compatible with the primary vertex, having $|dxy| < 0.3$ cm and $|dz|$ <20 cm.

- High-p_T ID: optimized for muons with p_T> 200 GeV. A high momentum muon is reconstructed as both a tracker muon and a global muon. The requirements on the tracker track and the transverse and longitudinal impact parameters are the same as for a tight muon, as well as the requirement that there be at least one hit from the muon system for the global muon. However, in contrast to the tight muon, the requirement on the global muon fit χ^2/ndf is removed. The removal of the this cut prevents inefficiencies at high p_T when muons radiate large electromagnetic showers as they pass through the steel flux-return yoke, giving rise to additional hits in the muon chambers. A requirement on the relative p_T error, $\sigma_{p_T}/p_T < 0.3$ is used to ensure a proper momentum measurement.

ID comparison efficiency between 2016, 2017 and 2018 data for the three identification types is shown in Figure 3.21. The effect of the new pixel detector (see sec. 2.2.1) is visible with a slight improvement in tight ID that imposes cuts on the number of pixel hits.

3.6.4 Muon Isolation

To distinguish between prompt muons and those from weak decays within jets, the isolation of a muon is evaluated relative to its p_T by summing up the energy of all particles in a geometrical cone with $\Delta R = \sqrt{\Delta\eta^2 + \Delta\phi^2}$, surrounding the muon. One strategy sums reconstructed tracks (track based isolation), while another uses charged hadrons and neutral particles coming from PF (PF isolation). For the computation of PF isolation, the p_T of charged hadrons [p_T^{ch}] within the ΔR cone originating from the primary vertex are summed together with the energy sum of all neutral particles (hadrons

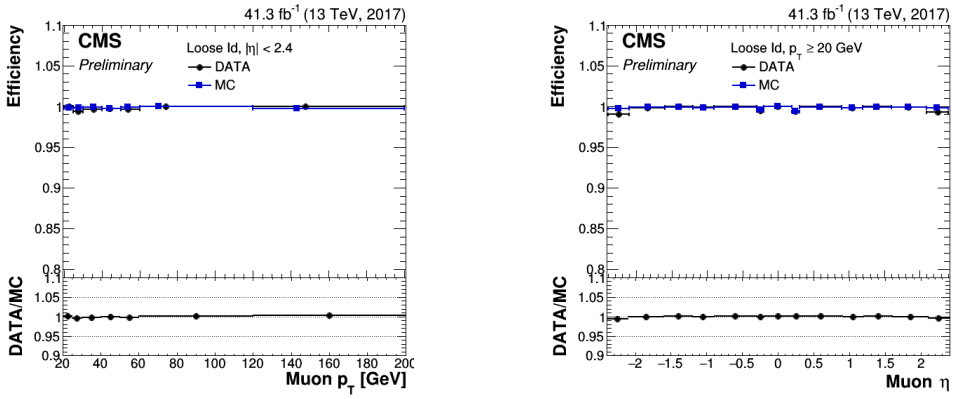

Figure 3.19: Loose ID efficiency as a function of p_T and η for 2017 data (collected at 13 TeV) and simulation.

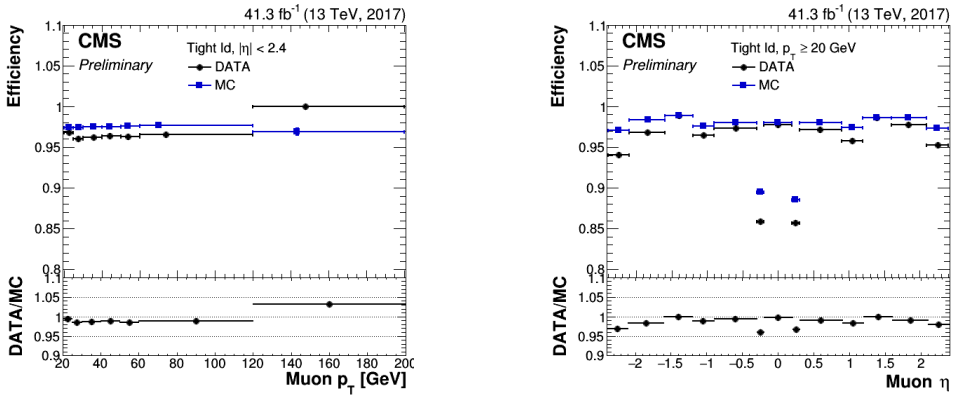

Figure 3.20: Tight ID efficiency as a function of p_T and η for 2017 data (collected at 13 TeV) and simulation. The drops in the forward region are due inactive chambers not modelled in MC.

$[E_T^{nh}]$ and photons $[E_T^{\gamma}]$) in the cone. The contribution from pileup to the neutral particles is corrected by computing the sum of charged hadron deposits originating from pileup vertices, scaling it by a factor of 0.5 $[p_T^{chPU}]$, and subtracting this from the neutral hadron and photon sums to give the corrected energy sum from neutral particles. The factor of 0.5 is estimated from simulations to be approximately the ratio of neutral particle to charged hadron production in inelastic proton-proton collisions. The corrected energy sum from neutral particles is limited to be positive or zero:

$$I^{PF} = p_T^{ch} + max(0, E_T^{nh} + E_T^{\gamma} - 0.5 * p_T^{chPU}) \tag{3.1}$$

For both strategies, tight and loose working points are defined to achieve efficiencies of 95% and 98%, respectively. They are tuned using simulated tight muons from $Z \to \mu^+\mu^-$ decays with $p_T >$ 20 GeV. The values for the tight and loose working points for relative

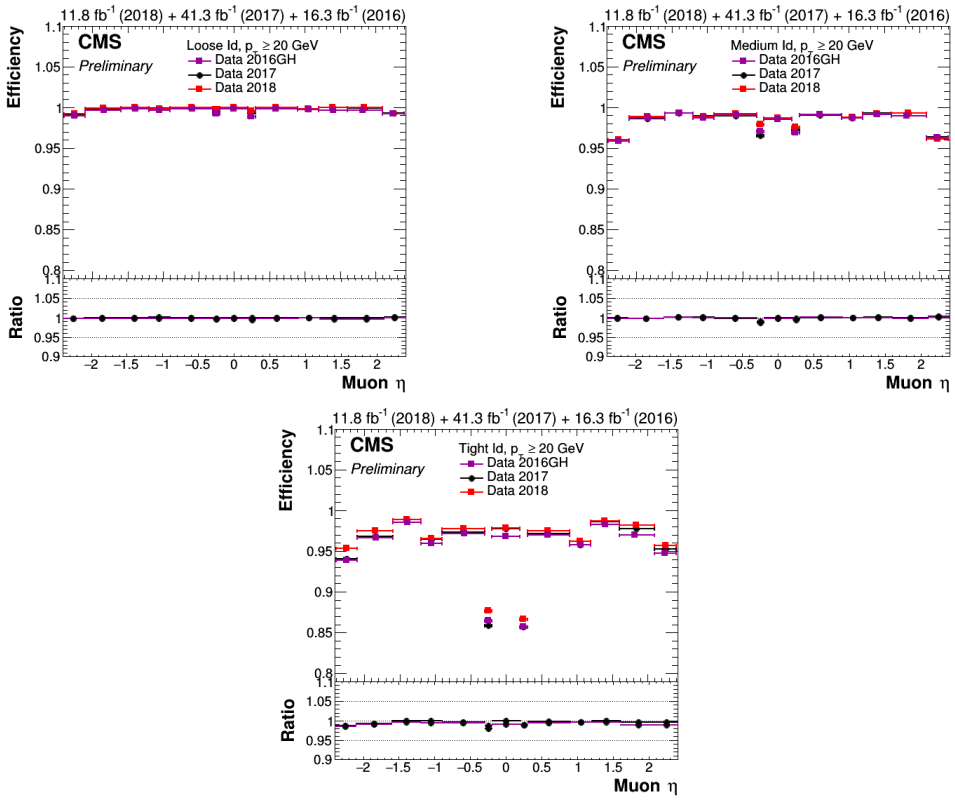

Figure 3.21: Loose (top left), Medium (top right) and Tight (bottom) ID efficiency as a function of η for 2016 (purple), 2017 (black) and 2018 (red) data, collected at 13 TeV.

PF isolation (I^{PF}/p_T) within $\Delta R < 0.4$ are 0.15 and 0.25, respectively, while the values for relative track based isolation (I^{tk}/p_T) within $\Delta R < 0.3$ are 0.05 and 0.10.
Figure 3.22 shows tracker isolation efficiency as a function of muon η comparing 2017 data with simulation [68].

3.6.5 Alignment

The alignment of muon chambers relative to each other and to the inner tracker is crucial to achieve optimal performance in muon reconstruction up to TeV-momentum.
With the exception of the CMS central wheel, which is fixed, the other wheels and disks are movable along the beam direction to allow opening the yoke for the installation and maintenance of the detectors. Gravitational distortions lead to static deformations of the yoke elements that generate displacements of the muon chambers with respect to their design position of up to several mm. These displacements can be measured within a few hundred microns by photogrammetry when the detector is open, both in the barrel and in the endcaps. However, the repositioning of the large elements of the yoke after opening and closing of the CMS detector, though rather precise, cannot be better than

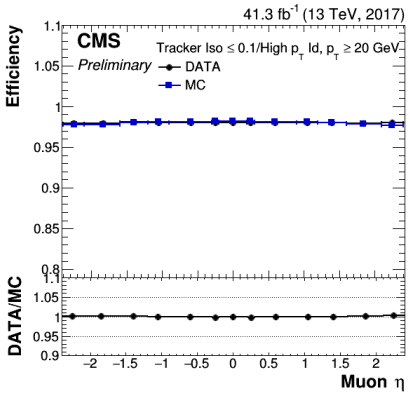

Figure 3.22: Tracker isolation efficiency as a function of muon η for 2017 data and MC. The denominator are muons with p_T>20 GeV passing the High-p_T ID.

a few mm given their size and weight. In addition, the magnetic flux induces huge forces that cause deformations and movements that may be as large as several mm, and must be carefully tracked by the alignment system.
After the first LHC shutdown period when CMS was opened, all DT chambers were first aligned by a hardware system, utilising lasers and cameras, in the startup phase, at the beginning of a data-taking period, as soon as the detector was closed and the magnetic field was turned on at its nominal value. The typical precision of the hardware alignment is $\approx 0.5-1$ mm on positions and $\approx 0.3-0.4$ mrad on angles of the individual chambers. The CSC chambers in the two endcaps did not feature an equally granular system and their initial geometry was measured by geometrical survey and photogrammetry with a precision of ≈ 2 mm on positions and ≈ 1 mrad on angles. The startup muon reconstruction performance was expected to be suboptimal due to large misalignments. The final alignment of the individual muon chambers (both DT and CSC) was determined starting from the aligned silicon tracker geometry, by extrapolating selected muon tracks from the inner tracker to the muon chambers (track-based muon alignment). With the track-based alignment the muon chambers' positions were determined with a precision of ≈ 200 μm in the most sensitive coordinate, which measures the magnetic bending of the muon track and was crucial for the precise momentum measurement.
From the beginning of the 2016 Run, the muon reconstruction has been using non-null muon alignment position errors (APEs) for the first time ever in CMS. Both data and MC simulation events have been analysed, spanning over the different sets of alignment conditions (from day-1 startup to the final track-based alignment, the so-called *asymptotic* alignment). The muon APEs have been introduced for all 6 degrees of freedom (3 positions: local-x, -y and -z, and 3 angles: local-ϕ_x, -ϕ_y and -ϕ_z) chamber-by-chamber, for both DT and CSC systems, and taken as uncorrelated as a first approximation.
Due to an overall rotation of the whole positive endcap detector after the 2015 LHC winter shutdown, the startup APEs mostly increased the HLT efficiency in the highest positive η region: this unphysical behaviour was cured by the track-based alignment,

and the corresponding updated conditions were introduced during the Summer 2016 data collection, after the startup phase. Run B - G data have been re-reconstructed with the asymptotic condition with APEs; only Run H data was used with the prompt reconstruction since the asymptotic plus APE conditions have already been deployed at the time of data collection.
Figure 3.23 shows relative momentum resolution as a function of the muon momentum for different alignment scenario for two η categories [94].

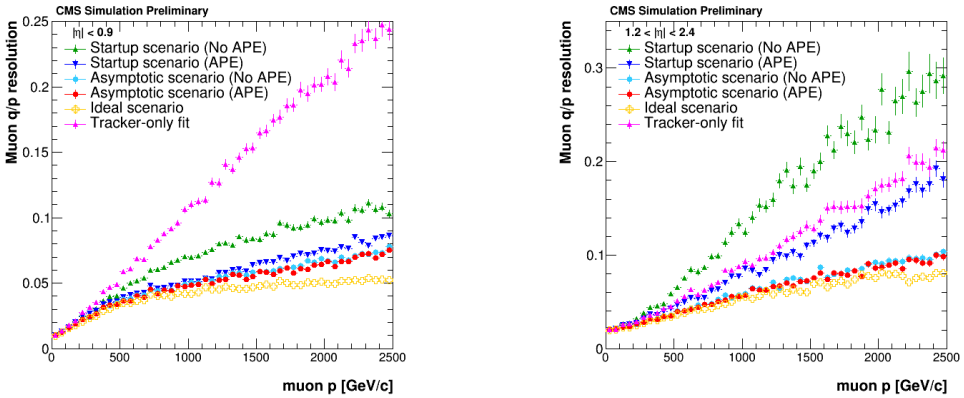

Figure 3.23: Relative momentum resolution as a function of muon momentum p using MC samples, for different misalignment scenarios with and without APE. The ideal scenario is also shown. The plotted values are obtained with a Gaussian fit to the relative residual distribution. Left plot shows muons with $|\eta|$ <0.9, right plot muons with $|\eta| > 1.2$.

3.7 Jets

Jets are reconstructed offline from the energy deposits in the calorimeter towers, clustered using the anti-k_T algorithm with a distance parameter of 0.4 (AK4 jets); for studies involving boosted topologies, jets are clustered with a larger distance parameter R = 0.8 (AK8 jets). In this process, the contribution from each calorimeter tower is assigned a momentum, the absolute value and the direction of which are given by the energy measured in the tower, and the coordinates of the tower. The raw jet energy is obtained from the sum of the tower energies and the raw jet momentum by the vectorial sum of the tower momenta. The raw jet energies are then corrected to establish a relative uniform response of the calorimeter in η and a calibrated absolute response in transverse momentum p_T. Jet momentum is determined as the vectorial sum of all particle momenta in the jet, and is found from simulation to be within 5 to 10% of the true momentum over the whole p_T spectrum and detector acceptance. Additional proton-proton interactions within the same or nearby bunch crossings can contribute additional tracks and calorimetric energy depositions to the jet momentum. To mitigate this ef-

fect, tracks identified to be originating from pileup vertices are discarded, and an offset correction is applied to correct for remaining contributions. Jet energy corrections are derived from simulation to bring the measured response of jets to that of particle level jets on average. In situ measurements of the momentum balance in dijet, photon+jet, Z+jet, and multijet events are used to account for any residual differences in jet energy scale in data and simulation. Additional selection criteria are applied to each jet to remove jets potentially dominated by anomalous contributions from various sub-detectors components or reconstruction failures. The jet energy resolution amounts typically to 15% at 10 GeV, 8% at 100 GeV, and 4% at 1 TeV, to be compared to about 40%, 12%, and 5% obtained when the calorimeters alone are used for jet clustering.

3.7.1 Heavy-flavour jets

Heavy-flavour jets (HF jets) [71] are jets originating from bottom or charm quarks: CMS has developed an algorithm to distinguish these jets from the light ones (the jets coming from lighter quarks). Algorithms for HF jet identification use variables connected to the properties of heavy-flavour hadrons present in jets resulting from the radiation and hadronization of b or c quarks. For instance, the lifetime of hadrons containing b quarks is of the order of 1.5 ps, while the lifetime of c hadrons is 1 ps or less. This leads to typical displacements of a few mm to one cm for b hadrons, depending on their momentum, thus giving rise to displaced tracks from which a secondary vertex (SV) may be reconstructed (Figure 3.24). In order to design and optimise heavy-flavour

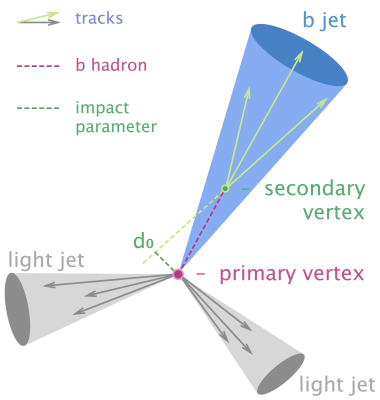

Figure 3.24: Illustration of a heavy-flavour jet with a secondary vertex (SV) from the decay of a b or c hadron resulting in charged-particle tracks (including possibly a soft lepton) that are displaced with respect to the primary interaction vertex (PV), and hence with a large impact parameter (d_0) value.

identification techniques, a reliable method is required for assigning a flavour to jets in simulated events. The jet flavour is determined by clustering not only the reconstructed final-state particles into jets, but also the generated b and c hadrons that do not have b and c hadrons as daughters respectively. Jets containing at least one b hadron are defined

as b jets; the ones containing at least one c hadron and no b hadron are defined as c jets. The remaining jets are considered to be light-flavour (or "udsg") jets. The properties of the tracks clustered within the jet represent the basic inputs of all heavy-flavour jet identification (tagging) algorithms. Input variables for the tagging algorithms are constructed from the tracks after applying appropriate selection criteria. In particular, the combined multivariate algorithm (cMVA) was developed combining the information from six different b jet identification discriminators with a Boosted Decision Tree. This algorithm has been tested to distinguish between light and heavy jets in the search for SM Higgs boson produced via VBF and decaying into muons.
Figure 3.25 shows the distribution of the discriminator value of the cMVA algorithm for two different simulation topologies compared to 13 TeV data [72] . The multijet topology is dominated by light-flavour jets and contains also contributions from jets from pileup collisions while the muon enriched jets topology is enriched in b jets.

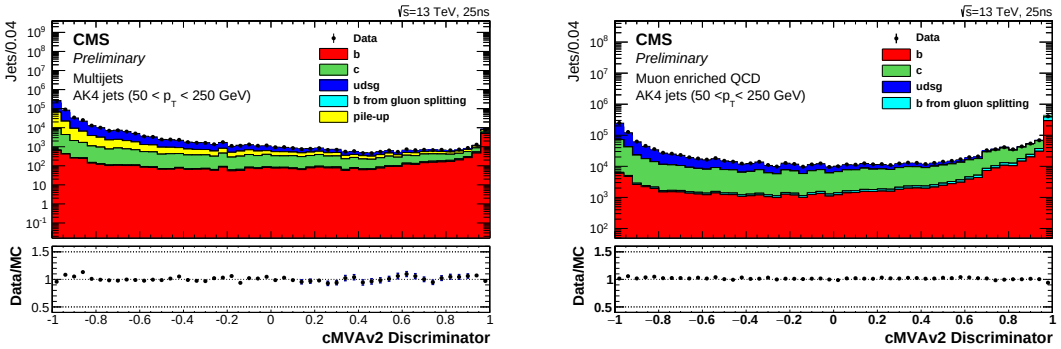

(a) Multijet topology

(b) Muon enriched jets topology

Figure 3.25: The distribution of the discriminator value of the cMVA algorithm for the inclusive multijet (left) and the muon enriched (right) topologies. Underflow and overflow are added to the first and last bins, respectively. The total number of entries in the simulation is normalised to the observed number of entries in data.

3.8 Taus

Due to its short life time ($c\tau = 87\mu m$), τ lepton decays before reaching the detector elements. In two thirds of the cases, τ leptons decay hadronically, typically into one or three charged mesons (predominantly $\pi^{\pm}$), often accompanied by neutral pions (decaying via $\pi^0 \rightarrow \gamma\gamma$), and a ν_τ. In the last third ($\approx 35\%$), τ decays into lighter leptons. Algorithms that use final-state photons and charged hadrons to identify hadronic decays of τ leptons (τ_h) through the reconstruction of the intermediate resonances have been developed: the hadron plus strips (HPS) and the tau neural classifier (TaNC), with this last one used to cross check the first.
Both algorithms start the reconstruction of a τ_h candidate from a PF jet, whose four-

momentum is reconstructed using the anti-k_T algorithm [69, 70] with a distance parameter R = 0.5. Using a PF jet as an initial seed, the algorithms first reconstruct the π^0 components of the τ_h, then combine them with charged hadrons to reconstruct the tau decay mode and calculate the tau four-momentum and isolation quantities.

3.8.1 HPS algorithm

HPS algorithm in based on the reconstruction in "strip" of photons produced by the π^0 decays and electrons produced by the photon conversions in the tracker material. The strip reconstruction starts by centering a strip on the most energetic electromagnetic particle within the PF jet. The algorithm then searches for other electromagnetic particles within a window of size $\Delta\eta = 0.05$ and $\Delta\phi = 0.20$ centred on the strip center. If other electromagnetic particles are found within that window, the most energetic one gets associated with the strip and the strip four-momentum is recalculated. The procedure is repeated until no further particles are found that can be associated with the strip. Strips satisfying a minimum transverse momentum requirement of $p_T^{strip} > 1$ GeV are finally combined with the charged hadrons to reconstruct individual τ_h decay modes. The decay topologies that are considered by the HPS tau identification algorithm are:

- Single hadron: corresponds to $h^-\nu_\tau$ and $h^-\pi^0\nu_\tau$ decays in which the neutral pions have too little energy to be reconstructed as strips.
- One hadron + one strip: reconstructs the decay mode $h^-\pi^0\nu_\tau$ in events in which the photons from π^0 decay are close together on the calorimeter surface.
- One hadron + two strip: corresponds to the decay mode $h^-\pi^0\nu_\tau$ in events in which photons from π^0 decays are well separated.
- Three hadron: corresponds to the decay mode $h^-h^+h^-\nu_\tau$. The three charged hadrons are required to come from the same secondary vertex.

The reconstructed tau has also to be isolated which means that no charged hadrons or photons present within an isolation cone of size $\Delta R = 0.5$ around the direction of the τ_h; its momentum have also to match the (η, ϕ) direction of the original PF jet within a maximum distance of $\Delta R = 0.1$.

3.8.2 TaNC algorithm

TaNC algorithm reconstructs the PF τ_h four-momentum as a sum of the four-momenta of all particles with p_T above 0.5 GeV in a cone of radius $\Delta R = 0.15$ around the direction of the leading particle. The decay mode is reconstructed from the particles that are contained within the signal cone of the τ_h candidate by counting the number of tracks and π^0 meson candidates and is uniquely determined by the multiplicity of reconstructed objects in the signal cone. The signal cone is defined as the region where the τ_h decay products are expected to be found.

3.9 MET: Missing transverse energy

The missing transverse energy (MET) [73] is defined as the negative vectorial sum of the transverse momenta of all the visible particles in the event and it represents the transverse momentum which escapes detection, leaving an imbalance in the transverse plane:

$$E_T^{miss} = -\sum_i p_T^i \tag{3.2}$$

The correct calculation of the MET depends on the precision with which the energy is measured in the event. CMS has developed three dedicated algorithms:

- PF E_T^{miss} is calculated from the reconstructed PF particles. PF $\sum E_T$ is the associated scalar sum of the transverse energies of the PF particles.
- Calo E_T^{miss} is calculated using the energies contained in calorimeter towers and their direction, relative to the centre of the detector, to define pseudo-particles. The sum excludes energy deposits below noise thresholds. Since a muon deposits only a few GeV on average in the calorimeter, independently of its momentum, the muon p_T is included in the Calo E_T^{miss} calculation instead of the small calorimetric energy deposit associated to the muon track. Calo $\sum E_T$ is the associated scalar sum of the transverse energies of the calorimeter towers and muons.
- MVA E_T^{miss} is calculated using multivariate analysis information from Calo and PF MET.

Non-linear response of the calorimeters, neutrinos and the inefficiency of the tracker can lead to underestimate the MET. For these reasons, two corrections are then applied: the first is aimed at reducing the contribution from the pile-up, improving the resolution, the second calibrates detector response.

Chapter 4

Search for low mass resonance decaying into muon pairs: SM Higgs boson

The Higgs boson observation in 2012 has been driven by $H \to ZZ^*$ and $H \to \gamma\gamma$ decay modes, thanks to their very high sensitivity. In the last years, the observation has been done also in $b\bar{b}$, $\tau^+\tau^-$ and WW^* decay channels. Despite the $H \to \mu\mu$ observation still misses, this decay mode plays a fundamental role to study the properties of the second generation leptons: it is the only way to directly measure the Higgs-muon Yukawa coupling strength (see Figure 1.12).
Latest CMS published results, using 2016 data and considering inclusive production mechanism for the SM Higgs boson decaying into muon pairs, are 2.45 on the expected σ/σ_{SM} at the 95% C.L. upper limit and a significance of 0.9 standard deviations. The significance is considered as the probability to observe a number of events N_o greater than the mean value N_b: this probability is then converted into standard deviation of a Gaussian statistic. The probability of 1.35×10^{-3}, corresponding to 3 σ, is the benchmark for the evidence, while 2.9×10^{-7}, corresponding to 5 σ, is the one for the observation. The dimuon mass distribution of CMS data with the signal-plus-background fit are shown in Figure 4.1 [1].

The analysis presented in this chapter consists in the search for the Standard Model Higgs with a mass of 125 GeV, produced via VBF (see section 1.2.1) and decaying into two muons. The final state studied includes therefore two muons and two light jets produced in the forward and backward regions due to the scattered quarks (see Figure 4.2). VBF has the second largest cross section (the first is the gluon-gluon fusion production, Figure 1.4) and a bigger experimental sensitivity thanks to its powerful discrimination against background: this mechanism proceeds by the scattering of two (anti-)quarks, mediated by exchange of a W or Z boson, with the Higgs boson radiated off the weak-boson propagator. The scattered quarks give rise to two hard jets in the forward and backward regions of the detector. Gluon radiation in the central-rapidity is suppressed thanks to the color-singlet nature of the weak-gauge boson exchanged: this feature al-

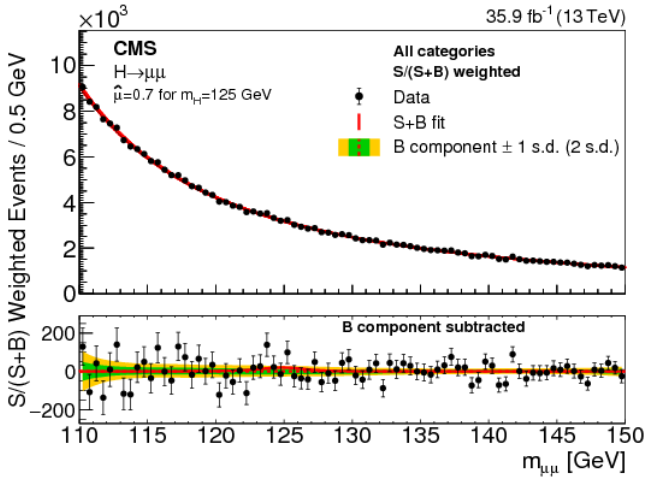

Figure 4.1: Data and sum of signal-plus-background fits.The lower panel shows the difference between the data and the background component of the fit.

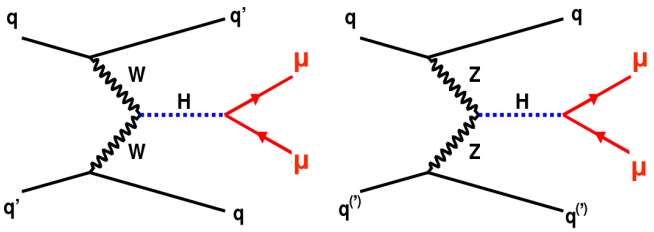

Figure 4.2: Schematic view of the Higgs boson produced via VBF and decaying into muon pair. This mechanism proceeds by the scattering of two (anti-)quarks, mediated by exchange of a W or Z boson, with the Higgs boson, radiated off the weak-boson propagator, decaying into two muons.

lows to distinguish VBF from overwhelming QCD backgrounds, including gluon-fusion induced Higgs plus two jets production and production of H in association with a W or Z boson, hadronically decaying. At the same time, thanks to the excellent muon momentum resolution at CMS, most $H \to \mu\mu$ events can be measured with an invariant dimuon mass resolution of 1.5 to 2.5 GeV, despite Higgs natural width (∼4 MeV). This allows to discriminate the expected signal events against the vast quantities of high-mass, off-shell $Z \to \mu^+\mu^-$ decays, as well as leptonic $t\bar{t}$ decays, which form the main backgrounds.
While the experimental sensitivity to the VBF process is very high, the dimuon decay channel suffers for its low branching ratio, 2.18×10^{-4} (compared to 5.84×10^{-1} for the $b\bar{b}$ that is the highest. See Table 1.4). So only 30 events were expected in 2016 data.
In order to face the limitations due to the low statistics, I have conducted a feasibility study on the use of the multivariate analysis (MVA) to distinguish signal events from the backgrounds. MVA technique consists in combining in different way a set of variables in order to extract one single output capable to discriminate between signal and background. The distribution of this discriminator has been used to extract final results. 2016 data have been used to validate plots of different distributions (e.g. p_T or η) to understand if the background is well modelled, while simulations only have been used in the dimuon mass and in the MVA distribution in the region where the signal is expected (blinded results). Cross section ratio and significance are obtained from simulation[1].

4.1 Data and MC samples

4.1.1 Data sets

I have analysed data collected during Run II in 2016 at $\sqrt{s} = 13$ TeV, corresponding to an integrated luminosity of $\mathcal{L} = 35.9\ fb^{-1}$. Although CMS has collected around 40 fb^{-1} in 2016, only runs that satisfy the data highest quality criteria ("Golden") at 3.8 T magnetic field are used. These runs are listed in a file in the JSON format. The data sets analysed are listed in Table 4.1.

4.1.2 Monte Carlo samples

The main SM background processes are Drell-Yan (DY), $t\bar{t}$, di-boson and single top production. I have used two samples for DY: one at leading order (LO) produced with MADGRAPH [52] and one at next-to leading order (NLO) using aMC@nlo [74]. Single top and $t\bar{t}$ samples are generated with POWHEG v2 [46–51], while di-boson are simulated at leading order (LO) using the PYTHIA 8.205 program along with the NNPDF3.0 PDFs [45,75]. Spin effects in multi-boson processes are simulated using MADSPIN [76]. The detector response is simulated using the GEANT4 package [53]. Each MC sample is re-weighted in order to better match the pile-up distribution observed in the collected

[1] In the following, *expected* results; *observed* results are instead the ones obtained with data.

2016 Data set	Run range	Int. Lum. [fb^{-1}]
/SingleMuon/Run2016B-03Feb2017_ver2-v2	272007–275376	5.788
/SingleMuon/Run2016C-03Feb2017-v1	275657–276283	2.573
/SingleMuon/Run2016D-03Feb2017-v1	276315–276811	4.248
/SingleMuon/Run2016E-03Feb2017-v1	276831–277420	4.009
/SingleMuon/Run2016F-03Feb2017-v1	277772–278808	3.102
/SingleMuon/Run2016G-03Feb2017-v1	278820–280385	7.540
/SingleMuon/Run2016H-03Feb2017_ver2-v1	280919–284044	8.606
/SingleMuon/Run2016H-03Feb2017_ver3-v1		

Table 4.1: Data sets used in this analysis.

proton-proton data (see Figure 2.5). The number of additional pileup interactions in data is measured from luminosity. The number of interactions for a bunch-bunch collision is given multiplying the instantaneous luminosity for a single collision for each bunch pair by the total inelastic cross section. The measured minimum bias cross-section corresponding to the 2016 data is 69.2 mb with a relative uncertainty of ±5% [77].

VBF and ggF[2] $H \to \mu^+\mu^-$ signal events are simulated at next to leading order (NLO) using the POWHEG v2 generator interfaced with PYTHIA (v8.212) for parton showering (PS) and hadronization.
In Table 4.2 the list of samples, their correspondent cross section and the number of events generated are reported.

Background process	**σ (pb)**	**Events (M)**
DYJetsToLL_M-105To160_Tune CUETP8M1_13TeV-madgraphMLM-pythia8	41.9	41
DYJetsToLL_M-105To160_TuneCUETP8M1_13TeV-amcatnloFXFX-pythia8	41.9	60
TT_TuneCUETP8M2T4_13TeV-powheg-pythia8	809	46
WW_TuneCUETP8M1_13TeV-pythia8	118.7	0.994
ZZ_TuneCUETP8M1_13TeV-pythia8	16.523	0.99
WZ_TuneCUETP8M1_13TeV-pythia8	47.13	1
ST_tW-channel-top-5f_inclusiveDecays_13TeV-powheg-pythia8_TuneCUETP8M2T4	35.85	2.7
ST_tW-channel-antitop-5f_inclusiveDecays_13TeV-powheg-pythia8_TuneCUETP8M2T4	35.85	6.9
ST_s-channel_4f_inclusiveDecays_13TeV-powhegV2-madspin-pythia8_TuneCUETP8M1	3.36	1
ST_t-channel- top_4f_inclusiveDecays_13TeV-powhegV2-madspin-pythia8_TuneCUETP8M1	136.02	62.3
ST_t-channel- antitop_4f_inclusiveDecays_13TeV-powhegV2-madspin-pythia8_TuneCUETP8M1	80.95	31.7
Higgs signal samples		
VBF_HToMuMu_M125_13TeV_powheg_pythia8	0.82	0.96
GluGlu_HToMuMu_M125_13TeV_powheg_pythia8	10.53	0.99

Table 4.2: Summary of simulated background and signal samples used in this analysis.

[2] ggF samples is used to take into account its contamination in the VBF phase space. See sec. 4.3.3

4.2 HLT

For this analysis I have used as HLT path the OR between `HLT_IsoMu24` and `HLT_IsoTkMu24`. `HLT_Iso(Tk)Mu24` is the lowest-p_T unprescaled single isolated muon trigger path, available during all included data taking periods. This trigger requires the event to have at least one isolated muon candidate with p_T above 24 GeV, with no explicit restriction on its pseudorapidity.
The event trigger efficiency is calculated as the logical-OR of the single muon-trigger efficiency (ϵ_{μ_i}) with $\varepsilon_{trg} = 1 - \prod_{i=1}^{N}(1 - \varepsilon_{\mu_i})$ where N is the total number of muons, with $p_T > 26$ GeV, that fired the trigger in the event. The corresponding scale factor (SF) is therefore:

$$SF_{trg} = \frac{\varepsilon_{trg}^{data}}{\varepsilon_{trg}^{MC}} \tag{4.1}$$

4.3 Reconstruction and selection

Proton-proton collisions events are selected by requiring at least one valid reconstructed primary vertex (PV). The PV with the highest scalar sum of the squared p_T of its associated tracks (must be at least 4) is considered as the PV of the given bunch crossing.

4.3.1 Muon reconstruction

The candidate muon is reconstructed using PF algorithm (see sec.3.1): it must have $p_T > 10$ GeV, must be in the CMS acceptance ($|\eta_\mu| < 2.4$) and must have a relative isolation $I_{rel}^{PF} = I^{PF}/p_T^{\mu} < 0.25$. The PF muons are further required to fulfill the muon Loose ID criteria (see 3.6.3).
In order to account for the differences between data and MC regarding the muon identification and isolation, the recommended scale factors in CMS are used to re-weight the MC distributions. Efficiency corrections are applied to the simulation in the form of SFs. The event reconstruction and isolation efficiencies are calculated as the logical-AND of the single muon efficiencies with $\varepsilon_{id/iso} = \prod_{i=1}^{N} \varepsilon_{\mu_i}$, yielding to the event SF being the product of the muons SFs:

$$SF_{id/iso} = \frac{\varepsilon_{id/iso}^{data}}{\varepsilon_{id/iso}^{MC}} \tag{4.2}$$

SFs are produced centrally for different data-taking periods (Run BCDEF and Run GH). Event SFs are averaged using as weights the corresponding integrated luminosity:

$$\begin{aligned} \omega_{BF} &= \mathcal{L}_{BF}/\mathcal{L}_{tot} \\ \omega_{GH} &= \mathcal{L}_{GH}/\mathcal{L}_{tot} \\ SF &= \omega_{BF} \cdot (SF_{trig}^{BF} SF_{id}^{BF} SF_{iso}^{BF}) + \omega_{GH} \cdot (SF_{trig}^{GH} SF_{id}^{GH} SF_{iso}^{GH}) \end{aligned} \tag{4.3}$$

Last equation in 4.3 represents the total muon efficiency correction applied to simulation.

Muon calibration

The theoretical width of the Higgs boson is around 4 MeV [6] so its mass peak is dominated by the detector resolution which is on the order of GeV. With such a narrow theoretical width, improving the dimuon mass resolution in data is an important factor in the sensitivity of the analysis. In general, the reconstruction of the momentum of muons is biased from detector misalignments, the reconstruction software, and uncertainties in the magnetic field. Moreover, the mean and the resolution of the dimuon mass peaks in Monte Carlo, must match in data in order to set limits accurately: for this reason, the Rochester Muon Corrections [78] are applied. The corrections depend on η, ϕ and the charge of the muon and they can be distinguished between: a muon momentum scale multiplicative correction that could originate from an incorrect integral of the magnetic field and an additive correction for the bias that could originates from misalignment.

4.3.2 Jets reconstruction

Jets are reconstructed from PF candidates with the AK4 algorithm (see sec.3.7); jets overlapping with the selected muons are not considered further in the analysis. The PF jets are further required to fulfill the jet Loose Identification criteria. Jets with $|\eta_\mu|$ less than 2.7 are required to contain at least one charged PF candidate and have a non-zero charged energy fraction, and a charged electromagnetic energy fraction less than 0.99. The neutral and photon energy fraction must be less than 0.99. Jets in the region 2.7 $< |\eta_\mu| <$ 3.0 are required to have a neutral electromagnetic fraction greater than 0.01 and neutral hadron fraction less than 0.98, while jets with pseudorapidity above 3.0 are required to have more than 10 neutral particles and a neutral electromagnetic energy fraction less than 0.9. Jet energy is calibrated in order to align simulation and data to the visible energy in the cluster.

4.3.3 Event selection

Offline event selection requires two opposite-charge muons which pass the muon identification criteria mentioned previously. The two highest-p_T selected muons with opposite charge are considered as the H$\rightarrow \mu^+\mu^-$candidate pair. At least one of these muons must have p_T greater than 30 GeV, and be matched to a trigger muon with $\Delta R < 0.1$.
The events must also contain at least 2 jets: the two highest-p_T jet must be respectively greater than 35 and 25 GeV. In order to select VBF-like event, the jets must be in the opposite direction so that $|\Delta\eta_{(jet_1,let_2)}| > 2.5$ and defined M_{jj} the mass of the system of the two jets, it must be greater than 250 GeV. An event balance variable, R(p_T^{hard}), is used to separate the signal from the background; it is defined as:

$$R(p_T^{hard}) = \frac{|\vec{p}_{T_{j1}} + \vec{p}_{T_{j2}} + \vec{p}_{T_H}|}{|\vec{p}_{T_{j1}}| + |\vec{p}_{T_{j2}}| + |\vec{p}_{T_H}|} = \frac{|\vec{p}_T^{\,hard}|}{|\vec{p}_{T_{j1}}| + |\vec{p}_{T_{j2}}| + |\vec{p}_{T_H}|}$$

where $\vec{p}_{T_{j1}}$, $\vec{p}_{T_{j2}}$ and $\vec{p}_{T_H}$ are, respectively, the transverse momenta of the two tagging jets and of the dilepton system (or Higgs boson), and the numerator, $\vec{p}_T^{\,hard}$, is the estimator of the p_T for the hard process. We require $\mathrm{R}(p_T^{hard}) < 0.4$.
Angular variables useful for signal discrimination include the difference between the rapidity of the H boson y_H and the average rapidity of the two tagging jets, i.e.

$$y^* = y_H - \frac{1}{2}(y_{j1} + y_{j2})$$

and the z^* Zeppenfeld variable [79] is defined as

$$z^* = \frac{y^*}{\Delta y_{jj}}$$

The condition imposed is $z^* < 2.5$ (see Figure 4.5).
After applying all the selection cuts and scale factors on leptons and jets, I have validated the MC simulation on data events in the signal region of the candidate muon pair ($M_{H_{\mu\mu}}$) with the invariant mass between 115 and 135 GeV: $115 < M_{H_{\mu\mu}} < 135$.
The results are reported in Figure 4.3, 4.4, 4.5 where simulations are compared to data, finding good agreement.

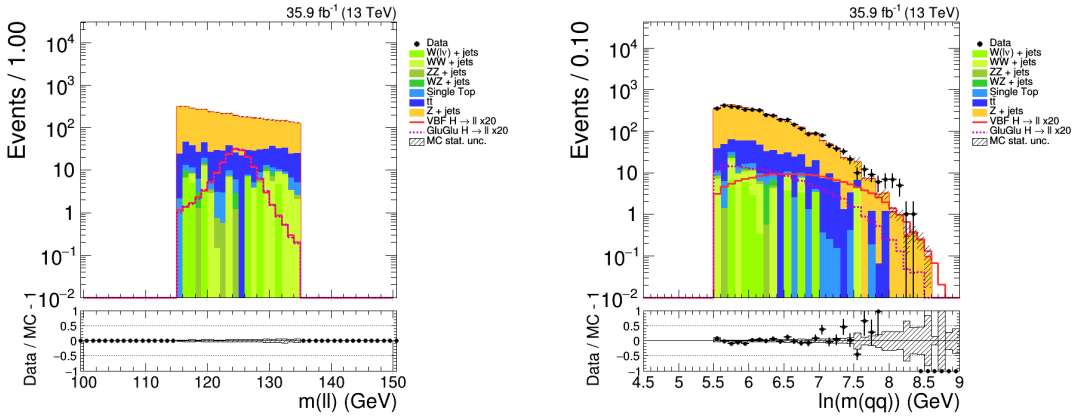

(a) Dimuon mass

(b) Dijet mass

Figure 4.3: Validation plots for dimuon (blinded) and dijet mass. Stack plot is the simulation; data are the black dots. Red line is the VBF signal (×20); purple dashed line is the ggF signal (×20). Hatched line is the statistical error. In the bottom panel, the relative difference between the data and expectations is reported with the statistical error.

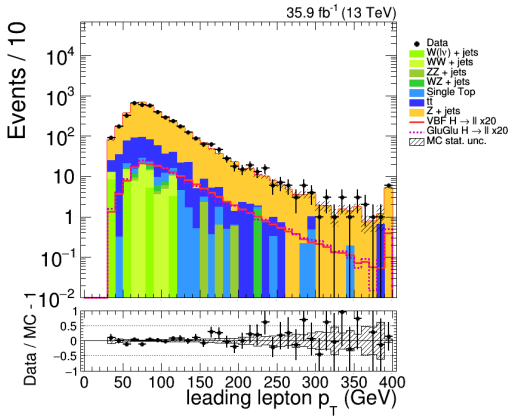

(a) Leading muon p_T

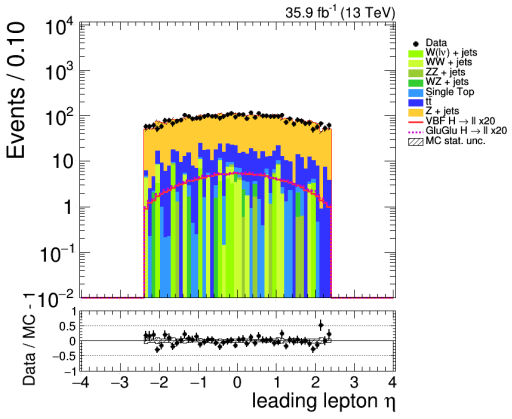

(b) Leading muon η

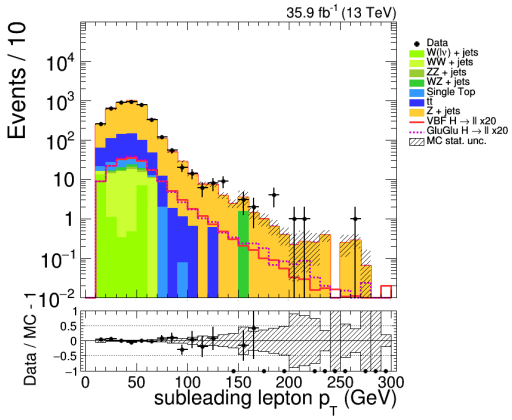

(c) Subleading muon p_T

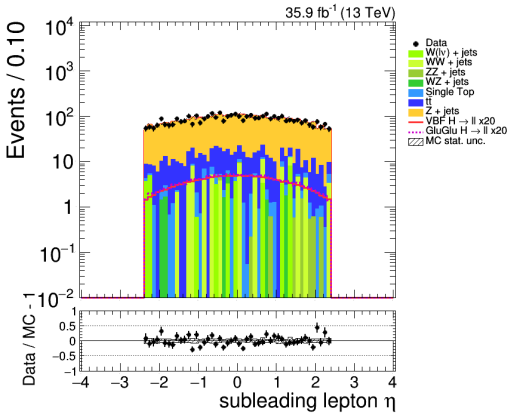

(d) Subleading muon η

Figure 4.4: Validation plots for p_T and η of the leading (top row) and subleading (bottom row) muon. Stack plot is the simulation; data are the black dots. Red line is the VBF signal ($\times 20$); purple dashed line is the ggF signal ($\times 20$). Hatched line is the statistical error. In the bottom panel, the relative difference between the data and expectations is reported with the statistical error.

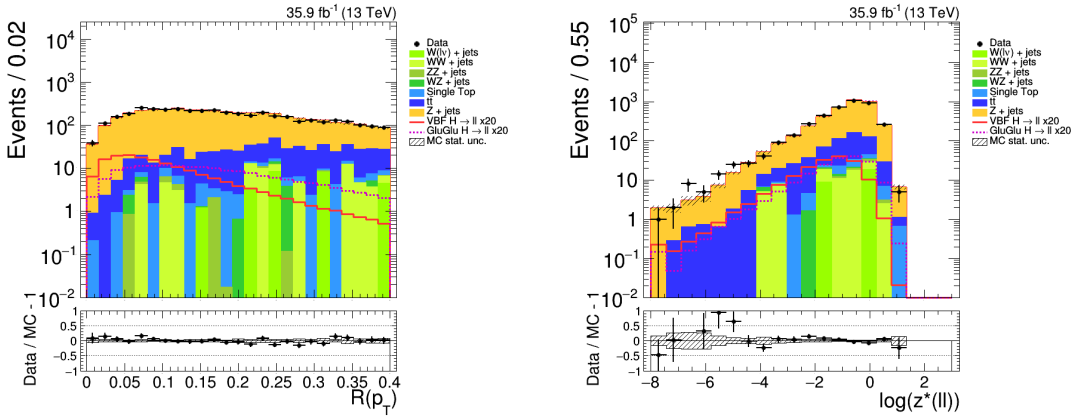

(a) R(p_T^{hard})

(b) z^*

Figure 4.5: Validation plots for R(p_T^{hard}) (on the left) and z^* on the right. Stack plot is the simulation; data are the black dots. Red line is the VBF signal ($\times$20); purple dashed line is the ggF signal ($\times$20). Hatched line is the statistical error. In the bottom panel, the relative difference between the data and expectations is reported with the statistical error.

4.4 Multivariate analysis approach

In order to face the limitations due to the low statistics, I have followed the Multivariate approach (MVA) for the separation of signal from background. The output distribution of this new method has been used to extract the 95% C.L. upper limits on the ratio of the expected cross-section and the SM predicted cross-section (σ/σ_{SM}) and the p-values for the background only hypothesis.

4.4.1 MVA

Given two ensembles of events, named signal and background, described by the same set of variables, the basic idea of the MVA is to combine in different way this set in order to extract one single output capable to discriminate between the two ensembles.
Defined $\vec{x} = (x_1, x_2, ..., x_d)$ the set of the d variables describing the signal and the background and $\vec{\omega}$ a set of parameters, the MVA discriminant can be defined as the function f so that

$$y = f(\vec{\omega}, \vec{x}) : \Re^d \mapsto \Re^N$$

with $N \ll d$.
Different functions f have been developed in the years with different performance, like the background rejection or the execution time: for this analysis I have implemented the decision tree and the neural network.

4.4.2 Decision tree

A decision tree [81] is a binary tree structured classifier similar to the one sketched in Figure 4.6. Repeated left/right (yes/no) decisions are taken on one single variable at a time until a stop criterion is fulfilled. The phase space is split in this way into many regions that are eventually classified as signal or background, depending on the majority of training events that end up in the final leaf node. Each output node represents a specific value of the target variable, the variable the regression function is trying to estimate. The boosting [3] of a decision tree extends this concept from one tree to several trees which form a forest. The trees are derived from the same training ensemble by reweighting events, and are finally combined into a single classifier which is given by a (weighted) average of the individual decision trees. The boosting procedure is employed to adjust the parameters such that the deviation between the model response F(x) and the true value y obtained from the training sample is minimised. The deviation is measured by the so-called loss-function L(F, y): a popular choice is the squared error loss L(F, y) = $(F(x) - y)^2$. The boosted used in this analysis is the Gradient (in the future BDTG) that uses the binomial log-likelihood loss, L(F, y) = ln(1+$e^{-2F(x)y}$).

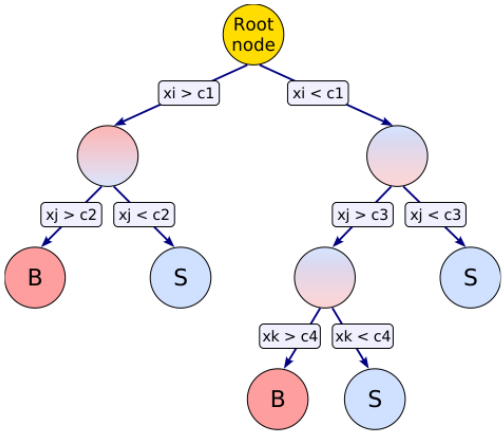

Figure 4.6: Schematic view of a decision tree. Starting from the root node, a sequence of binary splits using the discriminating variables x_i is applied to the data. Each split uses the variable that at this node gives the best separation between signal and background when being cut on. The leaf nodes at the bottom end of the tree are labeled "S" for signal and "B" for background depending on the majority of events that end up in the respective nodes.

Decision tree is trained defining the splitting criteria for each node. The training starts with the root node, where an initial splitting criterion for the full training sample

[3] Boosting consists in applying an MVA algorithm to reweighted (boosted) versions of the training data and then taking a weighted majority vote of the sequence of MVA algorithms thus produced in view of an increased stability with respect to statistical fluctuations in the training sample.

is determined. The split results in two subsets of training events that each go through the same algorithm of determining the next splitting iteration. This procedure is repeated until the whole tree is built. At each node, the split is determined by finding the variable and corresponding cut value that provides the best separation between signal and background. The node splitting stops once it has reached the minimum number of events tuned. The leaf nodes are classified as signal or background according to the class the majority of events belongs to. The separation criterion assesses the performance of a variable and a specific cut requirement. Because a cut that selects predominantly background is as valuable as one that selects signal, the criterion is symmetric with respect to the event classes. The separation criterion has a maximum where the samples are fully mixed and fall off to zero when the sample consists of one event class only. The criterion used in this analysis is the *Gini index* $= p \cdot (1 - p)$, where p is the purity defined as the ratio of signal events to all events in that node (hence pure background nodes have zero purity).
Once the training ends, the variables are ranked counting how often they are used to split decision tree nodes, and by weighting each split occurrence by the separation gain-squared it has achieved and by the number of events in the node.

4.4.3 Neural Network

A neural network is any simulated collection of inter-connected neurons, with each neuron producing a certain response at a given set of input signals. By applying an external signal to some (input) neurons the network is put into a defined state that can be measured from the response of one or several (output) neurons. One can therefore view the neural network as a mapping from a space of input variables x_1,..., $x_{n_{var}}$ onto a one-dimensional (e.g. in case of a signal-versus-background discrimination problem) or multi-dimensional space of output variables y_1, ..., $y_{m_{var}}$. The mapping is nonlinear if at least one neuron has a nonlinear response to its input. The neural network used in this analysis is the MultiLayer Perceptron (MLP).
While in principle a neural network with n neurons can have n^2 directional connections, the complexity can be reduced by organising the neurons in layers and only allowing direct connections from a given layer to the following layer (see Figure 4.7). The first layer of a multilayer perceptron is the input layer, the last one the output layer, and all others are hidden layers. For a classification problem with n_{var} input variables the input layer consists of n_{var} neurons that hold the input values, x_1, ..., $x_{n_{var}}$, and one neuron in the output layer that holds the output variable, the neural net estimator y_{MLP}.

4.4.4 Training and test

To train and test the MVA I have used the DY sample (at LO) and the VBF samples respectively as background and signal. Starting from a common set of variables between the BDTG and the MLP, final variables have been chosen maximising agreement between training and test (see Figure 4.8), the ROC curve (see Figure 4.9) and the ranking. In particular the variables chosen are listed in Table 4.3.

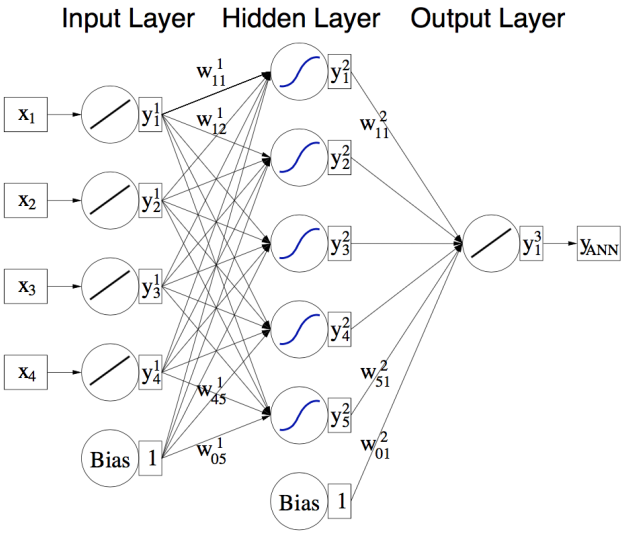

Figure 4.7: Multilayer perceptron scheme with one hidden layer.

The soft activity is defined as the additional hadronic activity between the VBF-tagging jets, excluding the more centrally produced Higgs boson decay products; ΔM_{rel} is defined as the ratio between lepton p_T uncertainties and the dimuon mass:

$$\Delta M_{rel} = \frac{\sqrt{\frac{p^2_{T_{err,1}} + p^2_{T_{err,2}}}{2}}}{M_{ll}}$$

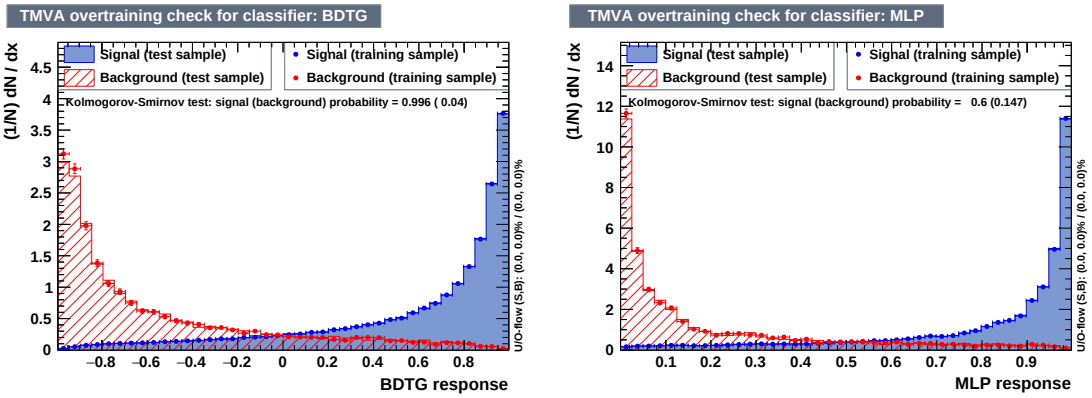

(a) BDTG (b) MLP

Figure 4.8: Training - test validation plots: BDTG on the left, MLP on the right.

BDTG	MLP
dimuon mass	dimuon mass
dimuon p_T	dimuon p_T
dijet mass	dijet mass
R(p_T^{hard})	R(p_T^{hard})
soft activity	soft activity
leading V mass	leading V mass
subleading V mass	subleading V mass
z^*	z^*
$\cos(\theta)(H, jet_2)$	$\cos(\theta)(H, jet_1)$
p_T of dimuon-dijet	ΔM_{rel}
-	leading jet p_T
-	third jet p_T
-	subleading V p_T
-	leading muon p_T

Table 4.3: List of the variables used to train and test the two MVA method: BDTG (left column) and MLP (right column).

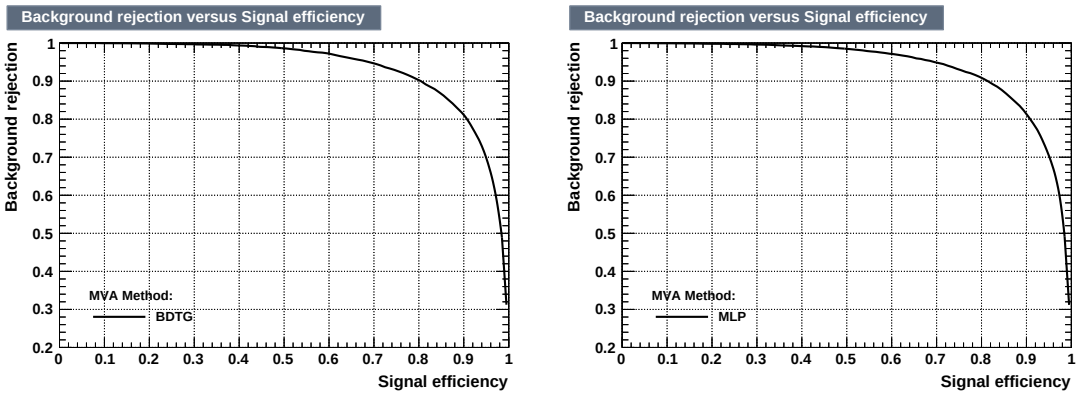

(a) BDTG

(b) MLP

Figure 4.9: ROC curve: BDTG on the left, MLP on the right.

4.4.5 Validation

Blinded validation plots for the MVA distributions are reported in Figure 4.10.

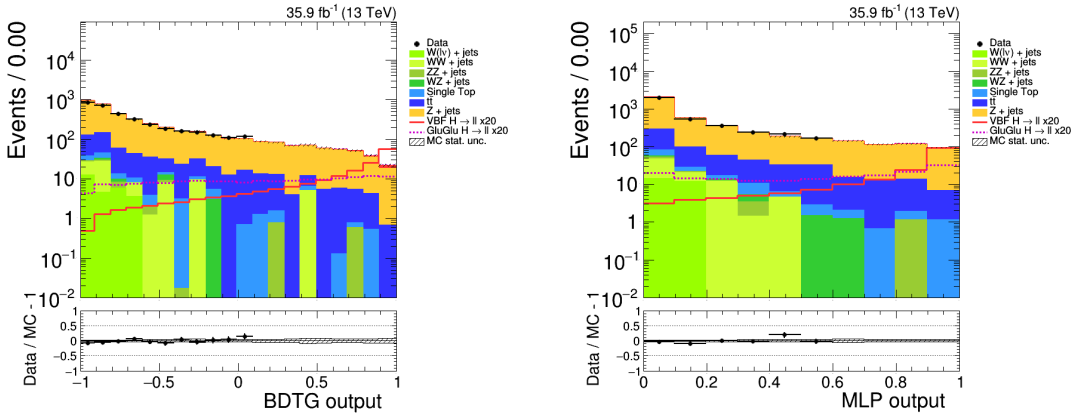

(a) BDTG (b) MLP

Figure 4.10: Blinded validation plots for BDTG (left) and MLP (right) distribution. Stack plot is the simulation; data are the black dots. Red line is the VBF signal (×20); purple dashed line is the ggF signal (×20). Hatched line is the statistical error. In the bottom panel, the relative difference between the data and expectations is reported with the statistical error.

In order to improve the extraction of the signal component, the transformation $X' = tanh^{-1}((X+1)/2)$ is applied to MVA output. This allows the purest signal region of the MVA output to be better sampled. Figure 4.11 shows the behaviour of the transformation function used.

Figure 4.12 shows MVA distribution after having applied the transformation. In this

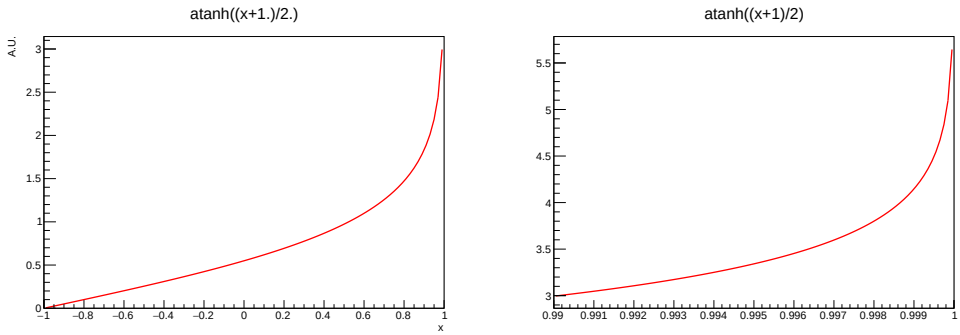

Figure 4.11: Transformation function used to improve the extraction of the signal component. On the right, a zoom in the interval [0.99, 1[.

case, I have chosen a binning so that at least 10 DY events (not weighted) are included

in each bin that must have at the same time a width greater than 0.1.

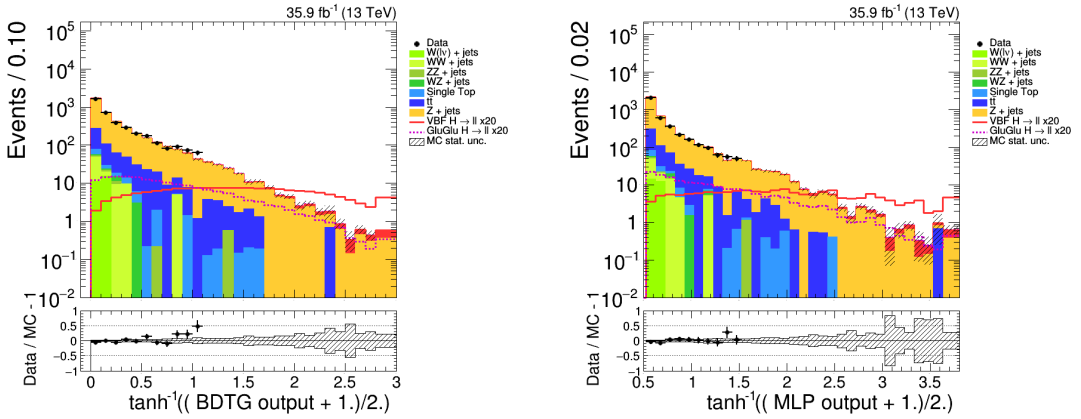

(a) BDTG (b) MLP

Figure 4.12: Blinded validation plots for BDTG (left) and MLP (right) distribution after applying the transformation. Stack plot is the simulation; data are the black dots. Red line is the VBF signal (×20); purple dashed line is the ggF signal (×20). Hatched line is the statistical error. In the bottom panel, the relative difference between the data and expectations is reported with the statistical error.

4.5 Statistical interpretation

A binned maximum likelihood fit [82] of the MVA output distribution is used for the statistical model in this analysis. Background and signal functional forms are given as inputs, as well as various systematics like normalisation and/or shape uncertainties. The fit also constrains the systematic uncertainties and finds the background normalisations. The likelihood function, for the input data sets given the expected background and the signal multiplied by the μ modifier, is:

$$\mathcal{L}(data|\mu,\theta) = \prod_{bins} Poisson(data|\mu \cdot s(\theta) + b(\theta)) \cdot p(\tilde{\theta}|\theta) \tag{4.4}$$

where $\tilde{\theta}$ are the nuisance parameters. The likelihood function is then used to build the test statistic

$$q_\mu = -2\ log\frac{\mathcal{L}(\mu,\hat{\theta}_\mu)}{\mathcal{L}(\hat{\mu},\hat{\theta})} \tag{4.5}$$

where $\hat{\theta}_\mu$ represents the values of the nuisance parameters obtained by maximising $\mathcal{L}$ at μ fixed, and $\hat{\mu}$, $\hat{\theta}$ in the denominator are the best values of the parameters obtained by maximising $\mathcal{L}$. The confidence level (C.L.(μ)) limits are set finding the signal strength

modifier μ value for which CL_s is equal to 95% [83]. The CL_s is defined as:

$$CL_s^{(\mu)} = \frac{CL_{s+b}^{(\mu)}}{CL_b^{(\mu)}}$$

with

$$CL_{s+b}(\mu) = \int_{q_\mu^{obs}}^{\infty} f(q_\mu/\mu) dq_\mu$$

$$CL_b(\mu) = \int_{q_\mu^{obs}}^{\infty} f(q_\mu/0) dq_\mu$$

where $f(q_\mu/\mu)$ and $f(q_\mu/0)$ are the q_μ pdfs in the signal+background and background only hypothesis. By increasing μ, C.L.(μ) decreases, and its value, for which $CL_s^{(\mu)} = 95\%$, is the upper limit on μ at the required confidence level.

4.5.1 Systematic uncertainties

Search for the Higgs boson decaying into two muons is largely dominated by the statistic uncertainty.
The main systematic uncertainties affecting the measurement are classified into experimental and theoretical sources. Some uncertainties affect only normalisations while other affect both the normalisation and shapes of the MVA output distributions.

Experimental uncertainties

- Luminosity: 2.5% uncertainty is assigned to the value of the integrated luminosity [84]

- Trigger and selection efficiencies: uncertainties in the data driven efficiency corrections for the leptonic trigger and offline selections are taken into account and amount to a total around 2-3%. These uncertainties are estimated by comparing the lepton efficiencies expected in simulation and measured in data with a tag and-probe method.

- Jet Energy Scale (JES) and Resolution (JER): uncertainties studied by rescaling up and down the reconstructed jet energy by SF depending on p_T and η [85].

- Pileup: uncertainty is evaluated by generating alternative distributions with different distributions of the number of pileup interactions, corresponding to a 5% uncertainty on the total inelastic pp cross section at $\sqrt{s} = 13$ TeV.

- Statistics of simulation: for each signal and background simulation components shape variations for the distributions are considered by shifting each bin content up or down by its statistical uncertainty.

Theoretical uncertainties

- Normalisation of top quark and diboson backgrounds: diboson and top quark production processes are modelled with MC simulations. An uncertainty in the normalisation of these backgrounds is assigned based on the PDF and μ_F, μ_R[4] uncertainties, following calculations in [86–88]. The final impact on the signal strength uncertainty amounts to less than 1%.

4.6 Results

Given the BDTG and MLP output distributions, I have done a maximum likelihood fit including all the systematic uncertainties mentioned, using only simulation. The 95% C.L. expected upper limit on σ/σ_{SM}, for the BDTG and MLP is shown in Figure 4.13. The final expected significance has been extracted and it is reported in Table 4.4. Best results are obtained using neural network: 95% upper limit is found to be 2.35 times the SM value and a significance of 0.94 standard deviations, improving latest CMS results.

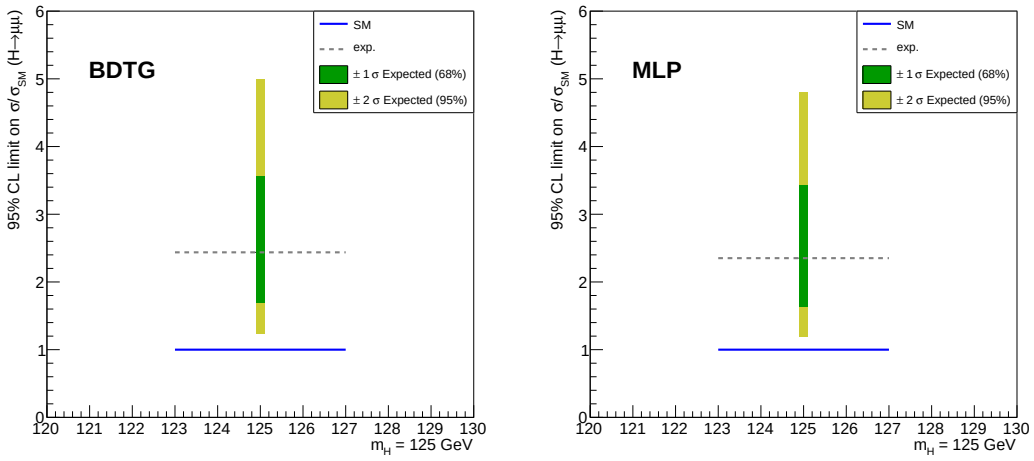

Figure 4.13: 95% C.L. upper limit on σ/σ_{SM} for BDTG (on the left) and MLP (on the right).

4.7 Outlook

Due to the very promising results, the VBF channel treated with the MVA method will be used in combination with the other production modes to extract final results on

[4] μ_F is the factorization scale (separates long and short- distance physics) and μ_R is the renormalization scale for α_s defined in the matrix element

MVA method	**Significance**
BDTG	0.90
MLP	0.94

Table 4.4: Summary of the significance for BDTG and MLP method.

the search for the Higgs boson decaying into two muons, in view of the 2019 Winter conferences.
For this search, I have considered 35.9 fb^{-1}; CMS during Run II (2016 - 2018) has collected $\sim 150 fb^{-1}$ and at the end of Run III it is foreseen an integrated luminosity of 300 fb^{-1}. This statistics will be enough for the $H \to \mu\mu$ evidence; the observation of this decay channel instead is foreseen during High - Luminosity LHC (starting from 2026), thanks to an integrated luminosity of around 3 ab^{-1}: with this statistics the results will be limited by only the systematic uncertainties.

Chapter 5

Search for high mass resonance decaying into muon pairs

Despite the Higgs boson observation, the SM is not complete and there are physics aspects it is not able to take into account. In order to try to solve these issues, many models have been developed beyond the Standard Model (BSM) and within these, new bosons are introduced.
In this chapter I will describe the search for new massive resonances decaying into two muons predicted in different models BSM: Sequential Standard Model and Grand Unified Theory, that involve the introduction of new Spin-1 boson, Z'_{SSM} and Z'_{ψ} respectively, and Extra Dimension Model with Kaluza-Klein Spin-2 graviton, G_{KK}. Spin-1 results have been also re-interpreted in the context of the Dark Matter (DM) sector, searching for the DM-SM mediator.
The search presented in this chapter involves new resonances with mass of the order of TeV and thus muons with TeV-p_T. These muons require a careful treatment of the information from the muon system: at high energy the probability for the muons to produce electromagnetic showers increases, and such showers can corrupt the measurement done in the muon detectors. Therefore, for these muons, a set of specially-developed TeV-muon track refits is performed: TuneP algorithm is in charge to assign the best track fits reconstruction (see sec.3.6.2). At high-p_T, muons are also sensitive to the detector alignment: there are different effects originating from the intrinsic limits of the apparatus used for the measurement (a non perfect alignment or a systematic distortion of the muon system chambers), which can bias the measurement of the muon curvature and thus of its transverse momentum.
In order to isolate potential problems or mis-measurements otherwise affecting the whole analysis, I have performed this search in different pseudorapidity regions: the mass resolution, for example, is known to be significantly better in the barrel region. Furthermore, the alignment conditions have a main issue in the forward negative endcap that degrade dramatically the momentum scale. For these reasons, I have decided to consider two pseudorapidity regions for this analysis:

- Barrel - Barrel (BB): events with both muons in the barrel and overlap region

($|\eta| < 1.2$).

- Barrel - Endcap and Endcap - Endcap (BE): events with at least one of the two muons in the endcap ($1.2 < |\eta| < 2.4$).

Every input used in the limit calculation (e.g. the invariant mass spectrum, background shape, Drell-Yan correction, efficiency and resolution parametrisation) as well as all the nuisance parameters are then studied for each of these two categories separately.

5.1 Data and MC samples

5.1.1 Datasets

For this analysis I have used data collected during Run II in 2016 and 2017 at $\sqrt{s}$ = 13 TeV, corresponding to an integrated luminosity of $\mathcal{L}_{2016} = 36.3\ fb^{-1}$ and $\mathcal{L}_{2017} = 42.4\ fb^{-1}$. The "MuonPhys" official JSON files, for data collected with 3.8 T magnetic field, are used: with respect to the search for SM Higgs boson, the subsystems not directly used in the studies, such as ECAL and HCAL, do not have to be marked as good. The datasets analysed are listed in Table 5.1.

2016 Dataset	Run range
/SingleMuon/Run2016B-23Sep2016-v3	273150 – 275376
/SingleMuon/Run2016X-23Sep2016-v1	275657 – 279656
/SingleMuon/Run2016H-PromptReco-vY	281145 – 284044
2017 Dataset	Run range
/SingleMuon/Run2017B-17Nov2017-v1	297020 – 299329
/SingleMuon/Run2017C-17Nov2017-v1	299337 – 302029
/SingleMuon/Run2017D-17Nov2017-v1	302030 – 303434
/SingleMuon/Run2017E-17Nov2017-v1	303435 – 304826
/SingleMuon/Run2017F-17Nov2017-v1	304911 – 306462

Table 5.1: Datasets used in this analysis; X stands for C, D, E, F, G, and Y stands for 1 to 3.

5.1.2 Monte Carlo samples

The simulated Monte Carlo (MC) background samples are generated for collisions at $\sqrt{s}$ = 13 TeV with PU included by mixing randomly chosen minimum bias events with the simulated ones to achieve the expected PU distribution, shown in Figure 2.5.
In Table 5.2 and 5.3 the list of samples, their correspondent cross section, the order of the matrix element calculation and the number of events generated are reported.

2016 Process	σ (pb)	Order	Events
POWHEG DY			
ZToMuMu_NNPDF30_13TeV-powheg_M_50_120	1975	NLO	2977600
ZToMuMu_NNPDF30_13TeV-powheg_M_120_200	19.32	NLO	100000
ZToMuMu_NNPDF30_13TeV-powheg_M_200_400	2.731	NLO	100000
ZToMuMu_NNPDF30_13TeV-powheg_M_400_800	0.241	NLO	98400
ZToMuMu_NNPDF30_13TeV-powheg_M_800_1400	1.678E-2	NLO	100000
ZToMuMu_NNPDF30_13TeV-powheg_M_1400_2300	1.39E-3	NLO	95106
ZToMuMu_NNPDF30_13TeV-powheg_M_2300_3500	0.8948E-4	NLO	100000
ZToMuMu_NNPDF30_13TeV-powheg_M_3500_4500	0.4135E-5	NLO	100000
ZToMuMu_NNPDF30_13TeV-powheg_M_4500_6500	4.56E-7	NLO	100000
aMC@nlo DY			
DYJetsToLL_Zpt-0To50_TuneCUETP8M1_13TeV-amcatnloFXFX-pythia8	5352.58	NLO	22782948
DYJetsToLL_Pt-50To100_TuneCUETP8M1_13TeV-amcatnloFXFX-pythia8	363.81	NLO	39612900
DYJetsToLL_Pt-100To250_TuneCUETP8M1_13TeV-amcatnloFXFX-pythia8	84.015	NLO	26998200
DYJetsToLL_Pt-250To400_TuneCUETP8M1_13TeV-amcatnloFXFX-pythia8	3.2283	NLO	7190820
DYJetsToLL_Pt-400To650_TuneCUETP8M1_13TeV-amcatnloFXFX-pythia8	0.43604	NLO	167272
DYJetsToLL_Pt-650ToInf_TuneCUETP8M1_13TeV-amcatnloFXFX-pythia8	0.04098	NLO	177101
Inclusive DY			
DYJetsToLL_M-50_TuneCUETP8M1_13TeV-amcatnloFXFX-pythia8	5765.4	LO	29082237
$\boldsymbol{t\bar{t}}$			
TTTo2L2Nu_TuneCUETP8M2_ttHtranche3_13TeV-powheg-pythia8	87.31	NNLO	79140880
TTToLL_MLL_500To800_TuneCUETP8M1_13TeV-powheg-pythia8	0.326	NNLO	200000
TTToLL_MLL_800To1200_TuneCUETP8M1_13TeV-powheg-pythia8	3.26E-2	NNLO	199800
TTToLL_MLL_1200To1800_TuneCUETP8M1_13TeV-powheg-pythia8	3.05E-3	NNLO	200000
TTToLL_MLL_1800ToInf_TuneCUETP8M1_13TeV-powheg-pythia8	1.74E-4	NNLO	40829
Single Top			
ST_tW_top_5f_inclusiveDecays_13TeV-powheg-pythia8_TuneCUETP8M1	35.6	NNLO	6952830
ST_tW_antitop_5f_inclusiveDecays_13TeV-powheg-pythia	35.6	NNLO	6933094
Di-bosons			
WWTo2L2Nu_13TeV-powheg	12.178	NNLO	1999000
WWTo2L2Nu_Mll_200To600_13TeV-powheg	1.386	NNLO	200000
WWTo2L2Nu_Mll_600To1200_13TeV-powheg	5.6665E-2	NNLO	200000
WWTo2L2Nu_Mll_1200To2500_13TeV-powheg	3.557E-3	NNLO	200000
WWTo2L2Nu_Mll_2500ToInf_13TeV-powheg	5.395E-5	NNLO	38969
WZ_TuneCUETP8M1_13TeV-pythia8	47.13	NLO	1000000
WZ_TuneCUETP8M1_13TeV-pythia8 (ext1)	47.13	NLO	2997571
ZZ_TuneCUETP8M1_13TeV-pythia8	16.523	NLO	990064
ZZ_TuneCUETP8M1_13TeV-pythia8 (ext1)	16.523	NLO	998034
W+lets			
WJetsToLNu_TuneCUETP8M1_13TeV-madgraphMLM-pythia8	61526	LO	29804825

Table 5.2: Summary of 2016 simulated background process samples used in this analysis.

2017 Process	σ (pb)	Order	Events
POWHEG DY			
ZToMuMu_NNPDF31_13TeV-powheg_M_50_120	2112.905	NLO	2961000
ZToMuMu_NNPDF31_13TeV-powheg_M_120_200	20.553	NLO	100000
ZToMuMu_NNPDF31_13TeV-powheg_M_200_400	2.886	NLO	100000
ZToMuMu_NNPDF31_13TeV-powheg_M_400_800	0.25126	NLO	100000
ZToMuMu_NNPDF31_13TeV-powheg_M_800_1400	0.01707	NLO	100000
ZToMuMu_NNPDF31_13TeV-powheg_M_1400_2300	1.366E-3	NLO	100000
ZToMuMu_NNPDF31_13TeV-powheg_M_2300_3500	8.178E-5	NLO	100000
ZToMuMu_NNPDF31_13TeV-powheg_M_3500_4500	3.191E-6	NLO	100000
ZToMuMu_NNPDF31_13TeV-powheg_M_4500_6500	2.787E-7	NLO	100000
Inclusive DY			
DYJetsToLL_M-50_TuneCP5_13TeV-amcatnloFXFX-pythia8	5765.4	LO	18574774
$t\bar{t}$			
TT_TuneCUETP8M2T4_13TeV-powheg-pythia8	831.76	NNLO	33844772
Single Top			
ST_tW_top_5f_inclusiveDecays_TuneCP5_13TeV-powheg-pythia8	35.6	NNLO	7581624
ST_tW_antitop_5f_inclusiveDecays_TuneCP5_13TeV-powheg-pythia8	35.6	NNLO	7780870
Di-bosons			
WW_TuneCP5_13TeV-pythia8	12.178	NNLO	7791498
WZ_TuneCP5_13TeV-pythia8	47.13	NLO	3928630
ZZ_TuneCP5_13TeV-pythia8	16.523	NLO	1949768

Table 5.3: Summary of 2017 simulated background process samples used in this analysis.

The dominant and irreducible SM background arises from Drell-Yan (DY) production ($Z/\gamma^* \rightarrow \mu^+\mu^-$): it is generated with POWHEG v2 from next-to-leading order (NLO) matrix elements using for 2016 the NNPDF3.0 PDFs and NNPDF3.1 [89] for 2017; parton showering and hadronization have been simulated with PYTHIA. All the DY binned in mass samples are multiplied by a k-factor to reach the NNLO precision.
The $t\bar{t}$, tW and WW backgrounds are simulated using POWHEG v2, with parton showering and hadronization described by PYTHIA. The NNPDF3.0 (NNPDF3.1) PDFs are used for all 2016 (2017) samples. The $t\bar{t}$ cross section is calculated at NNLO with TOP++ [90] assuming a top quark mass of 172.5 GeV. The inclusive diboson processes WZ, and ZZ are simulated using the PYTHIA program along with the associated PDFs. For 2016, for large dilepton mass values ($M_{\mu\mu}$), I have used $t\bar{t}$ and WW samples binned in $M_{\mu\mu}$: this allows to avoid large spikes at the large dimuon masses from these MC samples. The production of DY $\tau^+\tau^-$ and W+jets is simulated at LO with the MADGRAPH5 aMC@NLO version 2.2.2 program. The PDFs are evaluated using the LHAPDF library [91–93].
The detector response is simulated using the GEANT4 package.

5.2 HLT

Due to highest p_T with respect to the search for SM Higgs boson, for this analysis, in 2016, I have used as HLT path the OR between `HLT_Mu50` and `HLT_TkMu50`, that selects

single muons with $p_T > 50$ GeV in the pseudorapidity range $|\eta| < 2.4$: using the OR of these two trigger paths provides robustness to weaknesses from either path on its own. In 2017, `HLT_TkMu50` path has been integrated in the `HLT_Mu50` as part of a new algorithm.
Figure 5.1 shows HLT efficiency for 2016 and 2017 as a function of p_T. As can be seen,

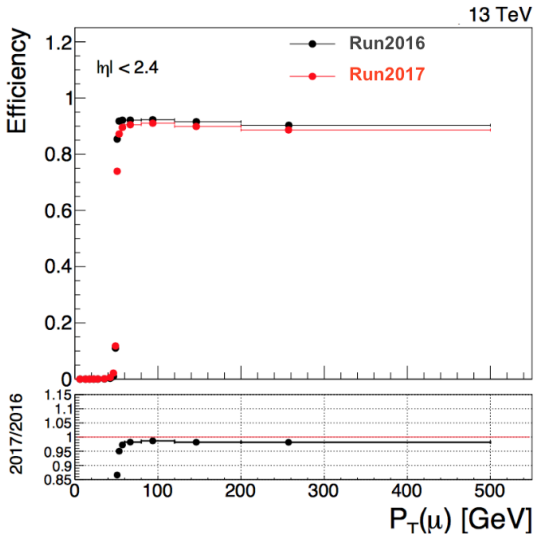

Figure 5.1: Single muon efficiency as a function of muon p_T: in black 2016 data, in red 2017. In the bottom panel, 2017/2016 ratio is reported.

2017 is less efficient than 2016 of about 2%; As precaution, I have decided to use in 2017 the OR among three paths: `HLT_Mu50`, `HLT_TkMu100` and `HLT_OldMu100`. Figure 5.2 shows the single muon efficiency for 2017 trigger as a function of muon p_T comparing different configuration: as can be seen, the OR recovers inefficiency with respect to the `HLT_Mu50` only.
The trigger dimuon efficiency is then computed separately: it is measured to be around 99.5% if both muons have $|\eta|$ <1.2 and 99.0% for events with one muon having $|\eta|$ >1.2. These efficiencies are validated using data relative to the full offline selection as a function of muon p_T and η. This is done using muons present in high mass dilepton or high-p_T Z boson events (free from background contributions) and other datasets (recorded by electron, missing transverse energy, or jet requirements). The measurements were found to be in agreement for muons with p_T up to 1.5 TeV and an uncertainty of 0.3% and 0.7% was chosen for the BB and BE category.

Z signal normalisation

Final results are evaluated normalising to the Z signal (see sec. 5.9): in order to collect enough events in the control region around the Z peak, the prescaled triggers

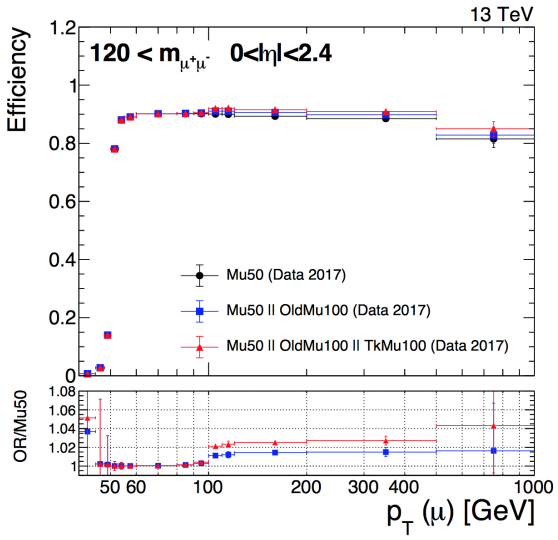

Figure 5.2: Single muon efficiency as a function of muon p_T for 2017 data, for different configurations. In the bottom panel, ratio plot for new OR paths over `HLT_Mu50` (Mu50).

`HLT_Mu(Tk)27` with a correspondingly reduced value of 30 GeV for the p_T cut for the offline muon are used. With `HLT_Mu(Tk)50` and the offline muon p_T at least 53 GeV, the number of the Z events would be reduced by roughly two orders of magnitude and would give a different kinematics than the original Z production, leading to a problem with systematic uncertainties of the procedure.
`HLT_Mu(Tk)27` had different values of prescale factors at different runs and luminosity sections during the data taking. In order to enlarge the statistics at the Z peak which is used for the Z-peak normalisation, the whole sample was divided into sub-samples with different prescale factors and different integrated luminosity for each η category (see Table 5.4). The mean `HLT_Mu27` prescale rate in data was found to be 1/167.737 [1].

5.3 Muon reconstruction

5.3.1 Reconstruction efficiency

Reconstruction efficiency as a function of the muon momentum has been measured using Tag and Probe technique (TnP). This technique utilises a known mass resonance (e.g. J/Ψ, Z) to select particles of the desired type, and probe the efficiency of a particular selection criterion on those particles. In general the "tag" is an object that passes a set of very tight selection criteria designed to isolate the required particle type. A generic set of the desired particle type (i.e. with potentially very loose selection criteria) known as "probes" is selected by pairing these objects with tags such that the invariant mass of the

[1] 2017 results are obtained from 2016 scaling by luminosity

Prescale factor	Int. lumi, pb^{-1}	Ratio Data / MC for 60< m_{ll} <120 GeV		
		All	**BB**	**BE + EE**
14	11	0.9573 ± 0.0490	0.9484 ± 0.0755	0.9637 ± 0.0645
35	59	1.0383 ± 0.0344	0.9934 ± 0.0521	1.0708 ± 0.0459
40	48	0.9500 ± 0.0391	0.9486 ± 0.0604	0.9511 ± 0.0513
70	1455	0.9738 ± 0.0096	0.9639 ± 0.0147	0.9812 ± 0.0126
100	7065	0.9809 ± 0.0052	0.9807 ± 0.0080	0.9815 ± 0.0068
120	479	0.9890 ± 0.0220	0.9995 ± 0.0342	0.9822 ± 0.0288
140	4516	0.9864 ± 0.0077	0.9850 ± 0.0118	0.9883 ± 0.0101
150	4828	0.9428 ± 0.0075	0.9370 ± 0.0116	0.9479 ± 0.0099
160	2738	0.9856 ± 0.0105	0.9931 ± 0.0163	0.9811 ± 0.0138
170	3081	0.9187 ± 0.0099	0.9471 ± 0.0155	0.8993 ± 0.0128
180	518	1.0002 ± 0.0261	1.0209 ± 0.0407	0.9865 ± 0.0340
200	3719	0.9327 ± 0.0098	0.9408 ± 0.0152	0.9280 ± 0.0128
230	3299	0.9479 ± 0.0112	0.9696 ± 0.0176	0.9337 ± 0.0146
250	1010	0.9510 ± 0.0214	0.9794 ± 0.0335	0.9321 ± 0.0277
260	2345	0.9447 ± 0.0141	0.9857 ± 0.0223	0.9168 ± 0.0183
290	1828	0.9481 ± 0.0169	0.9556 ± 0.0263	0.9446 ± 0.0222
320	196	0.9387 ± 0.0540	0.9145 ± 0.0825	0.9581 ± 0.0716
320	196	0.9387 ± 0.0540	0.9145 ± 0.0825	0.9581 ± 0.0716
Combined	36295	0.9638 ± 0.002	0.9688 ± 0.0042	0.9610 ± 0.0035

Table 5.4: Integrated luminosities for different prescale factors of prescaled triggers `HLT_(Tk)Mu27` for different categories. Values for ratio Data / MC in the range 60< m_{ll} <120 GeV used to normalise dimuon mass distribution are also reported for different categories.

combination is consistent with the mass of the resonance. Combinatoric backgrounds may be eliminated through any of a variety of background subtraction methods such as fitting, or sideband subtraction. The definition of the probe object depends on the specifics of the selection criterion being examined. The efficiency itself is measured by counting the number of "probe" particles that pass the desired selection criteria.
In this particular case, the tag and the probe muons are required to have opposite charge and a geometrical separation of $\Delta R > 0.6$ and reconstructed mass above 70 GeV. To ensure the origin of both muons from a common vertex, I have applied a cut on the common vertex of the two muons, χ^2 /ndf < 20 and on the transverse impact parameter (|tag $dz(BS)-$ probe $dz(BS)| < 0.05$ cm). The three-dimensional angle between muons momenta is required to be $< \pi - 0.02$ radiant to suppress cosmic muons. The tag muon is required to fire the trigger and to satisfy the analysis cuts defined in sec. 5.4. The probe muon is selected as a Tracker Muon satisfying the following criteria:

- p_T(innerTrk) > 50 GeV and $|\eta$(innerTrk)$| < 2.4$
- at least one pixel hit and at least six tracker layers
- $|dxy(BS)| < 0.2$ cm and $|dz(PV)| < 0.5$ cm

In addition to these cuts, both the tag and the probe are required to be isolated (relative tracker isolation < 0.05 and absolute tracker isolation < 15 GeV), and to have a relative p_T error $\delta p_T/p_T(\text{innerTrk}) < 0.5$. The probe muon is then used to calculate the efficiency of the muon reconstruction and of the muonic part of the muon identification. This has been calculated as the fraction of the probes passing the following cuts with respect to the selected probes:

- the muon has to be reconstruct as "Global"
- the global muon track fit must include at least one hit from the muon system
- the tracker muon must be matched to segments in at least one muon station if the muon station is not on the first layer of the muon system, or if matched to one muon station on the first layer also require that the muon matches to more than two RPC layers, or that the muon is matched in at least two muon stations.
- $\delta p_T/p_T(TuneP_{Trk}) < 0.3$

Figure 5.3 shows the reconstruction and identification efficiency as a function of the muon momentum in several η regions, fit with a first degree polynomial, for data and MC. The efficiency in barrel, overlap and endcap up to 1.6 shows a slight decreasing trend in both data (red points) and MC (black points). This trend is well described by a first degree polynomial, especially in the MC where there is enough statistics to perform a stable fit up to very high momentum. The same effect, but much more enhanced, is observed in the forward endcap (forth plot). A decreasing trend according to the muon momentum is caused by the electromagnetic shower. Given the very similar results, the barrel and the endcap up to eta 1.6 have been merged, in order to get more statistics and a more reliable fit.
The efficiency evaluated above can be factorised as follow:

$$Eff_{MuonRecoID} = Eff_{Reco} \times Eff_{Global} \times Eff_{MuonID} \tag{5.1}$$

where the Reco efficiency is calculated as the fraction of the probes reconstructed as Standalone with respect to all the probes (tracker muons); the Global efficiency is calculated as the fraction of the probes reconstructed as Global with respect to those probes passing also the Standalone; and the MuonID efficiency is calculated as the fraction of the probes passing the muonic cuts of the high-p_T identification with respect to those probes which are also Global. Figure 5.4 shown the factorised efficiency: the slope visible in Figure 5.3 is due to the reconstruction component, while there is only a tiny contribution from the MuonID which comes from the cut on the valid hits in the muon system. Figure 5.5 shows scale factors (SFs), for $|\eta|$ up to 1.6 and for $|\eta|$ above this value, varying with the muon momentum, introduced to take into account differences in data and simulation efficiencies and used to estimate the associated systematic uncertainties.

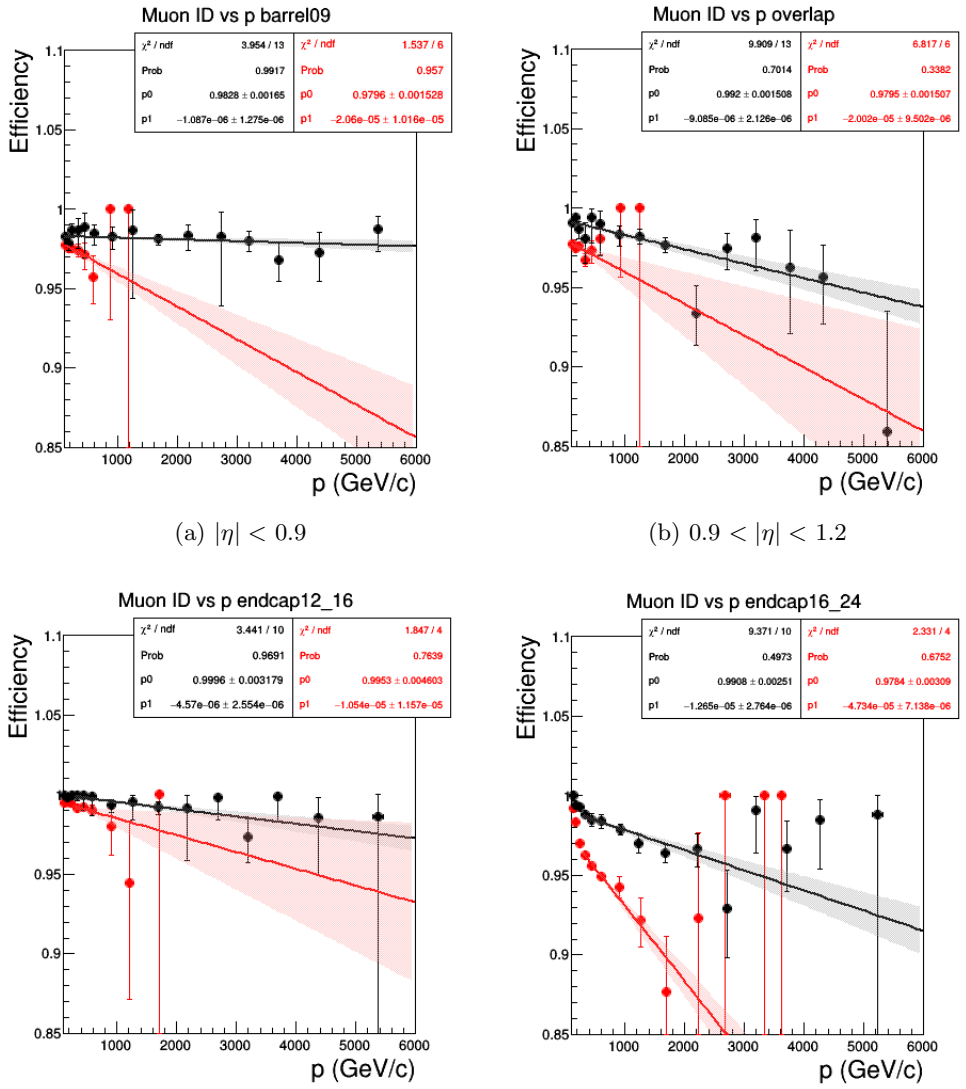

(a) $|\eta| < 0.9$

(b) $0.9 < |\eta| < 1.2$

(c) $1.2 < |\eta| < 1.6$

(d) $[1.6 < |\eta| < 2.4$

Figure 5.3: Muon reconstruction and identification efficiency as a function of muon momentum in different $|\eta|$ regions: barrel up to 0.9 (top left), overlap from 0.9 to 1.2 (top right), endcap from 1.2 to 1.6 (bottom left), and endcap from 1.6 to 2.4 (bottom right). The red points represent 2016 data, while the black points represent the MC. Both distributions are interpolated by a first degree polynomial.

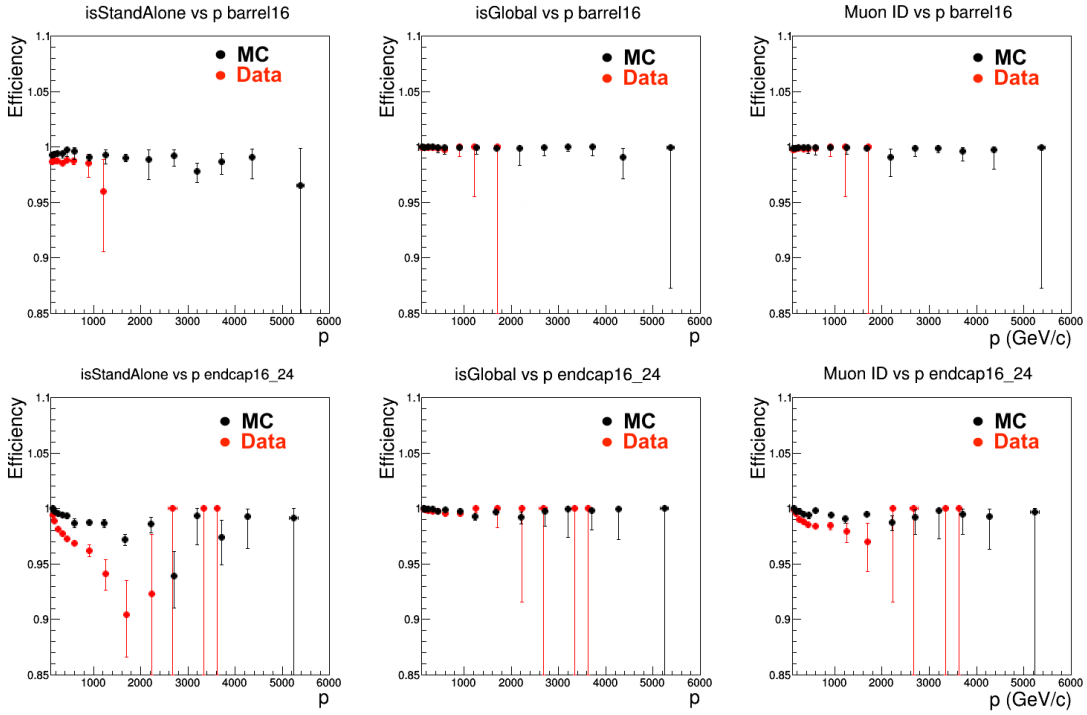

Figure 5.4: Factorised muon reconstruction and identification efficiency as a function of muon momentum in barrel up to 1.6 (top row) and endcap between 1.6 and 2.4 (bottom row): the red points represent 2016 data, while the black points represent the MC. The pure Standalone reconstruction efficiency is plotted on the left, the Global reconstruction efficiency calculated with respect to the probes passing also the Standalone is plotted in the middle, and the MuonID efficiency calculated with respect to the probes passing the Global reconstruction is plotted on the right.

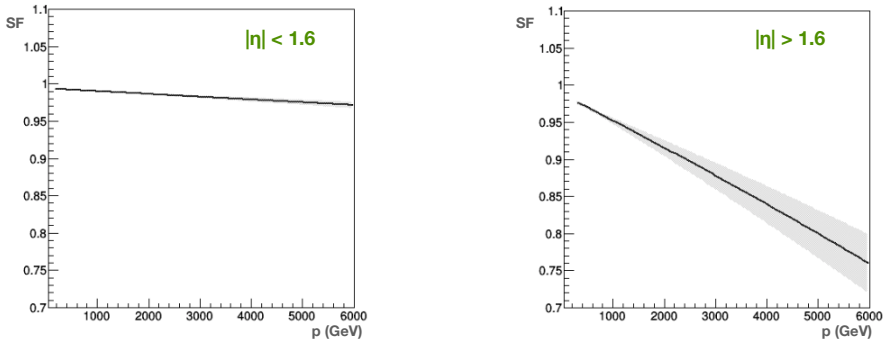

Figure 5.5: SFs, as a function of muon momentum, used to estimate the systematic uncertainty for two $|\eta|$ categories: $|\eta|$ <1.6 on the left, $|\eta|$ >1.6 on the right.

Reconstruction efficiency using 2017 datasets

Reconstruction efficiency in 2016 has been compared to the one evaluated in 2017. Figure 5.6 shows reconstruction efficiency as a function of muon p_T comparing 2016 and 2017: there is a good agreement within statistical errors.

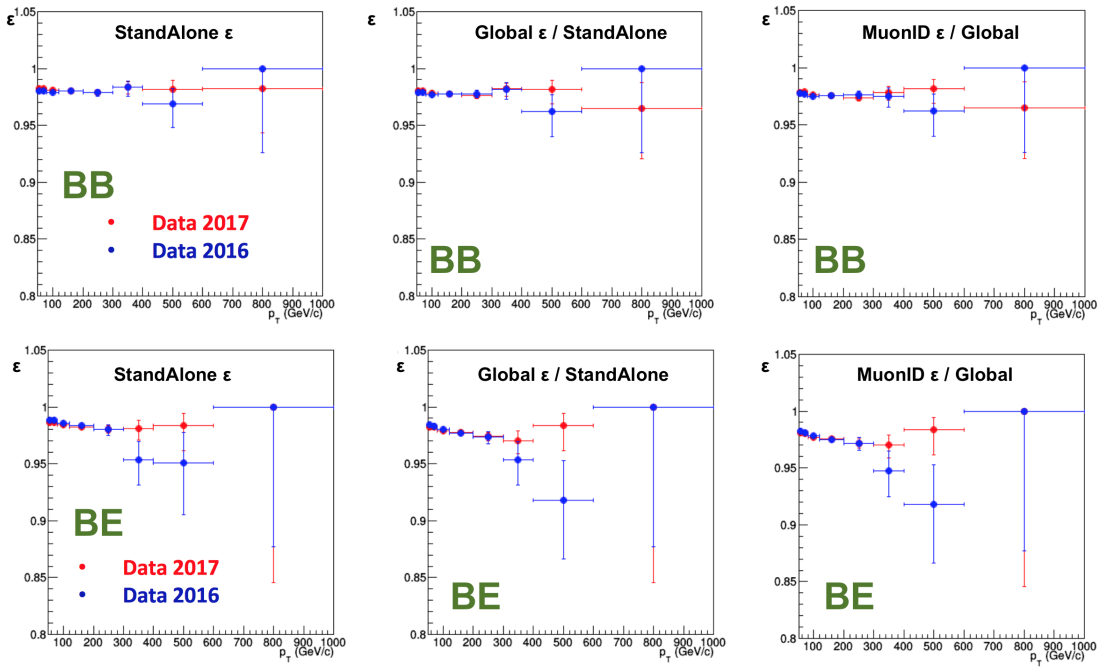

Figure 5.6: Factorised muon reconstruction and identification efficiency as a function of muon p_T in BB (top row) and BE (bottom row) category: the red points represent 2017 data, while the blue ones stand for 2016 data. The pure Standalone reconstruction efficiency is plotted on the left, the Global reconstruction efficiency calculated with respect to the probes passing also the Standalone is plotted in the middle, and the MuonID efficiency calculated with respect to the probes passing the Global reconstruction is plotted on the right.

5.4 Muon selection

In this analysis the high-p_T muon identification (High p_T ID), described in section 3.6.3, is used to select muon candidates. The main goal of the High p_T ID is to maintain a high efficiency for the muon candidate selection over a wide energy range, while remaining independent of the number of primary vertices. The High p_T ID selection criteria are listed in detail in the following:

- a good offline-reconstructed primary vertex (PV): at least four tracks must be associated to the vertex and the vertex must be located within $|r| < 2$ cm and

$|z| < 24$ cm of the nominal interaction point (IP)[2]. This cut has been established to ensure the quality of the hadronic collisions and discard detection of particles produced between beam particles and residuals present in the imperfect vacuum of LHC. On top of that, this cut allows to reject cosmic ray muons triggering in empty bunch-crossings, which can produce fake dimuons when traversing the detector near the IP.

- the muon must be reconstructed as a global muon and a tracker muon (see sec. 3.6.1).
- the offline muon p_T must be at least 53 GeV, to be in the plateau of the single-muon trigger efficiency (see Figure 5.1)
- the relative p_T error (δp_T / p_T) is required to be smaller than 0.3, to suppress grossly mismeasured muon tracks and especially ensure the quality of the p_T measurement.
- the muon's transverse impact parameter with respect to the primary vertex, as measured by the tracker-only fit, must be less than 0.2 cm.
- the muon must pass a relative tracker-only isolation cut: the scalar sum of the p_T of all other tracks in a cone of $\Delta R = \sqrt{\Delta\eta^2 + \Delta\phi^2} < 0.3$ around but not including the muon's tracker track must be less than 10% of the muon's p_T, also as measured by the tracker. To be used in the calculation of the tracker isolation, tracks have to be within $\Delta z = 0.2$ cm of the primary vertex with which the muon candidate is associated.
- the global muon track must have at least 6 tracker layers with hits in the fit.
- the global muon track fit must include at least one hit from each of the pixel detector and the muon system.
- the tracker muon must be matched to segments in at least one muon station if the muon station is not on the first layer of the muon system, or if matched to one muon station on the first layer also require that the muon matches to more than two RPC layers, or that the muon is matched in at least two muon stations.

To form a dimuon candidate, two muons of opposite charge passing the above selection have been considered. A fit to a common vertex (using the Kalman filter formulation) has been performed to compute the kinematics of the dimuon system, particularly its invariant mass. This also serves to ensure that the two muons originate from the same vertex, as a safety check against pile-up and as a check on reconstruction quality (χ^2 /ndf. < 20). To reduce the background from cosmic ray muons that are in-time with a collision event and pass the primary vertex and impact parameter cuts, the three-dimensional angle between the two muons' momenta must be less than π - 0.02 rad.
In events with more than one opposite-sign dimuon, I select the dimuon event closest to

[2]The nominal IP is the design position of the IP

Z mass in the window $70 < M_{\mu\mu} < 110$ GeV if it exist, otherwise the one with highest p_T sum between the muons.

5.4.1 Muon ID efficiency

The efficiencies of the muon selection requirements and isolation described above are measured with the TnP method, in data and in simulation (using only DY events). The ID efficiency as a function of p_T, η and ϕ is shown in Figure 5.7 and Figure 5.8. The drops observed in Figure 5.8 around $|\phi| = 1.5$ are compatible with the gaps formed when the BPix layer was inserted in 2015. The SFs between data and MC, used to estimate the associated systematic uncertainties, are shown as a function of p_T in Figure 5.9.

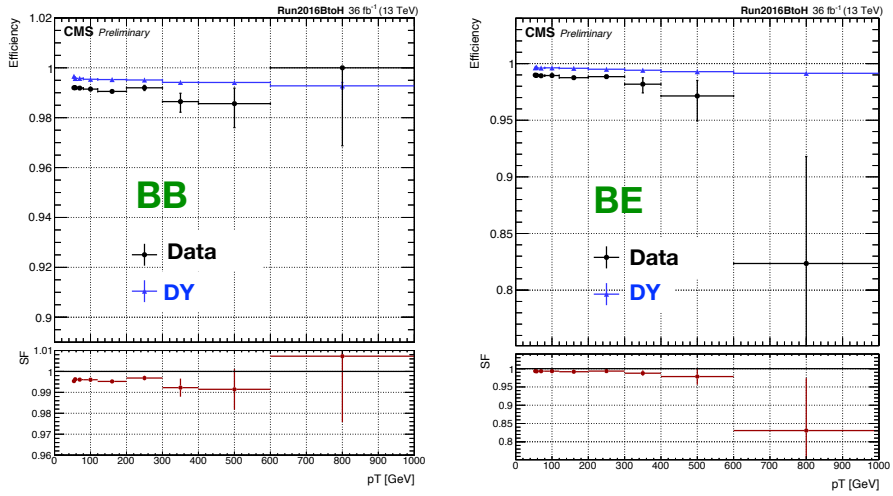

Figure 5.7: The ID efficiency as measured using TuneP for 2016 Run as a function of muon p_T for BB (left) and BE (right) categories. MC is in blue while data are black dots. In the bottom panel, data/MC ratio (SF) is reported.

5.4.2 Selection efficiency

Once the baseline selection has been set, I have also checked the N-1 efficiency for each cut to have a better idea on how the cuts work in data and simulations. N-1 efficiency is calculated as the ratio of the number of events that pass all the selection cuts to the number of events passing all the cuts but the one of interest. Figure 5.10 shows the 2016

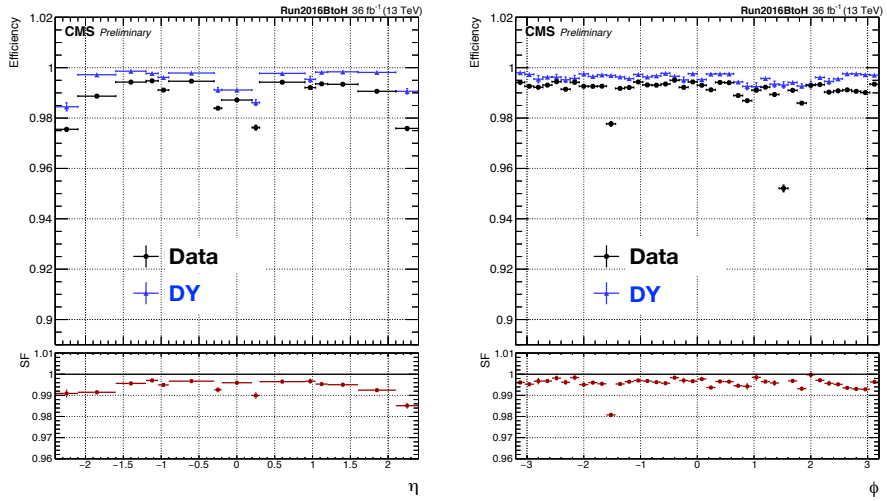

Figure 5.8: The ID efficiency as measured using TuneP for 2016 Run as a function of muon η (left) and muon ϕ (right). MC is in blue while data are black dots. In the bottom panel, data/MC ratio (SF) is reported.

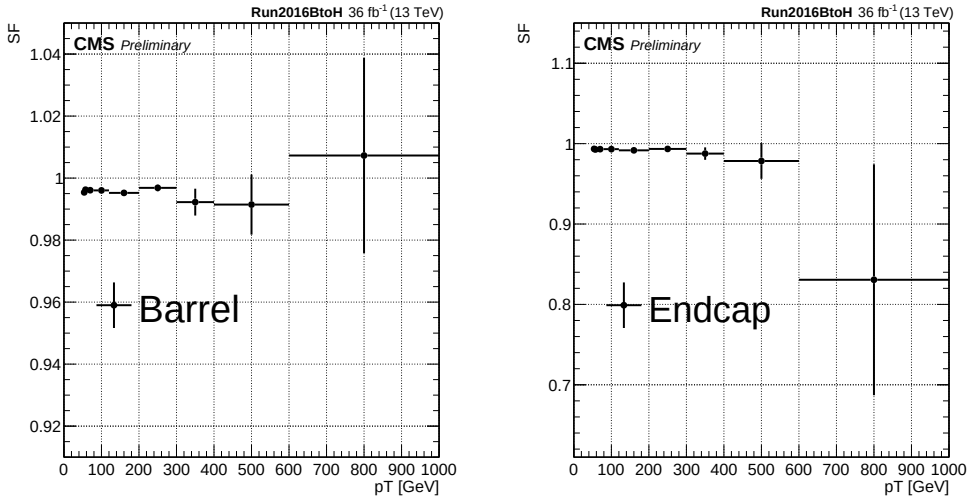

Figure 5.9: The ID muon efficiency SFs for 2016 data as a function of muon p_T for BB (left) and BE (right).

N-1 efficiencies for all cuts as obtained in data and MC for two different dimuon mass ranges:

- $60 < M_{\mu\mu} < 120$GeV
- $M_{\mu\mu} > 120$GeV

Same plots, done for the two η categories (BB and BE) are reported in Figure 5.11 and 5.12. The first mass range, around the Z peak, refers to a well known physics region and is used to check unexpected effects. There is a good agreement between data and simulation for all cuts except for the isolation: the drop in data efficiency is due to multijets events that are instead not considered in MC, since their contribution is evaluated with a data driven technique (see sec. 5.5.3)
In Figure 5.13 are reported the N-1 efficiencies as a function of dimuon mass, evaluated with 2016 data and compared with 2017 data, for different cuts. As can be seen, due to the upgrade of the tracker system, the efficiency for the cut on pixel hits and tracker layers is improved in 2017.

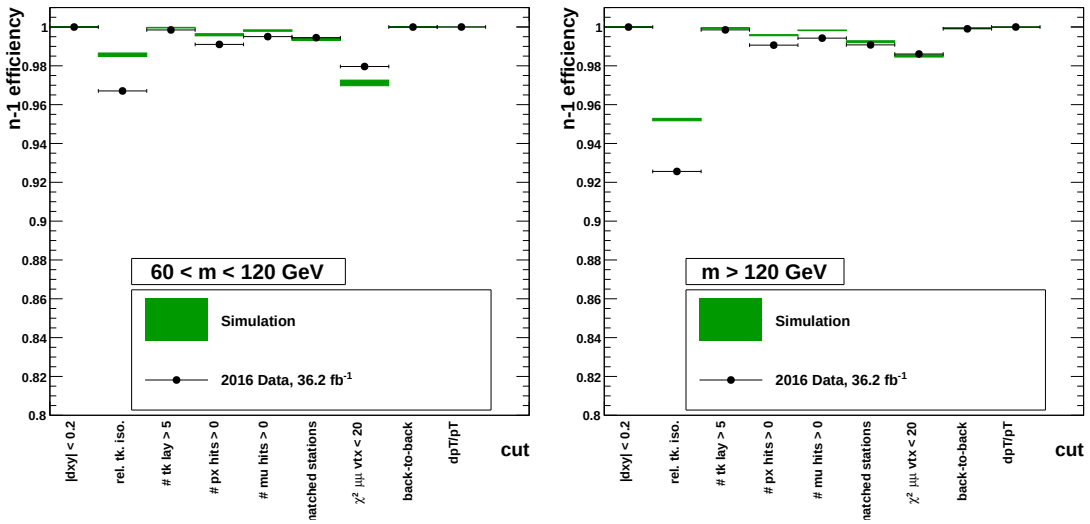

Figure 5.10: The ratio of the number of events that pass all selection cuts to the number of events passing all cuts but the one indicated, for the regions: $60 < M_{\mu\mu} < 120$ GeV (left) and $M_{\mu\mu} > 120$ GeV (right). Here "Simulation" includes all the backgrounds.

5.5 Background estimation

The main background of this analysis is related to dimuon events from DY production; at large dimuon mass the contribution from electroweak processes is not resonant but it is a continuum with a long tail. Events from $t\bar{t}$, tW, and di-bosons (WW,WZ and ZZ)

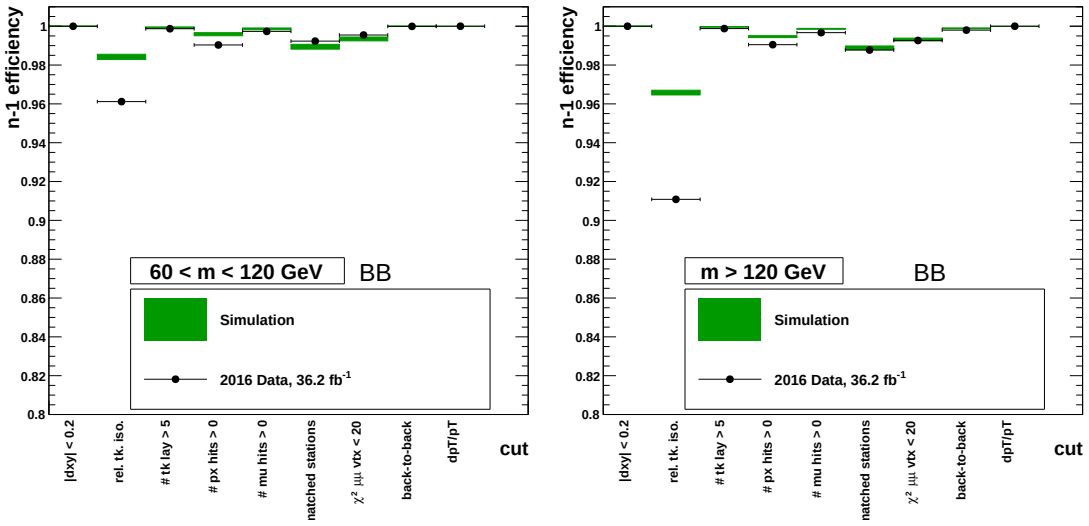

Figure 5.11: The ratio of the number of events that pass all selection cuts to the number of events passing all cuts but the one indicated, for BB category: $60 < M_{\mu\mu} < 120$ GeV (left) and $M_{\mu\mu} > 120$ GeV (right). Here "Simulation" includes all the backgrounds.

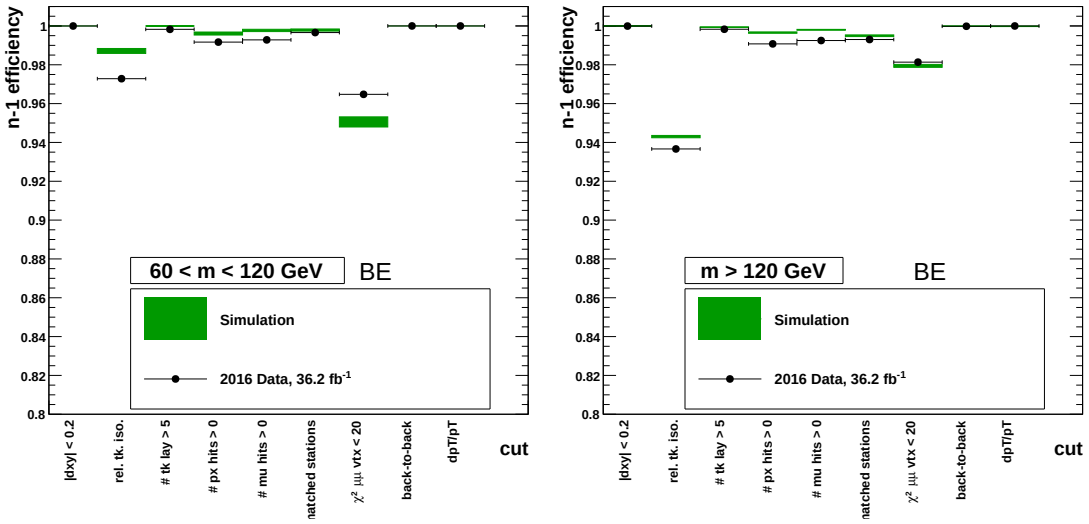

Figure 5.12: The ratio of the number of events that pass all selection cuts to the number of events passing all cuts but the one indicated, for BE category: $60 < M_{\mu\mu} < 120$ GeV (left) and $M_{\mu\mu} > 120$ GeV (right). Here "Simulation" includes all the backgrounds.

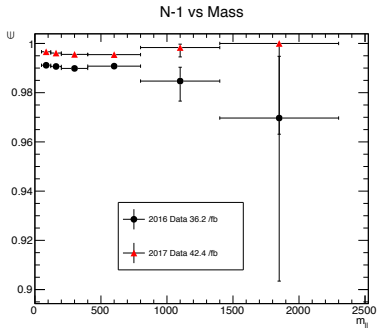

(a) Pixel hits

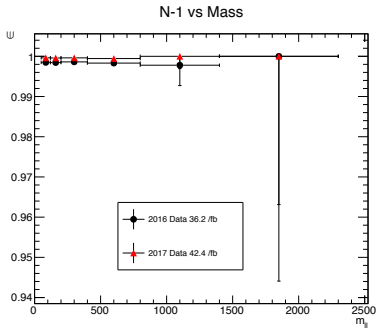

(b) Tracker layers

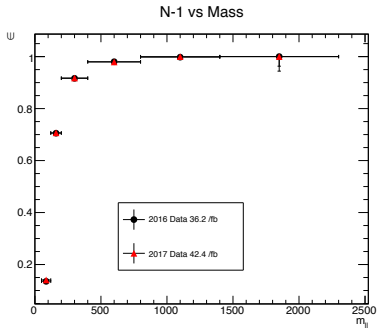

(c) p_T

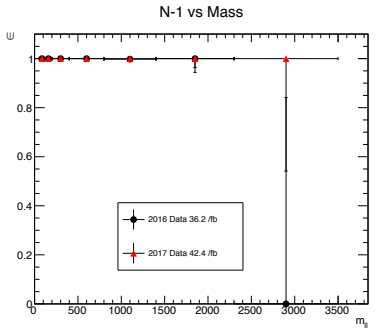

(d) $\delta p_T/p_T$

Figure 5.13: N-1 efficiency as a function of dimuon mass, for different cut, comparing 2016 data (black dots) with 2017 (red triangle): number of Pixel hits and tracker layers on top, p_T and $\delta p_T/p_T$ on bottom.

provide prompt dimuon contributing over the full dimuon invariant mass spectrum. Non-prompt leptons from b-jets and mis-identified leptons can also originate in $t\bar{t}$, W+jets and multi-jets QCD events.

5.5.1 Drell-Yan and Photon-induced background

DY samples used in this analysis are done with POWHEG at NLO in QCD and include the QED effects (initial and final state radiation), but not the quite important at high mass pure electroweak effects and the photon induced contributions (PI) in which $\gamma - \gamma$ collisions (where photons radiated by the incoming protons collide) can produce lepton pairs. In order to convert DY POWHEG samples to FEWZ [95] predictions that instead include all effects (NNLO+PI), a mass-dependent correction must be measured.
The ratio of DY + PI background with FEWZ to DY background with POWHEG ($R_{\mathrm{FEWZ\,/\,POWHEG}}$) is shown in Figure 5.14. The function extracted from the fit is the k factor, depending on the mass and used to correct DY POWHEG samples. It is parametrised as

$$R_{\mathrm{FEWZ\,/\,POWHEG}} = a + b \cdot m + c \cdot m^2 + d \cdot m^3 \tag{5.2}$$

with following values for the parameters for the inclusive category:

$$a = 1.067, \qquad b = -0.000112, \qquad c = 3.176 \cdot 10^{-8}, \qquad d = -4.068 \cdot 10^{-12}\,.$$

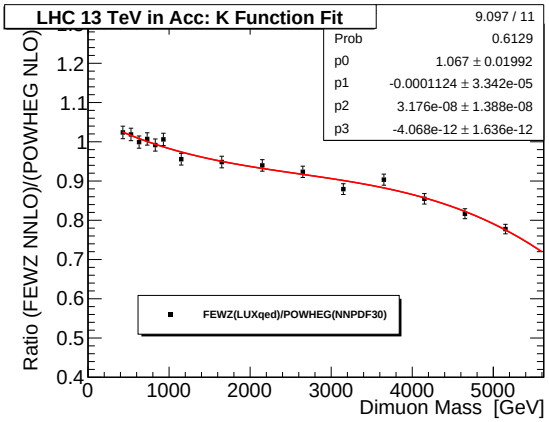

Figure 5.14: Ratio of dimuon cross section computed with FEWZ (including NNLO and PI effects) and POWHEG (as used in the analysis) with the fit function used for the k factor.

For BB and BE categories the k factors used are instead parametrised as:

$$K_{\mathrm{BB}} = 1.036 - 0.0001441\,X + 5.058 \cdot 10^{-8} X^2 - 7.581 \cdot 10^{-12} X^3\,,$$

$$K_{\mathrm{BE}} = 1.052 - 0.0001471\,X + 5.903 \cdot 10^{-8} X^2 - 9.037 \cdot 10^{-12} X^3\,,$$

where $X = Mass - 400$ GeV.

5.5.2 TTbar estimation

The largest background contributing to the dimuon invariant mass spectrum, following the DY production, comes from $t\bar{t}$ decays that could give two or more leptons in the final state including also two b-jets. The idea is to calculate the scale factor between the data and the simulation predictions for different mass ranges, once the DY contribution is removed. The corresponding invariant mass distribution is shown in Figure 5.15: the agreement between data and simulation is good and this proves the goodness of $t\bar{t}$ samples in representing data.

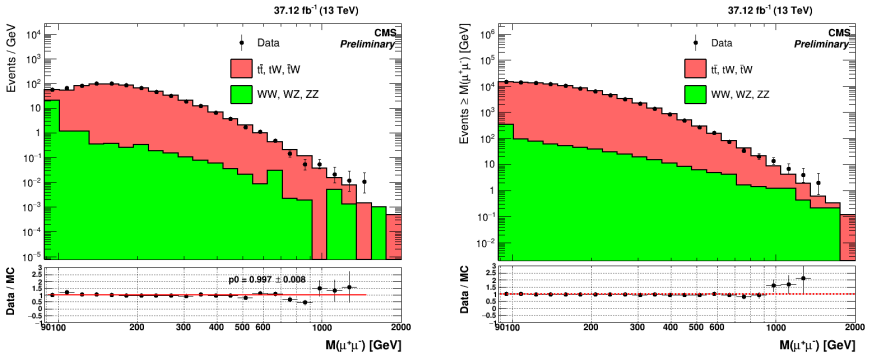

Figure 5.15: Observed opposite-sign dimuon invariant mass spectrum (right is cumulative one) obtained from data after subtraction of DY MC. High p_T muon criteria, with $70 < M_{\mu\mu} < 2000$ GeV and in addition two b-jets are required.

5.5.3 Multijets

Another contribution to the background in the dimuon invariant mass spectrum is due to objects mis-identified as prompt muons passing the entire selection chain, hereafter referred as "fake" muons. This contribution has been estimated using a data-driven technique due to difficulties in simulating this process: the idea is to measure, in a control region, the "fake rate" (FR), that is the probability that a fakeable object passes the high-p_T muon selection used for the current analysis and then use these FR to reweigh the events in order to extrapolate the contribution from "fakes" in the signal region.
The control region is defined by selecting the events firing the trigger and requiring that the muons satisfy the cuts reported in Table 5.5. The phase space so defined is used to measure the FR as the ratio between the number of muons passing the high-p_T muon ID and isolation selection (see sec. 5.4) and those passing the selection cuts reported in Table 5.5. As example, Figure 5.16 and 5.17 show FR distribution evaluated from 2016 data in BB and BE category respectively, with a fit function in different p_T ranges.

The final contribution is determined by applying the FR measured from data to both a real data samples and simulated events selected with two muons both failing to pass the high-p_T muon ID and the isolation requirements while passing the selection defining

variable	cut value
is GlobalMu and is TrackerMu	true
$\lvert d_z \rvert$	< 1.0
$\lvert d_{xy} \rvert$	< 0.2
Nb. of Tracker Layers with Measurement	> 5
Nb. of Valid Pixel Hits	> 0
Matching with HLT object (Mu50 || TkMu50)	true

Table 5.5: The selection requirements to define the control region for the fake rate calculation.

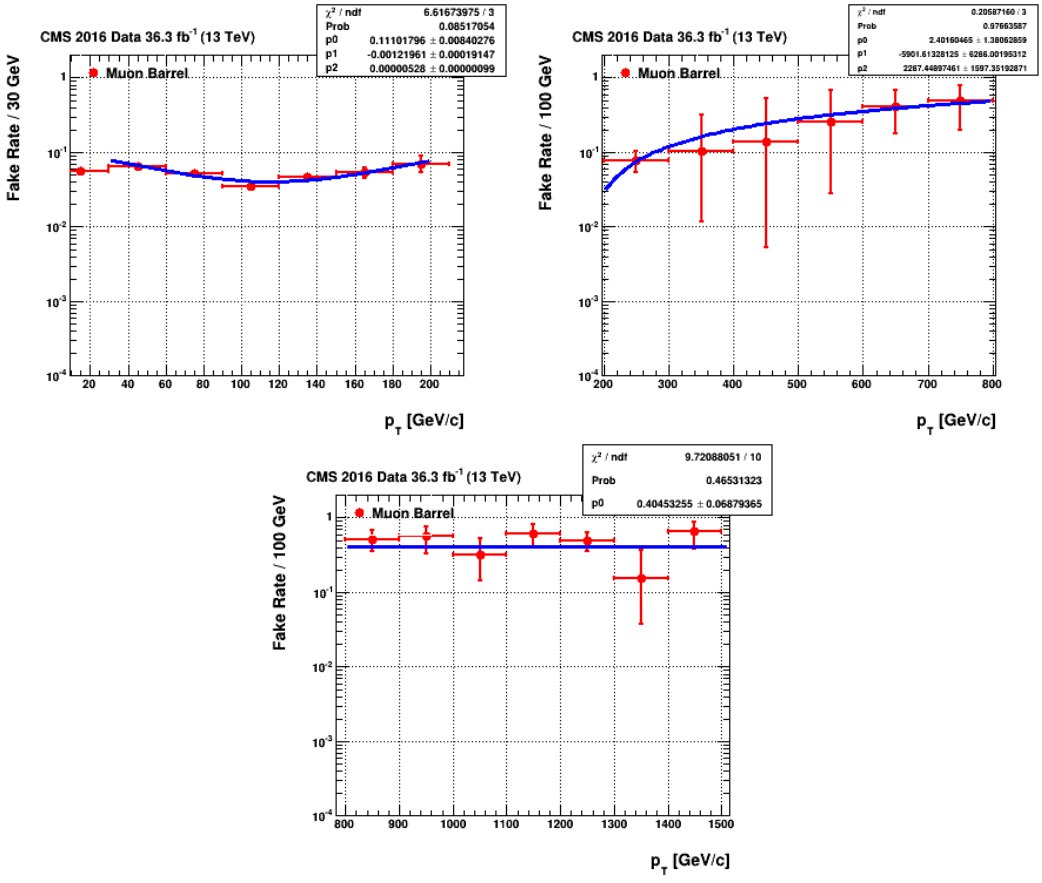

Figure 5.16: FR vs p_T in BB category, for three p_T ranges; $p_T < 200$ GeV (top left), $200 < p_T < 800$ GeV (top right) and for $p_T > 800$ GeV (bottom).

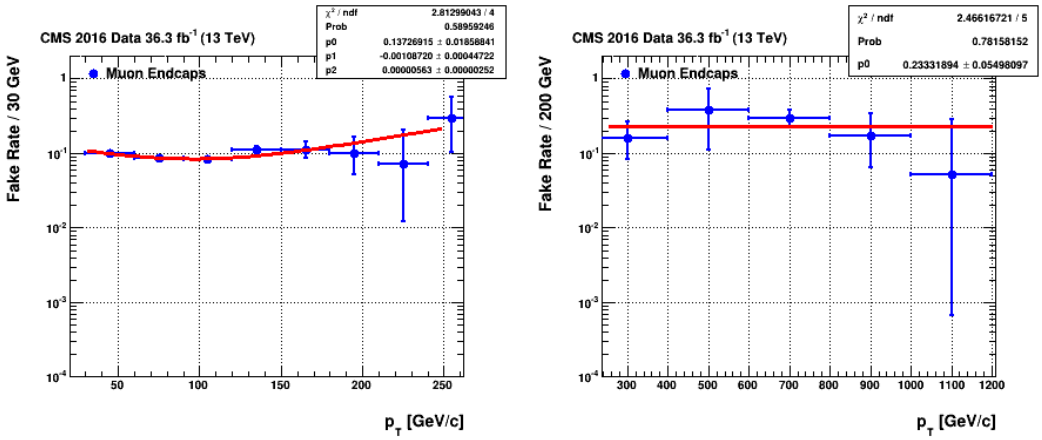

Figure 5.17: FR vs p_T in BE category, for two p_T ranges; $p_T < 250$ GeV (left) and for $p_T > 250$ GeV (right).

the control region. As a result, each event selected in that way is then weighted by a factor FR/(1 - FR) for each muon with a given p_T and η; so the factor is applied two times in order to estimate the contribution of dimuon from "fakes" (di-jets contributions). The distribution of the dimuon invariant mass reweighted in this way provides the expected dimuon contribution from "fakes", once the contribution from all the electroweak processes, is subtracted. In some events, one muon passes the high-p_T muon ID and isolation requirements and a second one fail them while passing the control region selection; these events are then weighted by FR/(1 - FR) once.

5.6 Background shape

The background shape is obtained adding all the backgrounds; its parametrisation is determined by the fit of the simulated dimuon mass spectrum using the following function.

$$f_{bkg}(m \mid a_L, b_L, c_L, k_L, a_H, b_H, c_H, d_H, k_H) = \begin{cases} e^{a_L + b_L \times m + c_L \times m^2} m^{k_L}, & \text{if } m \leq 500 \text{ GeV} \\ e^{a_H + b_H \times m + c_H \times m^2 + d_H \times m^3} m^{k_H}, & \text{if } m > 500 \text{ GeV} \end{cases} \tag{5.3}$$

I have performed the fit in the mass range 150-5000 GeV for every pseudorapidity category. Splitting function in two mass ranges, led to better fit the tail of the distribution, with a good agreement also in the low mass region. In Figure 5.18 and 5.19 are shown the fits and the residuals of the background shape, for both the categories.
The same function (5.3) has been used also to fit 2017 background shape, as can be seen in Figure 5.20.

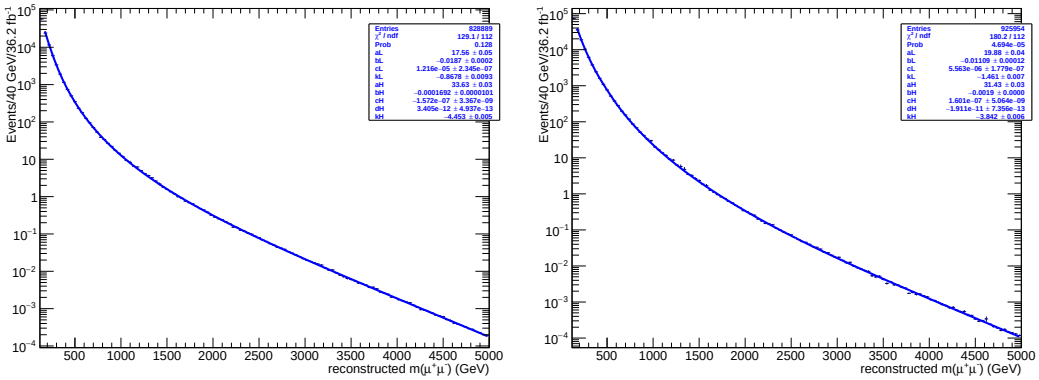

Figure 5.18: Fit of the 2016 background shape for different η categories: BB category on the left, BE category on the right.

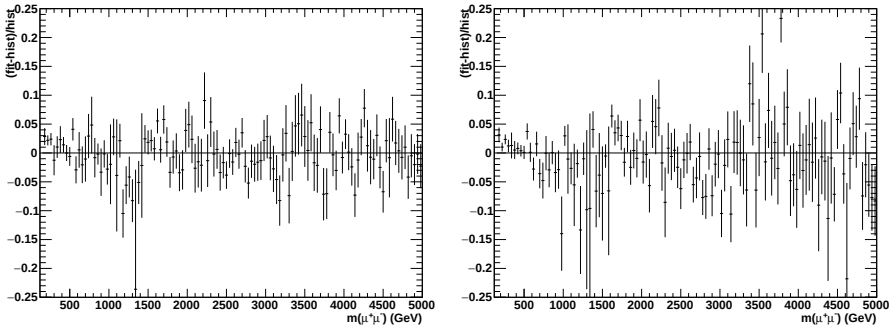

Figure 5.19: Residual of the 2016 fits for different η categories: BB category on the left, BE category on the right.

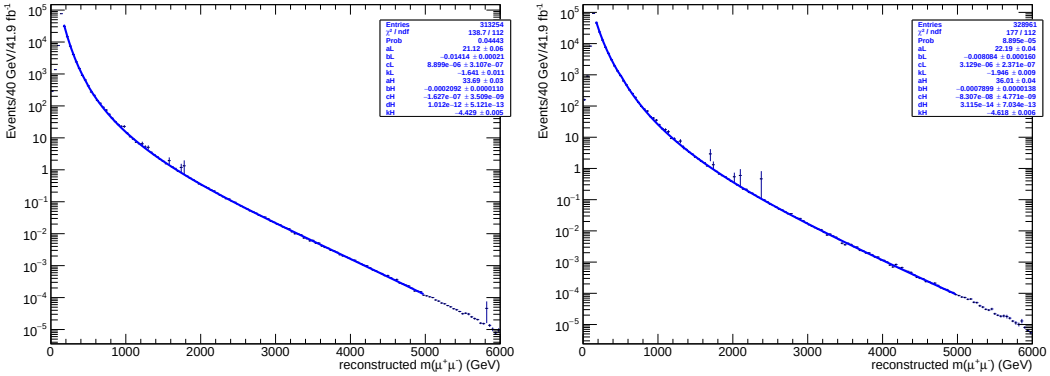

Figure 5.20: Fit of the 2017 background shape for different η categories: BB category on the left, BE category on the right.

5.7 Dimuon mass and Data-MC comparison

In Figure 5.21 the comparison between data and simulation for the dimuon invariant mass spectrum over the full pseudorapidity range, in 2016 and 2017, is shown. No evidence for a signal deviation from the SM expectations is observed. In Figure 5.22 and 5.23 invariant mass plots distributions for different categories of pseudorapidity are shown, with the different backgrounds highlighted.
The MC simulated events for all processes are normalised such that the total background prediction agrees with the data in the mass region around Z peak.

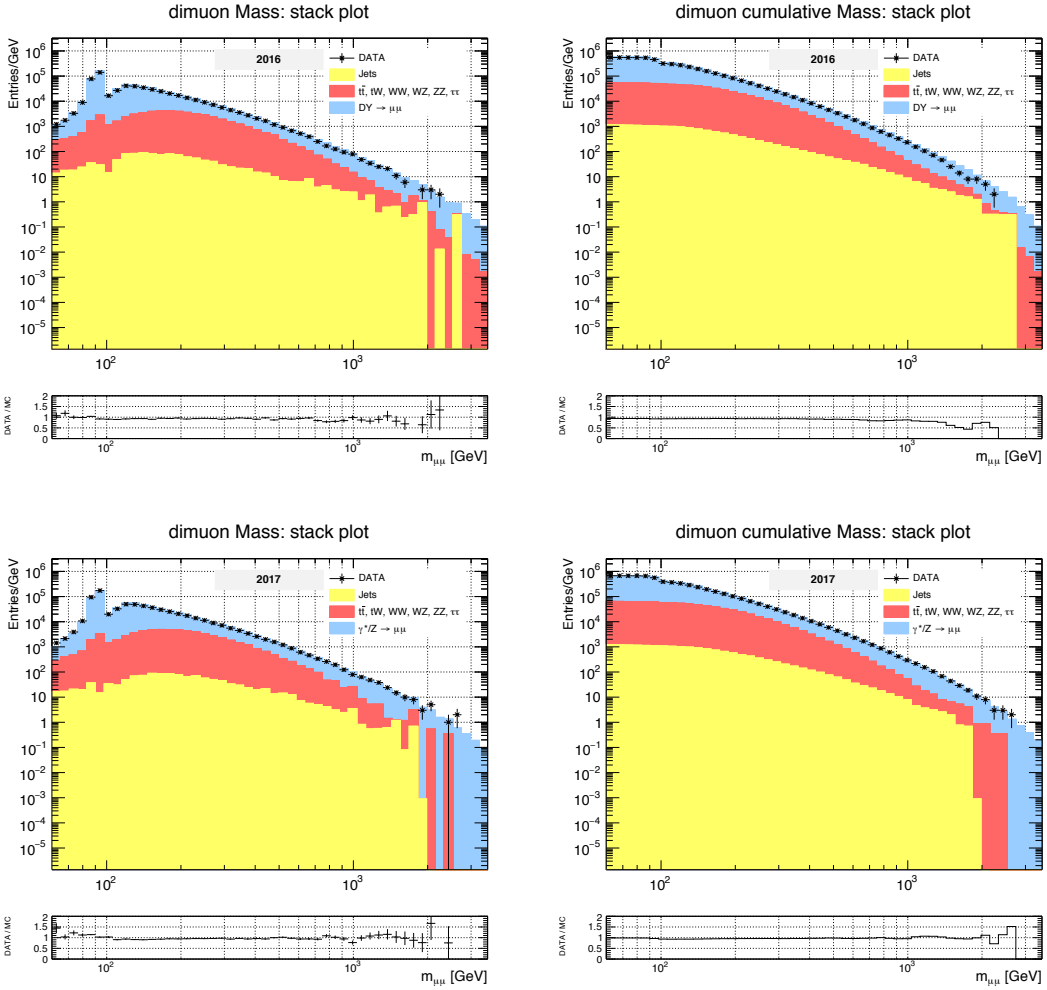

Figure 5.21: The observed invariant mass spectra for 2016 (on top) and 2017 (on bottom), together with the predicted SM backgrounds (on the right the cumulative one). In the bottom panel, data/MC ratio.

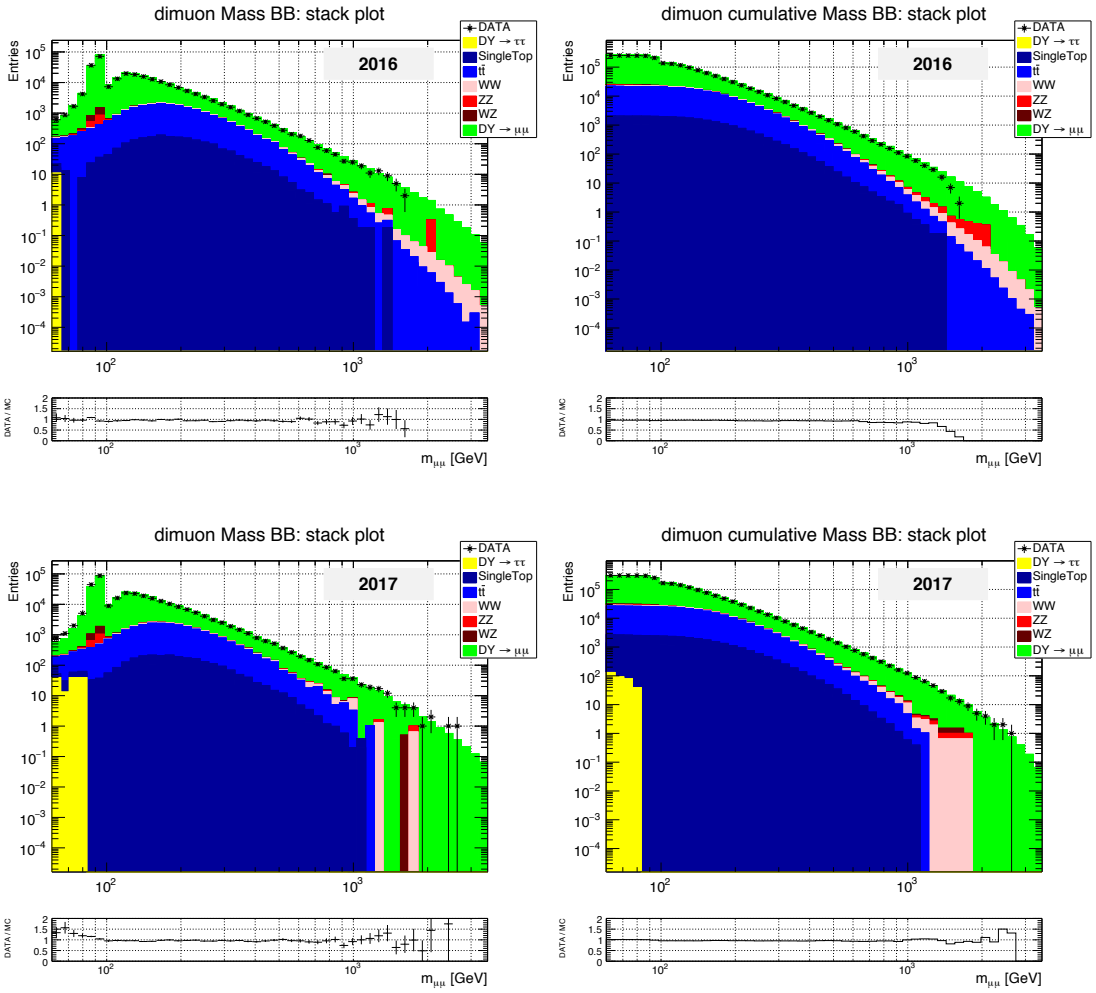

Figure 5.22: The observed invariant mass spectra, for BB category, for 2016 (on top) and 2017 (on bottom), together with the different SM backgrounds highlighted (on the right the cumulative one). In the bottom panel, data/MC ratio.

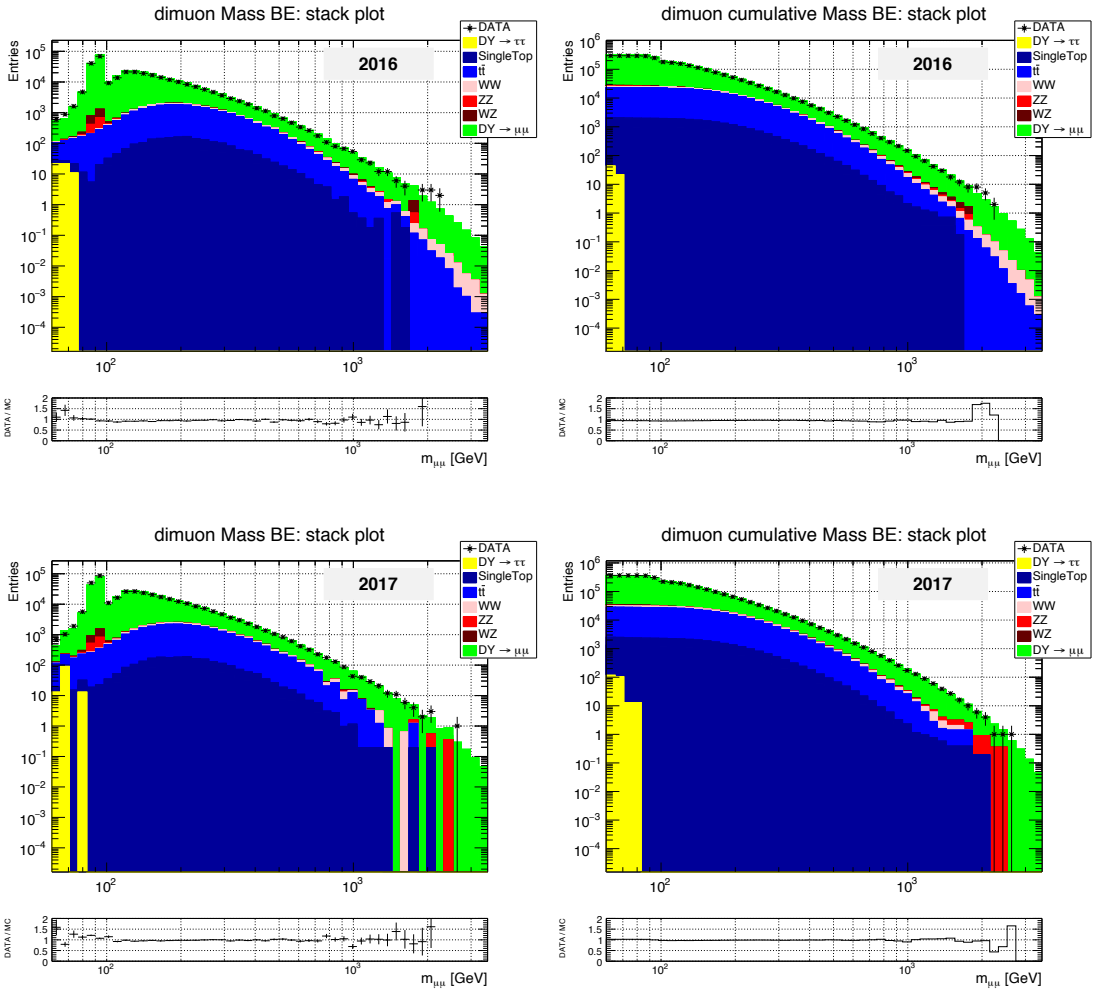

Figure 5.23: The observed invariant mass spectra, for BE category, for 2016 (on top) and 2017 (on bottom), together with the different SM backgrounds highlighted (on the right the cumulative one). In the bottom panel, data/MC ratio.

2016 Muon p_T, η and ϕ distributions are shown in Figure 5.24. Looking at the muon p_T distribution in the barrel region ($|\eta| < 1.2$), Figure 5.24(b), a deficit in data with respect to simulation starting at around 700 GeV can be observed. I have therefore performed different checks (L1 pre-firing, shower, TuneP assignment) but nothing suspicious was found. The deficit is still compatible with a statistical fluctuation (2.9σ).
Figure 5.25 shows the distribution of number of pixel hits and number of tracker layers comparing 2016 and 2017. It is clearly visible the upgrade in 2017 of the tracker system.

5.8 Signal parametrisation

5.8.1 Signal acceptance and efficiency

For dimuons passing the selection defined in sec. 5.4, I have evaluated the combined reconstruction and selection efficiency as a function of the dimuon mass: the result for 2016 is shown in Figure 5.26: similar results were found in 2017. These acceptance $\times$ efficiency values, evaluated using DY samples from 50 to 6000 GeV, are valid for Spin-1 resonances. For the interpretation of the analysis in Spin-2 models, I have used the RS Graviton signal samples. The muons from the decay of the resonance are more central, the efficiency is higher in the BB category and slightly lower in the BE category. The overall efficiency is higher compared to Spin-1 resonances. The resulting efficiency curves, for 2016 and 2017, are shown in Figure 5.27.
The fit of the acceptance times efficiency is used to parametrise the Z' efficiency and is one of the inputs to the final limit setting that will be discussed in sec. 5.9.
These results are then corrected for the single muon ID and reconstruction efficiencies in data (see sec. 5.4.1 and 5.3.1), applying a SF for each muon, depending on the muon momentum and on η. The new acceptance $\times$ efficiency parametrisation obtained from DY simulation as a function of mass are displayed in Figure 5.28. The ratio between the nominal one (weight = 1, black curve) and the new parametrisation (red curve) is taken as systematic on the signal efficiency (for both 2016 and 2017).

5.8.2 Mass resolution

Mass experimental resolution is determined from DY simulation as a function of the generated dimuon mass in different pseudorapidity categories. For each considered mass bin, the residual has been measured comparing the reconstructed mass with the generated one: each residual is then fit using Cruijff function, the experimental function describing the resolution. This function is a Gaussian with asymmetric exponential tails, described in Eq. 5.4:

$$f(m) = N \times e^{\frac{-(m-\bar{m})^2}{2\sigma^2+\alpha(m-\bar{m})^2}} \tag{5.4}$$

The resolution is defined as the σ of the aforementioned function. The resolution parametrisation obtained from MC is shown in Figure 5.29.

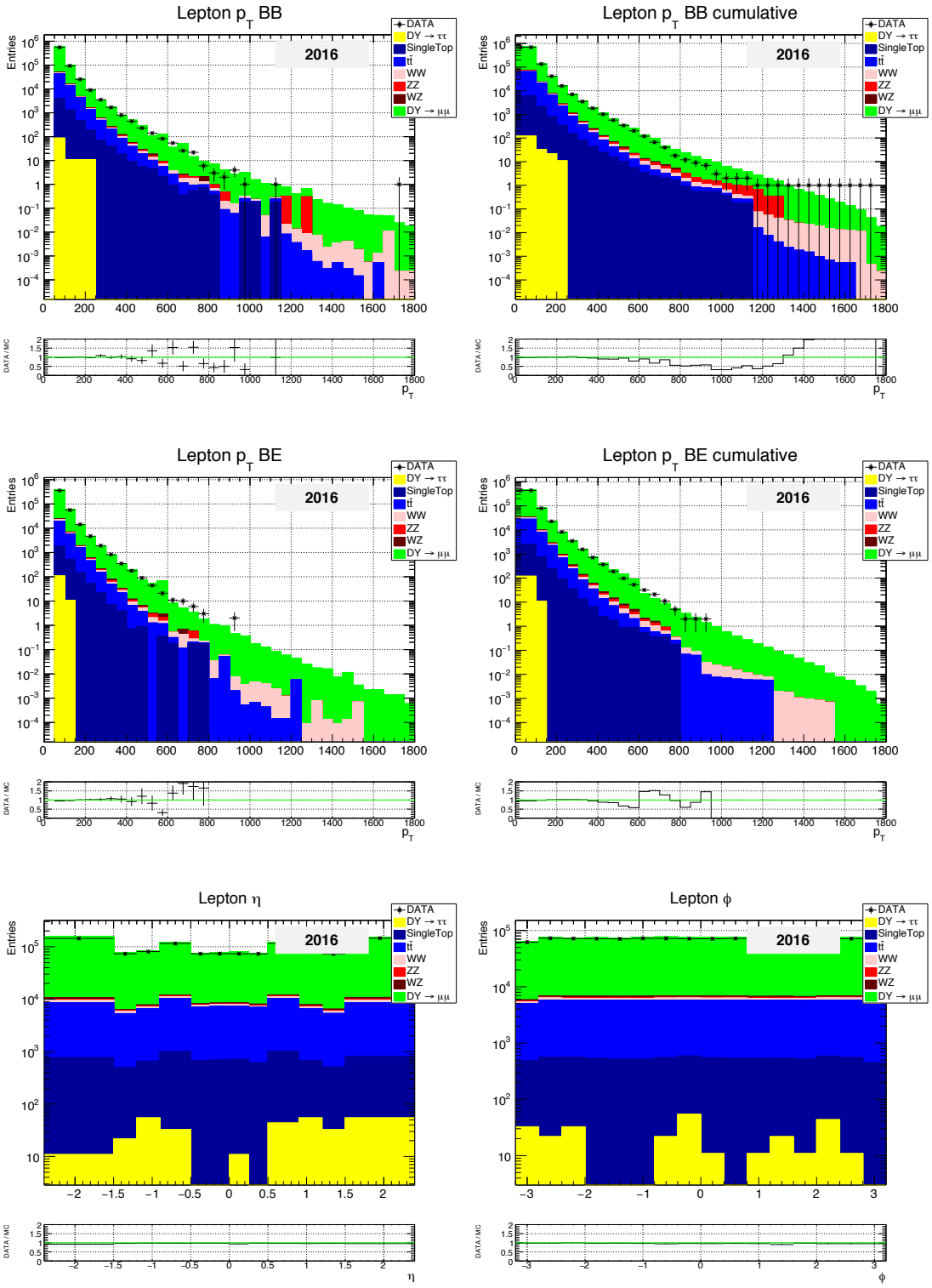

Figure 5.24: Data (black dots) and MC (stack histogram) distribution for different variables: BB lepton p_T (on the right the cumulative plot) on top; BE lepton p_T (on the right the cumulative plot) in the middle; lepton η on the left, lepton ϕ on the right, on bottom. In each plot, in the bottom panel, data/MC ratio is shown.

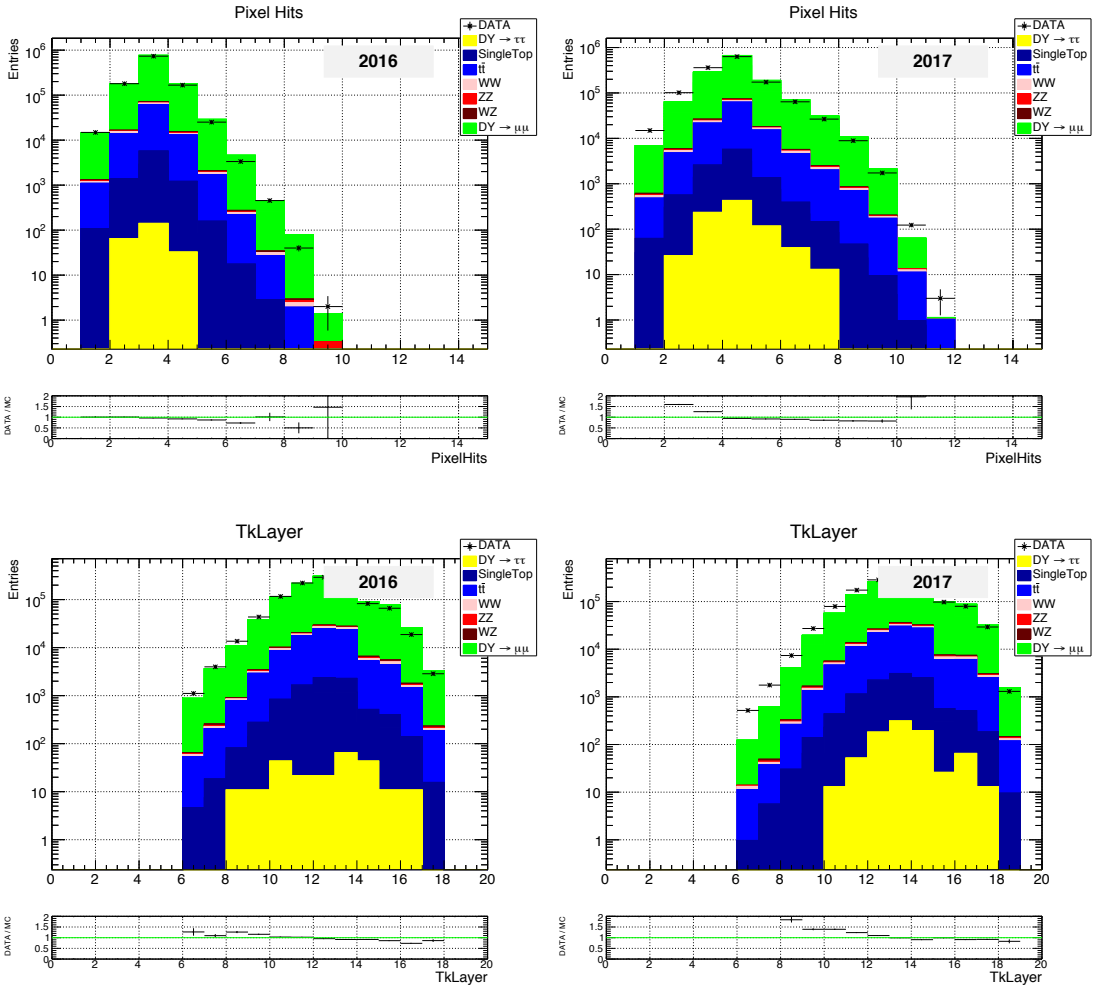

Figure 5.25: Data (black dots) and MC (stack histogram) distribution for different variables in 2016 and 2017: number of pixel hits distribution in 2016 (on the left) and in 2017 (on the right) on top; number of tracker layers distribution in 2016 (on the left) and in 2017 (on the right) on bottom. In each plot, in the bottom panel, data/MC ratio is shown.

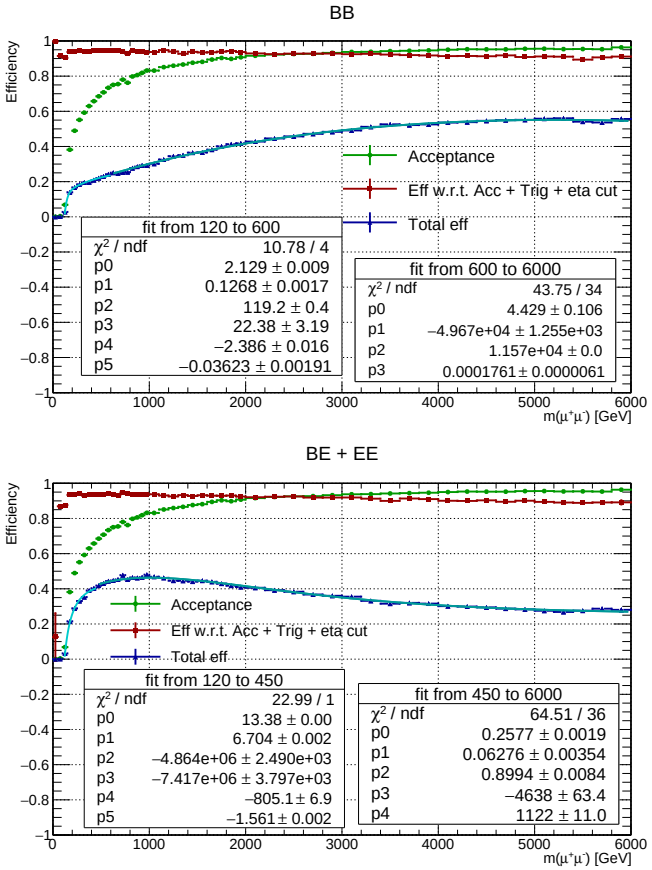

Figure 5.26: The combined reconstruction and selection efficiency, for Spin-1 resonance, as a function of the invariant mass, for dimuon passing the selection (section 5.4) with respect to all events in acceptance (red), the total acceptance times efficiency (blue), and the acceptance (green), as evaluated on simulated Drell-Yan events: on top for BB category and on bottom for BE category.

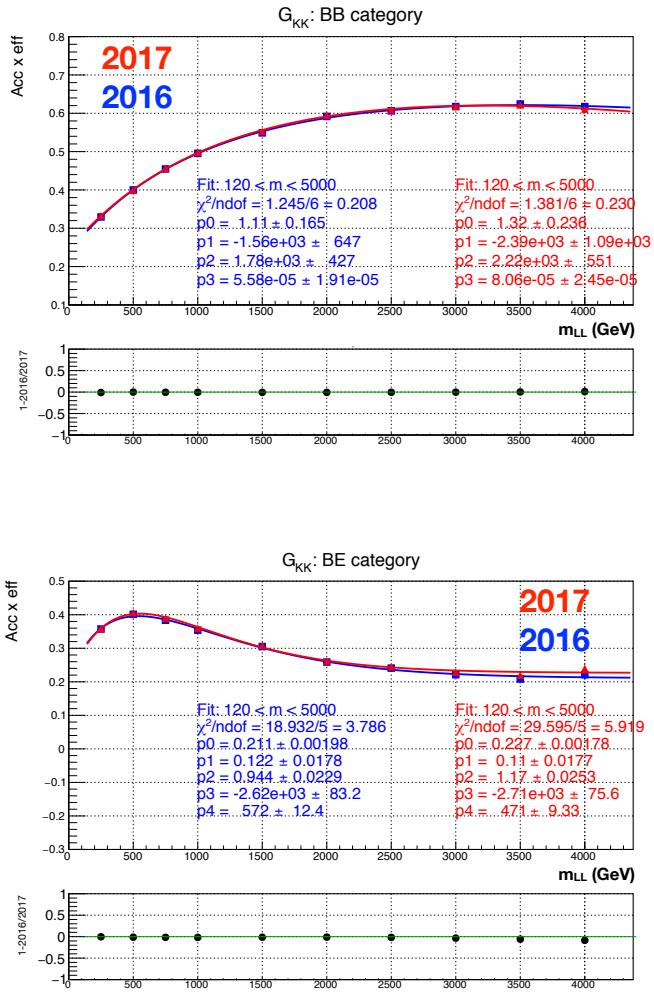

Figure 5.27: Acceptance × efficiency, as a function of the invariant mass, for 2016 (in blue) and 2017 (in red) for dimuons passing the selection for the case of Spin-2 resonances, for BB on top and BE on bottom. In the bottom panel, relative difference in reported.

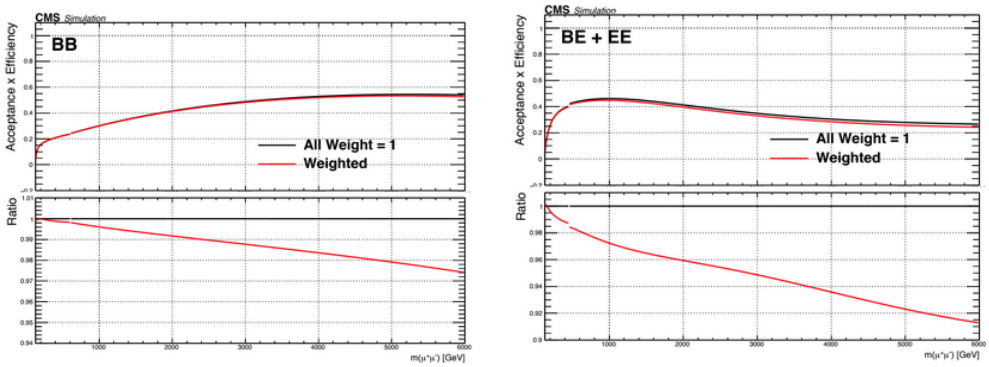

Figure 5.28: Shown is the acceptance × efficiency as a function of mass obtained after applying the weights on single muon (p, η) coming from the reconstruction and ID efficiencies (see sec. 5.3.1 and 5.4.1).

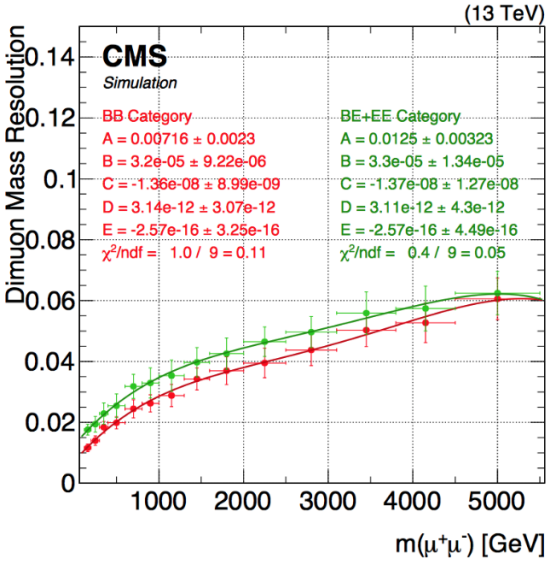

Figure 5.29: Dimuon mass resolution parametrisation as a function of the invariant mass, obtained from DY samples: in red for BB and in green for BE category. The values of the fit function are also displayed.

For each of the rapidity categories, the resolution is parametrised using a fourth order polynomial:

$$\sigma_{\mu^+\mu^-}(m) = A + B \cdot m + C \cdot m^2 + D \cdot m^3 + E \cdot m^4 \tag{5.5}$$

A systematic uncertainty, for 2016 and 2017, used in the limit setting tools, is derived for each point, by fitting the residual using a Crystal–Ball and take as uncertainty on the resolution the difference between this value and the one obtained using the Cruijff function. This uncertainty is displayed as a function of the mass in Figure 5.30: as the dependence is almost flat, a 15% is taken as uncertainty for both categories for all masses.

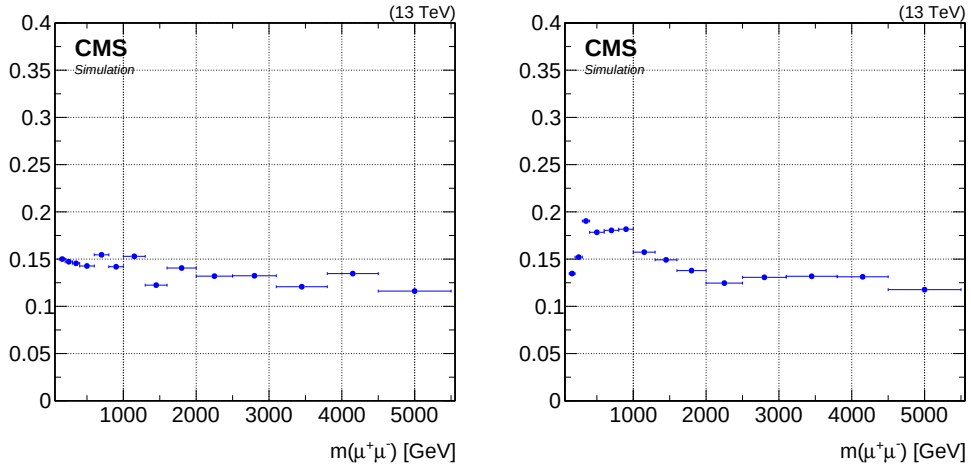

Figure 5.30: Systematic error of the dimuon mass resolution as a function of the invariant mass, obtained from Drell–Yan samples. Left shows the systematic error obtained for the BB category and right the one for BE category.

Mass resolution has also been evaluated as a function of muon p_T comparing data and simulation. In this case, the resolution is defined as the σ of the function used (the convolution of the Cruijff with the Breit-Wigner) to fit the reconstructed mass in the range around Z peak (75 - 105 GeV). In the BB category the simulated resolution is about 5% better than the resolution from data; for the BE category, which is extremely limited by statistics, it is between 10% and 20% better than the one from data. Results are displayed in Figure 5.31.

Dimuon mass resolution comparison between 2016 and 2017

Figure 5.32 shows dimuon mass resolution evaluated comparing 2016 with 2017: as can be seen, there is an improvement of about 25% in the barrel region ($|\eta|$ <0.9). This improvement is mainly due to new alignment scenario evaluated using full 2016 data.

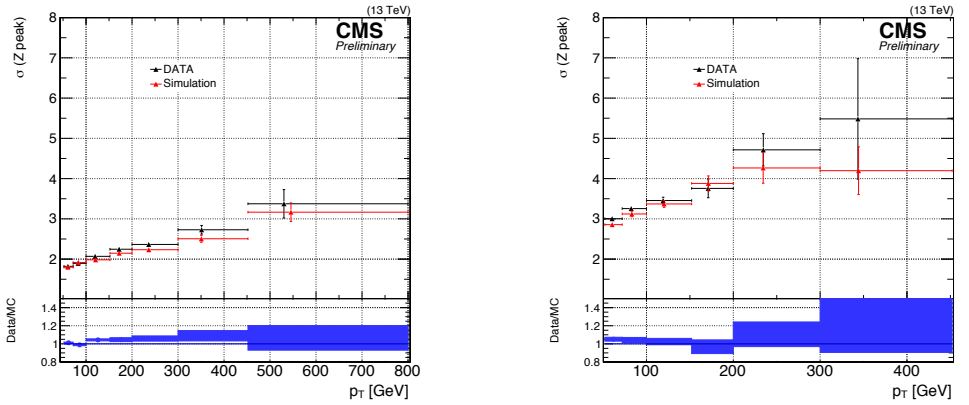

Figure 5.31: Mass muon resolution parametrisation as a function of the muon p_T for BB (left) and BE (right) events. In red simulation while in black data. In the bottom panel, data/MC ratio is shown.

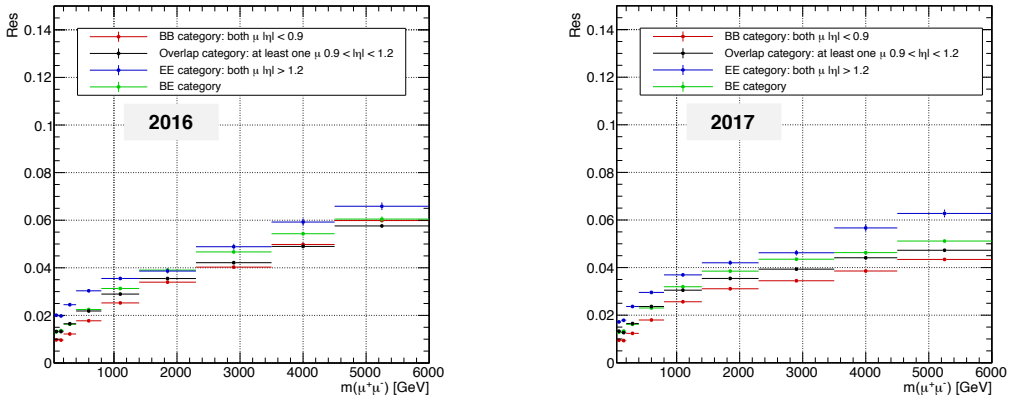

(a) 2016 resolution

(b) 2017 resolution

Figure 5.32: Dimuon mass resolution as a function of the mass for different $|\eta|$ regions comparing 2016 (on the left) and 2017 (on the right).

5.8.3 Mass scale

The response of the detector to the dimuon mass may evolve as the mass increases due to the fact that at high-p_T, muons are sensitive to the detector alignment. There are a number of effects originating from the intrinsic limits of the apparatus used for the measurement (a non perfect alignment or a systematic distortion of the muon system chambers), which can bias the measurement of the muon curvature and thus of its transverse momentum. In order to evaluate the uncertainty related to the measurement of the transverse curvature, the generalised endpoint method is used: this method consists in injecting a bias in Drell-Yan simulated events and evaluate if, and eventually how, it modifies the mass spectrum. This bias is estimated looking at the value must be applied to simulated events to match the charge/p_T (q/p_T) distribution found in data: these values are displayed in Figure 5.33 and represent the bias that minimise the differences in bins of η and ϕ. These results are obtained for TuneP p_T assignment and for muon above 200 GeV in the region $|\eta| < 2.1$ and above 100 GeV in the forward region $|\eta| > 2.1$ (due to low statistics in the forward region above 200 GeV). Once the bias has been

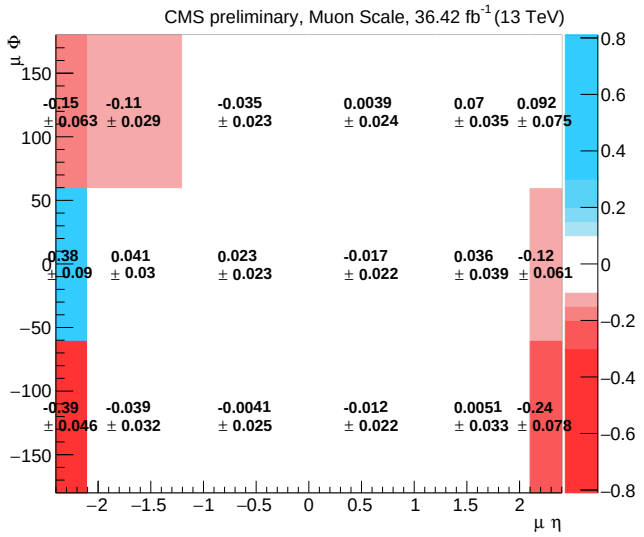

Figure 5.33: Scale bias as a function of η and ϕ for muon with p_T >200 (100) GeV in the region $|\eta| < 2.1$ ($|\eta| > 2.1$), to apply in the MC in order to reproduce the q/p_T data distribution.

evaluated, it is applied to each muon and as a function of its charge, η and ϕ according to Figure 5.33. For each muon, the shift is done according to a Gaussian that takes as central value the central correction and as width the error assigned on the measurement. This correction has been performed only for the BE category, given the p_T bias consistent with zero in the barrel. Figure 5.34 shows dimuon mass resolution with and without the p_T corrected by the q/p_T bias for the BE category.

To estimate instead the effect of the measured q/p_T bias to the dimuon mass recon-

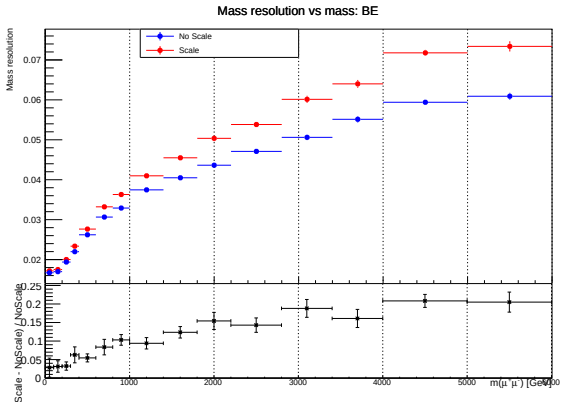

Figure 5.34: Dimuon mass resolution with (in red) and without (in blue) the p_T scale propagated, for DY simulated events. In the bottom panel, the relative difference is reported.

structed with data, the mass is measured after applying a shift to the muon p_T. The shift is applied to each muon and as a function of the charge, η and ϕ according to figure 5.33 only considering the central correction. This correction has been performed only for the BE events. For different mass ranges, the relative residuals have been plotted comparing the reconstructed mass with the value obtained correcting the muon p_T: $(mass - mass_{corrected})/mass$. Figure 5.35 shows the relative residual distribution in the region $M > 800$ GeV and the mean value of such distributions as a function of the mass. No shift is observed in the mass value corrected by the q/p_T bias. The maximum shift observed is within 0.2% up to 800 GeV and within 1% at higher masses.

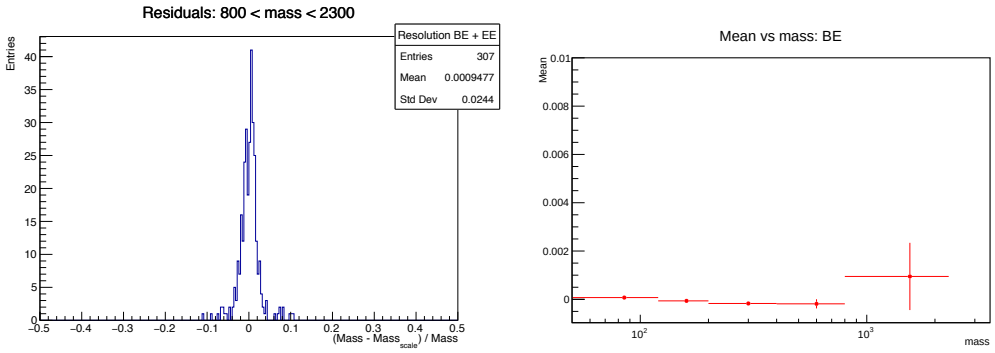

Figure 5.35: Relative mass residuals (left) estimated comparing the reconstructed mass with and without the p_T bias correction in data, for events with $M > 800$ GeV. Mean values (right) of the relative mass residuals, as a function of the mass.

5.9 Results

A shape analysis using an unbinned maximum likelihood fit of dimuon invariant mass values m (the observable) to search for a resonant peak on-top of the smooth background distribution is used to test the existence of a new resonance. Data is fit with a sum of signal and background shapes, with the signal fraction as a free parameter.
In the absence of an excess over the SM expectation, the 95% confidence level (C.L.) upper limits are set on the ratio R_σ of the production cross section times branching fraction for high-mass resonances to that for the Z boson:

$$R_\sigma = \frac{\sigma(pp \to Z' + X \to \mu^+\mu^- + X)}{\sigma(pp \to Z + X \to \mu^+\mu^- + X)} = \frac{N(Z' \to \mu^+\mu^-)}{N(Z \to \mu^+\mu^-)} \times \frac{A(Z \to \mu^+\mu^-)}{A(Z' \to \mu^+\mu^-)} \times \frac{\varepsilon(Z \to \mu^+\mu^-)}{\varepsilon(Z' \to \mu^+\mu^-)}\,, \tag{5.6}$$

where N is the number of events, A is the detector acceptance, and ε is the total selection efficiency.

5.9.1 Systematic

The idea to extract limit on the ratio R_σ of $\sigma \times Br$ for high-mass resonances with respect to the Z boson led to cancel out a lot of experimental and theoretical uncertainties, leaving only the ones depending on the mass. The following sources of uncertainties have been studied for each of the two pseudorapidity categories and are considered in the limit setting tools:

- **Selection and reconstruction efficiency**: based on the observed Data/MC disagreement/agreement, for a 4 TeV mass the systematic applied for BB events is -1.5 % and -6.5 % for BE events (see Figure 5.28).

- **Trigger Efficiency**: based on the trigger efficiency measurements a systematic uncertainty of 0.3% in the BB and 0.7% in the BE category is assigned.

- **Momentum resolution**: a systematic uncertainty of 15% has been assigned based on differences in the measured resolution obtained with different parameterisations.

- **Momentum scale**: no significant shift in mass to higher or lower values has been observed within statistical uncertainties. A conservative uncertainty of 1% for barrel and 3% in endcap, based on the uncertainty in the highest mass bin in Figure 5.35, is assigned to the mass scale and used in the statistical interpretation.

5.9.2 Likelihood

An extended unbinned likelihood function is used; the signal-plus-background likelihood is defined as:

$$\mathcal{L}(\mathbf{m}|R_\sigma,\boldsymbol{\nu}) = \frac{\mu(R_\sigma,\boldsymbol{\nu})^N e^{-\mu(R_\sigma,\boldsymbol{\nu})}}{N!} \cdot \prod_{i=1}^{N} \left(\frac{\mu_{sig}(R_\sigma,\boldsymbol{\nu})}{\mu(R_\sigma,\boldsymbol{\nu})} f_{sig}(m_i|\boldsymbol{\nu}) + \frac{\mu_{bkg}(\boldsymbol{\nu})}{\mu(R_\sigma,\boldsymbol{\nu})} f_{bkg}(m_i|\boldsymbol{\nu}) \right), \tag{5.7}$$

where the product is taken over all N events observed above 200 GeV (events in the data set $\mathbf{m}$), $\boldsymbol{\nu}$ is the vector of the nuisance parameters and $\mu(R_\sigma,\boldsymbol{\nu}) = \mu_{sig}(R_\sigma,\boldsymbol{\nu}) + \mu_{bkg}(\boldsymbol{\nu})$ is the sum of the Poisson mean of the signal and background event yields (total number of events expected). The $f_{sig}(m_i|\Gamma,M,\omega)$ and $f_{bkg}(m_i|\boldsymbol{\nu})$ are the probability density functions that describe the signal and the background respectively. The signal is parametrised by the convolution of a Breit-Wigner of width Γ and mass M (describing the intrinsic signal shape) and a Cruijff distribution of width ω (describing the experimental resolution); the background instead is described by the fit function 5.3.
The expected signal yield μ_{sig} is a function of the signal cross section to that of the Z:

$$\mu_{sig} = R_\sigma \frac{\epsilon_{Z'}}{\epsilon_Z} N_Z. \tag{5.8}$$

where $\epsilon_{Z'}$ and ϵ_Z are, respectively, the acceptance times efficiency (A$\times\varepsilon$) of the Z' and the Z, and N_Z is the number of selected events at the Z peak.

5.9.3 Limits

Starting from Equation 5.7, confidence intervals are computed using Bayesian approach [96]. Only events in a window of ± 6 times the mass resolution around the probed signal mass are considered in the likelihood fit. At high masses, the edges of the window are symmetrized so that there is a minimum of 100 events in the window. This procedure sets the level of the statistical uncertainty in the local background amplitude; the level is chosen to dominate the expected systematic uncertainties in the background shape at high mass. The total background uncertainty ranges from approximately 3% at 200 GeV to 12% at 5 TeV. At low mass it is driven by normalisation uncertainties (5%); while at high mass, PDFs (7%) are the dominant sources of uncertainty.
A positive, flat prior is used for the signal cross section (which yields good frequentist coverage properties, since μ_{sig} is Poisson mean), and log-normal priors for the systematic uncertainties.

The 95% C.L. upper limits, for 2016, 2017 and their combination, for an assumed intrinsic width of 0.6% of the resonance mass, are shown in Figure 5.36. There is good agreement between expected and observed limits, with all fluctuations staying within the two-sigma uncertainty band. The resulting mass limits are 4.6 TeV for the Z'_{SSM} and

4.0 TeV for the Z'_ψ, to be compared with the previous one of 3.22 and 2.77 TeV [3].
Wider resonances, 3%, 5%, and 10%, are also considered and the corresponding limits

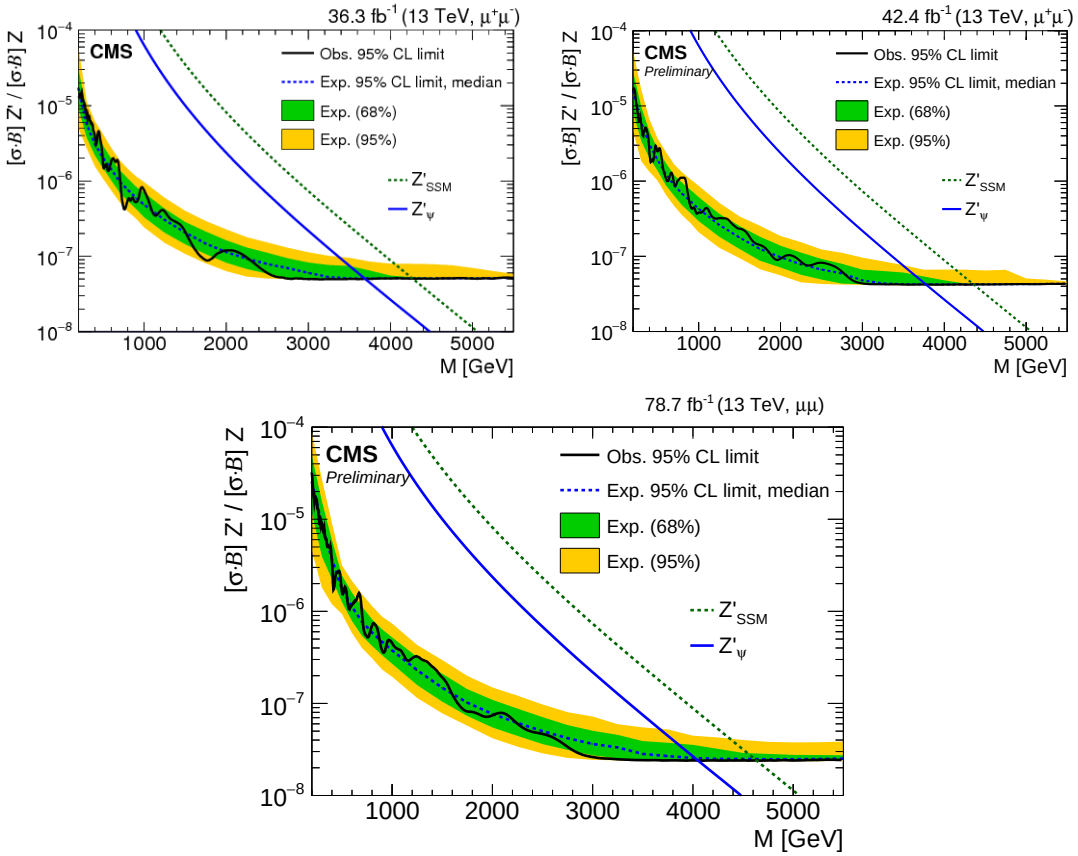

Figure 5.36: The 95% C.L. upper limits on the product of production cross section and branching fraction for a Spin-1 resonance with a width equal to 0.6% of the resonance mass, relative to the product of production cross section and branching fraction of a Z boson for 2016 data (top left), 2017 (top right) and their combination (bottom). The shaded bands correspond to the 68% and 95% quantiles for the expected limits. Theoretical predictions are shown for comparison.

are shown in Figure 5.37 (only for 2016 data). At high masses, where no events are observed, no difference between the widths assumptions is observed. Towards lower masses, the sensitivity decreases slightly for wider resonances, as they are less easily distinguished from the background. Compared to the default width of 0.6%, an increased width results in less stringent observed and expected limits, and the structures of the observed limit curve are washed out.

In Figure 5.38, the 95% C.L. upper limits, for Spin-2 resonances are shown. As the intrinsic width of the RS graviton is very small, reaching only about 1.4% at $k/\bar{M}_{\rm pl} = 0.1$,

[3] obtained combining Run I data at 8 TeV with 2015 data from Run II at 13 TeV [3]

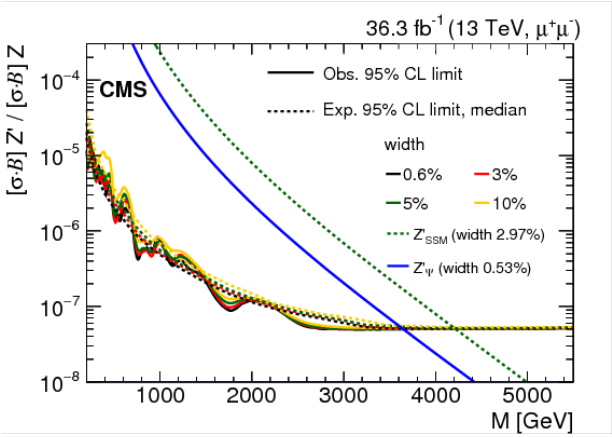

Figure 5.37: The 95% C.L. upper limits on the product of production cross section and branching fraction for a Spin-1 resonance, for widths equal to 0.6, 3, 5, and 10% of the resonance mass, relative to the product of production cross section and branching fraction of a Z boson for 2016 data. Theoretical predictions are shown for comparison [5].

the limits are calculated with an assumed width of 0.6%. Given the increased signal efficiency, the limits are slightly more stringent compared to ones for Spin-1 resonances, especially at lower masses. Depending on $k/\bar{M}_{\rm pl}$, the limits are 2.2, 3.8 and 4.39 TeV for 0.01, 0.05 and 0.1 coupling parameter values, to be compared with the previous one of 1.26 and 3.03 TeV respectively [4].

5.10 Dark Matter interpretation

The results of the analysis performed searching for a new massive resonance can be reinterpreted in the context of simplified models of Dark Matter (DM) particles that obtain sizeable interactions with fermions through an additional Spin-1 high-mass particle mediating the SM - DM interaction. The simplified models contain a Dirac DM particle, χ, and a mediator, Z', which can be a (pseudo-)scalar, vector, or axial-vector particle, which is produced in the s-channel. (Pseudo-)Scalar mediator are not relevant in the leptonic final state as the branching fraction into leptons would be very small because of their small Yukawa couplings. The free parameters of the models are the masses of the DM particle and the mediator, $m_{\rm DM}$ and $m_{\rm med}$, and the couplings of the mediator to quarks and the DM particle, g_q and $g_{\rm DM}$. For the new models relevant to this search, a non-zero couplings to lepton g_ℓ has been added. The two relevant models are

- Vector model (V2) with small couplings to leptons: $g_{\rm DM} = 1.0$, $g_q = 0.1$, $g_\ell = 0.01$.
- Axial-vector model (A2) with equal couplings to leptons and quarks: $g_{\rm DM} = 1.0$, $g_q = g_\ell = 0.01$.

[4] obtained combining Run I data at 8 TeV with 2015 data from Run II at 13 TeV. Coupling constant of 0.05 was considered for the first time for this thesis [3]

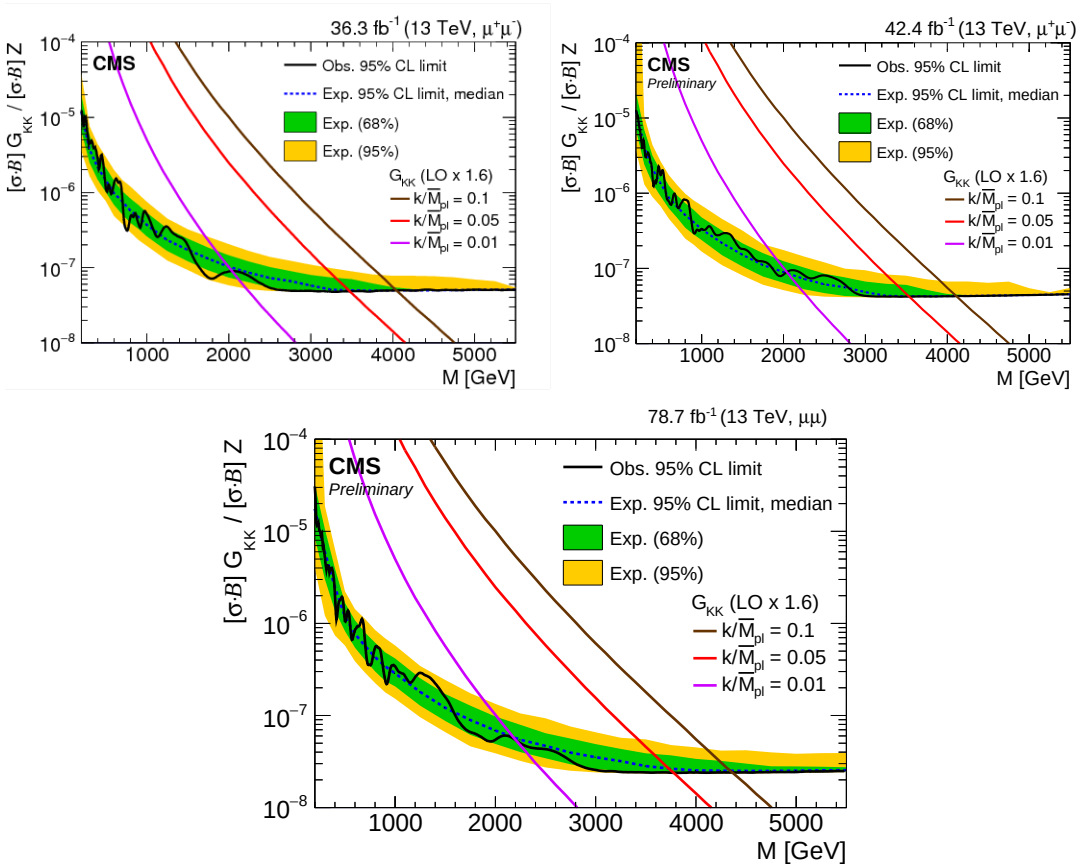

Figure 5.38: The 95% C.L. upper limits on the product of production cross section and branching fraction for a Spin-2 resonance, relative to the product of production cross section and branching fraction of a Z boson for 2016 data (top left), 2017 (top right) and their combination (bottom). The shaded bands correspond to the 68% and 95% quantiles for the expected limits. Theoretical predictions for the Spin-2 resonances with widths equal to 0.01, 0.36, and 1.42 GeV corresponding to coupling parameters $k/\bar{M}_{\mathrm{pl}}$ of 0.01, 0.05, and 0.10 are shown for comparison.

Limits in the $m_{\mathrm{DM}}-m_{\mathrm{med}}$ plane are shown in Figure 5.39 for V2 and A2 signal model, for 2017 only data. In the V2 model, the impact of the dilepton search is moderate, as expected from the small size of the couplings of the mediator to leptons in this case. In the A2 model, however, where the couplings to leptons are equal to those to quarks, the inclusion of the dimuon final state greatly improves the exclusion limit. In the first case, the limit on the mediator mass reaches up to 1.3 TeV, depending on m_{DM}, in the latter the limit reaches roughly 3 - 3.8 TeV, again depending on the mass of the DM particle.

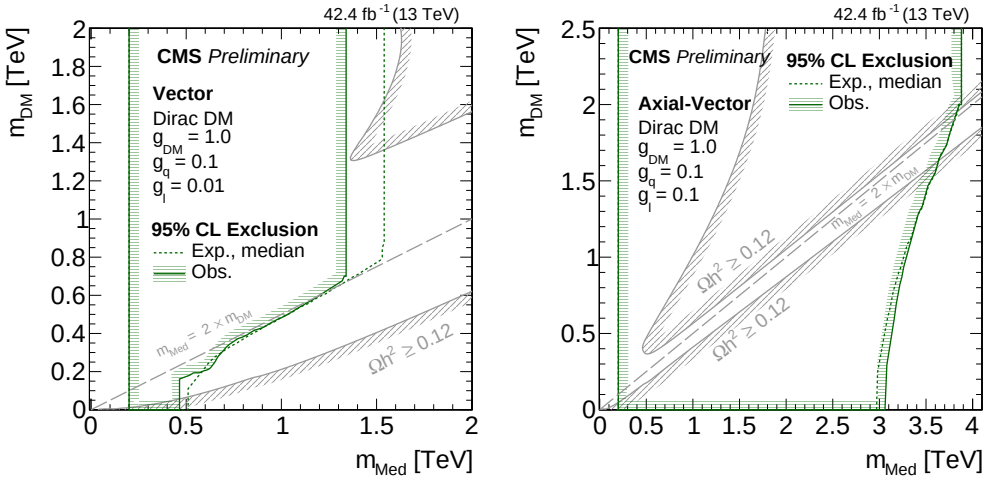

Figure 5.39: The 95% C.L. expected and observed exclusion limits on the masses of a mediator boson and of a DM particle in a simplified model, assuming vector (left) or axial-vector (right) couplings between the mediator, and the SM fermions and DM particle, also assumed to be Dirac fermion, for 2017 only data. The parameter exclusion is obtained by comparing the limits on the production cross section times branching fraction for a Z boson to the values obtained from calculations in the simplified model. The lines with the hatching represents the excluded regions. The solid grey lines, marked as "Ωh^2 >0.12", correspond to parameter regions that reproduce the observed DM relic density in the universe [28,97–99], with the hatched area indicating the region where the DM relic abundance exceeds the observed value.

5.11 Outlook

The analysis for the search for new resonances predicted in many models BSM has been done using only 2016 and 2017 data at 13 TeV: 2018 data will double the statistics. A further increase to the centre-of-mass energy of 14 TeV is planned until the end of LHC run. With the full dataset of an integrated luminosity around 3 ab^{-1}, foreseen before the end of High - Luminosity LHC, the discovery potential (5σ) for new resonances can reach masses beyond 5.5 TeV.

Conclusion

Searches for resonances decaying into muon pairs with the CMS experiment at LHC have been presented.
Since 2012, using data collected during Run I and Run II at 7, 8 and 13 TeV, the Higgs boson has been observed in various decay modes, e.g. diboson, diphoton, $b\bar{b}$ and $\tau^+\tau^-$. Despite the $H \to \mu\mu$ observation still misses, this decay mode plays a fundamental role to study the properties of the second generation leptons. A precise measurement of the Higgs boson, produced via Vector Boson Fusion (VBF) and decaying into two muons has been performed using 2016 data collected at 13 TeV corresponding to 35.9 fb^{-1}. While the experimental sensitivity to the VBF process is very high, the dimuon decay channel suffers for its low branching ratio, 2.18×10^{-4} (compared to 5.84×10^{-1} for the $b\bar{b}$ that is the highest). So only 30 events were expected in 2016 data.
In order to face this low statistics, I have performed a feasibility study on the implementation of a new approach to distinguish signal events from the backgrounds, the multivariate analysis (MVA). This technique consists in combining in different way a set of variables in order to extract one single output capable to discriminate between signal and background. In this work I have used a binary tree (BDTG) and a neural network (MLP). The first is a binary tree structured classifier in which repeated left/right (yes/no) decisions are taken on one single variable at a time until a stop criterion is fulfilled; the latter is a simulated collection of inter-connected neurons, with each neuron producing a certain response at a given set of input signals. By applying an external signal to some (input) neurons the network is put into a defined state that can be measured from the response of one or several (output) neurons. Given the MVA outputs, I have done a maximum likelihood fit of the full distributions using 2016 data, corresponding to an integrated luminosity of 35.9 fb^{-1}, including the systematic uncertainties, finding best results using MLP. The 95% C.L. upper limit on expected σ/σ_{SM} is 2.35. The final expected significance has been extracted and it is 0.94. Latest CMS published results, using 2016 data and all Higgs boson production mechanism (not only VBF), were 2.45 for σ/σ_{SM} and a significance of 0.9 [1].
VBF Higgs boson production decaying into muon pairs search has been presented during the CMS Collaboration Meeting in Budapest on the 4th of October 2018. Due to the very promising results, the VBF channel treated with the MVA method will be used in combination with the other production modes to extract final results on the search for the Higgs boson, in view of the 2019 Winter conferences.

For this thesis I have analysed 2016 data: at the end of Run III (2023), LHC will have collected around 300 fb^{-1} enough for the $H \to \mu\mu$ evidence; the observation of this decay channel instead is foreseen during High - Luminosity LHC (starting from 2026), thanks to an integrated luminosity greater than 1 ab^{-1}.
Despite the Higgs boson observation, the SM is not complete and there are physics aspects it is not able to take into account. In order to try to solve these issues, many models have been developed beyond the Standard Model (BSM) and within these, new bosons are introduced. New physics would manifest itself in a change of the dimuon invariant mass spectrum. In this thesis, different models have been probed: Sequential Standard Model and Grand Unified Theory that involve the introduction of one new Spin-1 boson Z'_{SSM} and Z'_{ψ}; Extra Dimension Model with the introduction of Gravity and the associated Kaluza-Klein Spin-2 graviton, G_{KK}. The results have been also reinterpreted in the context of the Dark Matter (DM) sector, searching for the DM-SM mediator. Since these new bosons are predicted with mass of the order of TeV, muon reconstruction and selection was optimised for high efficiency at high energies. The muon reconstruction plays a crucial role since the muon performance at high momentum is strongly affected by radiative processes (electromagnetic showers or hard bremsstrahlung) and by the muon detector alignment. Specialised algorithms for high-energy muon reconstruction, known as "TeV-muon" refits, have been developed in CMS and the final momentum assignment is performed by the so called "TuneP" algorithm, which chooses the best muon track candidate. TuneP performances have also been studied in this thesis.
The search for new resonances has been performed using data collected during 2016 and 2017 at 13 TeV corresponding to 36.2 fb^{-1} and 42.4 fb^{-1}. The results have been found consistent with Standard Model predictions and exclude at 95% C.L. a Spin-1 Z'_{SSM} from the Sequential Standard Model with SM-like couplings, with a mass less than 4.60 TeV and a Spin-2 Z'_{ψ} from Grand Unified Theories with the E_6 gauge group, with a mass less than 4.0 TeV improving previous published results of 3.22 TeV and 2.77 TeV [3]. The corresponding limits for Spin-2 Kaluza-Klein Graviton arising in the Randall-Sundrum model of Extra Dimensions are 2.2 TeV, 3.8 TeV and 4.39 TeV with coupling parameters of 0.01, 0.05 and 0.1, respectively, raising previous published results of 1.26 TeV and 3.03 TeV [3] (the coupling 0.05 has been considered for this thesis). The results based on 2017 data have been reinterpreted, for the first time in CMS experiment, in the context of Dark Matter, where a vector (V2) or axial-vector (A2) Dark Matter-Standard Model mediator is introduced. In the V2 model, the impact of the dilepton search is moderate, as expected from the small size of the couplings of the mediator to leptons in this case. In the A2 model, however, where the couplings to leptons are equal to those to quarks, the dimuon final state greatly improves the exclusion limit. In the V2 model, the limit on the mediator mass reaches up to 1.3 TeV, depending on M_{DM}, while in the A2 model the limit reaches roughly 3 - 3.8 TeV, again depending on the mass of the DM particle.
The search for physics BSM, using 2016 and 2017 data, has been approved on the 9th of January 2019 by the CMS Collaboration. I have presented results using 2016 data [5] at La Thuile conference, during the *Les Rencontres de Physique de la Vallèe d'Aoste* at

the end of February 2018.
The analysis of the search for new resonances predicted in models BSM has been performed using 78.6 fb^{-1}: 2018 data will double the statistics. A further increase to a centre-of-mass energy of 14 TeV is planned until the end of LHC run. With the full dataset of an integrated luminosity around 3 ab^{-1}, foreseen before the end of High - Luminosity LHC, the discovery potential (5σ) for new resonances can reach masses beyond 5.5 TeV [100].

Bibliography

[1] The CMS Collaboration, "*Search for the Higgs boson decaying to two muons in proton-proton collisions at* $\sqrt{s}$ *= 13 TeV*", Submitted to: Phys. Rev. Lett, 2018, arXiv:1807.06325.

[2] The ATLAS Collaboration, "*Search for the Dimuon Decay of the Higgs Boson in pp Collisions at* $\sqrt{s}$ *= 13 TeV with the ATLAS Detector*", Phys. Rev. Lett. 119, 051802, Published 4 August 2017

[3] The CMS Collaboration, "*Search for narrow resonances in dilepton mass spectra in proton-proton collisions at* $\sqrt{s}$ *= 13 TeV and combination with 8 TeV data*, Phys. Lett. B 768 (2017) 57, 10.1016/j.physletb.2017.02.010

[4] The ATLAS Collaboration, "*Search for high-mass new phenomena in the dilepton final state using proton-proton collisions at* $\sqrt{s}$ *= 13 TeV with the ATLAS detector*, Physics Letters B 761 (2016) 372-392

[5] The CMS Collaboration, "*Search for high-mass resonances in dilepton final states in proton-proton collisions at* $\sqrt{s}$ *= 13 TeV*", JHEP 1806 (2018) 120, 10.1007/JHEP06(2018)120

[6] C. Patrignani et al. "*Particle Data Group*", Chin. Phys. C, 40, 100001 (2016) and 2017 update.

[7] UA1 Collaboration, "*Experimental observation of isolated large transverse energy electrons with associated missing energy at* $\sqrt{s}$*=540 GeV.*", Phys.Lett. B122 (1983) 103-116, DOI: 10.1016/0370-2693(83)91177-2

[8] UA1 Collaboration, "*Experimental observation of lepton pairs of invariant mass around* 95 GeV/c^2 *at the CERN SPS collider.*", Phys.Lett. B126 (1983) 398-410, DOI: 10.1016/0370-2693(83)90188-0

[9] S. Weinberg, "*A model of leptons*", Phys. Rev. Lett. 19 (1967) 1264.

[10] MuLan Collaboration, "*Improved Measurement of the Positive Muon Lifetime and Determination of the Fermi Constant*", Phys.Rev.Lett.99:032001,2007, arXiv:0704.1981. C.H. Llewellyn Smith, Phys. Lett. B46, 233 (1973).

[11] ATLAS Collaboration, "*Observation of a new particle in the search for the Standard Model Higgs boson with the ATLAS detector at the LHC*", Phys.Lett. B716 (2012), pp. 1-29, DOI: 10.1016/j.physletb.2012.08.020.

[12] The CMS Collaboration, "*Observation of a new boson at a mass of 125 GeV with the CMS experiment at the LHC*", Physics Letters B716 (2012), pp. 30-61. DOI: http://dx.DOI.org/10.1016/j.physletb.2012.08.021 .

[13] LHC Higgs Cross Section Working Group, https://twiki.cern.ch/twiki/bin/view/LHCPhysics/LHCHXSWG.

[14] D. de Florian et al., "*LHC Higgs Cross Section Working Group*", CERN-2017-002-M, arXiv:1610.07922[hep-ph] (2016).

[15] The CMS Collaboration, "*Observation of $t\bar{t}H$ production*", arXiv:1804.02610 [hep-ex] (2018)

[16] The CMS Collaboration, "*An event candidate for the production of a top quark and top anti-quark pair in conjunction with a Higgs Boson in the CMS detector.*", CMS-PHO-EVENTS-2018-004, https://cds.cern.ch/record/2621446

[17] The CMS Collaboration, "*Figures used for the CMS update on LHCP2018 Conference*", CMS-PHO-EVENTS-2018-005, https://cds.cern.ch/record/2622190

[18] The ATLAS Collaboration, "*Measurement of the Higgs boson coupling properties in the $H \to ZZ^* \to 4l$ decay channel at $\sqrt{s}$ =13 TeV with the ATLAS detector*", High Energ. Phys. (2018) 2018: 95. https://doi.org/10.1007/JHEP03(2018)095

[19] S. Heinemeyer et al., "*LHC Higgs Cross Section Working Group*", CERN-2013-004, arXiv:1307.1347 [hep-ph] (2013).

[20] The CMS Collaboration, "*Combined measurements of the Higgs boson's couplings at $\sqrt{s} = 13 TeV$*", CMS-PAS-HIG-17-031, http://cds.cern.ch/record/2308127

[21] The ATLAS Collaboration, "*Combined measurements of Higgs boson production and decay using up to 80 fb^{-1} of proton–proton collision data at $\sqrt{s}$ = 13 TeV collected with the ATLAS experiment*", ATLAS-CONF-2018-031, http://cds.cern.ch/record/2629412

[22] J. Ellis and T. You, "*Global analysis of the Higgs candidate with mass ≈125 GeV*", J. High Energy Phys. 09 (2012) 123, doi:10.1007/JHEP09(2012)123, arXiv:1207.1693.

[23] J. Ellis and T. You, "*Updated global analysis of Higgs coupling*", J. High Energy Phys. 06 (2013) 103, doi:10.1007/JHEP06(2013)103, arXiv:1303.3879.

[24] G. Altarelli, B. Mele, and M. Ruiz-Altaba, "*Searching for New Heavy Vector Bosons in pp Colliders*", Z.Phys., vol. C45, p. 109, 1989. doi:10.1007/BF01552335,10.1007/BF01556677.

[25] A. Leike, "*The Phenomenology of Extra Neutral Gauge Bosons*", arXiv:hep-ph/9805494v1

[26] N. Arkani-Hamed, S. Dimopoulos and G. Dvali "*The Hierarchy Problem and New Dimensions at a Millimeter*", arXiv:hep-ph/9803315v1

[27] L. Randall and R. Sundrum, "*A Large Mass Hierarchy from a Small Extra Dimension*", arXiv:hep-ph/9905221v1

[28] A. Albert et al., "*Recommendations of the LHC Dark Matter Working Group: Comparing LHC searches for heavy mediators of dark matter production in visible and invisible decay channels*", (2017). arXiv:1703.05703.

[29] Lyndon Evans and Philip Bryant, "*LHC Machine*", 1748-0221-3-08-S08001, Journal of Instrumentation (2008), http://stacks.iop.org/1748-0221/3/i=08/a=S08001

[30] The CMS Collaboration, "*CMS Luminosity - Public Results.*", https://twiki.cern.ch/twiki/bin/view/CMSPublic/LumiPublicResults

[31] W.J. Stirling, private communication.
http://www.hep.ph.ic.ac.uk/wstirlin/plots/crosssections2012_v5.pdf

[32] Dulat, Sayipjamal and Hou, Tie-Jiun and Gao, Jun and Guzzi, Marco and Huston, Joey and Nadolsky, Pavel and Pumplin, Jon and Schmidt, Carl and Stump, Daniel and Yuan, C.-P., "*New parton distribution functions from a global analysis of quantum chromodynamics*", Phys. Rev. D 93, 033006, 10.1103/PhysRevD.93.033006

[33] The CMS Collaboration, "*The Compact Muon Solenoid technical proposal*", CERN-LHCC-94-38, http://cdsweb.cern.ch/record/290969

[34] The CMS Collaboration, "*The CMS tracker system project: technical design report*", CERN-LHCC-98-006, http://cdsweb.cern.ch/record/368412.

[35] The CMS Collaboration, "*The CMS tracker: addendum to the technical design report* CERN-LHCC-2000-016, http://cdsweb.cern.ch/record/490194.

[36] Anirban Saha, "*Phase 1 upgrade of the CMS pixel detector*", Journal of Instrumentation (2017), http://stacks.iop.org/1748-0221/12/i=02

[37] The CMS Collaboration, "*The hadron calorimeter project: technical design report*", CERN-LHCC-97-031, http://cdsweb.cern.ch/record/357153.

[38] The CMS Collaboration, "*Precise Mapping of the Magnetic Field in the CMS Barrel Yoke using Cosmic Rays*", JINST 5:T03021,2010, 10.1088/1748-0221/5/03/T03021

[39] The CMS Collaboration, "*The CMS muon project, technical design report*", CERN-LHCC-97-032, http://cdsweb.cern.ch/record/343814.

[40] The CMS Collaboration, "*Performance of the CMS muon detector and muon reconstruction with proton-proton collisions at $\sqrt{s}$ = 13 TeV*", JINST 13 (2018) no.06, P06015 arXiv:1804.04528 [physics.ins-det] CMS-MUO-16-001, CERN-EP-2018-058

[41] The CMS Collaboration, "*Performance of the CMS Muon Detectors in 2016 collision runs*", CERN-CMS-DP-2016-046

[42] The CMS Collaboration, "*CMS. The TriDAS project. Technical design report, vol. 1: The trigger systems.*" 2000, CERN publication CERN-LHCC

[43] The CMS Collaboration, "*CMS The TriDAS Project: Technical Design Report, Volume 2: Data Acquisition and High-Level Trigger. CMS trigger and data-acquisition project. Technical Design Report CMS.* Geneva: CERN, 2002. url: http://cds.cern.ch/record/578006.

[44] The CMS Collaboration, "*The computing project Technical Design Report*", CERN/LHCC 2005-23, June 2005.

[45] T.Sjöstrand et al., "*An Introduction to PYTHIA 8.2*", Comput. Phys. Commun.191(2015) 159, doi:10.1016/j.cpc.2015.01.024, arXiv:1410.3012.

[46] P. Nason, "*A new method for combining NLO QCD with shower Monte Carlo algorithms*", JHEP 11 (2004) 040, doi:10.1088/1126-6708/2004/11/040, arXiv:hep-ph/0409146.

[47] S. Frixione, P. Nason, and C. Oleari, "*Matching NLO QCD computations with parton shower simulations: the POWHEG method*", JHEP 11 (2007) 070, doi:10.1088/1126-6708/2007/11/070, arXiv:0709.2092.

[48] S. Alioli, P. Nason, C. Oleari, and E. Re, "*A general framework for implementing NLO calculations in shower Monte Carlo programs: the POWHEG BOX*", JHEP 06 (2010) 043, doi:10.1007/JHEP06(2010)043, arXiv:1002.2581.

[49] S. Alioli, P. Nason, C. Oleari, and E. Re, "*NLO vector-boson production matched with shower in POWHEG*", JHEP 07 (2008) 060, doi:10.1088/1126-6708/2008/07/060, arXiv:0805.4802.

[50] S. Frixione, P. Nason, and G. Ridolfi, "*A positive-weight next-to-leading-order Monte Carlo for heavy flavour hadroproduction*", JHEP 09 (2007) 126, doi:10.1088/1126-6708/2007/09/126, arXiv:0707.3088.

[51] E. Re, "*Single-top Wt-channel production matched with parton showers using the POWHEG method*", Eur. Phys. J. C 71 (2011) 1547, doi:10.1140/epjc/s10052-011-1547-z, arXiv:1009.2450.

[52] J. Alwall, M. Herquet, F. Maltoni, O. Mattelaer, and T. Stelzer, "*MadGraph 5 : Going Beyond*", JHEP 1106 (2011) 128, [arXiv:1106.0522].

[53] GEANT4 Collaboration, "*GEANT4: a simulation toolkit*", Nucl. Instrum. Meth. A 506 (2003) 250, doi:10.1016/S0168-9002(03)01368-8.

[54] ROOT, http://root.cern.ch.

[55] Sirunyan, A. M. and others, "*Particle-flow reconstruction and global event description with the CMS detector*", JINST, 12, 2017, P10003, 10.1088/1748-0221/12/10/P10003

[56] Chatrchyan, Serguei and others, "*Description and performance of track and primary-vertex reconstruction with the CMS tracker*", JINST 9 (2014) P10009, 10.1088/1748-0221/9/10/P10009,

[57] P. Billoir, "*Progressive track recognition with a Kalman like fitting procedure*", Comput. Phys. Commun. 57 (1989) 390.

[58] P. Billoir and S. Qian, "*Simultaneous pattern recognition and track fitting by the Kalman filtering method*", Nucl. Instrum. Meth. A 294 (1990) 219.

[59] The CMS Collaboration, "*https://twiki.cern.ch/twiki/bin/view/CMSPublic/PhysicsResultsTRK*"

[60] K. Rose, "*Deterministic Annealing for Clustering, Compression, Classification, Regression and related Optimisation Problems*", Proc. IEEE 86 (1998) 2210.

[61] R. Frühwirth, W. Waltenberger and P. Vanlaer, "*Adaptive Vertex Fitting*", CMS Note 2007-008 (2007).

[62] Khachatryan, Vardan and others, "*Electron and photon performance in CMS with the full 2016 data sample.*", CMS-DP-2017-004 ; CERN-CMS-DP-2017-004

[63] W.Adam, R.Frühwirth, A.Strandlie, and T.Todorov, "*Reconstruction of electrons with the Gaussian-sum filter in the CMS tracker at LHC*", J. Phys. G 31 (2005) N9, doi:10.1088/0954-3899/31/9/N01.

[64] The CMS Collaboration "*Electron and Photon performance in CMS with the full 2017 data sample and additional 2016 highlights for the CALOR 2018 Conference*", CMS-DP-2018-017 ; CERN-CMS-DP-2018-017

[65] The CMS Collaboration, "*Performance of the CMS muon detector and muon reconstruction with proton-proton collisions at* $\sqrt{s}$ *= 13 TeV*", JINST 13 (2018) P06015, DOI: 10.1088/1748-0221/13/06/P06015, arXiv:1804.04528

[66] The CMS Collaboration, "*Performance of CMS muon reconstruction in pp collision events at* $\sqrt{s}$ *= 7TeV*", JINST 7 (2012) P10002, doi 10.1088/1748-0221/7/10/P10002, arXiv 1206.4071

[67] R.Frühwirth, "*Application of Kalman filtering to track and vertex fitting*", Nucl.Instrum. Meth. A 262 (1987) 444, doi:10.1016/0168-9002(87)90887-4.

[68] The CMS Collaboration, "*Muon identification and isolation efficiencies with 2017 and 2018 data*", CMS DP -2018/042

[69] Cacciari, Matteo and Salam, Gavin P. and Soyez, Gregory, "*The anti-k_t jet clustering algorithm*", JHEP, 04, 2008, 063, 10.1088/1126-6708/2008/04/063

[70] Cacciari, Matteo and Salam, Gavin P. and Soyez, Gregory, "*FastJet user manual*", Eur. Phys. J. C, 72, 2012, 1896, 10.1140/epjc/s10052-012-1896-2

[71] Sirunyan, Albert M and others, "*Identification of heavy-flavour jets with the CMS detector in pp collisions at 13 TeV*", JINST, 13 (2018) P05011, doi 10.1088/1748-0221/13/05/P05011,

[72] The CMS Collaboration, "*Identification of b quark jets at the CMS Experiment in the LHC Run 2*, CMS-PAS-BTV-15-001

[73] Chatrchyan, Serguei and others, "*Missing transverse energy performance of the CMS detector*", JINST, 16 (2011), P09001, doi 10.1088/1748-0221/6/09/P09001, arXiv:1106.5048

[74] J. Alwall et al., "*The automated computation of tree-level and next-to-leading order differential cross sections, and their matching to parton shower simulations*", JHEP 07 (2014) 079, doi:10.1007/JHEP07(2014)079, arXiv:1405.0301.

[75] NNPDF Collaboration, "*Parton distributions for the LHC Run II*", JHEP 04 (2015) 040, doi:10.1007/JHEP04(2015)040, arXiv:1410.8849.

[76] P. Artoisenet, R. Frederix, O. Mattelaer, and R. Rietkerk, "*Automatic spin-entangled decays of heavy resonances in Monte Carlo simulations*", JHEP 03 (2013) 015, doi:10.1007/JHEP03(2013)015, arXiv:1212.3460.

[77] Sirunyan, Albert M and others, "*Measurement of the inelastic proton-proton cross section at $\sqrt{s} = 13$ TeV*", JHEP, 07(2018), P161, doi:10.1007/JHEP07(2018)161, arXiv:1802.02613

[78] A. Bodek, A. van Dyne, J. Y. Han, W. Sakumoto, A. Strelnikov, "*Extracting Muon Momentum Scale Corrections for Hadron Collider Experiments*", JHEP 10 (2012) 72, DOI:10.1140/epjc/s10052-012-2194-8, arXiv:1208.3710v3 [hep-ex]

[79] F. Schissler and D. Zeppenfeld, "*Parton shower effects on W and Z production via vector boson fusion at NLO QCD*", JHEP 04 (2013) 057, doi:10.1007/JHEP04(2013)057, arXiv:1302.2884.

[80] The CMS Collaboration, "*Search for the Higgs boson decaying to two muons in proton-proton collisions at $\sqrt{s}$= 13 TeV*", arXiv:1807.06325 [hep-ex]

[81] Hoecker, A.; Speckmayer, P.; et al.,"*TMVA - Toolkit for Multivariate Data Analysis*", arXiv:physics/0703039.

[82] Glen Cowan, Kyle Cranmer, Eilam Gross, Ofer Vitells, "*Asymptotic formulae for likelihood-based tests of new physics*", 10.1140/epjc/s10052-011-1554-0, arXiv:1007.1727v3

[83] A. L. Read, "*Presentation of search results: the CLs technique*", J. Phys. G 28 (2002) 2693, doi:10.1088/0954-3899/28/10/313.

[84] The CMS Collaboration, "*CMS Luminosity Measurements for the 2016 Data Taking Period*", Tech. rep. CMS-PAS-LUM-17-001. Geneva: CERN, 2017

[85] The CMS Collaboration, "*Determination of Jet Energy Calibration and Transverse Momentum Resolution in CMS*", In: JINST 6 (2011), P11002. DOI:10.1088/1748-0221/6/11/P11002, arXiv:1107.4277

[86] N. Kidonakis, "*Differential and total cross sections for top pair and single top production*", in Proceedings of the XX International Workshop on Deep-Inelastic Scattering and Related Subjects. Bonn, Germany, 2012. arXiv:1205.3453. doi:10.3204/DESY-PROC-2012-02/251.

[87] M. Czakon, P. Fiedler, and A. Mitov, "*Total top-quark pair-production cross section at hadron colliders through $O(\alpha_s^4)$*", Phys. Rev. Lett. 110 (2013) 252004, doi:10.1103/PhysRevLett.110.252004, arXiv:1303.6254.

[88] J. M. Campbell and R. K. Ellis, "*MCFM for the Tevatron and the LHC*", Nucl. Phys. B Proc. Suppl. 205-206 (2010) 10, doi:10.1016/j.nuclphysbps.2010.08.011, arXiv:1007.3492.

[89] NNPDF Collaboration, "*Parton distributions from high-precision collider data*", arXiv:1706.00428

[90] M. Czakon and A. Mitov, "*Top++: A Program for the Calculation of the Top-Pair Cross-Section at Hadron Colliders*", Comput. Phys. Commun. 185 (2014) 2930, doi:10.1016/j.cpc.2014.06.021, arXiv:1112.5675.

[91] M. R. Whalley, D. Bourilkov, and R. C. Group, "*The Les Houches accord PDFs (LHAPDF) and LHAGLUE*", in HERA and the LHC: A Workshop on the implications of HERA for LHC physics. Proceedings, Part B. 2005. arXiv:hep-ph/0508110.

[92] D. Bourilkov, R. C. Group, and M. R. Whalley, "*LHAPDF: PDF use from the Tevatron to the LHC*", in TeV4LHC Workshop - 4th meeting Batavia, Illinois, October 20-22, 2005. (2006). arXiv:hep-ph/0605240.

[93] A. Buckley et al., "*LHAPDF6: parton density access in the LHC precision era*", Eur. Phys. J. C 75 (2015) 132, doi:10.1140/epjc/s10052-015-3318-8, arXiv:1412.7420.

[94] The CMS Collaboration, "*Performance of muon reconstruction including Alignment Position Errors for 2016 Collision Data*", CMS DP-2016/067

[95] Y. Li and F. Petriello, "*Combining QCD and electroweak corrections to dilepton production in FEWZ*, Phys. Rev. D86 (2012) 094034, doi:10.1103/PhysRevD.86.094034, arXiv:1208.5967.

[96] The CMS Collaboration, "*Search for physics beyond the standard model in dilepton mass spectra in proton-proton collisions at* $\sqrt{s} = 8\ TeV$", arXiv:1412.6302

[97] Planck Collaboration, "*Planck 2015 results. XIII. Cosmological parameters*", Astron. Astrophys. 594 (2016) A13, doi:10.1051/0004-6361/201525830, arXiv:1502.01589.

[98] M. Backovic, K. Kong, and M. McCaskey, "*MadDM v.1.0: Computation of Dark Matter Relic Abundance using MADGRAPH5*", Phys. Dark Univ. 5-6 (2014) 18, doi:10.1016/j.dark.2014.04.001, arXiv:1308.4955.

[99] M. Backovic et al., "*MadDM: New dark matter tool in the LHC era*", AIP Conf. Proc. 1743 (2016) 060001, doi:10.1063/1.4953318, arXiv:1509.03683.

[100] The CMS Collaboration, "*Projected performance of an upgraded CMS detector at the LHC and HL-LHC: Contribution to the snowmass process.*", arXiv:1307.7135.